UNIVERSITAT DE BARCELONA

Directed cell migration: forces, shapes, and fluctuations in tissues

From active hydrodynamics to experiments

Irina Pi Jauma

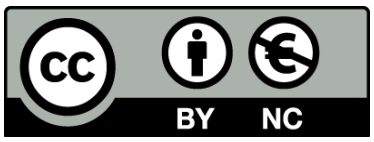

PhD Thesis

UNIVERSITAT DE BARCELONA

Directed cell migration: forces, shapes, and fluctuations in tissues

From active hydrodynamics to experiments

Irina Pi Jaumà

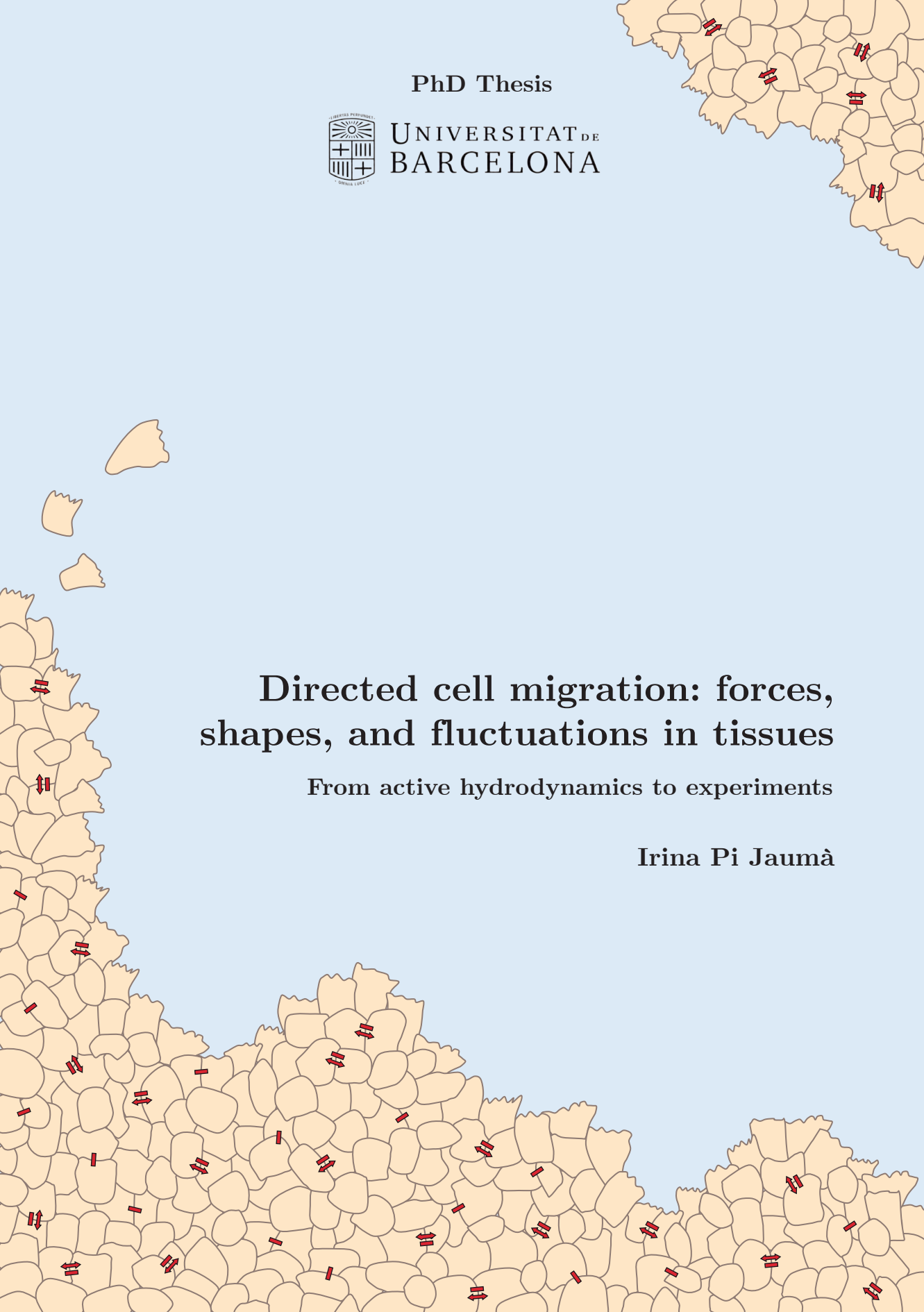

Directed cell migration: forces, shapes, and fluctuations in tissues

From active hydrodynamics to experiments

Memòria presentada per optar al grau de doctora per la

Universitat de Barcelona

Programa de doctorat en Física

Autora:

Irina Pi Jaumà

Director:

Jaume Casademunt Viader

Tutor:

Giancarlo Franzese

Universitat de Barcelona

Irina Pi Jaumà
Departament de Física de la Matèria Condensada
Facultat de Física
Universitat de Barcelona

Directed cell migration: forces, shapes, and fluctuations in tissues.
Ph.D. Thesis
Programa de doctorat en Física
Barcelona, Novembre 2024

The work described in this thesis has been financially supported by Ministerio de Ciencia, Innovación y Universidades (MICIU) through the Ph.D. Fellowship FPU19/05492. The research stay in the Max Planck Institute for the Physics of Complex Systems in Dresden (MPI-PKS) was also funded by MICIU through a short-term fellowship EST24/00183 and by a complementary grant from G-Research (February 2024 Grant Winners).

The work has also been supported by Ministerio de Economía, Comercio y Empresa (MINECO) under the projects PID2019-108842GB-C21 and PID2022-137713NB-C22; and from Generalitat de Catalunya under the projects AGAUR SGR-2017-SGR-1061 and SGR-2021-00450, and an ICREA-Academia award to J.C.

"Here's a pool of water
Let's jump in!
Ooh- there's a whale.
Yeah, let's grab it by the tail.
Wow, it's pulling us to the moon!"

Uri Alon.
Performing Science (2013).

Als meus pares, i
a l'àvia Rosa.

Acknowledgements

These four years have been an incredible journey, both scientifically and personally, of discovering and contributing to an exciting research topic, and of learning about myself and from all the people I've shared the path with. I feel immensely grateful to have encountered such amazing people during these years, and it is without a doubt thanks to each and every one of you that I made it here. This thesis is also yours.

Jaume, per on començo? Gràcies per tantes coses. Per confiar en mi des del treball de fi de grau, quan jo pràcticament no sabia què era fer recerca, pels teus consells sobre on fer el màster i per voler-me de tornada a fer el doctorat. Gràcies de fet, per confiar amb mi tot i que jo no ho feia, i per preocupar-te per mi quan jo estava nerviosa per no tenir resultats. Gràcies per transmetre'm amb passió els teus coneixements i ajudar-me sempre. He gaudit molt aprenent física de tu al dia a dia, sempre en un ambient tan proper i amigable. Però també aprenent de la vida i del que és fer investigació. Gràcies per haver-me donat la llibertat i l'empenta d'anar a escoles d'estiu, d'embrancar-me a fer experiments, i animar-me a marxar uns mesos d'estada a l'estranger. Per fer-me veure, en definitiva, que si bé els resultats i les publicacions són importants per la satisfacció de contribuir al coneixement, l'experiència de fer el doctorat era molt més que això.

No tinc germans grans, però Ricard, tu n'ets el meu acadèmic! Inevitablement els germans petits es comparen—i els comparen—molt amb els grans, però des d'una sana admiració per mi això ha estat també tot un aprenentatge. Tot i que quan vaig començar tu ja volaves per Princeton, t'agraeixo moltíssim que hagis estat sempre tan accessible, amb un tracte proper i comprensiu. Gràcies per la teva ajuda amb el model de durotaxi, les teves idees i visió científica global, i la teva paciència. Venir tres mesos a Dresden va ser certament de les millors experiències que n'he tret del doctorat, ampliant la visió de la recerca i de com es treballa a altres instituts. Gràcies per rebre'm amb els braços oberts i de fer-me sentir tant part del group.

Un altre agraïment molt important és per en Xavi i en Pere, per obrir-me les portes primer dels seus lab meetings, i després les del laboratori mateix. Tot i que vam començar la col·laboració totalment de forma telemàtica, aprendre de vosaltres, Xavi, Macià, Raimon i Isabela, va ser súper enriquidor i motivant per veure que els nostres models teòrics eren aplicables a quelcom real. Macià,

gràcies també per les xerrades properes i sinceres, només ens coneixíem a través d'una pantalla i jo tenia la sensació de conèixer-te de feia molt més temps. Potser no te'n vas adonar, però vas ser molt important per mi durant aquells inicis del doctorat, tot i que no era un moment fàcil per tu. Gràcies per portar-me dins el lab i ensenyar-me com cuidaves les cèl·lules. Crec que això em va motivar a voler-m'hi embrancar a fer-ho jo després. And this is what I did! Thank you Marija for getting involved in the project from the beginning and for teaching everything from scratch to someone with zero experience or knowledge of cells, pipetting, or basically anything in the lab. Thanks for your help, your patience, and also not only your scientific advice but life-regarding. Talking with you always took a weight off my shoulders.

A la facultat de Física, i sobretot amb el grup de la planta 6, hi he trobat un suport indispensable durant aquests anys. Va costar una mica d'arrencar, amb torns per no coincidir massa al despatx i coneixent-nos primer amb mascaretes, però no sé què hauria fet sense vosaltres. Sergio, començar alhora que tu ens va unir ja des del primer dia; Carla, gràcies per la teva immediata amistat, la nostra connexió i per fer que tot amb tu sigui tant fàcil; i Carol pel teu suport, empenta organitzant els lab tours, i per ser una referent per a mi en aquest camí. Als del despatx: Mattia, Aleix, Josep I, Josep II, Andreu i Honglian, gràcies per alleugerir els dies pesats quan les coses no sortien, veure-us al dia a dia i compartir les frustracions ha fet sovint el camí més planer. Joan, gràcies per explicar-me i posar en comú la part teòrica que va motivar els experiments que jo he fet, i Adrià i Gaspard, per ser amb mi els "caballeros del apocalipsis". Andreu, tu també et mereixeries aquest títol, gràcies per fluir tant com ho fas, i gràcies Giacomo per convertir-te en poc temps en un pilar i un referent dins i fora la universitat. Jasper, gràcies per organitzar amb mi els seminaris de l'UBICS i les colònies i per venir a viure amb nosaltres, et trobarem a faltar. I també gràcies Ana, Óscar, Jordi, Alex, Enric, Guille, Matt. Em deixo molts noms, però m'agradaria que tots els qui heu compartit algun moment amb mi entre passadissos, seminaris, classes, Sant Alberts o colònies durant aquests anys, us hi sentíssiu interpel·lats. De ben segur que m'heu alegrat molts moments.

People from IBEC in Xavi and Pere's labs: thanks for your warm and welcoming atmosphere since the very beginning, for the discussions in the lab meetings, your constant help with the experiments, and your friendship and plans outside the lab. You certainly create a beautiful, inspiring, and safe atmosphere for doing science. Marija, again, without you I wouldn't have enjoyed the lab so much for a year. Miquel, gràcies per cuidar sempre de tothom, i Kandela, per entendre'm tant i apuntar-te sempre a un bombardeo. I would love to say words for every one of you, but this would be too long—as if it's not going

to be—, so I really subscribe to all words of acknowledgement for every single one of you. Thanks to the master and PhD students, with whom I always felt understood: Miguel, Alice, Ona, Janet, Aina, Thomas, Rohit, Eva, Clément, Margherita, Yudish, Ibrahim, and Emmanuel. To those who graduated while I was in the lab, and were models to follow: Gerardo, Ignasi, Marc, Sefora, Sri, Nimesh, Zarina, and Isabela. And all the postdocs and technicians, from whom I appreciated a lot their experience and advice: Meng, Pau, Özge, Juanfra, Leone, Tom, Amy, Elena, Guillermo, Steffen, Manu, Anabel-Lise, Jorge, Laura, Mamatha, Valeria, Mònica, and Evelyn. Finally, thanks to Carlos and Marina who offered me access to their data. I wish I could have split myself in two to be fully present both in IBEC and in the Physics faculty at the same time, since I've often felt I wasn't fully in either one. But even if I was there partially, I'm very grateful to have met all of you. Being part of your lab was very rewarding and so much fun!

The stay in Dresden was just what I needed at that moment. Thanks to all the biophysics community from the PKS for making the scientific experience extremely enriching. Specially Ricard for welcoming me into his group and to all the members for the discussions. Hanno, thank you for including me everywhere and for your help from day one; thanks Peter for your contagious passion, and also Suchismita, Malcolm, Ashot and Rahul. Ahan, and Sagnik for being the best office mates I could ask for—except for Max/Harry the cat—, and also thanks Tarun, Kathrin, Ali, Omar, Talía, Ursa and Mariona. Giacomo, I need to say it again: thanks for having placed me in a WG of amazing people who made me understand better what Dresden meant for you. Grazie Marti, Ivan, Pippo, and Ale, for making me aware that another way of living and sharing is possible, and for making me feel at home and myself since the very first day. Gracias MJ por nuestras confesiones y ser mi aliade en el PKS. And thanks to all those who were also part of the WG, especially Jack, Lara, Julia, Burak, Vincenzo, Linda, Davide, Matteo and Daniel. It wouldn't have been the same without you.

I also want to thank Claudio and Lucas, whose friendship started in Cargèse but I'm certain that will last for much more time.

Gràcies als meus companys del grau, pels anys patint plegats anant amunt i avall entre dues facultats, però sobretot per la vostra amistat i aventures durant aquell temps. Txell i Sergi, gràcies per demostrar-me que hi seguiu sent, i també Jose, Pol, Elies, Blai, Marc i tots els altres.

A les Patxangueres, no m'imagino l'etapa de Barcelona sense vosaltres. Eli D, Vidi, Rous, Eli A, Chals, Mar, Anna Pla, Clara, Gemma i Mire. Judith, Flors i Laura, que feliç soc de compartir amb vosaltres el títol de físiques del

grup enmig de tanta metgessa! I Laura, quin privilegi compartir pis amb tu i en Joan, mira però que encara he d'aprendre a fer pa amb massa mare! Gràcies als dos pels dos anys compartits a Cal Cul. Paula, vas ser una descoberta molt bonica al pis. I Sara i Carla, que feliç que em fa saber del cert que us seguiré tenint sempre.

M'agradaria també recordar la Lluïsa, la meva professora de física de l'institut, que indiscutiblement és gran part de les raons que m'han portat fins aquí. Gràcies per despertar-me en mi la curiositat per la física, des d'una vessant tant humana.

Soc afortunadíssima de tenir una família meravellosa. Gràcies als de la Pera i als de Blanes, que veig menys del que voldria però sé que estan allà. Gràcies avi i Santi, que també esteu entre nosaltres. Gràcies als de Quart i la Bisbal, que aporteu il·lusió i vida sempre que ens veiem i amb tot el que feu. A la Neus, has sigut sempre una segona mare per a mi, igual que la Nona i el Tete els meus germans grans. Gràcies àvia per ser simplement, la millor. I perquè tot i no entendre bé el que faig i creure que ens perdem en tantes possibilitats, em transmets el que realment importa. Arlet, no podria tenir una millor companya d'aventures, gràcies per entendre'm tant i per compartir la lluita. Tu també ets la millor. Finalment papa i mama, gràcies per ensenyar-nos-ho tot i fer que la nostra educació fos una prioritat, per estar sempre aquí i recolzar-me en el mar de dubtes on molts cops m'he perdut. Em sap greu si us he fet patir a vegades, us estimo molt.

Quim, tu has sigut el pilar més important durant aquests anys. Sé que a vegades no ha sigut fàcil, gràcies pel teu suport i per creure en mi molt més que jo, per fer-me gaudir dels anys que hem compartit, i per encarar amb ganes els que venen.

And finally, thanks to anyone who has read all the way to the end! I couldn't keep it shorter because of how much this means to me.

Preface

This thesis presents my PhD research in biophysics, performed under the supervision of Jaume Casademunt at the University of Barcelona between November 2020 and November 2024. It covers different topics on collective cell migration in confluent epithelial tissues from a physics perspective.

Publications

The work in this thesis has been published in two articles:

- Pi-Jaumà, I., Alert, R. and Casademunt, J. Collective durotaxis of cohesive cell clusters on a stiffness gradient. *Eur. Phys. J. E* **45**, 7 (2022) — Chapter 2
- Pallarès, M.E.*, Pi-Jaumà*, I., Fortunato, I.C., Grazú, V., Gómez-González, M., Roca-Cusachs, P., de la Fuente, J.M., Alert, R., Sunyer, R., Casademunt, J. and Trepat, X. Stiffness-dependent active wetting enables optimal collective cell durotaxis. *Nat. Phys.* **19**, 279–289 (2023) — Chapter 3

And three more are in preparation, with the following tentative titles

- Pi-Jaumà, I. Casademunt, J. and Alert, R. Traction bistability of cell monolayers on strain-stiffening substrates. — Chapter 4
- Térmens, J.*, Pi-Jaumà, I.*, Lavi, I., Matejčić, M., Trepat, X. and Casademunt, J. Shape-sensing spontaneous motility of cell clusters. — Chapter 5
- Pi-Jaumà, I. and Casademunt, J. Fluctuating hydrodynamics of tissues: stochastic modeling of cell monolayers. — Chapter 6

* Equal contributions

Contents

Chapter 1

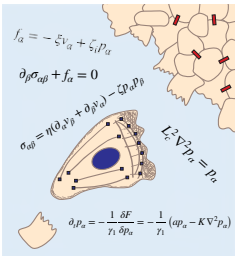

General introduction

Cell migration is a fundamental biological process that plays a crucial role in various physiological and pathological phenomena. In unicellular systems, the ability of a cell to migrate is essential, for instance, for finding the nutrients they need for survival. In many instances, however, cells tend to cluster and form crowded environments, coordinating their movement at a supra-cellular scale. Such collective cell migration is crucial in the embryonic development of multicellular organisms, generating the different functional organs and tissue shapes in processes such as morphogenesis and organogenesis. Collective cell migration also allows for tissue regeneration in wound healing and is crucial for homeostasis and immune response, whereas abnormal motility might lead to different pathologies. For instance, in cancer, the migration of tumor cells to healthy tissues triggers the metastasis.

Given its relevance and complexity, collective cell migration is usually tightly regulated at the transcriptional, protein localization, and functional levels, and the underlying mechanisms and signaling pathways are extremely intricate and difficult to decipher. However, the result is groups of cells translocating from one place to another, and so it is inherently a mechanical phenomenon, which must be governed by the general and most basic laws of physics. Consequently, in recent years, the emergence of the field of mechanobiology and the paradigm of active matter has shed light on its study in terms of physical forces and material parameters, shifting the focus away from the myriad of protein-ligand interactions or the triggered signaling cascades accompanying cell migration.

Then, within the hydrodynamic point of view developed in this thesis, tissues are modeled as active fluids. The complexity of biological regulation is thus phenomenologically encoded in a small number of material parameters, possibly space and time-dependent, but the equations of motion rely on the firm grounds of symmetries, conservation laws, and thermodynamics.

This thesis aims to tackle collective cell migration from this perspective, within the framework of continuum active matter physics. This approach has been proven very powerful for describing and understanding a broad range of different phenomena in nature, including living systems, and in particular, at the scale of cell tissues. Throughout the thesis, we focus on modeling various scenarios relevant to directed cell migration in tissues, which occurs when the collective migration of cells within the tissue is guided by external or internal cues. We bridge the gap between theory and experiments by comparing our models with experiments conducted by other research groups and also performing experiments ourselves. Though not delving deeply into the molecular and biological mechanisms, this introduction provides a fundamental overview of cell biology necessary for understanding migration at all levels: subcellular, cellular, and supra-cellular. We begin by discussing key cellular components involved in single-cell migration, namely the cytoskeleton and adhesion molecules. Then, we explore how cells establish directionality and velocity, which are crucial for coordinating movement with neighboring cells in a collective, and review how cell-cell adhesions regulate contractility and cell-substrate forces, facilitating this collective motion.

Finally, we examine active matter models, specifically focusing on active gels theory, as a framework for studying collective cell migration. We highlight the effectiveness of these simple yet powerful phenomenological models in offering valuable insights into the complexities of collective dynamics.

1.1 Single-cell migration

The cell cytoskeleton is a complex dynamic 3D network of protein filaments present in the nucleus and the cytoplasm of every cell. It is the structural backbone that supports the mechanical properties of the cell, regulates adhesion, drives cell shape changes, and generates the necessary forces for cell migration [Murrell2015, Blanchoin2014]. In eukaryotic cells, it is composed of actin filaments, microtubules, and intermediate filaments.

Actin filaments, with typical diameters of 5-9 nm, are polar filaments that constantly undergo polymerization and depolymerization through ATP hydrolysis [Dominguez2011]. The majority of actin is localized at the cell periphery,

right beneath the plasma membrane (Fig. 1.1), constituting the cell cortex together with actin-binding proteins and molecular motors such as myosin [Blanchoin2014, Chugh2018]. At the front of the cell, called the leading edge, actin filaments are essential for the formation of protrusions like lamellipodia (branched and crosslinked networks in a quasi-2D sheet) [Krause2014] and filopodia (aligned bundles underlying a fingerlike structure) [Khurana2011], which drive the movement forward. The rest of the cell contains a network of crosslinked filaments, including stress fibers, that mechanically couple the cytoskeleton of one cell to neighboring cells through cell-cell junctions, and to the extracellular matrix (ECM)—a polymer network of macromolecules such as collagen, laminin, enzymes, and glycoproteins that provide structural and biochemical support to cells—via protein complexes known as focal adhesions [Seetharaman2020]. This coupling is essential for transmitting the self-propelling forces exerted by cells to the ECM, enabling movement [Garcia2019].

Microtubules are cylindrical structures, essential for establishing and maintaining cell polarity [Garcin2019]. They serve as tracks for the intracellular cargo

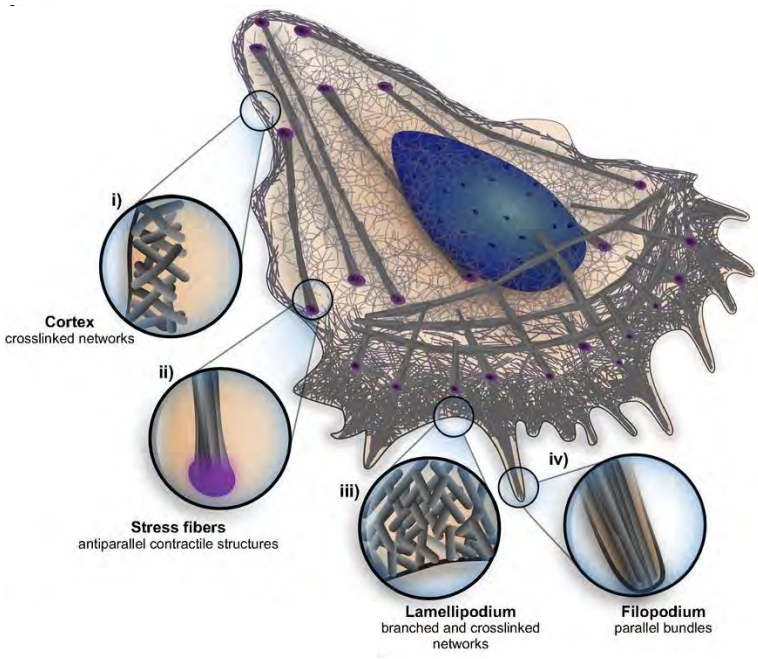

Figure 1.1: Actin structures in a migrating cell. Interaction between actin, myosin, and other actin-binding proteins allows the formation of specialized structures for cell migration. From [Blanchoin2014].

transport to the leading edge of the cell, such as membrane components, adhesion proteins, or other signaling molecules. Although the microtubule network is less directly involved in generating force, it is important in regulating cell polarity and directionality by facilitating the delivery of key molecules and organizing the spatial distribution of the cytoskeleton. Consequently, microtubules significantly influence the cell's migratory behavior.

The third component of the cell cytoskeleton, intermediate filaments, provides mechanical resilience, enabling the cell to maintain its integrity bearing up the high strains experienced during migration [Alberts2002]. These filaments are highly interconnected with other cytoskeletal components and play a regulatory role in processes such as the formation of stress fibers and membrane protrusions [Tang2017], as well as influencing the velocity of actin retrograde flow [Costigliola2017]. The coordinated interaction among the three cytoskeletal components, along with cell-substrate adhesions and dynamic remodeling of the actin cytoskeleton, generates the forces required for an effective cell migration.

1.1.1 Actin-based motility

Cellular crawling on a substrate is driven by the interplay between actin polymerization, cell-ECM adhesion dynamics, and actomyosin contractility [Gardel2010, Parsons2010]. Various modes of cell motility are based on the different cellular protrusions (either lamellipodia, filopodia, or blebs), leading to significant variability in migration velocities across cell types and conditions, ranging from 1 to 600 μm/h and length scales of 10 to 100 μm.

The so-called mesenchymal motility is characterized by cells moving in an elongated, slow, and highly adhesive manner, commonly observed in cancer cells, fibroblasts, and mesenchymal stem cells. Establishing directionality and polarity within a cell is essential for sustaining movement, and the spatial asymmetry between the proteins Rac1 and RhoA is crucial for this to happen [Mayor2010]. Rac1 localizes at the leading edge, promoting actin polymerization, while RhoA is predominantly found at the trailing edge, regulating myosin contractility. Once this polarity is established, mesenchymal motility occurs, which can be summarized in three cyclic steps (Fig. 1.2).

Initially, regulatory proteins such as Wasp and the Arp2/3 complex [Svitkina1999] facilitate the treadmilling of actin filaments at the leading edge of the cell. This polymerization pushes the membrane forward, generating protrusion forces at the front and forming the lamellipodium. It results in a net retrograde flow of actin monomers toward the rear part of the cell, where actin depolymerization takes place (Fig. 1.3).

Next, cell-substrate adhesion proteins, such as integrins, are recruited to form

new focal adhesions, establishing mechanical connections between the lamellipodium and the underlying substrate. These focal adhesions are linked to the cell's trailing edge via stress fibers, which sustain the tension generated by actomyosin contractility [Jacobs2013]. This tension arises from the interaction between myosin molecular motors and the actin network, resulting in the sliding of actin filaments and generating contractile forces in the cell body, besides the tension at the focal adhesion sites [Sonal2018] (Fig. 1.3, zoom-in). The transmission of these forces to the ECM through focal adhesions produces traction forces, essential for cell movement. Subsequently, at the rear edge of the cell, older cell-substrate adhesions are disassembled through myosin motors and depolymerization of actin filaments.

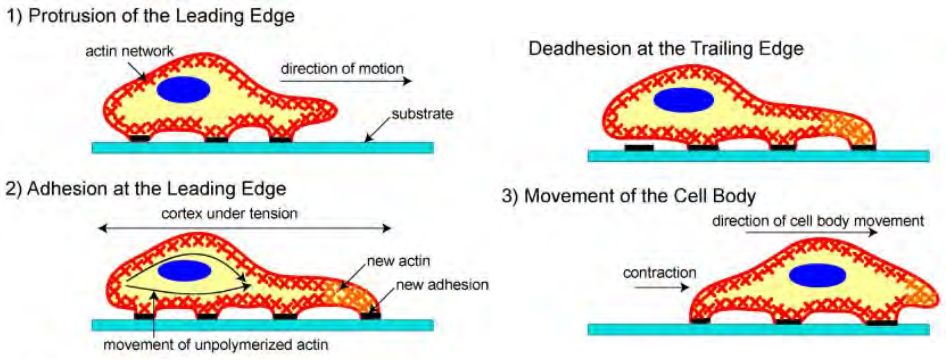

Figure 1.2: Scheme of the actin-based cell motility. Schematic of the three stages of cell movement, based on [Alberts2002, Lodish2000]. After determining its direction of motion, the cell extends a protrusion in this direction by actin polymerization at the leading edge. It then adheres its leading edge to the surface and de-adheres at the cell body and rear part. Finally, the generated contractile forces pull the whole cell body forward. Adapted from [Ananthakrishnan2007].

Ultimately, the retraction of the trailing edge, driven by the force imbalance created by disassembled adhesions and the collective contractile forces of myosin motors, induces a flow of depolymerized actin monomers toward the leading edge. Traction forces at both the front and rear of the cell point inwards (Fig. 1.3), establishing a force dipole in the direction of migration [Fournier2010, Tanimoto2014]. When there is enough friction between the cell and the substrate, movement can be generated.

In contrast to mesenchymal motility, amoeboid motility is characterized by rapid movement in a more rounded shape and reduced reliance on strong adhesions to the ECM [Paluch2013]. In this mode, the cell uses membrane blebs, which are ballon-like protrusions of the membrane formed from the underlying

actin cortex. Typical cell types exhibiting amoeboid motility include amoebae and embryonic cells. However, the migratory mode may depend not only on the cell type but also on external environmental conditions, with both modes potentially cooperating to enhance the cell's migratory abilities.

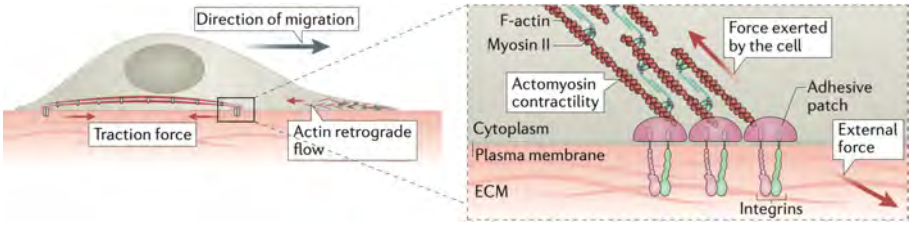

Figure 1.3: Single-cell migration. Sketch of the migration mechanism for a single cell, representing the basic structures (actin, myosin, and focal adhesions) that allow this motion. From [Ladoux2017].

1.1.2 Directed single-cell migration

The asymmetry in cytoskeletal architecture between the leading and the trailing edge of a polarized cell facilitates migration by transporting the required molecules to each side of the cell via microtubules. Consequently, this cell polarity is crucial in determining the direction of movement [Petrie2009]. Cells can establish this front-rear polarity either randomly or in response to external cues. In the case of random polarization, cells re-polarize and change their direction of movement in a stochastic manner [Wong2021], resembling a persistent random walk with typical persistence times of 10 to 100 min. Although this varies significantly among different cell types, the persistence time features an exponential function with the instantaneous cell speed [Maiuri2015].

In other cases, cells might establish their polarity by following gradients of external physiochemical properties in their microenvironment. Various guidance mechanisms have been reported in recent years. Among the most common ones (Fig. 1.4), cells track gradients of chemical factors dissolved in the medium (chemotaxis) [Jin2008, Poukkula2011], of the density of proteins immobilized on the substrate (haptotaxis) [Nguyen2000, Palsson2000, Ricoult2015], of substrate topology (contact guidance or curvotaxis) [Baptista2019, Vassaux2020], of electric fields (electrotaxis) [Cortese2014, Liu2014, Prescott2021], or of the stiffness of the ECM (durotaxis) [Lo2000, Vincent2013, DuChez2019, Sunyer2020].

This latter process is the guiding mechanism that will be studied most extensively during the thesis (in Chapters 2–3). The first evidence of single-cell

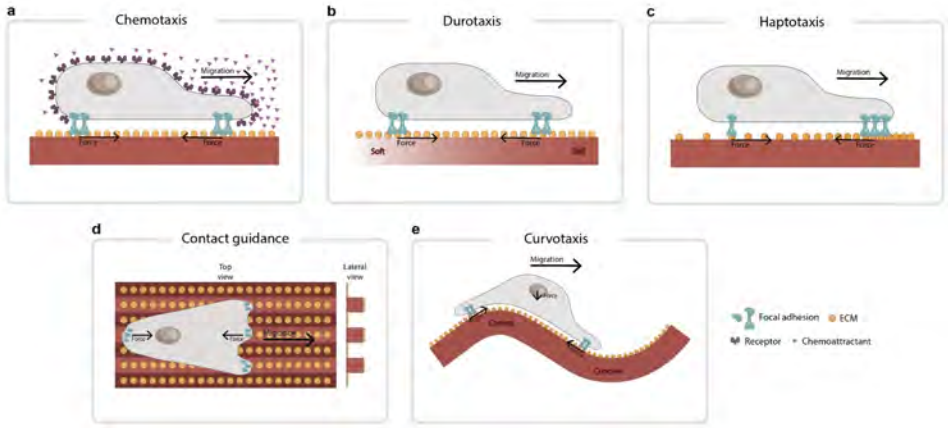

Figure 1.4: Common types of directed single-cell migration. Cells might follow gradients of chemical factors dissolved in the medium (**a**), gradients of stiffness in the ECM (**b**), gradients of chemical factors immobilized in the ECM, of proteins such as fibronectin or collagen (**c**), geometrical patterns such as grooves on the substrates (**d**) or might even avoid convex regions and position themselves in concave valleys (**e**). From [Fortunato2022].

durotaxis was observed in isolated fibroblasts [Lo2000]; since then, durotaxis has also been found in many different cell types, including mouse embryonic fibroblasts [Plotnikov2012], vascular smooth muscle cells [Isenberg2009], mesenchymal stem cells [Tse2011] and various human cancer cell lines [DuChez2019]. Most of our knowledge of the driving mechanisms behind single-cell durotaxis stems from *in vitro* studies, where coated hydrogels are used to mimic the ECM. Recent technological advances have enabled the fabrication of these gels with stiffness gradients [Sunyer2012, Vincent2013], which is very convenient for assessing durotaxis. While the precise mechanisms by which cells integrate mechanical stimuli to trigger migration remain to be fully elucidated, it is known that stiffness, among other biomechanical cues, influences the rheology of the cell cytoskeleton (Fig. 1.5), transitioning from fluid-like to solid-like behavior with increasing stiffness [Gupta2015] and promoting emerging actin orientational order [Ladoux2016]. Additionally, focal adhesions in stiffer regions are more stable due to increased force loading rates, resulting in slower actin retrograde flow and enabling the formation of lamellipodia [Gardel2010].

Although understanding the cellular mechanisms of migration is valuable for a global understanding, typically cells migrate as collectives. This comprises more complexity, as it involves coordination and force transmission throughout the group, but in most cases turns out to be more efficient than single-cell migra-

tion. This migratory behavior, commonly referred to as collective cell migration, is the main focus of this thesis.

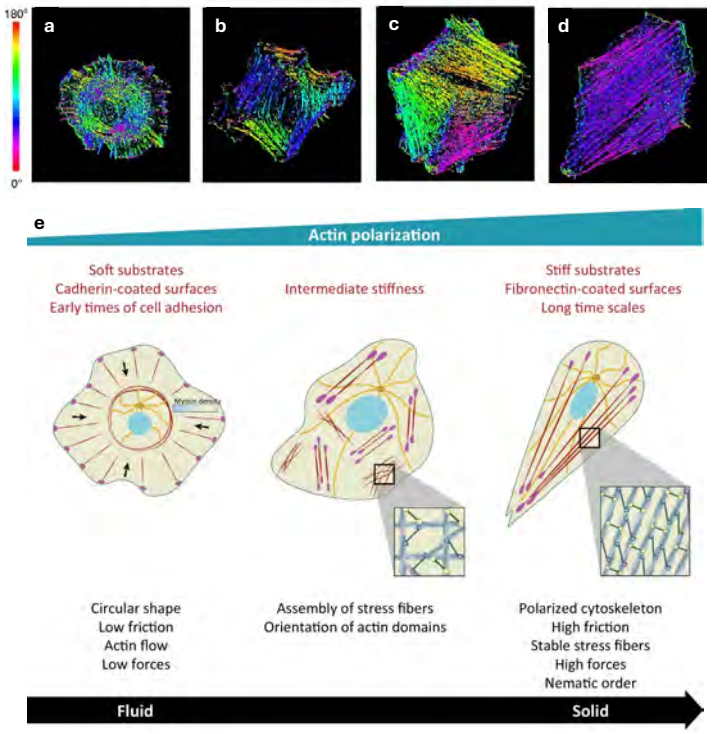

Figure 1.5: Single-cell polarization by biomechanical cues. a-d, Color-coded actin orientation in rat embryonic fibroblasts on micropillar substrates with stiffness of $9, 43, 64, 85$ nN/μm, increasing to the right. Scale bar, $20\,\mu$m. Adapted from [Gupta2015]. **e,** Schematic representation of actin polarization (red) under various conditions, showing also microtubules (orange), focal adhesions (purple), and the direction of the actin retrograde flow (black arrows). From [Ladoux2016].

1.2 Collective cell migration

Collective cell migration plays a key role in many instances of morphogenesis, tissue regeneration, and cancer invasion [Friedl2009, Vedula2013, Mayor2016, Ladoux2017, Hakim2017, Alert2020]. The mechanisms by which cells coordinate their movement are diverse and often not fully understood, in part because each cell's behavior influences, and is influenced by its neighbors [Mayor2016]. Tissue migration thus emerges from intercellular communication, with local cell-cell

contact being the most effective form of interaction.

Epithelial tissues, which constitute protective barriers over most vital organs, are useful model systems for studying collective cell migration and cell-cell interactions. This is both because of their migration properties and their tissue confluence, since in mature states of an epithelial monolayer cells occupy all the available area and leave almost no gaps between them. This results in cohesive layers that, when exposed to a free edge, migrate into the empty space by forming a protruding, finger-like structure composed of tens of cells [Poujade2007]. Epithelial cells exhibit apical-basal polarity, being the basal membrane the one in contact with the ECM, and the apical membrane the one facing the interior of the organ [Weiss1988, Cote2022]. This polarity leads to a non-uniform distribution of organelles and proteins along the cell's vertical axis. Various types of cell-cell junctions—such as tight junctions, adherens junctions, desmosomes, and gap junctions—are crucial for the assembly of monolayers and the stabilization of apical-basal polarity [Dufort2011].

The main adhesive complexes in adherens junctions are the cadherin-catenin complexes, which couple the actomyosin cytoskeleton of neighboring cells, enabling the transmission of forces that drive motion deep into the monolayer (Fig. 1.6a, zoom-in). Cell-cell junctions are thus mechanically connected to the cell-ECM adhesions, which transmit the myosin-generated forces to the substrate, thereby producing the traction forces needed for movement. Additionally, it has been demonstrated that E-cadherin specifically regulates cell contractility. Higher levels of this protein are associated with increased dephosphorylation of the myosin light chain, leading to greater contractility [Pérez-González2019]. This highlights the importance of cell-cell junctions, not only in providing and maintaining tissue integrity but also in modulating the mechanical properties, influencing how cells respond to their environment and migrate collectively.

Cells coordinate their behaviors and migrate collectively exhibiting a wide range of dynamical modes (Fig. 1.6b), which are also influenced by the spatial distribution of proteins like growth factors that promote cell division. Leader cells, positioned at the edges of the migrating group, exert the highest traction forces and are followed by the so-called follower cells, which organize finger-like structures and extend cryptic lamellipodia beneath the front cells, strengthening cell-cell adhesion [Ozawa2020]. By defining cell orientation based on the location of protrusions relative to the cell's center of mass, various flow patterns have been observed, such as parallel, swirling, and turbulent motion. Intrinsic events like cell division and extrusion can also affect significantly the tissue dynamics, by altering the tensional state and organization of the monolayer. For example, after a cell division event, tissue flow is directed outward along the axis connecting

the two daughter cells [Rossen2014]. Similarly, a cell extrusion event is often preceded by a coordinated, long-range flow of cells moving toward the extrusion site. These events, while intrinsic, influence the overall behavior and structure of the migrating cell group.

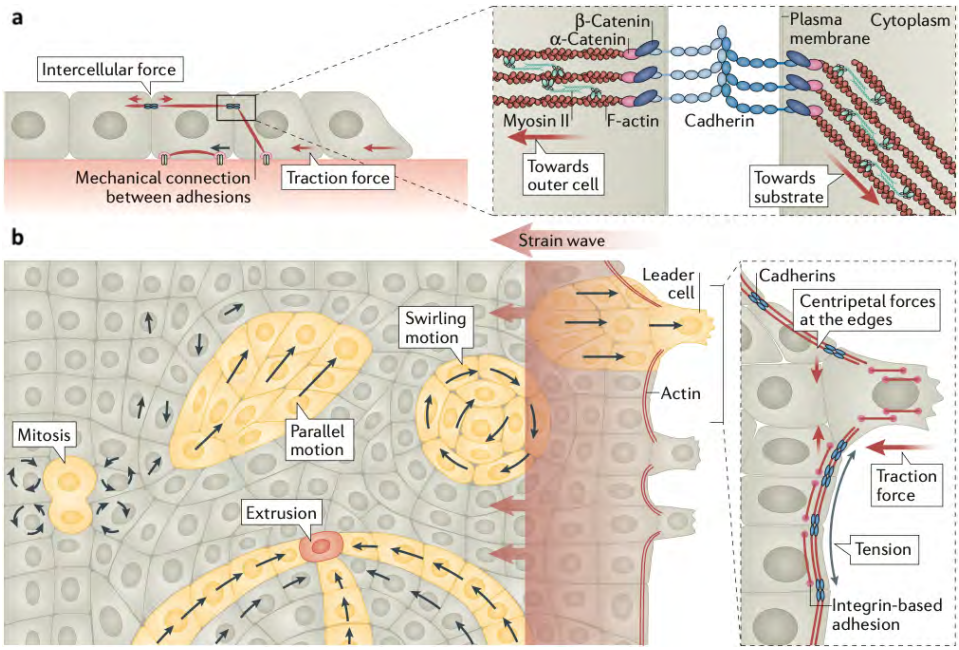

Figure 1.6: Collective cell motion. a, Transmission of traction forces through intercellular complexes. **b,** As in single cells, cells in monolayers extend lamellipodia at their contact with the substrate at the edge, leading to large-scale polarization [Poujade2007], and forming finger-like structures (right). Different modes of collective dynamics are possible. Typically, in a free-edge monolayer, strain and velocity waves are propagated from the edge toward the bulk, suggesting that the migrating monolayer is in a tensile state. From [Ladoux2017].

1.2.1 Mechanics of collective cell migration

Tissue motion is essentially a mechanistic problem, so understanding the mechanical basis is relevant to gaining insights into the overall process. Collective cell migration emerges from the interplay of cell-cell adhesion, cell-substrate adhesion, and cell contractility [Ng2012]. Similar to single cells, tissues must establish a front-rear polarity to be able to migrate collectively [Mayor2016]. This polarity is achieved through the mechanical contributions of both leader

and follower cells [Farooqui2005, Trepat2009], gradients of Rho-GTPase activity, and force transmission via cell-cell junctions.

As a result of this supra-cellular organization, traction forces are not evenly balanced within each cell. Developments in experimental techniques have enabled the measurement of traction and intercellular forces in cultured cell monolayers. Intercellular tensions can be inferred using methods such as laser ablation [Mayer2010], optical tweezers [Bambardekar2015], deformable artificial particles like oil microdroplets in living embryonic tissues [Campas2014], or by embedding beads within the bulk of a 3D tissue [deMercado2024]. Traction forces can be assessed by measuring the deflection of micron-sized flexible pillars caused by motile cells [Tan2003, Eckert2021], or through traditional Traction Force Microscopy techniques (TFM). In TFM, traction forces exerted by cells on the substrate are experimentally quantified by analyzing the deformation they cause. In an epithelial monolayer, this method reveals an asymmetrical force distribution (Fig. 1.7), with traction forces perpendicular to the leading edge decreasing systematically from the edge to the center of the monolayer, while intercellular tension showing the opposite trend [Trepat2009].

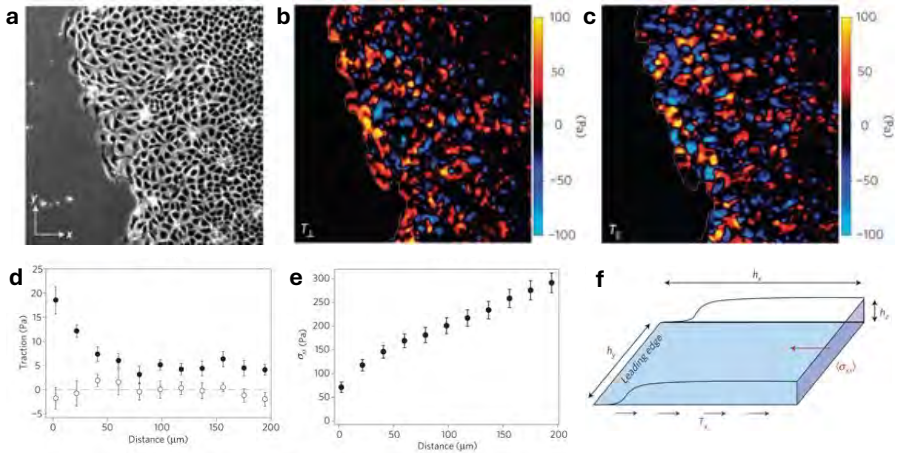

Figure 1.7: Traction forces generated by a migrating monolayer. a, Phase contrast image of a migrating monolayer of MDCK cells. **b,c** Traction forces components, perpendicular (**b**) and parallel (**c**) to the monolayer edge. The field of view is $750\,\mu\text{m}\times750\,\mu\text{m}$. **d,** Traction profile (parallel in black and normal in white) as a function of distance from the leading edge. **e,** Intercellular stress profile as a function of distance from the leading edge, calculated by integrating tractions T_x along h_x. **f,** Sketch depicting the different quantities in a cell monolayer. Adapted from [Trepat2009].

1.2.2 Directed cell migration in tissues

Like in single cells, cell clusters also feature directed migration due to the establishment of their polarity. For instance, through optogenetic activation, highly protrusive leader cells at the edge of 1D cell lines are generated [Rossetti2024], directing the migration. The induced leader, however, can robustly drag one follower cell but not larger groups. Instead, in 2D collectives, gradient sensing is typically significantly enhanced, making directed migration more efficient compared to single cells, and driving numerous biological processes in both health and disease [Majumdar2014, Haeger2015]. Like single cells, directed migration of collectives can occur in response to various external stimuli, including gradients in chemical concentrations [Camley2016], in ligand density [Nguyen2012], in electric signals [Lyon2019], or in the stiffness of the environment [Sunyer2016]. This latter phenomenon, known as collective durotaxis, will be the primary focus of Chapters 2–3 of this thesis, and a more detailed introduction of the topic can be found in those chapters.

Remarkably, large cell monolayers can exhibit durotaxis collectively even if the individual cells do not display this behavior [Sunyer2016], and in some cases, an optimal intermediate stiffness enhances tissue spreading [Ng2012, Balcioglu2020]. Durotaxis has significant implications in processes such as morphogenesis [Zhu2020, Shellard2021a], wound healing [Evans2013], and cancer invasion [DuChez2019].

1.3 Tissues as soft active matter

From a physical perspective, living tissues consist of deformable cells that display large-scale spontaneous coordination, local alignment, and macroscopic flows. These properties are similar to those of soft materials like foams, liquid crystals, gels, and colloidal suspensions. However, living tissues are active systems because cells have an internal energy source that drives them out of equilibrium. The chemical energy released from ATP hydrolysis is transduced into mechanical work, both through actin polymerization and myosin molecular motor activity, generating pulling forces that facilitate the relative sliding between the filaments. Ultimately, this results in cellular motion. Thus, living tissues can be categorized as soft active materials.

In recent years, active matter has emerged as a new paradigm in nonequilibrium physics [Marchetti2013], describing condensed systems composed of self-driven units, capable of converting stored or ambient free energy into motion [Schweitzer2003]. Living matter provides the most obvious examples of active systems, ranging from molecular motors in the cytoskeleton of living cells, bacte-

rial suspensions, and cellular tissues, to larger scales systems like fish schools or bird flocks (Fig. 1.8). Active particles are often elongated, exhibiting a privileged direction, and the interaction among each other gives rise to collective motion and emergent phenomena, such as pattern formation, order-disorder transitions, and turbulence, which are absent at the level of the constituents. The complexity of active materials arises from their multiscale organization. For example, as discussed earlier, the development of contractile forces driving collective tissue motion results from the intricate actomyosin machinery within the cell cytoskeleton, which is coordinated and transmitted through cell-cell junctions and focal adhesions.

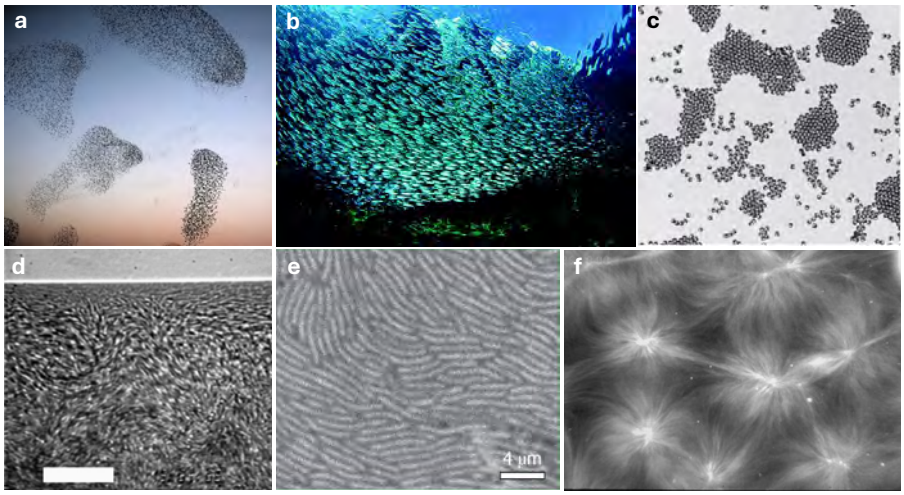

Figure 1.8: Active matter through scales. a, Bird flocks undergoing collective motion. Image courtesy of A. Cavagna, Institute for Complex Systems of the National Research Council, Rome, from [Obyrne2022]. **b,** Polar order in a sardine school. Image from Jon Bertsch, from underwater images from the Sea of Cortez, from [Marchetti2013]. **c,** Interrupted motility-induced phase separation in self-propelled colloids. Adapted from [vanderLinden2019]. **d,** Bacterial turbulence in a sessile drop of *Bacillus subtilis*. The horizontal white line is the air-water-plastic contact line, and gravity is perpendicular to the plane of the picture. Scale bar: 35 μm. Adapted from [Dombrowski2004]. **e,** Dense colony of *Myxococcus xanthus* forming an active nematic layer. Adapted from [Copenhagen2020]. **f,** Pattern of asters formed through the self-organization of microtubules and kinesins. Adapted from [Nédélec1997].

Active gel theories were originally devised to describe active matter at the cellular scale, particularly the actin cytoskeleton [Kruse2005, Jülicher2007, Marchetti2013, Prost2015], but since then, they have been extended to multicellu-

lar systems [Jülicher2018, Brückner2024]. This approach has provided valuable insights into the physical mechanisms underlying various biological processes, especially when cellular-scale details are less relevant [Arciero2011, Lee2011a, Lee2011b, Marel2014, Recho2016]. This is often the case in the collective migration of epithelial cells, which is organized at supra-cellular scales. In such instances, epithelia are described using a phenomenological continuum approach, where the system's large-scale and long-time behavior is captured by a few continuum fields, such as velocity, cell density, and polarization, which are coarse-grained into smooth fields varying over scales larger than individual cells. This framework is a natural generalization of the hydrodynamics of liquid crystals.

The predictive success of this approach, which anticipated phenomena later observed in experiments [Pérez-González2019, Beaune2018, Copenhagen2020], has fostered confidence in its ability to capture the mechanics of epithelia. The research presented in this thesis builds on the framework of active polar gel theory, focusing on epithelial tissue dynamics and using simple models to predict and explain experimental results, thereby providing deeper insights into the fundamental processes governing epithelial dynamics.

1.3.1 Active gels

The theory of active gels relies on a hydrodynamic approach based on irreversible thermodynamics and fundamental symmetries, such as microscopic time-reversibility and rotational invariance [Kruse2004, Kruse2005, Jülicher2007, Marchetti2013, Jülicher2011]. This approach provides a comprehensive description of the long-time and large-scale behavior of systems that share the same symmetries of active polar gels. The microscopic details of the system are encoded in a set of phenomenological transport coefficients; thus, this approach is generic for many situations.

The units of active gels, active particles, can be either polar or nematic (Fig. 1.9). Polar active particles, such as birds and bacteria, are those with an asymmetry between their front and rear. Cells in a tissue are often an example of polar particles too, when there is an internal front-rear asymmetry on the cytoskeleton structure. This may take the form of lamellipodia (or cryptic lamellipodia in tissue inner cells) pulling on the cell leading edge and contractility detaching focal adhesions on the trailing edge (Fig. 1.2), thus mimicking single-cell motility. In other cases, the cell's orientation is defined by elongated shapes, displaying front-rear symmetry, thus defining a nematic order [Duclos2014, Saw2017, Duclos2017, Kawaguchi2017, Duclos2018, Maroudas-Sacks2021, Hadjifrangiskou2023]. In general, both nematic and polar order parameters may coexist, as discussed in [Doostmohammadi2018, Amiri2022]. Re-

cently, not only polar or nematic order, but also hexatic order has been identified in small length scales of epithelial monolayers [Armengol2023, Armengol2024, Chiang2024]. Throughout this thesis, however, we will only deal with cases where cells display polar order.

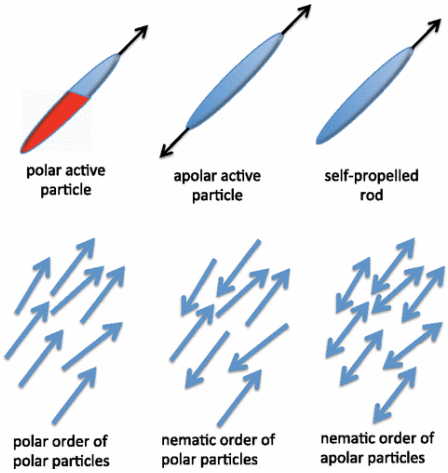

Figure 1.9: Types of active particles and orientationally ordered states. Polar active particles have a head and a tail and are generally self-propelled along their long axis. They order in polar or nematic states. Apolar active particles are head-tail symmetric and order in nematic states. Self-propelled rods, while also head-tail symmetric, self-propel along their long axis, which renders the particles polar, but for exclusively apolar interactions. They order only in nematic states. From [Marchetti2013].

To derive the hydrodynamic equations, one begins by identifying the slow or hydrodynamic variables, which may consist of densities of conserved quantities or order-parameter fields arising from broken continuous symmetries. In a simple fluid, conserved quantities encompass mass, energy, and momentum. In a polar medium, additional slow variables include the rotational degrees of freedom and the modulus of the polarization field, as orientational order arises from the rotational invariance symmetry. With the introduction of activity, the density of reactant molecules responsible for continuous energy transduction also becomes a slow variable.

Next, a coarse-grained free energy of the system is constructed in terms of these slow variables, allowing for the identification of generalized fluxes and forces. These generalized fluxes are then expressed as linear combinations of the generalized forces, leading to constitutive equations valid in the linear response regime. The coefficients of these combinations form the Onsager matrix. Constitutive equations must respect the symmetries of the problem as dictated by the Curie principle, which prevents coupling between different tensorial characters, due to rotational invariance. This implies, for instance, the need for an orientational order parameter to couple the force associated with the (scalar) chemical reaction, to a (tensorial) momentum flux. Similarly, due to microscopic reversibility, the Onsager reciprocity relations for crossed couplings limit the number of independent transport coefficients. Finally, by combining the consti-

tutive equations with continuity equations that express the balance of conserved quantities, and with an equation of state for the material, one obtains the closed hydrodynamic equations.

Depending on the nature of the active particles, either extensile or contractile stresses can arise. In extensile stresses, active particles induce expansion along the long axis while contracting in the orthogonal direction, whereas contractile stresses result from expansion in the orthogonal direction and contraction along the long axis (Fig. 1.10a). If individual elements tend to pull together in all directions, an isotropic contractile deformation results; conversely, if they push apart in all directions, an isotropic expansion occurs. In systems with extensile particles, dipolar extensile deformations arise, whereas contractile particles produce dipolar contractile deformations [Needleman2017]. Both types of stress are observed in various biological active gels. In particular, actin filaments behave as contractile units [Thoresen2011] while microtubules are largely extensile [Sanchez2012].

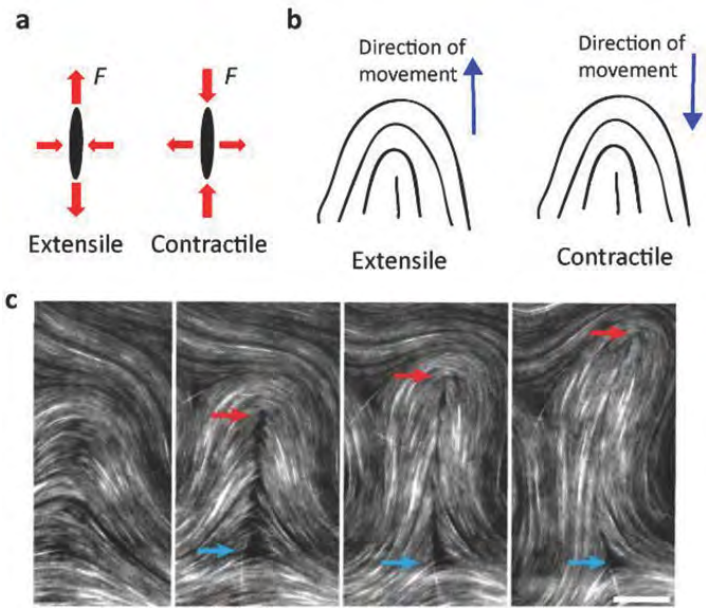

Figure 1.10: Active nematics. a, The force dipole directions for extensile and contractile active nematic particles that are opposite to each other. **b,** Direction of activity driven movement of $+1/2$ defects in the two different active systems. **c,** Tail-to-head movement of a $+1/2$ defect (red arrow) in a reconstituted microtubule system (time increasing from left to right), showing that it is an extensile system. The $-1/2$ defect (blue arrow) is stationary. Scale bar: 20 μm. From [Saw2018].

One way to discern whether a system is contractile or extensile is by measuring the dynamics of $+1/2$ defects (Fig. 1.10b,c). Topological defects are singularities in the orientation field of the active particles, classified based on the degree and direction of rotation of director vectors around the defect cores [DeGennes1993]. The tail-to-head movement of these $+1/2$ defects is a signature of an extensile system, as observed in a reconstituted microtubule system (Fig. 1.10c). Interestingly, despite the contractile nature of single cells, neural progenitor and epithelial cell colonies have predominantly been found to be extensile [Saw2017,Kawaguchi2017]. In contrast, in fibroblast or myoblast colonies, $+1/2$ defects move in the head-to-tail direction, indicating that they are contractile [Kawaguchi2017, Duclos2017].

In summary, despite the dramatic simplification of this phenomenological approach, compared to the full biological complexity, these general theories have made a significant contribution to our understanding of living systems and our quest for universal organizing principles and generic mechanisms [Kruse2004, Voituriez2005,Kruse2006,Voituriez2006,Joanny2007,Basu2008,Salbreux2009]. Nevertheless, this general theory may be limited if systems exhibit strong spatiotemporal variations, nonlinear effects, or interactions with biochemical regulators [Jülicher2007, Prost2015], which should be modeled specifically.

1.3.2 Tissue spreading

Continuum models based on active gel theory have focused on the spreading of epithelial monolayers, addressing, for instance, the formation of multicellular fingers [Lee2011a, Köpf2013, BenAmar2016, Alert2019a]. A long-standing debate is whether elastic or fluid models are better suited to describe tissue spreading [Banerjee2019]. In reality, tissues exhibit a viscoelastic behavior: At short timescales, they act as elastic solids, with tension mostly dependent on strain and with a relaxation time of 1 to 10 min due to the turnover of cytoskeletal and cell-cell junction components [Harris2012]; at longer timescales, tension depends on strain rate, and the tissue behaves as a viscous fluid [Alert2020]. Yet, even at long timescales, tissues might display elastic responses, such as elastic mechanical waves during spreading [Serra-Picamal2012, Vincent2015]. To capture these behaviors, some models directly assume an elastic rheology, while others use viscous models with time-dependent parameters [Blanch-Mercader2017b]. Both approaches have effectively reproduced experimental data, and the choice depends on the specific biological process of interest.

In *in vitro* assays, cells or cellular aggregates are placed on flat surfaces, like polyacrylamide (PAA) gels, to study their collective migration over long timescales. The spreading of a cellular aggregate on a substrate has been stud-

ied in analogy with the classical wetting problem of a passive fluid droplet on a surface [Douezan2011, González-Rodríguez2012]. The outcome—whether the aggregate spreads, forming a precursor film of cells or remains spheroid, partially wetting the substrate—depends on the balance between cell-cell and cell-substrate adhesion energies. These energies can be modified by altering the expression of cell-cell junction proteins, by surface treatments, or by modifying the substrate rigidity [Ryan2001, Douezan2011, Douezan2012a]. When the aggregate spreads cohesively as a monolayer, it resembles a water droplet wetting a hydrophilic surface (Fig. 1.11b), whereas if cell-cell adhesion is too weak, the spreading occurs via scattered cells rather than a cohesive monolayer (Fig. 1.11c).

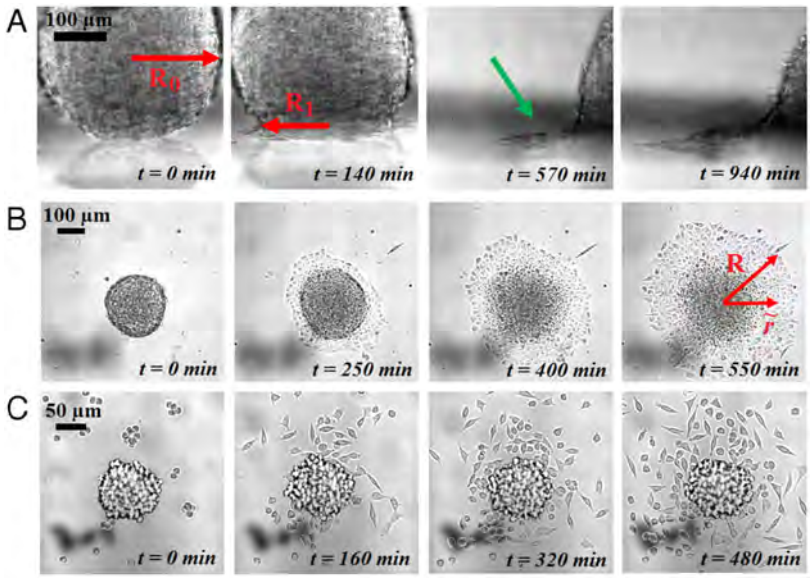

Figure 1.11: Wetting of a cell aggregate. a, Precursor film of cells leaving the aggregate when spreading on an adhesive substrate. **b,** Liquid-like state: spreading of a cohesive monolayer onto the substrate. **c,** Gas-like state: spreading of scattered cells when cell-cell adhesion is too weak. From [Douezan2011].

This picture, however, overlooks the specific forces within the monolayer that govern wetting or dewetting. A continuum active model was proposed in [Pérez-González2019] for a 2D circular monolayer of radius R, comparing the wetting-dewetting transition of a cellular aggregate to the spreading-retraction of the monolayer. While wetting and dewetting were often used interchangeably with spreading-retraction, wetting specifically involves a 3D shape and the formation of a precursor film. The transition depends on the monolayer's radius and the substrate's ligand density (Fig. 1.12), which influence migration under different

conditions. The critical radius is given by

$$R^* \approx \frac{1}{2}\left(3L_c + \frac{|\zeta|}{\zeta_i}\right), \tag{1.1}$$

above which the monolayer spreads (for $R > R^*$) and below which it retracts (for $R < R^*$), assuming $L_c \ll R$. L_c is the nematic length, which defines the spatial persistence of the polarity field, ζ encodes the cells' contractility and ζ_i the active traction parameter, which models the active cell-substrate interaction.

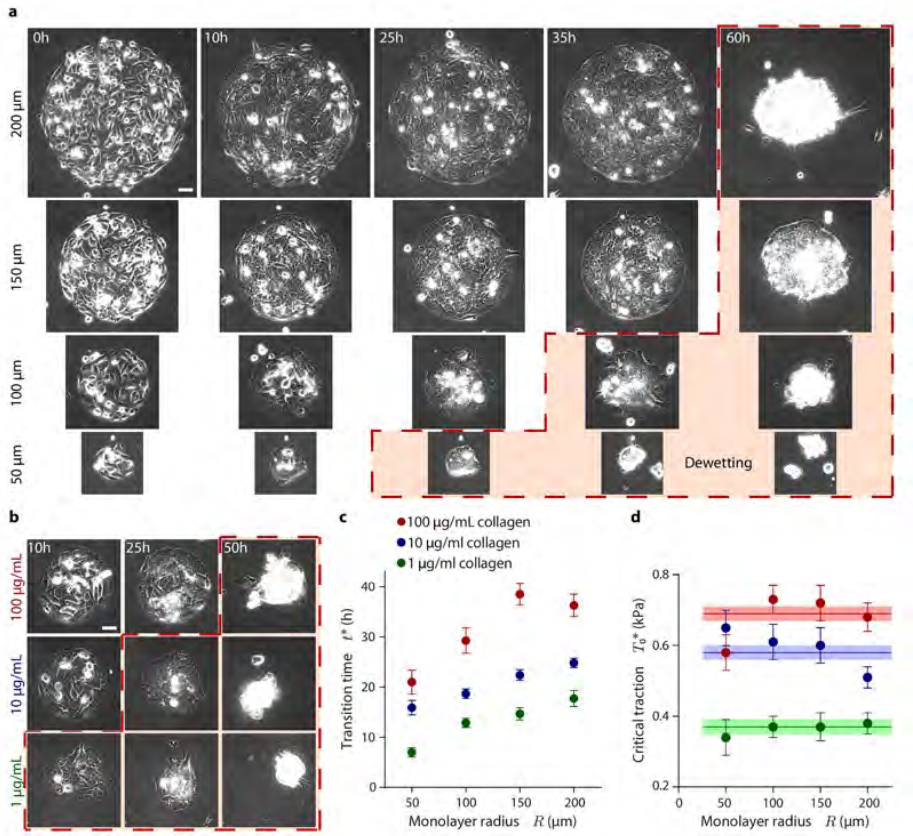

Figure 1.12: Active wetting of tissue spreading. a, Time evolution of MDA-MB-231 epithelial monolayers of different initial radii. Larger monolayers dewet later. **b,** Time evolution of monolayers on substrates with different ligand densities, of 100 μm in radius. Monolayers on substrates with higher ligand density dewet later. Scale bars, 40 μm. **c,** Wetting transition time as a function of the monolayer radius and substrate ligand density. **d,** Critical traction as a function of the monolayer radius and substrate ligand density. From [Pérez-González2019].

Throughout this thesis, we model epithelial monolayers using this same continuum active model. Therefore, these model parameters, together with other basic ideas of the model, are better described in Section 2.2. In [Pérez-González2019] there was no distinction between "wetting", referring to the relative advance of the fluid with respect to the substrate, and "spreading", which refers to the increase of contact area, because the cluster did not have a global displacement. In this thesis, however, we will encounter that the area growth and the global displacement due to some external guidances, such as in durotaxis, coexist and are independent. Therefore, we will refer to the transition described in [Pérez-González2019] as the "spreading transition", which is more appropriate in this more general case.

1.4 Outline of the thesis

The goal of this thesis is to understand and characterize diverse behaviors of collective cell migration in epithelial tissues across different scenarios, particularly focusing on directed migration, where tissues are guided by external or internal cues instead of following a random walk. Using the theoretical framework of active gel theory, we model these tissues as active polar fluids (as discussed in Section 1.3) and explore their migration under various conditions. The thesis is structured as follows:

- In Chapter 2, we build upon an existing model for collective durotaxis in cell monolayers, providing a more detailed classification of the dynamical regimes in terms of the physical parameters. The model is based on active gel theory and describes, with a few mechanical parameters, both the passive and active forces in tissue migration. The phenomenological coupling between these parameters and the stiffness of the substrate allows us to study the durotactic behavior. We solve the model analytically in some simple yet relevant situations, that allow a better grasp of the underlying physical mechanisms.
- In Chapter 3, we develop a 3D active wetting model for cell clusters to study collective durotaxis. Based on the model for a tissue monolayer from the previous chapter, we extend it to account for the 3D structure of a cellular aggregate, adding the contribution of surface tension. The main goal of this chapter is to compare the findings with some experimental results, thereby providing insights into the physical mechanisms of collective durotaxis.
- In Chapter 4, we examine the influence of cellular traction forces on the

stiffness of substrates, which are typically biopolymer networks that display strain-stiffening responses. It is known that traction forces increase with the stiffness of the substrate, but the feedback to what extent this increase in the forces also influences the stiffness remains to be elucidated.

- In Chapter 5, we conduct experiments tracking the migration of epithelial monolayers, to understand under which conditions a morphological symmetry breaking can generate spontaneous collective migration in cell clusters. The goal is to study whether an asymmetry in the shape can induce movement in cell clusters that are not globally polarized, and to see which conditions enhance this movement. The theoretical results motivated the search for these migratory modes in the experiments.
- In Chapter 6, we extend the continuum model for a cell monolayer into a continuum stochastic model, to account for the inherent stochasticity of biological systems. The goal is to study the different consequences of different sources of noise in the model. We can either introduce an internal noise in the dynamics of the polarity or an external noise in a cell-substrate coupling parameter, called the active traction, which is related to the attachment and detachment kinetics of the substrate adhesions with the cells in the monolayer. We predict the effects of these different noise types and compare them with experimental data on traction force fluctuations in epithelial monolayers, to validate the approach as a characterization of the fluctuations in tissues.

Each chapter includes conclusions and appendices with technical details or additional information. In Chapter 7, we present a comprehensive summary of the thesis conclusions and the most relevant results, along with future perspectives for each topic. A brief motivation in Catalan for the research in this thesis, together with the most relevant results, are briefly summarized in Resum en català.

Chapter 2

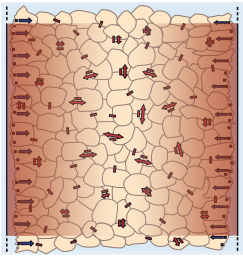

Collective durotaxis of 2D cell monolayers

2.1 Introduction

As explained in the general introduction, the phenomenon of durotaxis is a type of directed migration due to a response of cells to stiffness gradients in their environment, which, *in vivo*, is the extracellular matrix. For single cells, it was discovered at the beginning of the 21st century by [Lo2000]. More recently, it was observed for collective cell migration in epithelial monolayers [Sunyer2016] (Fig. 2.1), with long-range intercellular force transmission (Fig. 2.2). This collective durotaxis turned out to be much more efficient than single-cell durotaxis, with the large cell monolayers performing durotaxis collectively even when their constituent cells do not.

Collective durotaxis has been modeled via hybrid computational models [Escribano2018, González-Valverde2018, Garcia-Gonzalez2020, Deng2021], which, although being very accurate in describing the behavior, have the disadvantage that too many model parameters and interactions need to be considered. Otherwise, a continuum active polar fluid model of a tissue, as described in [Alert2019b], is a quite powerful phenomenological model with much fewer ingredients. This continuum model revealed two modes of possible collective durotaxis: either asymmetric spreading or motion of both edges of the monolayer towards the same direction. Building on this framework, this chapter aims to

provide a more comprehensive classification of the dynamical regimes in terms of physical parameters, solving the model analytically in some simple but relevant situations that allow a better grasp of the physical mechanisms at play.

To this end, the active polar fluid model of the monolayer, which is the base of our study, is introduced in Section 2.2, and simplified and solved in Section 2.3 for uniform conditions. In Section 2.4, it is solved for stiffness gradients, both for unrealistic but simple profiles of the model variables that give us insights into the mechanism (Section 2.4.1), and for more realistic situations (Section 2.4.2). Finally, the observed dynamical regimes are commented in Section 2.5.

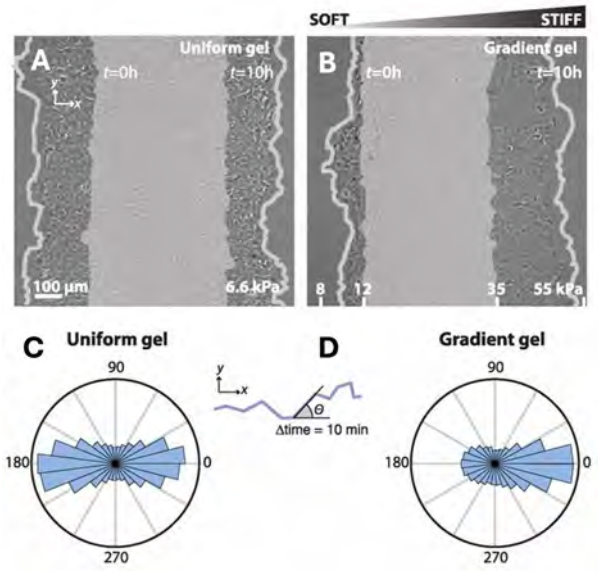

Figure 2.1: Asymmetric spreading of an epithelial monolayer. a, Symmetric spreading of an MCF-10A monolayer on a uniform stiffness gel. **b,** Asymmetric spreading of a monolayer on a gradient of stiffness. **c,d,** Angular distributions of cell trajectories for experiments shown in **a** and **b**, respectively, showing that monolayers durotaxis on gradients of stiffness. Adapted from [Sunyer2016].

2.2 Active polar model for an epithelial monolayer

In this section, we present the physical model proposed to describe an epithelial cell monolayer. The model was initially introduced in [Blanch-Mercader2017b] for studying epithelial tissue spreading and has proven to be useful in many other situations. For instance, in [Pérez-González2019] for describing the dewetting

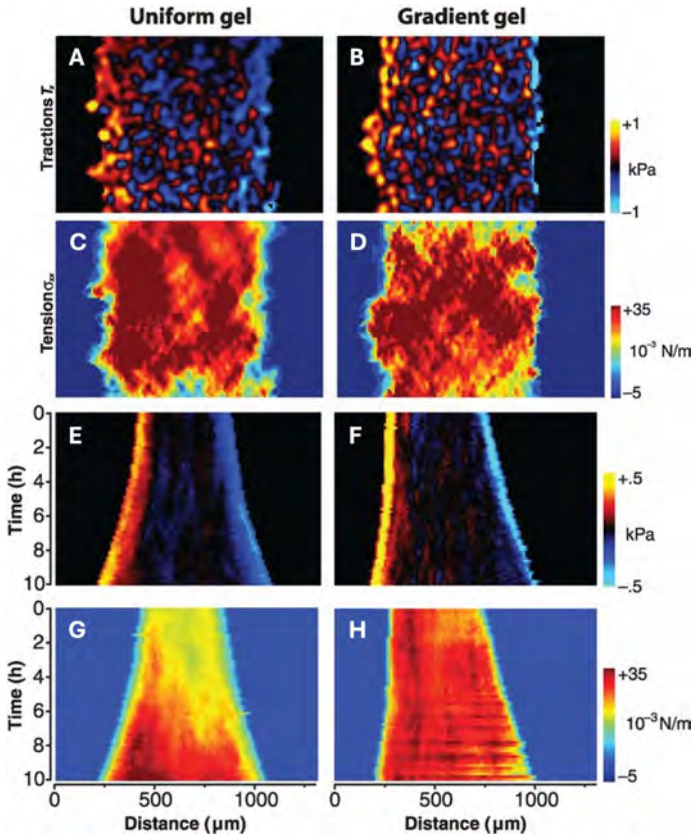

Figure 2.2: Long-range intercellular force transmission in collective durotaxis. a-d, x component of the traction forces T_x (**a, b**) and intercellular tension σ_{xx} (**c, d**) in a MCF-10A monolayer. **e-h,** Kymographfs of the tractions and tensions. Adapted from [Sunyer2016].

of a 2D monolayer onto a spherical aggregate, in [Alert2019a] for predicting a fingering instability of the leading edge of the tissue, or in [Alert2019b] for describing two possible mechanisms of collective durotaxis.

The idea behind it is that, in many instances, tissues can be modeled, to some extent, as continuous active materials, in such a way that the biological properties are encoded in a series of physical parameters, including passive ones such as viscosity or friction, and active ones such as contractility or traction. Therefore, we will treat the tissue as a thin layer of an active polar viscous fluid placed on top of a substrate, as depicted in the side view of Fig. 2.3. Considering that the height of the monolayers ($h \sim 5 - 10$ μm) is smaller than spatial variations of the physical observables on the plane of the substrate (~ 50 μm), we

can describe the monolayer as an effective 2D system, in which the physical observables are averaged along the third dimension. Then, taking a coarse-grained approach, we describe the long-time and large-scale dynamics of the tissue, and so we consider only two main physical observables: the velocity field v_α and the polarization field p_α. It is worth noting that they do not correspond to the velocity and polarization of single cells. The velocity can be accessed experimentally via Particle Image Velocimetry (PIV) methods, but the polarization cannot be measured directly from cells, beyond estimates based on cell shapes or the orientation of stress fibers. With the help of our model, we will infer the polarization from measurements of traction forces on the substrate.

Below we explain the ingredients of the model before studying in depth the implications in collective durotaxis, which is the focus of our study.

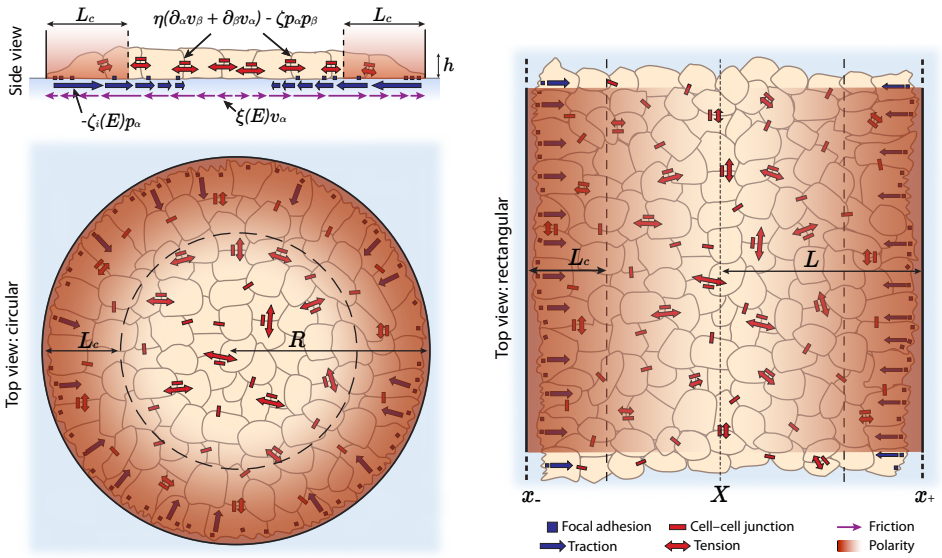

Figure 2.3: Sketch of the active polar fluid model for monolayer spreading. The red color gradient indicates the cell polarization field (strongly polarized at the edge and unpolarized at the center). Adapted from [Pérez-González2019].

2.2.1 Polarity dynamics

Cells in epithelial tissues exhibit in-plane polarity, which reflects the internal polarization of the cytoskeleton. Thus, the polarization field p_α is defined as the orientational degree of freedom of the cells which arises from the polarization of its internal cytoskeletal structure. In epithelial tissues, cells at the leading edge

are strongly polarized as they develop lamellipodia. Cells that are hundreds of microns away from the edge may also be polarized, extending basal cryptic lamellipodia underneath their neighbors [Farooqui2005], but cells further away are either unpolarized or exhibit a residual polarization that is randomly oriented and thus averages to zero. From a coarse-grained point of view, thus polarization decays from maximal at the edges to zero far from them. Similarly, it is also observed that traction forces are maximal at the leading edge and vanish towards the center of the monolayer [Sunyer2016, Pérez-González2019] (Fig. 1.7, Fig. 2.2). Thus, the capacity of cells to exert traction forces on substrates, and the direction along which they are exerted, is a direct signature of polarization.

The way cells polarize in an epithelial sheet is usually described as a consequence of contact inhibition of locomotion (CIL), an interaction that causes cells repolarize and generate traction forces in the opposite direction to the contact with other cells [Mayor2010, Theveneau2013, Vedula2013, Ladoux2016, Mayor2016, Zimmermann2016, Coburn2016, Smeets2016, Hakim2017]. This leads to polarization of cells towards free space in the boundary layer, and to unpolarized cells in the center of the monolayer. Also, cells tend to align with their neighbors [Trepat2009, Angelini2011], so by analogy with nematic particles, we can use a phenomenological description. The general constitutive equation for the polarity of a $d-$dimensional active polar fluid reads [Kruse2005, Jülicher2011, Marchetti2013, Prost2015]

$$\frac{Dp_\alpha}{Dt} = \frac{1}{\gamma_1} h_\alpha - \frac{\bar{\nu}_1}{d} v_{\gamma\gamma} p_\alpha - \nu_1 \tilde{v}_{\alpha\beta} p_\beta + \epsilon p_\alpha, \tag{2.1}$$

where $\frac{Dp_\alpha}{Dt} = (\partial_t + v_\beta \partial_\beta) p_\alpha + \omega_{\alpha\beta} p_\beta$ is the co-rotational convected derivative, being $\tilde{v}_{\alpha\beta} = \frac{1}{2}(\partial_\alpha v_\beta + \partial_\beta v_\alpha) - \frac{1}{d} v_{\gamma\gamma} \delta_{\alpha\beta}$ and $\omega_{\alpha\beta} = \frac{1}{2}(\partial_\alpha v_\beta - \partial_\beta v_\alpha)$ the traceless symmetric and antisymmetric parts of the strain rate tensor, with $v_{\gamma\gamma} = \partial_\gamma v_\gamma$. $h_\alpha = -\delta F / \delta p_\alpha$ is the so-called molecular field, being $F[p]$ the coarse-grained free energy of the orientational degrees of freedom and γ_1 the rotational viscosity. $\bar{\nu}_1$, ν_1, and ϵ are the bulk, the shear, and the active flow alignment coefficients, respectively. Assuming that the CIL mechanism is the main responsible for repolarization events, we neglect the advection, corotation, flow alignment, and active spontaneous polarization effects, and so the full constitutive equation for the polarity gets greatly simplified. It is given by a purely relaxational dynamics,

$$\partial_t p_\alpha = \frac{1}{\gamma_1} h_\alpha = -\frac{1}{\gamma_1} \frac{\delta F}{\delta p_\alpha}, \tag{2.2}$$

and so the molecular field gives the generalized restoring force of the polarity. The tendency of cells to align with their neighbors is thus accounted for by

an effective free energy that takes the form of the Frank elastic free energy [DeGennes1993], which for a planar polarization field reads

$$F = \int_{\mathcal{V}} \left[\frac{a}{2}p^2 + \frac{b}{4}p^4 + \frac{K_1}{2}\left(\vec{\nabla}\cdot\vec{p}\right)^2 + \frac{K_2}{2}\left(\vec{\nabla}\times\vec{p}\right)^2 \right] \mathrm{d}^3\boldsymbol{r}, \tag{2.3}$$

where a and b are coefficients of the Landau expansion of the local free energy density. The restoring coefficient a is taken positive such that the unpolarized state ($p = 0$) is energetically favored in the bulk. K_1 and K_2 are the Frank constants associated with splay and bend distortions, respectively. Keeping only the quadratic term in the Landau expansion and assuming $K_1 = K_2 \equiv K$, which is the usual one-constant approximation, we get the simplified free energy,

$$F = \int_{\mathcal{V}} \left[\frac{a}{2}p^2 + \frac{K}{2}(\partial_\alpha p_\beta)(\partial_\alpha p_\beta) \right] \mathrm{d}^3\boldsymbol{r}. \tag{2.4}$$

Note that α and β run over the cartesian coordinates, and from now on we use the Einstein summation convention over repeated Greek indices. Then, from Eq. 2.2, the dynamics of the polarity is given by

$$\partial_t p_\alpha = \frac{1}{\gamma_1}\left(-a p_\alpha + K\nabla^2 p_\alpha\right). \tag{2.5}$$

The time scales associated with the spreading of a monolayer are of the order of hours [Blanch-Mercader2017b], much slower than cell polarization events associated with CIL, which usually occur within a time scale of ~ 10 min [Smeets2016]. Thus, we assume a quasistatic evolution of the polarization field $\partial_t p_\alpha = 0$ (and thus $h_\alpha = 0$). Then, from Eq. 2.5,

$$L_c^2\nabla^2 p_\alpha = p_\alpha, \tag{2.6}$$

where $L_c \equiv \sqrt{K/a}$ is the nematic length that defines the spatial persistence of the polarization field [Pérez-González2019, Alert2019a, Alert2019b]. Since epithelial cells are maximally polarized at the edge, we enforce a boundary condition of maximum polarization $|\boldsymbol{p}| = 1$ directed normally and outwards at the tissue edge. Then, L_c defines the thickness of a polarization boundary layer near the edge, such that the polarization field decays from one at the edge to zero deep into the tissue (red shade in Fig. 2.3). All in all, this energetic approach provides a simple phenomenological model that effectively captures the essential alignment interactions of cells at a coarse-grained level, without getting hindered into intricate details.

2.2.2 Force balance

The momentum conservation equation for an active polar fluid, up to first order in gradients of the polarization field, reads [DeGennes1993]

$$\rho(\partial_t + v_\beta \partial_\beta) v_\alpha = -\partial_\alpha P + \partial_\beta(\sigma^s_{\alpha\beta} + \sigma^a_{\alpha\beta}) + f_\alpha, \tag{2.7}$$

where ρ is the density, P the pressure, $\sigma^s_{\alpha\beta}$ and $\sigma^a_{\alpha\beta}$ the symmetric and antisymmetric parts of the deviatoric stress tensor, and f_α the external force density. For our epithelial monolayer, here we can make further simplifications. First, we can neglect inertia, since flows in cell monolayers occur at low Reynolds numbers ($\mathrm{Re} = \rho v R/\eta \sim 10^{-13}$ estimating $\rho \sim 10^3$ kg/m^3, $v \sim 10$ μm/min, $R \sim 200$ μm and $\eta \sim 10^5$ Pa·s [Forgacs1998]). Moreover, in our 2D description, the cell monolayer is compressible, with $\partial_\alpha v_\alpha \neq 0$, because the in-plane compression and expansion of the cell monolayer can be accommodated by changes in the monolayer height h. We assume that in-plane deformations do not amount to significant changes in pressure as the layer can deform in 3d and, hence, pressure gradients are neglected in front of the rest of the contributions of Eq. 2.7. This approximation has been used and discussed in many previous studies, for instance in [Lee2011a, Lee2011b, Blanch-Mercader2017a, Blanch-Mercader2017b, Alert2019a, Alert2019b, Pérez-González2019]. With these two assumptions, force balance reduces to

$$\partial_\beta(\sigma^s_{\alpha\beta} + \sigma^a_{\alpha\beta}) + f_\alpha = 0. \tag{2.8}$$

Finally, recalling the quasistatic approximation for the polarization $\partial_t p_\alpha = 0$, which implies $h_\alpha = 0$, the antisymmetric part of the stress tensor vanishes, since $\sigma^a_{\alpha\beta} = \frac{1}{2}(p_\alpha h_\beta - h_\alpha p_\beta)$. Therefore, force balance is just

$$\partial_\beta \sigma^s_{\alpha\beta} + f_\alpha = 0. \tag{2.9}$$

These quantities are directly related to the experimentally measured monolayer tension, $\sigma_{\alpha\beta} \equiv \sigma^s_{\alpha\beta} h$, and traction stress, $T_\alpha \equiv -f_\alpha h$, being h the height of the monolayer [Pérez-González2019]. Thus, the traction forces exerted by the cells onto the substrate are balanced by the averaged internal stresses, and so with the effective two-dimension approximation, in cartesian components, this reads

$$\partial_x \sigma_{xx} + \partial_y \sigma_{xy} = T_x, \tag{2.10}$$

$$\partial_x \sigma_{yx} + \partial_y \sigma_{yy} = T_y. \tag{2.11}$$

2.2.3 Constitutive equations

To close the system of equations, we need the constitutive equations for a compressible active polar fluid. Because spreading occurs at time scales much

longer than the turnover time scales of proteins in the cytoskeleton or in cell-cell junctions [Wyatt2016, Khalilgharibi2016], which are associated with elastic responses of the tissue, we consider only a fluid behavior of the monolayer. In the viscous limit, the internal stress of an active polar medium reads [Kruse2005, Jülicher2011, Marchetti2013, Prost2015]

$$\sigma^s_{\alpha\beta} = 2\eta\tilde{v}_{\alpha\beta} + \frac{\nu_1}{2}\left(p_\alpha h_\beta + h_\alpha p_\beta - \frac{2}{d}p_\gamma h_\gamma \delta_{\alpha\beta}\right) - \zeta q_{\alpha\beta} + \left(\bar{\eta}\, d\, v_{\gamma\gamma} + \bar{\nu}_1\, d\, p_\gamma h_\gamma - \bar{\zeta} - \zeta' p_\gamma p_\gamma\right)\delta_{\alpha\beta}, \tag{2.12}$$

where $q_{\alpha\beta} = p_\alpha p_\beta - \frac{1}{d}p_\gamma p_\gamma \delta_{\alpha\beta}$ is the traceless symmetric nematic order parameter tensor, η and $\bar{\eta}$ are the shear and bulk viscosities, ζ is the anisotropic active stress coefficient, and $\bar{\zeta}$ and ζ' are two isotropic active stress coefficients. The interfacial force reads [Oriola2017]

$$f_\alpha = -\xi v_\alpha + \nu_i \dot{p}_\alpha + \zeta_{\mathrm{i}} p_\alpha, \tag{2.13}$$

where ξ, ν_i and ζ_{i} are the cell-substrate friction, the polar friction, and the contact active force, which actually correspond to the interfacial counterparts of the viscosity, the flow alignment and the active stress coefficients respectively. The friction drag force is assumed to depend only on the local velocity of the cell sheet because the turnover time associated with cell-substrate adhesions (typically through integrins) is ~ 1 min [Thomas2013], much smaller than spreading times. The contact active force (hereinafter referred to as the active traction parameter), accounts for the maximal traction stress $T_0 \equiv h\zeta_{\mathrm{i}}$ exerted by polarized cells on the substrate, and so their capability of grabbing and pulling the substrate.

Following [Pérez-González2019], and to reduce the number of parameters and define the simplest possible equations, we assume that the bulk viscosity is $\bar{\eta} = \eta$ and that the isotropic contractility is given by $\zeta' = \zeta/2$. Similarly, active stresses not associated with polarization are also neglected, that is, $\bar{\zeta} \ll \zeta$, and due to the quasistatic approximation for the polarization all the terms with $h_\alpha = 0$ vanish. Hence, the equations that define our active polar fluid model for the spreading of an epithelial monolayer reduce to the simple form [Oriola2017, Pérez-González2019]

$$\sigma^s_{\alpha\beta} = \eta(\partial_\alpha v_\beta + \partial_\beta v_\alpha) - \zeta p_\alpha p_\beta, \tag{2.14}$$

$$f_\alpha = -\xi v_\alpha + \zeta_{\mathrm{i}} p_\alpha, \tag{2.15}$$

where the polar friction ν_i has also been neglected. A summary of the symbols for the variables and parameters, together with their units and estimates for

some of them, can be found in List of symbols. If the contrary is not specified in the figures' captions, the values taken by the parameters are those appearing there.

2.3 Semi-infinite rectangular geometry

In this section, we focus on describing the motion of circular monolayers of radius R on a gradient of stiffness by tracking the position of the center of mass and the monolayer size. In general, the boundary of the cell monolayer is free to deform and move, as its normal velocity coincides with that of the adjacent fluid, and so the evolution of the shape and position of the boundary is part of the solution to the problem. However, here we are interested in studying the effect of durotaxis, so we will ignore boundary deformations. Chapter 5 will explicitly address the opposite case, when deformations are allowed and are the leading cause of motion. We may also assume that the effective surface tension of the tissue is strong enough, and the monolayers small enough, to suppress the active fingering instability that is inherent to this model, as reported in [Pérez-González2019, Alert2019a] and discussed also in Chapter 5.

To simplify even further, we can map the 2D circular monolayer to an effective 1D setup corresponding to strips of half-width $L = R$, finite in the spreading direction (x) and infinite in the transverse direction (y), and hence presenting translational invariance in the y coordinate (Fig. 2.3). This setup corresponds to the experiments on collective durotaxis of [Sunyer2016], and was also used in the numerical study of the present model [Alert2019b].

The basic physics of this 1D formulation is the same as in circular monolayers, and the results are equivalent up to geometric factors, being the analysis much simpler in the rectangular geometry, as already illustrated in preceding studies in both geometries [Pérez-González2019, Alert2019a, Alert2019b]. Furthermore, having a solvable model with simple enough analytical predictions is very valuable for gaining insights into the underlying physical mechanisms, especially when there are a lot of factors involved. We will also demonstrate how some of the limitations of the 1D formulation, including the absence of the Young-Laplace pressure drop due to tissue surface tension, can be easily incorporated.

2.3.1 Reduction to a 1D solvable model

In the 1D setup, Eq. 2.9 and Eqs. 2.14–2.15 reduce to

$$2\eta\partial_x^2 v = 2\zeta p\partial_x p + \xi v - \zeta_{\mathrm{i}} p. \tag{2.16}$$

The polarization profile is given by the solution of Eq. 2.6 satisfying $p = \pm 1$ at the respective edges $x = x_+$ and $x = x_- < x_+$. In terms of the center-of-mass position $X \equiv (x_+ + x_-)/2$ and the monolayer half-width $L \equiv (x_+ - x_-)/2$, it reads

$$p(x) = \frac{\sinh\left((x - X)/L_c\right)}{\sinh\left(L/L_c\right)}. \tag{2.17}$$

There are several length scales whose ratios determine different physical scenarios in the model. The scale L_c is typically the smallest one, as the polarized boundary layer of the tissue is often thin compared to the system size $2L$ and the other length scales [Sunyer2016, Pérez-González2019, Blanch-Mercader2017b]. The so-called screening or hydrodynamic length $\lambda \equiv \sqrt{2\eta/\xi}$, is a measure of the range of hydrodynamic interactions [Marchetti2013, Blanch-Mercader2017a, Alert2019a, Alert2019b], and it defines two important limits:

- Wet limit ($\lambda \gg L$): long-ranged hydrodynamic interactions produce non-local effects and the system behaves globally as a whole.
- Dry limit ($\lambda \ll L$): the spreading dynamics are governed by local forces, i.e. the two edges behave independently from each other.

Another relevant length scale is the so-called active polar length $L_p \equiv |\zeta|/(2\zeta_\mathrm{i})$ [Pérez-González2019], which arises as a ratio of contractility and traction forces. In the wet case, this length defines the critical tissue size for the wetting-dewetting transition, as reported in [Pérez-González2019].

To obtain the spatial velocity profile $v(x)$, Eq. 2.16 is solved with initial conditions $L_0 \equiv L(0)$ and $X_0 \equiv X(0)$, and typically with stress-free boundary conditions, $\sigma|_{x_\pm} \equiv \sigma_\pm = 0$. If a normal stress component is required to mimic the effect of an effective surface tension, as if L would be the monolayer radius, we impose $\sigma_\pm = -\gamma/L$, which implies $\partial_x v|_\pm = (\zeta - \gamma/L)/(2\eta)$ (form Eq. 2.14 and $p_\pm^2 = 1$). Then, with the edges' velocities $v_\pm \equiv v(x_\pm)$, we can finally obtain the center-of-mass velocity $U \equiv \dot{X}$ and the spreading velocity $V \equiv \dot{L}$.

2.3.2 Solutions for a uniform substrate

As a reference, we first consider the case of a spreading monolayer on top of a uniform stiffness substrate. The model parameters that account for the cell-substrate interactions, which are the passive friction ξ and the active traction ζ_i, are thus constant. Consequently, $v_+ = -v_-$, and there is no net monolayer displacement: $U = 0$. This case was studied in the wet limit ($\xi \to 0$) in [Pérez-González2019] with a circular geometry, and in the wet-dry crossover with a rectangular geometry in [Alert2019a]. The exact solution for the spreading velocity (solid lines in Fig. 2.4) is given in Eq. 2.A.3 of Appendix 2.A. Taking $\gamma = 0$

and assuming $L_c \ll L$, in the wet limit $\lambda \gg L$ it is simply

$$V^{wet} = \pm v_{\pm}^{wet} \approx \frac{L_c}{2\eta}\left[L\zeta_{\mathrm{i}} - \frac{|\zeta|}{2}\right] = \frac{L_c\zeta_{\mathrm{i}}}{2\eta}\left(L - L_p\right), \tag{2.18}$$

and so we recover Eqs. (5) and (7) from [Alert2019a] (dashed line in Fig. 2.4, converging to the full expression, and so to the solid lines, for very small tissue sizes L). Instead in the dry limit $L_c \ll \lambda \ll L$, we obtain

$$V^{dry} = \pm v_{\pm}^{dry} \approx \frac{L_c}{2\eta}\left[\lambda\zeta_{\mathrm{i}} - \frac{|\zeta|}{2}\right] = \frac{L_c\zeta_{\mathrm{i}}}{2\eta}\left(\lambda - L_p\right), \tag{2.19}$$

which is independent of the monolayer size L (dotted lines in Fig. 2.4, converging to the full expression, and so to the solid lines, for very large tissue sizes L).

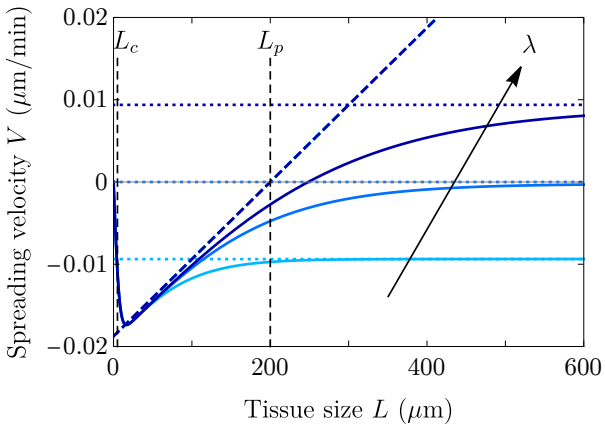

Figure 2.4: Spreading velocity on a uniform substrate. Solid lines are full expressions (Eq. 2.A.3), and the dashed and dotted lines correspond to the wet (Eq. 2.18) and dry (Eq. 2.19) limits respectively. $L_p = 200\ \mu$m and $\lambda = 100, 200$ and $300\ \mu$m. Only for the largest value, the critical size $L^* \approx 200\ \mu\mathrm{m} = L_p$ approaches the wet limit prediction; for the other two values of λ, the dry approximation is better. $L_c = 5\ \mu$m to see the convergence better.

In the wet limit, we can observe from Eq. 2.18 that there is a critical tissue size $L^* \approx L_p$, that defines the so-called active wetting transition in [Pérez-González2019]. Since $V^{wet}(L^*) = 0$, this transition distinguishes whether the cluster is expanding (positive spreading velocity $V > 0$ for $L > L^*$) or contracting (negative spreading velocity $V < 0$ for $L < L^*$). Here we refer to it as "spreading transition" and avoid the term "wetting", which refers to the relative motion motion of a fluid front with respect to the substrate. This is meant to avoid

confusion in cases where the center of mass of the tissue is moving, since one edge may recede with respect to the substrate while the tissue is globally expanding. We discuss such examples in Section 2.4.1.

In the dry limit, the spreading transition is controlled by the screening length λ. From Eq. 2.19, there is a critical $\lambda^* \approx L_p$ ($V^{dry}(\lambda^*) = 0$) such that for $\lambda < \lambda^*$ the cluster contracts ($V < 0$), regardless of its size L, and for $\lambda > \lambda^*$ the cluster expands ($V > 0$).

The full velocity and stress profiles are plotted in Fig. 2.5. The velocity is odd and the stress is even with respect to the center of the monolayer, and they allow the model predictions to be tested against experimental data, providing a simple visualization of where the system stands in the wet-dry axis. For example, the stress plateau in the bulk of the monolayer (darkest curves in Fig. 2.5b) is a signature of the wet limit (large λ), whereas two peaks of width L_c near the edges (lighter curves in Fig. 2.5b) are indicative of the dry limit (small λ). In this case, the velocity profile features a plateau of null velocity in the bulk (lightest curve in Fig. 2.5a). The comparison of these theoretical profiles with experimental data was already done for different cell types in [Blanch-Mercader2017b], and so it is not the focus of our study.

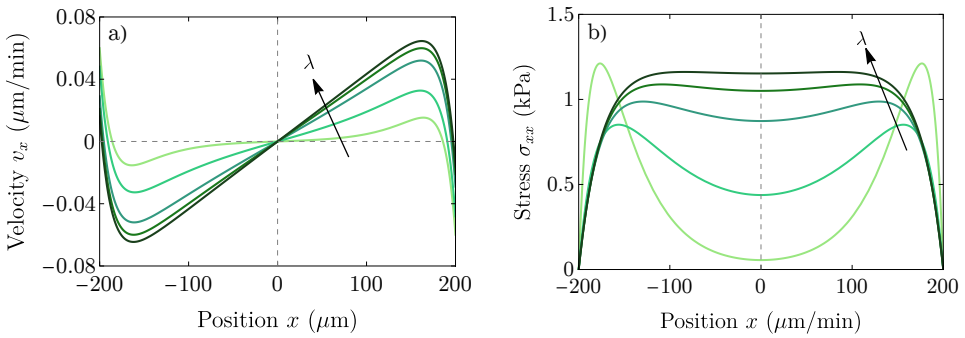

Figure 2.5: Velocity and stress profiles on a uniform substrate. The hydrodynamic length is $\lambda = 40, 100, 200, 300, 450$ μm, from light to dark green.

2.4 Solutions for a stiffness-gradient substrate: durotaxis

We now consider a spreading monolayer on top of a substrate presenting a stiffness gradient. The difference in the stiffness at different points of the substrate affects the interactions between the cells and the substrate, thus altering both

traction and friction forces, and so we take space-dependent $\xi(x)$ and $\zeta_\mathrm{i}(x)$. The relationship between these spatial variations and that of the substrate stiffness must be determined independently of the hydrodynamic model, either empirically or from a microscopic model of cell-substrate interactions. An explicit derivation requires a detailed knowledge of the molecular mechanisms at play. It has been shown that an increasing and saturating function, arising from the in-series connection of two linear elastic media (the substrate and the cellular structures bound to the substrate, with Young's modulus E and E^* respectively), fits well the experimental data [Walcott2010, Saez2010, Marcq2011, Trichet2012, Sens2013, Gupta2015], and so we take,

$$\zeta_\mathrm{i}(E) = \zeta_\mathrm{i}^\infty \frac{E}{E+E^*}, \quad \xi(E) = \xi^\infty \frac{E}{E+E^*} + \xi_0, \tag{2.20}$$

as in [Alert2019b], where ζ_i^∞ and ξ^∞ are saturation values, E^* is a characteristic stiffness of force saturation, and ξ_0 is the friction coefficient at vanishing substrate stiffness. This ξ_0 is added to avoid the strict "wet" limit $\lambda \to \infty$ ($\xi \to 0$), which is ill-defined in the presence of a traction gradient: In the absence of friction, the total force density is given by $f_\alpha = \zeta_\mathrm{i} p_\alpha$, whose integral over the tissue does not vanish if the traction is different on the stiff and the soft edges, and so global force balance cannot be satisfied.

However, to avoid introducing additional parameters and to make the interpretation of the results more transparent, we mostly consider cases where those parameters are either space-independent or have a uniform gradient, hence introducing only two new parameters associated to the stiffness variation, namely $\xi' \equiv \partial_x \xi(x)$ and $\zeta_\mathrm{i}' \equiv \partial_x \zeta_\mathrm{i}(x)$ (Section 2.4.1). This restriction is relaxed in Section 2.4.2.

2.4.1 Constant active traction gradient

To obtain analytical solutions, we take the simplest possible spatial dependence of these parameters: a linear active traction profile $\zeta_\mathrm{i}(x) = \zeta_\mathrm{i}^0 + \zeta_\mathrm{i}'(x - X)$ (where $\zeta_\mathrm{i}^0 \equiv \zeta_\mathrm{i}(X_0)$ is the initial traction offset), and a uniform friction coefficient, with $\xi' = 0$. The results, given in Appendix 2.B, are locally valid for more general traction profiles as long as $\zeta_\mathrm{i}'' L / \zeta_\mathrm{i}' \ll 1$.

Importantly, we obtain that the spreading velocity V is the same as the one on a uniform substrate V^u with the traction evaluated at the monolayer center, that is $V(\zeta_\mathrm{i}^0, \zeta_\mathrm{i}') = V^u(\zeta_\mathrm{i}^0)$. Therefore, the spreading behavior is independent of the existence of an active traction gradient, and everything that has been discussed in the previous section applies here. More generally, in cases where the traction gradient is not quite uniform, the spreading velocity will be relatively insensitive

to that gradient. The velocity of the center of mass U, however, depends on the active traction gradient, which gives rise to the phenomenon of durotaxis. The full expression for this velocity is given in Eq. 2.B.3 (solid lines in Fig. 2.6). For $\gamma = 0$, the expression of the edge velocities in the dry limit $L_c \ll \lambda \ll L$ reads

$$v_\pm^{dry} \approx \pm\frac{L_c}{2\eta}\left[\lambda\zeta_\mathrm{i}^\pm - \frac{|\zeta|}{2} \pm 2\zeta_\mathrm{i}' L_c^2\right] = v_\pm^{u,dry}(\zeta_\mathrm{i}^\pm) + \frac{\zeta_\mathrm{i}' L_c^3}{\eta}, \tag{2.21}$$

where $\zeta_\mathrm{i}^\pm$ are the local values of the active traction at the edges. The corresponding center-of-mass or durotactic velocity (dotted lines in Fig. 2.6, converging to the full expression, and so to the solid lines, for very large tissue sizes L), neglecting $2L_c^2$ in front of $L\lambda$, is

$$U^{dry} \approx \frac{L_c\lambda}{2\eta} L\zeta_\mathrm{i}' = \frac{L_c\lambda}{4\eta}(\zeta_\mathrm{i}^+ - \zeta_\mathrm{i}^-). \tag{2.22}$$

The spreading velocity is $V^{dry} = V^{u,dry}(\zeta_\mathrm{i}^0)$, with $\zeta_\mathrm{i}^0 = (\zeta_\mathrm{i}^+ + \zeta_\mathrm{i}^-)/2$. Although L appears in the first equality of Eq. 2.22, U can be rewritten in terms of the active traction difference, emphasizing that the spreading dynamics is local in the sense that the two edges behave independently from each other. Tissue durotaxis is thus directly driven by the active traction difference at the edges.

In the wet limit $L_c \ll L \ll \lambda$, the two edges are coupled through hydrodynamic interactions, and we get

$$\begin{aligned} v_\pm^{wet} &\approx \pm\frac{L_c}{2\eta}\left[L\zeta_\mathrm{i}^\pm - \frac{|\zeta|}{2} \pm \zeta_\mathrm{i}'\left(\lambda^2 - \frac{2}{3}L^2\right)\right] \\ &= v_\pm^{u,wet}(\zeta_\mathrm{i}^\pm) + \frac{L_c\zeta_\mathrm{i}'}{2\eta}\left(\lambda^2 - \frac{2}{3}L^2\right), \end{aligned} \tag{2.23}$$

which yields a center-of-mass velocity (dashed lines in Fig. 2.6, converging to the full expression, and so to the solid lines, for small tissue sizes L),

$$U^{wet} \approx \frac{\zeta_\mathrm{i}' L_c}{2\eta}\left(\lambda^2 + \frac{L^2}{3}\right) \approx \frac{L_c\lambda}{2\eta}\lambda\zeta_\mathrm{i}', \tag{2.24}$$

and a spreading velocity $V^{wet} = V^{u,wet}(\zeta_\mathrm{i}^0)$. Both $v_\pm$ and U depend on the system size L and the active traction gradient ζ_i', which illustrates that the two edges are hydrodynamically coupled.

Two main conclusions emerge, which are general in the whole wet/dry range for this case of uniform active traction gradient ζ_i' and uniform friction ($\xi' = 0$). On the one hand, the center-of-mass velocity U is proportional to the traction gradient ζ_i' and independent of the traction offset ζ_i^0. U has the same sign as ζ_i',

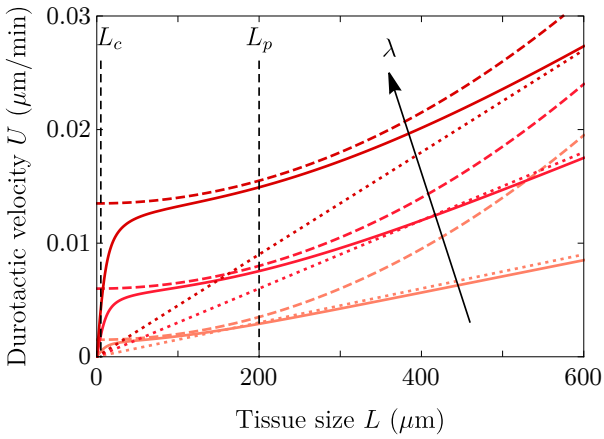

Figure 2.6: Center-of-mass velocity for a constant active traction gradient. As in Fig. 2.4, the solid lines represent the full expression (Eq. 2.B.3), and the dashed and dotted lines represent the wet (Eq. 2.24) and the dry (Eq. 2.22) limits, respectively. $L_p = 200$ μm, $L_c = 5$ μm and $\lambda = 100, 200, 300$ μm.

and there is durotaxis towards stiffer regions as long as the traction is a monotonically increasing function of the stiffness. On the other hand, the spreading velocity depends on the traction offset and not on the traction gradient. Accordingly, Fig. 2.4 still applies in the present case, and durotaxis is independent of whether the monolayer is spreading or contracting (Fig. 2.6).

In fact, the following situations are possible: First, the monolayer can contract either with the two edges moving in opposite directions ($v_- > 0$ and $v_+ < 0$) or in the same direction ($0 < v_+ < v_-$). In the former case, both edges are retracting, or dewetting. In the latter case, the + edge is wetting and the − edge is dewetting. Second, the monolayer can expand, or spread, if both edges move away from each other ($v_- < 0$ and $v_+ > 0$), both wetting the substrate, but also if both edges move in the same direction ($0 < v_- < v_+$), with the + edge wetting and the − one dewetting. It is thus clear that the condition of spreading or contraction, which is a property of the cell monolayer as a whole, and the condition of wetting or dewetting, which refers to the direction of motion of each tissue edge, are two distinct conditions that only coincide when the center of mass does not move ($U = 0$), as in [Pérez-González2019].

We show examples of these distinct situations in Fig. 2.7, corresponding to the same values as those in Fig. 2.4 and Fig. 2.6. The monolayer contracts with both edges dewetting for all L in Fig. 2.7a, for $L \lessapprox 127$ μm in Fig. 2.7b and for $L \lessapprox 54$ μm in Fig. 2.7c (solutions of $v_+ = 0$ in the wet predictions). It

contracts with the + edge wetting but the − edge dewetting faster for $L \gtrapprox 127$ μm in Fig. 2.7b, and for 54 μm $\lessapprox L \lessapprox 200$ μm in Fig. 2.7c (solutions of $v_+ = v_-$ in the wet predictions). And finally, it expands with the − edge dewetting but slower than the + one wetting for $L \gtrapprox 200$ μm in Fig. 2.7c. To have an

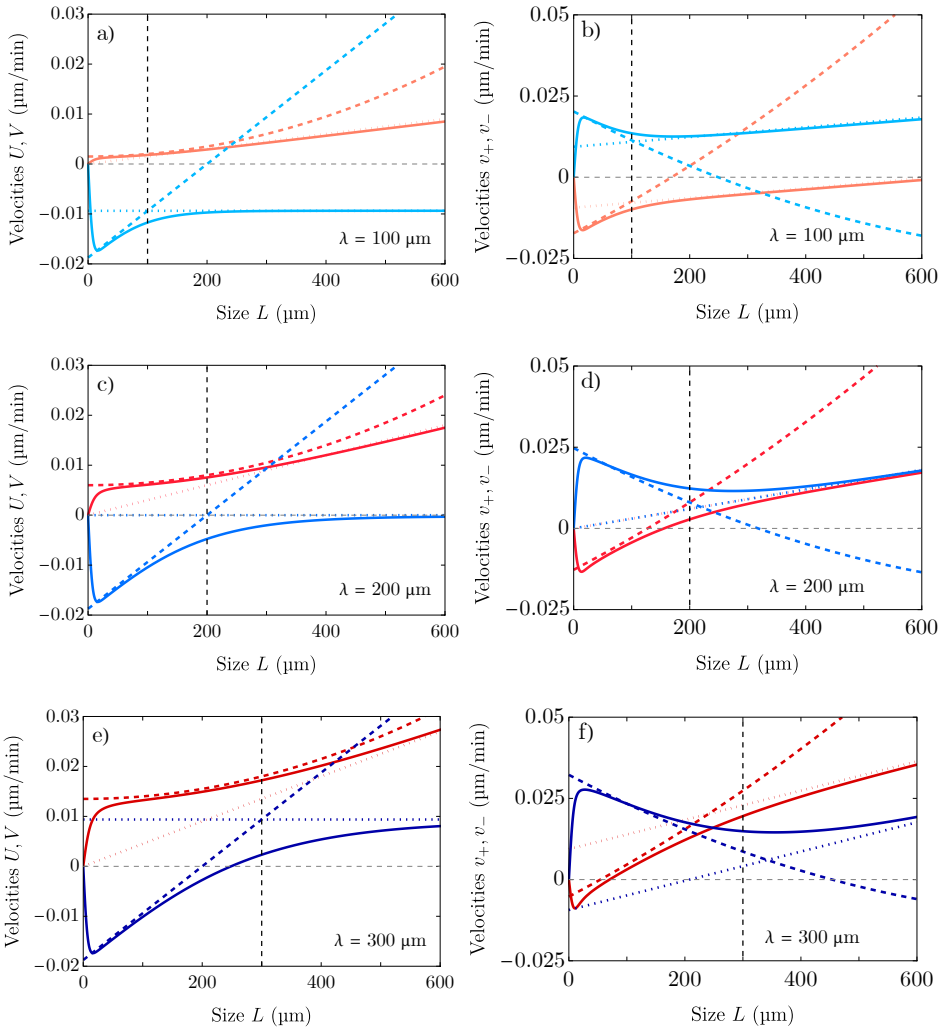

Figure 2.7: Velocities for a constant active traction gradient. Spreading velocity V (blue) and center-of-mass velocity U (red) (**a**, **c** and **e**), or edge velocities v_- (blue) and v_+ (red) (**b**, **d** and **f**), in their full expressions (solid), wet (dashed) and dry (dotted) limits, for three different values of λ (vertical dashed lines), with $L_p = 200$ μm and $L_c = 5$ μm.

expanding monolayer with both edges wetting the substrate, we should set lower contractilities or larger reactions.

The repertoire of dynamical behaviors contained in the model as a function of parameters is quite rich. Spreading V (blue lines) and center-of-mass velocities U (red lines), are plotted against monolayer size (Fig. 2.8) and active traction offset (Fig. 2.9), which are two quantities that can be easily varied and controlled in experiments [Sunyer2016]. Importantly, in addition to being independent of active traction offset, the durotactic velocity does not depend on the contractility either, which is a parameter that is more difficult to infer from experiments, and is assumed to be uniform throughout the system. An increase in either monolayer size or active traction gradient implies an increase of the difference of local tractions at the edges, $\zeta_{\mathrm{i}}^{+} - \zeta_{\mathrm{i}}^{-}$, and thus an increase in the durotactic velocity. The spreading velocity, which is independent of the traction gradient, increases with the monolayer size L, the screening length λ, and the traction offset ζ_{i}^{0}, and it decreases with the contractility $|\zeta|$.

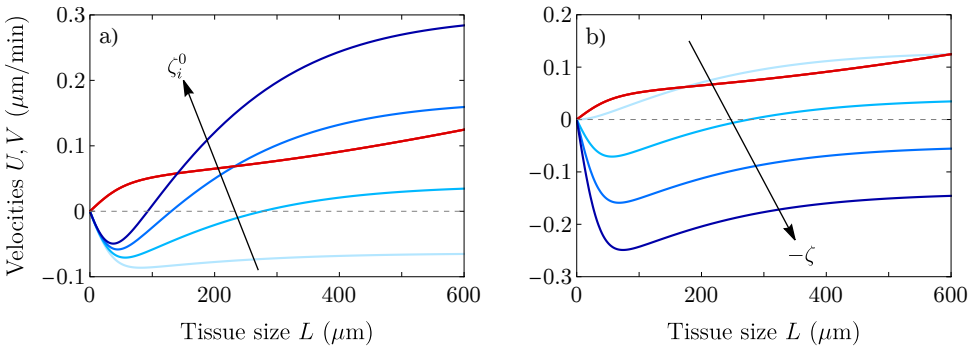

Figure 2.8: Effect of the traction offset and the contractility in the velocities. Plots of the full expressions for V (blue curves) and U (red curves) as a function of tissue size L, changing the traction offset $\zeta_{\mathrm{i}}^{0} = 0.01, 0.05, 0.10, 0.15$ kPa/μm (**a**), and the contractility $-\zeta = 0, 20, 40, 60$ kPa (**b**).

The velocity and stress profiles, plotted in Fig. 2.10 for a range of λ, are qualitatively similar to those of the uniform stiffness substrate from Fig. 2.5, except that they become asymmetric due to the stiffness gradient.

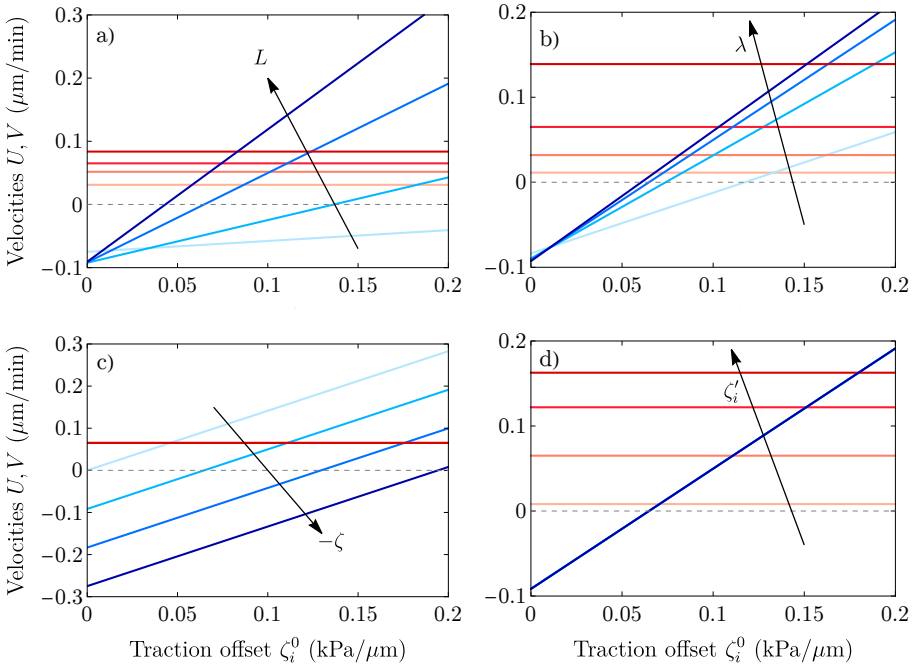

Figure 2.9: Effect of the size, the hydrodynamic length, the contractility and the active traction gradient in the velocities. Plots of the full expressions for V (blue curves) and U (red curves) as a function of the traction offset ζ_i^0, changing $L = 40, 100, 200, 350$ μm (**a**), $\lambda = 100, 200, 300, 450$ μm (**b**), $-\zeta = 0, 20, 40, 60$ kPa (**c**), and $\zeta_i' = 10^{-5}, 8 \cdot 10^{-5}, 1.5 \cdot 10^{-4}, 2 \cdot 10^{-4}$ kPa/μm^2 (**d**).

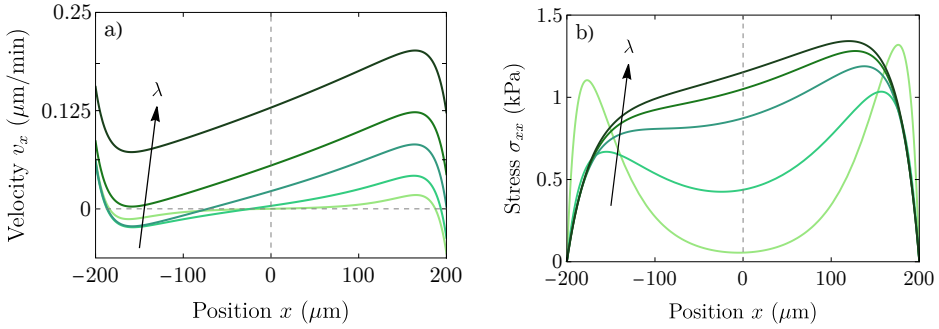

Figure 2.10: Velocity and stress profiles for a constant active traction gradient. The screening length is $\lambda = 40, 100, 200, 300, 450$ μm. With v_x at the edges we would obtain U and V in Fig. 2.9b, for $\zeta_i^0 = 0.05$ kPa/μm.

2.4.2 Constant friction gradient and active traction saturation

In this section, we relax the restriction of a uniform friction coefficient. This is a more realistic situation since both active traction and passive friction rely on the dynamics of cell-substrate adhesion molecules [Oriola2017], and hence they both depend on substrate stiffness. To illustrate the role of this effect on tissue durotaxis, and for the sake of simplicity, we consider a linear friction increase $\xi(x) = \xi_0 + \xi' x$, now with $\xi' \neq 0$. The problem with space-dependent ξ can no longer be solved analytically. Solving Eq. 2.16 numerically with a finite-difference method, we find that the center-of-mass velocity now decreases with the traction offset, as shown in Fig. 2.11. This is because larger active traction correlates with larger friction, which yields smaller velocities. Accordingly, the spreading velocity grows more slowly with the active traction offset than in the uniform friction case.

The use of linear profiles is particularly convenient from a theoretical point of view since it avoids introducing too many parameters. However, to obtain a more realistic description and to compare with experimental data, the increasing and saturating profiles from Eq. 2.20 may be taken, where E corresponds to the space-dependent Young modulus of the substrate. For *in vitro* experiments, such as those in [Sunyer2016], a simple choice is to prepare the substrate with a linear stiffness profile $E(x) = E_0 + E'(x - X)$. Numerical results for this more general case are qualitatively very similar to those in Fig. 2.11, but, at high stiffness, the saturation of traction and friction brings the dynamics to those of the uniform stiffness case, with vanishing durotactic velocity U. The parameters controlling this approach are $\zeta_{\mathrm{i}}^{\infty}$, ξ^{∞}, E^* and E'.

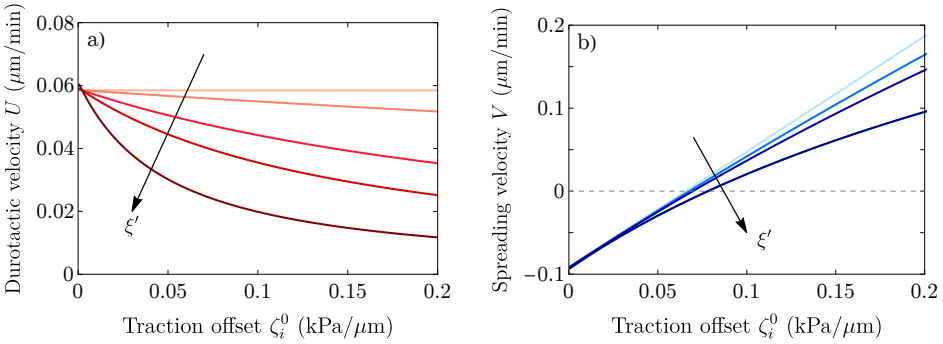

Figure 2.11: Velocities for a positive friction gradient. Center-of-mass or durotactic velocity U (**a**) and spreading velocity V (**b**), varying the friction gradient $\xi' = 0, 10^{-4}, 5 \cdot 10^{-4}, 10^{-3}, 3 \cdot 10^{-3}$ kPa·s/μm^3, and taking a stiffness offset $\xi_0 = 2$ kPa·s/μm^2.

2.5 Dynamical regimes

For a given set of parameters, η, ζ, L_c, $\zeta_\mathrm{i}(x)$ and $\xi(x)$, initial conditions X_0 and L_0, our model supplies a velocity profile $v(x)$ as the solution of the equation

$$\left(2\eta\partial_x^2 - \xi(x)\right) v(x) = \left(2\zeta p(x)\partial_x - \zeta_\mathrm{i}(x)\right) p(x), \tag{2.25}$$

where $p(x)$ is given by Eq. 2.17. For the plots in Section 2.5.1, stress-free boundary conditions are considered, but then they are generalized in Section 2.5.1 to account for a surface tension and an elastic force.

The position of the center of mass $X(t)$ and the cluster size $L(t)$ satisfy the differential equations

$$\dot{X} = \frac{v(X+L) + v(X-L)}{2}, \tag{2.26}$$

$$\dot{L} = \frac{v(X+L) - v(X-L)}{2}. \tag{2.27}$$

As X and L evolve, however, the cell cluster is visiting different regions of the substrate, so the profiles $\zeta_\mathrm{i}(x)$ and $\xi(x)$ used to solve Eq. 2.25 are changing with time. For instance, in the case of a linear active traction profile, the traction offset changes with time according to $\zeta_\mathrm{i}^0(t) = \zeta_\mathrm{i}^0(0) + \zeta_\mathrm{i}'(X(t) - X_0)$. In the rest of this section, we focus on this case with no friction gradient ($\xi' = 0$).

2.5.1 Constant active traction gradient

Since the durotactic motion is towards larger stiffness and hence larger active traction ($U > 0$ for $\zeta_\mathrm{i}' > 0$), the local active traction offset ζ_i^0 increases with time. In a uniform traction gradient, however, the durotactic velocity is insensitive to this local ζ_i^0 (Section 2.4.1), and so increasing it does not lead to an increase in the durotactic speed. Nonetheless, U depends also on the monolayer size L, which may grow or decay according to the sign of the spreading velocity V. But in general, U increases monotonically with L. Being L^* and L^{*c} two critical tissue sizes, we distinguish three different regimes in the spreading dynamics:

- For large enough sizes ($L \geq L^*$): The monolayer expands for all times ($V(t) > 0$), and due to this increase in L, then the center-of-mass velocity U also increases. Thus, monolayer spreading produces increasingly faster durotaxis.
- For intermediate sizes ($L^{*c} < L < L^*$): The monolayer initially contracts ($V < 0$). However, as the tissue moves towards stiffer regions, it may reach values of traction that are large enough to change the sign of V and produce

a transition to spreading. In this case, the evolution of L is non-monotonic in time, corresponding to initial contraction followed by spreading.

- For small sizes ($L \leq L^{*c}$): The durotactic velocity U may not be enough big to reach sufficiently large values of traction and reverse the sign of V to produce spreading. In this case, the monolayer contracts completely into a 3D spheroid ($V(t) < 0$ for all times).

Actually, L^* is the critical size for spreading on uniform substrates ($V(L^*) = 0$), and an explicit and exact expression for L^* is given by equating Eq. 2.A.3 and Eq. 2.B.4 to zero. The three dynamical regimes are illustrated in Fig. 2.12 and Fig. 2.13, increasing the size from lighter to darker curves (and so going from the full contraction, to the initial contraction and later expansion, and finally

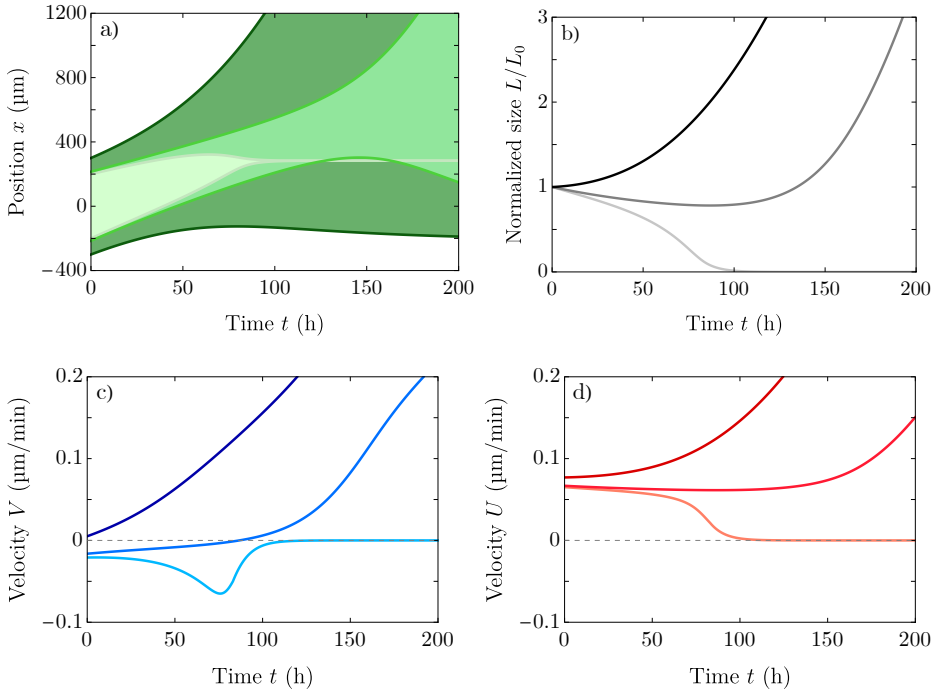

Figure 2.12: Dynamical regimes for a constant active traction gradient. **a,** Position of the monolayer edges $x_\pm(t)$, filling the area between them to represent the tissue width. **b,** Monolayer width divided by its initial value. **c,** Spreading velocity. **d,** Center-of-mass velocity. The curves, from lighter to darker lines, show an increasing $L_0 = 200, 215$ and 300 μm, characteristic of the three different dynamical regimes. The initial center-of-mass position is $X_0 = 0$ μm in all three cases, ζ_i' is constant and ξ is uniform. $L^* = 276.35$ μm and $L^{*c} \approx 213$ μm.

to the full expansion). The tissue expands when L and U increase and $V > 0$, whereas it contracts when the normalized L and U decrease and $V < 0$. The regime with initial contraction and later expansion presents an almost constant durotactic velocity U and tissue width L. Given the initial monolayer size L_0, it is possible to predict the critical lengths as a function of the active traction offset, as shown in Fig. 2.14.

The asymptotic behavior of the system at long times is thus either an indefinite expansion or a collapse. In both situations, the model is no longer adequate as additional physics will take over at long times. For the asymptotic spreading, even if the traction forces do not saturate, other forces such as elastic forces may eventually slow down and even suppress the spreading, as discussed below. In the case of monolayer retraction and collapse with $L \to 0$, the quasi-2D description breaks down and treatment of the 3D structure of the tissue is necessary.

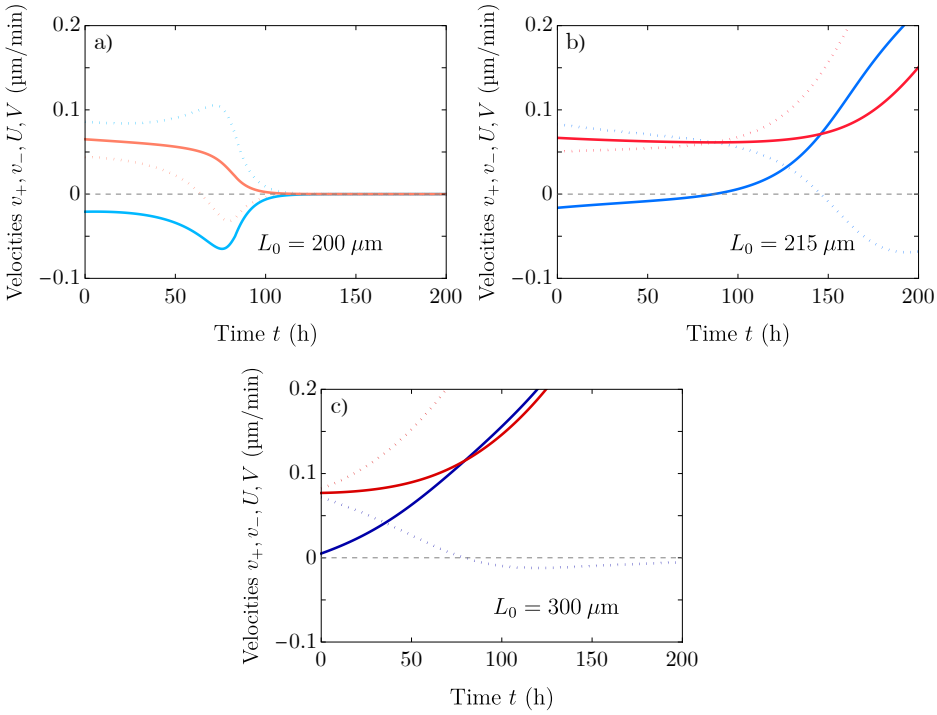

Figure 2.13: Temporal evolution of velocities for a constant active traction gradient. Evolution of the v_- (blue dotted), v_+ (red dotted), V (blue) and U (red) velocities, for clusters starting in three different values of L_0, characteristic of the three regimes: full contraction (**a**), initial contraction and later expansion (**b**) and full expansion (**c**). Same evolutions as in Fig. 2.12.

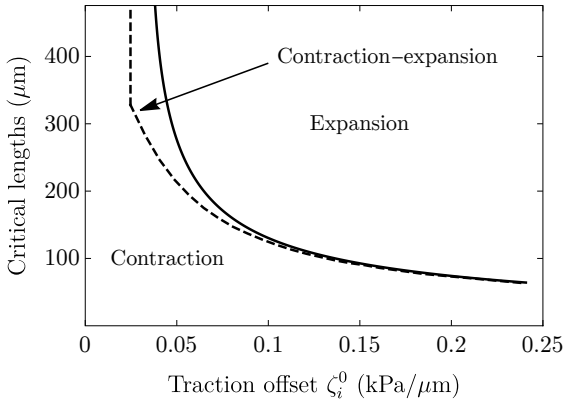

Figure 2.14: Critical lengths for the dynamical regimes. The solid curve corresponds to L^*, which is the solution of $V(L^*) = 0$ obtained from Eq. 2.B.4. The dashed curve corresponds to L^{*c}, which defines the length below which the monolayer contracts for all times, and is obtained numerically. The region between both curves defines the intermediate contraction-expansion regime.

2.5.2 Adding surface tension and an elastic force

More general profiles of the active traction and the friction parameters can also be used for studying the time evolution, but as long as the profiles are both monotonically increasing, the qualitative behavior is similar. The three spreading regimes discussed above, separated by the critical lengths L^* and L^{*c}, still exist, but their expressions and values change.

As mentioned above, the two possible asymptotic behaviors of the monolayer dynamics are not particularly interesting. This is because the traction profile cannot grow indefinitely, and other physical effects will either stop the extreme stretching of the cells in the case of spreading, or enable the formation of a 3D cell aggregate in the case of contraction. The latter will be tackled in Chapter 3. Regarding the former, different effects may be easily introduced in our current model, either to slow down the indefinite spreading of the cluster size or even to stop it.

The first possibility is to introduce an effective surface tension γ at the tissue edge, as already mentioned at the end of Section 2.3.1. The introduction of this surface tension can be understood if we interpret our 1D model as an approximation for a circular monolayer of radius L. This surface tension slows down the spreading process, less effectively for larger monolayers. For contracting monolayers, surface tension accelerates the contraction.

A less trivial but more determinant modification is to introduce an effective elastic force that prevents excessive cell stretching. This type of force has been introduced at a phenomenological level for single cells to favor a characteristic cell size. It was used for instance in [Recho2013, Hennig2018], in effective 1D models for single-cell motility. Both effects are implemented as a boundary condition for the stress:

$$\sigma_{\pm} = -\frac{\gamma}{L} - k\frac{(L - L^r)}{L^r}, \tag{2.28}$$

where k is an elastic constant and L^r is a characteristic size of the cell monolayer, proportional to the number of cells if the cell size is somehow regulated. For a constant active traction gradient ζ_{i}' and no friction gradient ($\xi' = 0$), the center-of-mass velocity U turns out to be independent of both surface tension and elasticity (see Eq. 2.B.3 in Appendix 2.B). The spreading velocity V, however, is affected, respectively giving

$$V(\gamma) = V(\gamma = 0) - \frac{\gamma}{L}\frac{\lambda}{2\eta}\tanh\left(\frac{L}{\lambda}\right), \tag{2.29}$$

$$V(k) = V(k = 0) - k\frac{L - L^r}{L^r}\frac{\lambda}{2\eta}\tanh\left(\frac{L}{\lambda}\right), \tag{2.30}$$

when either surface tension or elasticity is added.

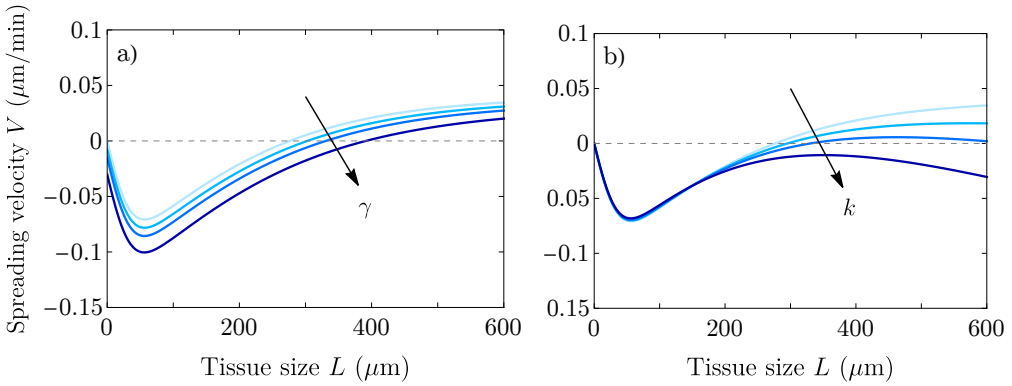

Figure 2.15: Effect of the surface tension and the elastic force in the spreading velocity. **a,** $k = 0$ and surface tension changes with values $\gamma = 0, 20, 40, 80$ kPa·μm. **b,** $\gamma = 0$ and the elastic constant changes with values $k = 0, 0.05, 0.1, 0.2$ kPa ($L^r = 150$ μm). To showcase its effects, γ is taken larger than what is measured experimentally for cell aggregates, and k is comparable to $\zeta_{\mathrm{i}} L_c \approx \sigma$.

The surface tension γ always decreases the spreading velocity, while the elastic term contributes with a different sign depending on whether the monolayer size is larger or smaller than L^r, always in the direction of approaching the reference value L^r (Fig. 2.15). Both effects influence the spreading dynamics, changing for instance the critical lengths, but the phenomenology and qualitative evolution of the monolayer typically remain unchanged.

For large k and $L > L^r$ (Fig. 2.16a), a monolayer that starts spreading can eventually change its behavior and become contracting. In this case, similar to surface tension (Fig. 2.16c), elasticity slows down expansion and accelerates contraction. Instead, if $L < L^r$ (Fig. 2.16b), elasticity accelerates expansion and slows down contraction, although only very large k ($k \gg \zeta_i L_c \sim \sigma$), presumably not biologically possible, enable this contraction-to-expansion transition.

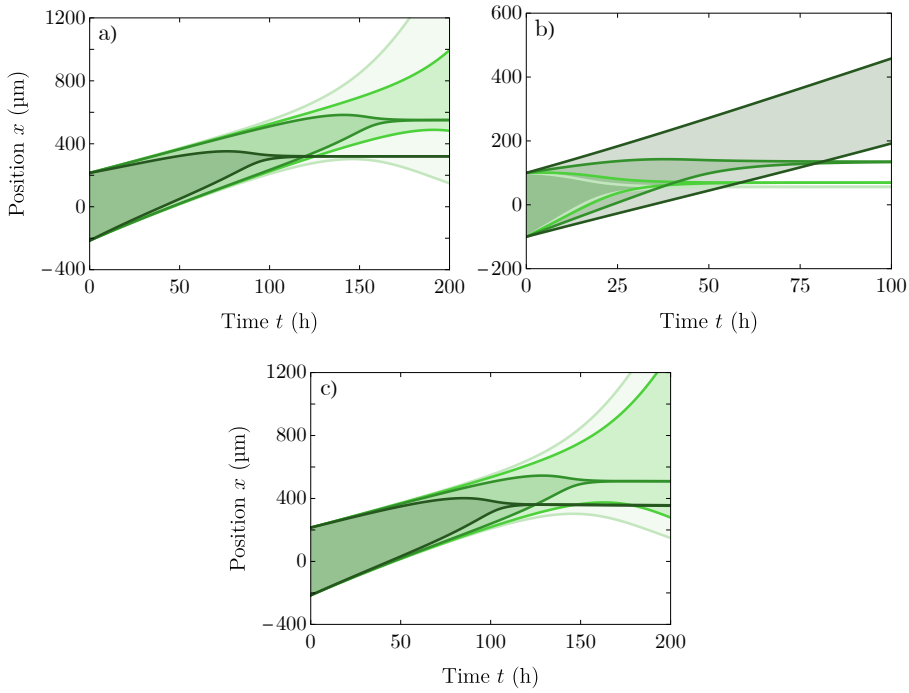

Figure 2.16: Effect of the surface tension and the elastic force in the dynamical regimes. Curves of the same color show the evolution of the position of the edges $x_\pm(t)$, filling the area between them to represent the tissue width. **a,b** $\gamma = 0$ and $L^r = 150$ μm. The initial size is $L_0 = 215$ μm and $k = 0, 0.03, 0.05, 0.5$ kPa in **a**, whereas $L_0 = 100$ μm and $k = 0, 2, 3, 5$ kPa in **b**. **c,** $k = 0$ and only the $L_0 = 215$ μm case is shown with $\gamma = 0, 1, 3, 10$ mN/m. In both cases, the parameters increase from lighter to darker green curves.

2.6 Discussion and conclusions

In this chapter, we studied generic scenarios of collective durotaxis based on a continuum model of epithelial monolayers as 2D active fluids. Effectively, we mapped the system to a 1D setup and related the stiffness gradient of the substrate to space-dependent cell-substrate parameters, namely the friction $\xi(x)$ and the active traction $\zeta_i(x)$. For the simplest case of a linear active traction profile and a uniform friction (constant ζ_i' and $\xi' = 0$), the spreading velocity is exactly the same as that for the uniform substrate case, so the spreading behavior is independent of the existence of a traction gradient. The velocity of the center of mass, instead, is proportional to ζ_i', and so the cell monolayer performs durotaxis as long as the traction is a monotonically increasing function of the substrate stiffness. These conclusions are locally valid for more general traction profiles provided that the gradient does not change significantly over the monolayer size.

The physical parameters of the model play a key role in characterizing the durotactic dynamics. The durotactic velocity increases with both the traction gradient ζ_i' and the monolayer size L, as also seen in [Escribano2018], but is independent of the contractility ζ and the traction offset ζ_i^0. Therefore, the same monolayer placed at different positions along the stiffness gradient would have the same durotactic velocity. However, the spreading dynamics would be different, since although the spreading velocity is independent of the traction gradient ζ_i', it increases with the offset ζ_i^0, the monolayer size L and the hydrodynamic length λ, and decreases with contractility ζ.

For non-uniform friction ($\xi' \neq 0$), or for traction and friction profiles saturating with stiffness, the model predicts lower velocities for larger stiffness offsets, recovering the results from [Sunyer2016, Escribano2018, González-Valverde2018]. At high stiffness, parameter saturation makes the system asymptotically approach the dynamics on uniform substrates, and therefore vanishing durotaxis.

In addition to the predictions for local durotaxis and spreading, we have discussed the temporal evolution of a monolayer along the stiffness gradient as it changes its position and size. Combining states of spreading and contraction of the monolayer, with states of interface wetting and dewetting, we identify three different regimes of durotactic motion: Large monolayers spread indefinitely, small monolayers contract indefinitely, and monolayers in an intermediate size range display a non-monotonic evolution whereby they switch from contraction to spreading at a specific time. These three regimes are separated by two critical lengths, which can be determined analytically in simple cases (like constant ζ_i' and $\xi' = 0$), or illustrated numerically for more general situations. If additional physical ingredients are added to the model, such as surface tension and elastic

forces that oppose large deformations of the tissue, the expansion is typically slowed down and the contraction accelerated.

In the context of soft active matter models of living systems, our study contributes to the view of epithelial tissues as active viscous polar systems and provides simple predictions that could be tested in experiments and used to infer model parameters. It could also guide the design of experiments on collective durotaxis, for instance, to tune the dynamical regimes depending on the tissue size. However, in the majority of the experiments done up to now, the tissues expand indefinitely [Sunyer2016]. Either contractilities are not large enough or active tractions are too large, and thus the sweet spot to observe other dynamical regimes is not easy to find. Nevertheless, it is always interesting to elucidate to what extent a purely mechanical, phenomenological description, with no need to invoke complex biochemical regulation, can account for the observed phenomenology in different forms of collective cell migration.

The model discussed here has some limitations, such as the absence of cell proliferation or the unrealistic long-time behavior. To address these problems, we should include additional forces to prevent indefinite spreading (as explained with the surface tension or the elastic restoring force), and include effects from the 3D structure of the tissue or multiple-layer structure resulting from the monolayer contraction. Cell proliferation is not expected to significantly modify the physical picture of the problems addressed in this thesis, and will therefore not be considered. The effects of a 3D structure of durotactic clusters are examined in the next chapter.

Contributions and acknowledgements

The work described in this chapter was a direct continuation from [Alert2019b]. I performed analytical calculations, numerical integration, and contributed to the development and interpretation of the theory.

Appendices

2.A Complete solution for a uniform substrate

Here we assume a constant active traction ζ_i and friction ξ. In the boundaries, the normal component of the stress is due to two different effects: an effective surface tension γ (interpreting our 1D model as an approximation for a circular cluster of radius L), and an effective elastic stiffness k, accounting for a mean-field-type linear elastic interaction as in [Recho2013] that prevents the tissue from excessive stretching, being L^r the reference length (an extended explanation can be found in Section 2.5.2). Thus, with the constitutive equation for the stress in Eq. 2.14 and $p_\pm^2 = 1$,

$$\sigma|_{x_\pm} \equiv \sigma_\pm = -\frac{\gamma}{L} - k\frac{L-L^r}{L^r} \longrightarrow \partial_x v|_\pm = \frac{1}{2\eta}\left(\zeta - \frac{\gamma}{L} - k\frac{L-L^r}{L^r}\right). \quad (2.A.1)$$

Taking the solution for the polarization from Eq. 2.17, the solution for the velocity profile from Eq. 2.16 reads

$$\begin{aligned} v(x) = \frac{\lambda}{2\eta}\Bigg[&\left(\zeta - \frac{\gamma}{L} - k\frac{L-L^r}{L^r} + \frac{\lambda^2 L_c \zeta_\mathrm{i}}{\lambda^2 - L_c^2}\coth\left(L/L_c\right)\right. \\ &\left. - \frac{2\zeta\lambda^2}{4\lambda^2 - L_c^2}\left(2 + \operatorname{csch}^2\left(L/L_c\right)\right)\right)\frac{\sinh\left(x/\lambda\right)}{\cosh\left(L/\lambda\right)} \\ &+ \frac{\lambda L_c}{\sinh\left(L/L_c\right)}\left(\frac{\zeta}{4\lambda^2 - L_c^2}\frac{\sinh\left(2x/L_c\right)}{\sinh\left(L/L_c\right)} - \frac{\zeta_\mathrm{i} L_c}{\lambda^2 - L_c^2}\sinh\left(x/L_c\right)\right)\Bigg]. \end{aligned} \quad (2.A.2)$$

Because $v(x)$ is an odd function, there is no motion of the center of mass $U = 0$, and so without loss of generalization we can take $X = 0$. Then, we can easily

write $v_+ = v(L)$ and $v_- = v(-L)$, giving

$$v_\pm = \pm\frac{\lambda}{2\eta}\Bigg[\left(\zeta - \frac{\gamma}{L} - k\frac{L-L^r}{L^r} + \frac{\lambda^2 L_c\zeta_\mathrm{i}}{\lambda^2 - L_c^2}\coth\left(L/L_c\right) - \frac{2\zeta\lambda^2}{4\lambda^2 - L_c^2}\left(2 + \mathrm{csch}^2\left(L/L_c\right)\right)\right)\tanh\left(L/\lambda\right) + \lambda L_c\left(\frac{2\zeta}{4\lambda^2 - L_c^2}\coth\left(L/L_c\right) - \frac{\zeta_\mathrm{i}L_c}{\lambda^2 - L_c^2}\right)\Bigg], \tag{2.A.3}$$

and thus the spreading velocity is $V = v_+ = -v_-$. The exact critical L^* is such that Eq. 2.A.3 $= 0$. In the relevant limit $L_c \ll L$ and $L_c \ll \lambda$,

$$v_\pm \approx \pm\frac{1}{2\eta}\left[\lambda\tanh\left(L/\lambda\right)\left(L_c\zeta_\mathrm{i} - \frac{\gamma}{L} - k\frac{L-L^r}{L^r}\right) + L_c\left(\frac{\zeta}{2} - \zeta_\mathrm{i}L_c\right)\right], \tag{2.A.4}$$

and further, in the wet ($L \ll \lambda$) and dry ($L \gg \lambda$) cases,

$$v_\pm^{wet} \approx \pm\frac{L_c}{2\eta}\left[\zeta_\mathrm{i}(L - L_c) + \frac{\zeta}{2}\right] \mp \frac{L}{2\eta}\left(\frac{\gamma}{L} + k\frac{L-L^r}{L^r}\right), \tag{2.A.5}$$

$$v_\pm^{dry} \approx \pm\frac{L_c}{2\eta}\left[\zeta_\mathrm{i}(\lambda - L_c) + \frac{\zeta}{2}\right] \mp \frac{\lambda}{2\eta}\left(\frac{\gamma}{L} + k\frac{L-L^r}{L^r}\right). \tag{2.A.6}$$

Setting $\gamma = k = 0$, neglecting L_c in front of λ or L, and writing the contractility as $\zeta = -|\zeta| < 0$, we respectively obtain Eq. 2.18 and Eq. 2.19.

2.B Complete solution for a constant active traction gradient

For a linear active traction profile $\zeta_\mathrm{i}(x)$ (constant gradient ζ_i'), constant friction ξ ($\xi' = 0$), and same boundary conditions as in Appendix 2.A, the solution to Eq. 2.16 with the polarization field from Eq. 2.17, yields

$$
\begin{aligned}
v(x) = {} & \frac{\lambda^2 L_c}{2\eta \sinh\left(L/L_c\right)} \Bigg[\frac{\zeta}{4\lambda^2 - L_c^2} \frac{\sinh\left(2(x-X)/L_c\right)}{\sinh\left(L/L_c\right)} - \frac{L_c \zeta_\mathrm{i}(x)}{\lambda^2 - L_c^2} \sinh\left(\frac{x-X}{L_c}\right) \\
& + \frac{2\zeta_\mathrm{i}' \lambda^2 L_c^2}{(\lambda^2 - L_c^2)^2} \cosh\left(\frac{x-X}{L_c}\right) \Bigg] + C_1 e^{x/\lambda} + C_2 e^{-x/\lambda}, \text{ where} \\
C_1 = {} & \frac{-\lambda e^{-\frac{X}{\lambda}}}{4\eta \cosh\left(L/\lambda\right)} \Bigg[- \left(\zeta - \frac{\gamma}{L} - k \frac{L - L^r}{L^r} \right) + \lambda^2 L_c \Bigg(\frac{2\zeta(1 + \coth^2\left(L/L_c\right))}{L_c(4\lambda^2 - L_c^2)} \\
& - \frac{\zeta_\mathrm{i}(x)}{\lambda^2 - L_c^2} \coth\left(L/L_c\right) + \frac{\zeta_\mathrm{i}' \coth\left(L/\lambda\right)}{\lambda^2 - L_c^2} \left(\frac{2\lambda^2 L_c}{\lambda^2 - L_c^2} - L_c - L \coth\left(L/L_c\right) \right) \Bigg) \Bigg], \\
C_2 = {} & \frac{\lambda e^{\frac{X}{\lambda}}}{4\eta \cosh\left(L/\lambda\right)} \Bigg[- \left(\zeta - \frac{\gamma}{L} - k \frac{L - L^r}{L^r} \right) + \lambda^2 L_c \Bigg(\frac{2\zeta(1 + \coth^2\left(L/L_c\right))}{L_c(4\lambda^2 - L_c^2)} \\
& - \frac{\zeta_\mathrm{i}(x)}{\lambda^2 - L_c^2} \coth\left(L/L_c\right) + \frac{\zeta_\mathrm{i}' \coth\left(L/\lambda\right)}{\lambda^2 - L_c^2} \left(\frac{2\lambda^2 L_c}{\lambda^2 - L_c^2} - L_c - L \coth\left(L/L_c\right) \right) \Bigg) \Bigg] \\
& - \frac{\zeta_\mathrm{i}' \lambda^3 L_c e^{\frac{X}{\lambda}}}{2\eta \sinh\left(L/\lambda\right)(\lambda^2 - L_c^2)} \left(\frac{2\lambda^2 L_c}{\lambda^2 - L_c^2} - L_c - L \coth\left(L/L_c\right) \right) \Bigg].
\end{aligned}
\tag{2.B.1}
$$

Now, the center-of-mass velocity $U \neq 0$, and so its position $X \neq 0$. The expressions for v_+ and v_- are directly obtained by substituting $x_+ = X + L$ and $x_- = X - L$, giving

$$
\begin{aligned}
v_\pm = {} & \pm \frac{\lambda^2 L_c}{2\eta} \left[\frac{2\zeta \coth\left(L/L_c\right)}{4\lambda^2 - L_c^2} - \frac{L_c \zeta_\mathrm{i}^\pm}{\lambda^2 - L_c^2} \pm \frac{2\zeta_\mathrm{i}' \lambda^2 L_c^2 \coth\left(L/L_c\right)}{(\lambda^2 - L_c^2)^2} \right] \\
& + C_1 e^{\frac{X \pm L}{\lambda}} + C_2 e^{-\frac{X \pm L}{\lambda}}.
\end{aligned}
\tag{2.B.2}
$$

Then, $U = (v_+ + v_-)/2$ and $V = (v_+ - v_-)/2$, giving

$$U = \frac{\zeta_\mathrm{i}'}{2\eta}\frac{L_c\lambda^2}{\lambda^2 - L_c^2}\left[\lambda\coth\left(\frac{L}{L_c}\right)\left(\frac{2L_c^2\lambda}{\lambda^2 - L_c^2} + L\coth\left(\frac{L}{\lambda}\right)\right)\right.$$
$$\left. - \frac{L_c\lambda(L_c^2 + \lambda^2)}{\lambda^2 - L_c^2}\coth\left(\frac{L}{\lambda}\right) - LL_c\right], \tag{2.B.3}$$

$$V = \frac{\lambda}{2\eta}\left[\left(\zeta - \frac{\gamma}{L} - k\frac{L - L^r}{L^r} + \frac{\lambda^2 L_c\zeta_\mathrm{i}(X)}{\lambda^2 - L_c^2}\coth\left(L/L_c\right)\right.\right.$$
$$\left.\left. - \frac{2\zeta\lambda^2}{4\lambda^2 - L_c^2}\left(2 + \mathrm{csch}^2\left(L/L_c\right)\right)\right)\tanh\left(L/\lambda\right)\right.$$
$$\left. + \lambda L_c\left(\frac{2\zeta}{4\lambda^2 - L_c^2}\coth\left(L/L_c\right) - \frac{\zeta_\mathrm{i}(X)L_c}{\lambda^2 - L_c^2}\right)\right]. \tag{2.B.4}$$

V is equal to the spreading velocity from the uniform case (Eq. 2.A.3), with $\zeta_\mathrm{i} = \zeta_\mathrm{i}(X)$, and U does not depend on the traction offset $\zeta_\mathrm{i}^0 = \zeta_\mathrm{i}(X)$, contractility ζ, surface tension γ or elastic constant k. In the relevant limit $L_c \ll \lambda$ and $L_c \ll L$,

$$v_\pm \approx \pm\frac{L_c}{2\eta}\left[\frac{\zeta}{2} - L_c\zeta_\mathrm{i}^\pm \pm 2\zeta_\mathrm{i}'L_c^2\right] \mp \frac{\lambda}{2\eta}\left[\left(\frac{\gamma}{L} + k\frac{L - L^r}{L^r} - L_c\zeta_\mathrm{i}(X)\right)\tanh\left(\frac{L}{\lambda}\right)\right.$$
$$\left. \mp L_cL\zeta_\mathrm{i}'\coth\left(\frac{L}{\lambda}\right)\right], \tag{2.B.5}$$

and further, in the wet ($L \ll \lambda$) and dry ($L \gg \lambda$) cases,

$$v_\pm^{wet} \approx \pm\frac{L_c}{2\eta}\left[L\zeta_\mathrm{i}^\pm + \frac{\zeta}{2} \pm \zeta_\mathrm{i}'\left(\lambda^2 - \frac{2}{3}L^2\right)\right] \mp \frac{L}{2\eta}\left(\frac{\gamma}{L} + k\frac{L - L^r}{L^r}\right) \tag{2.B.6}$$

$$v_\pm^{dry} \approx \pm\frac{L_c}{2\eta}\left[\lambda\zeta_\mathrm{i}^\pm + \frac{\zeta}{2} \pm 2\zeta_\mathrm{i}'L_c^2\right] \mp \frac{\lambda}{2\eta}\left(\frac{\gamma}{L} + k\frac{L - L^r}{L^r}\right). \tag{2.B.7}$$

Setting $\gamma = k = 0$, and writing the contractility as $\zeta = -|\zeta| < 0$, we respectively obtain Eq. 2.21 and Eq. 2.23.

Chapter 3

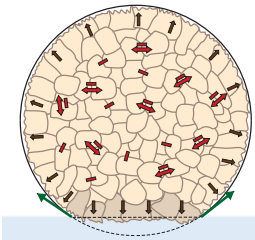

Collective durotaxis and 3D wetting of spheroidal clusters

3.1 Introduction

In Chapter 2 we discussed the underlying mechanisms of collective durotaxis of 2D epithelial monolayers. However, in many experiments, cells form spheroidal aggregates sitting on a substrate, and a fully 3D theory must be addressed, particularly in the context of collective durotaxis. Three-dimensional collective migration is obviously of great relevance since nature operates mostly in three dimensions and so *in vivo*, cells tend to migrate cohesively as 3D clusters more often than as quasi-2D monolayers. Remarkably, collective durotaxis has recently been reported as the key mechanism driving the cohesive migration of neural crest clusters during the development of *Xenopus laevis* [Shellard2021a]. These results are summarized in Fig. 3.1, where it is shown that neural crest cells in abrogated stiffness gradients undergo random movement rather than directional migration, indicating that the stiffness gradient strongly impacts directionality (Fig. 3.1g) rather than motility in general (Fig. 3.1h).

In vivo experiments present significant challenges, and controlling environmental conditions is often very difficult, which obscures the ability to isolate the fundamental mechanisms driving the behavior. In contrast, *in vitro* experiments offer more controlled and tunable conditions. With this perspective in mind, this chapter aims to elucidate the minimal physical principles of the underlying

mechanism of collective durotaxis of 3D cell clusters and its interplay with the wetting properties, showing how it arises from the competition of forces in the tissue and the substrate. We will also compare our findings with experiments.

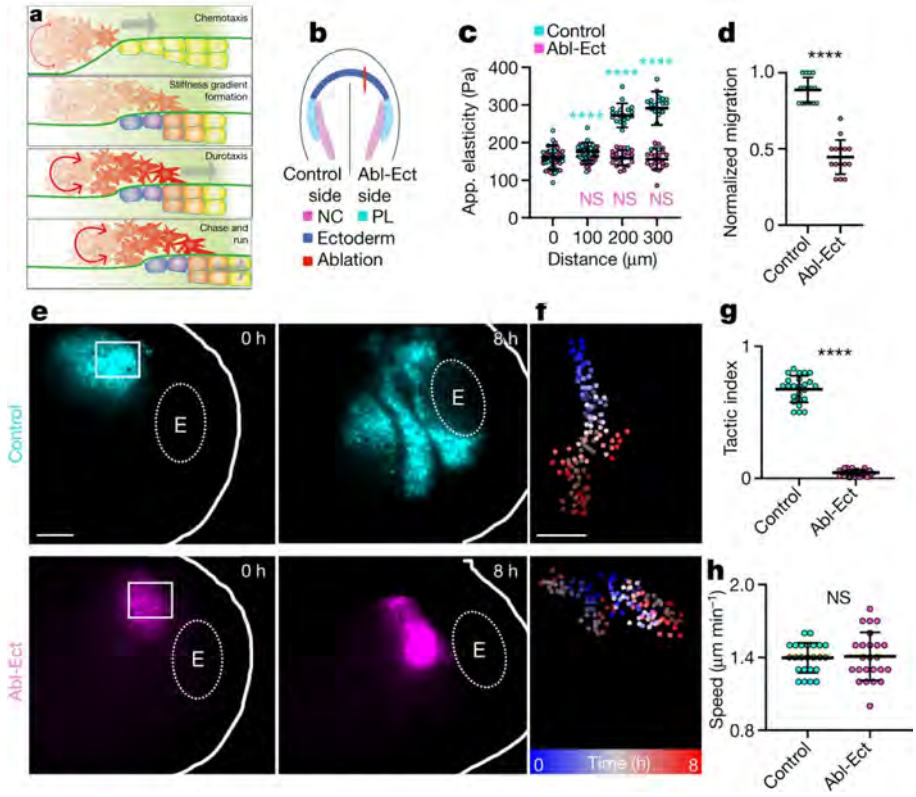

Figure 3.1: Neural crest durotaxis *in vivo*. **a,** Model of the neural crest cells (in red) self-generated stiffness gradient in the adjacent placodal tissue (purple stiff, yellow soft). **b,** Schematic of the dorsal view of a *Xenopus laevis* embryo. **c,d,** Stiffness measurements by nanoindentation on the placodes (**c**), showing that the gradient of stiffness is abrogated when ablation of the ectodermal tissue is done, and neural crest migration is impaired (**d**). **e–h,** Graft of fluorescently labeled neural crest into control (cyan) or ablated (magenta) embryos (**e**), time-coded projected cell tracks (**f**), tactic index, defined as the ratio between the distance traveled by a cell in the direction of the gradient and the total distance (**g**) and quantification of speed (**h**). Scale bars, 150 μm (**e**) and 50 μm (**f**). Adapted from [Shellard2021a].

To this end, a systematic mechanical analysis of collective durotaxis in 3D epithelial clusters was performed by Macià-Esteve Pallarès in Xavier Trepat's group (IBEC, Barcelona). So far, durotaxis of single cells and clusters has been studied *in vitro* in the presence of gradients in the stiffness of the extracellular ma-

trix (ECM) [Lo2000, Isenberg2009, Vincent2013, Sunyer2016, Hartman2016, Shellard2021b]). However, important migratory processes during early development and cancer progression take place in contexts lacking ECM [Richardson2010, Cai2014], for instance:

- In *Drosophila* oogenesis, border cell clusters migrate anteroposteriorly in the egg chamber by establishing dynamic protrusions with neighboring nurse cells through E-cadherin receptors [Cai2014, Dai2020].
- In zebrafish primordial germ cells' migration [Grimaldi2020], as well as that of progenitor cells and cell sheets during epiboly [Babb2004, Shimizu2005].
- In mouse retinal endothelial cells [Dorrell2002] and neuronal precursors' migration [Luccardini2013].
- In collective invasion and remodeling of epithelial tumors, where E-cadherin is the dominant adhesion molecule between cancer cells [Shamir2014, Padmanaban2019].
- In interneuron precursors and neurite outgrowth, N-cadherin mediates the long-distance migration [Giannone2009, Luccardini2013, Nguyen2019].

Although collective migration through cadherin receptors is well established, whether these cell-cell adhesion proteins can mediate durotaxis is unknown. This is the reason why all the performed experiments (explained in Section 3.2), were done in E-cadherin-coated gels. However, this is not relevant to the theoretical model, which does not distinguish between different protein coating and so predicts that all the phenomenology should be independent of it. We will thus not deep into this during the chapter, but the generic behavior was indeed validated also in experiments with gels functionalized with fibronectin, an ECM protein, provided that the clusters were brought close to the neutral wetting regime [Pallarès2023].

In Section 3.2 we briefly explain and comment on the experiments and the results, and in Section 3.3 a 3D active wetting model for spheroidal cell clusters is developed. The results regarding the non-monotonic durotactic behavior and the interpretation of the mechanism are described in Section 3.4 and Section 3.5, and examples of the dynamical evolutions are commented in Section 3.6 for a better understanding of the mechanisms at play. Finally, in Section 3.7, we give a brief note on the limitations of the theory.

Like in Chapter 2, all the values of model parameters that are not specified in the figures' captions are taken from the List of symbols.

3.2 Durotaxis of epithelial cell clusters

The goal of the experiment is to study the dynamics of the migration and the morphology of 3D clusters of cells in response to different stiffness of the substrates. To this end, A431 cells are used, which are a human cell line established from an epidermoid carcinoma.

Polyacrylamide (PAA) gels are prepared following conventional protocols, well-established in the laboratory, and their stiffness is tuned by changing the concentration of the different components, mainly acrylamide and bisacrylamide [Serra-Picamal2012, Uroz2018, Pérez-González2019]. A gradient is achieved by sliding an opaque mask during the UV-triggered polymerization, and the rates at which the mask is moved define the steepness of the stiffness gradients [Sunyer2012]. Gel stiffness is measured with Atomic Force Microscopy (AFM) after every experiment, and fluorescent beads are embedded in the gels to infer the traction forces. With the beads, gel displacements are measured, comparing two images: one with the cells, and the other without, giving the relaxed state of the gel. From these, traction forces are inferred using a custom Particle Imaging Velocimetry (PIV) software [Trepat2009]. Finally, the gels must be coated with proteins to allow cell attachment. In the majority of the performed experiments, they are coated with oriented E-cadherin proteins instead of ECM proteins (like fibronectin or collagen which tend to be more common), to study the migration through these intracellular proteins. However, the generality of the phenomena is also demonstrated in fibronectin-coated gels.

Clusters of A431 cells are formed by seeding $5 \cdot 10^3$ cells in low attachment wells with starvation media for 24 h, and they are mechanically disaggregated into smaller clusters exhibiting heterogeneous sizes. Then, they are seeded on top of the coated PAA gels, and imaging starts approximately after 4 h. Experiments run typically for more than 10 h, with image acquisitions every 10 min.

3.2.1 Experiments on uniform gels

When clusters are seeded on uniform-stiffness gels (Fig. 3.2), their speed is non-monotonic with the stiffness of the gel: minimal at low stiffness (0.2 kPa), peaking at intermediate stiffness (24 kPa) and then decreasing again at high stiffness (200 kPa) (Fig. 3.3a). This non-monotonic behavior coincides with different regimes of cluster spreading, which we interpret within the conceptual framework of active tissue wetting [Douezan2011, Douezan2012b, González-Rodríguez2012, Beaune2014, Wallmeyer2018, Beaune2018, Alert2019b, Pérez-González2019]. At low stiffness, clusters are nearly spherical and the contact angle between the cluster and the substrate is close to 180°, indicating full dewetting (or complete

retraction of the basal monolayer in contact with the substrate). By contrast, at high stiffness clusters spread to form a monolayered epithelium with a low contact angle, indicating full wetting (complete spreading) (Fig. 3.2 and Fig. 3.3b).

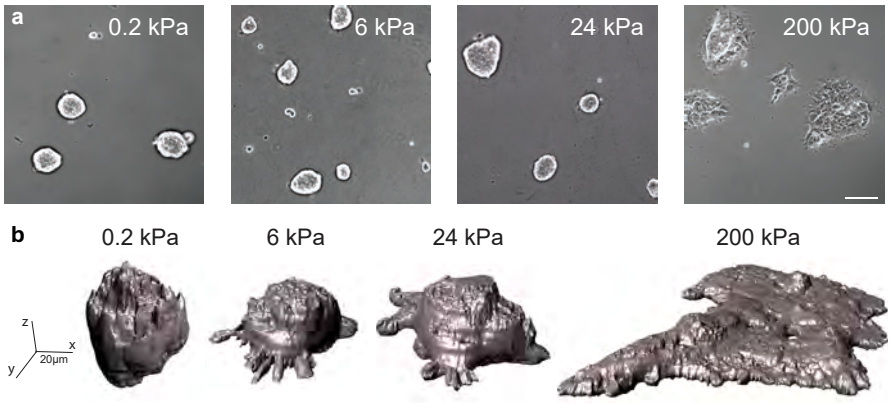

Figure 3.2: Cluster wetting on uniform-stiffness gels. a, Phase contrast images of A431 cell clusters seeded on E-cadherin-coated gels of uniform stiffness, of 0.2, 6, 24, and 200 kPa from left to right. Scale bar, 100 μm. **b,** 3D renderings of some representative clusters in the different stiffness.

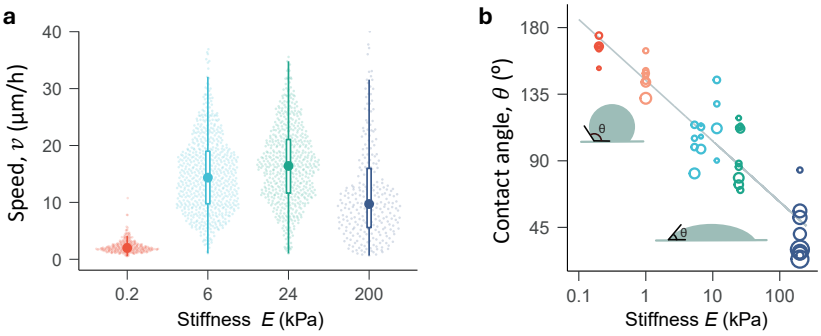

Figure 3.3: Cell clusters show optimal motility in the neutral wetting regime. a, Cluster speed at different substrate stiffness. The central dot is the median and small ones represent individual clusters ($n = 296$ clusters for 0.2 kPa, $n = 646$ clusters for 6 kPa, $n = 561$ clusters for 24 kPa and $n = 266$ clusters for 200 kPa). **b,** Angle θ between the cell cluster and the substrate, for uniform-stiffness gels, of 0.2, 1, 6, 11, 24 and 200 kPa. Each dot is the average contact angle for one cluster, and the circle size is proportional to the cluster's average diameter ($n = 43$ clusters).

At intermediate stiffness, for contact angles of around 90°, clusters display highly dynamic protrusions (Fig. 3.2b). These data suggest that at the crossover between low and high wettability ($\theta \approx 90°$), which we call the neutral wetting regime, clusters become maximally motile by rapidly engaging and disengaging actin-rich protrusions with the substrate.

Traction force microscopy (TFM) can only be performed on clusters seeded on gels of 1 and 6 kPa, because at higher stiffness there is insufficient resolution to measure the three components of the traction robustly. Radial tractions T_r (in-plane tractions with the substrate) point towards the center of the cluster,

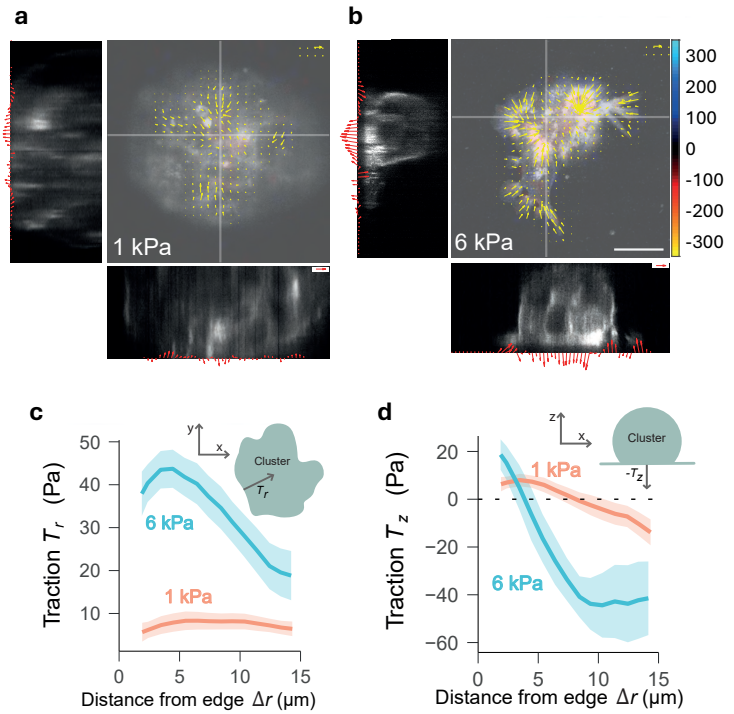

Figure 3.4: Traction forces increase with stiffness. **a,b,** Traction forces exerted by representative clusters on 1 kPa (**a**) and 6 kPa (**b**) gels. Yellow vectors represent traction forces in the x–y plane while red vectors represent traction forces projected on the corresponding lateral planes (x–z and y–z) along the grey lines shown in the central panels (reference vectors are 50 Pa), and the color bar indicates T_z. Scale bar, 25 μm. **c,** Mean of the radial component of the traction force in the x–y plane T_r as a function of distance from the cluster edge, for 1 kPa ($n = 35$ clusters) and 6 kPa gels ($n = 19$ clusters). **d,** Mean of the vertical component T_z as a function of distance from the cluster edge, for 1 kPa ($n = 13$ clusters) and 6 kPa gels ($n = 7$ clusters). In both, shaded envelopes represent 95% CIs.

and normal tractions T_z (vertical plane) are positive near the cluster edges and become negative towards the cluster center (Fig. 3.4). Based on this, a cluster surface tension γ pulls the cluster edge upwards at the contact line with the substrate, with the cell protrusions forming acute angles with the substrate instead of being parallel to it. This vertical traction pointing upwards at the cluster edge is balanced by a pressure that pushes the cluster core into the substrate. Although the spatial profiles of T_z and T_r display qualitative similarities on both 1 kPa and 6 kPa substrates, the magnitude of both components increases with stiffness, indicating that both in-plane tractions and also surface tension are mechanosensitive [Riveline2001, Ghibaudo2008, Barry2014, Elosegui-Artola2016].

3.2.2 Experiments on gels with a stiffness-gradient

When clusters are seeded on substrates exhibiting stiffness gradients (Fig. 3.5), they show a significantly positive velocity v_X along the direction of the gradient, indicating motion towards increasing stiffness (Fig. 3.6). This v_X is also called durotactic velocity. A large dataset is built matching the local mechanical properties of the substrate with the instantaneous velocity of each cluster, showing a non-monotonic profile of the durotactic velocity (Fig. 3.7): Like in uniform-stiffness gels, clusters dewet regions of low stiffness and wet those of high stiffness, giving low velocities in both extreme cases. However, in intermediate stiffness, they are near the neutral wetting regime and durotaxis peaks.

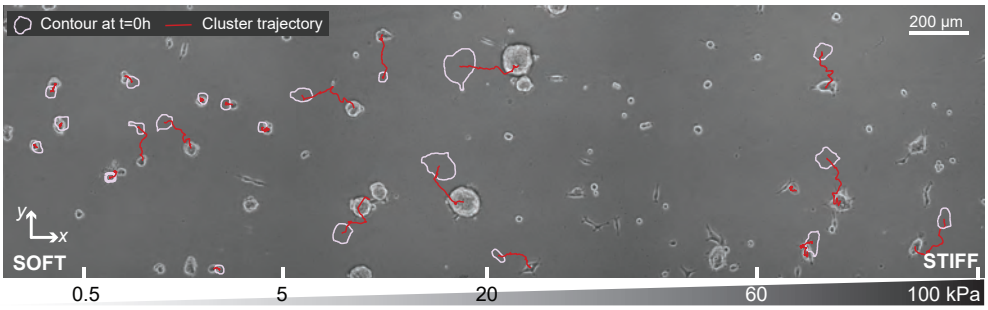

Figure 3.5: Cluster migration on stiffness-gradient gels. Representative phase-contrast image of A431 cell clusters migrating on a gel with a stiffness gradient (values shown in the bottom scale) coated with E-cadherin. The image was taken at time $t = 10$ h and the trajectories were obtained by time-lapse microscopy.

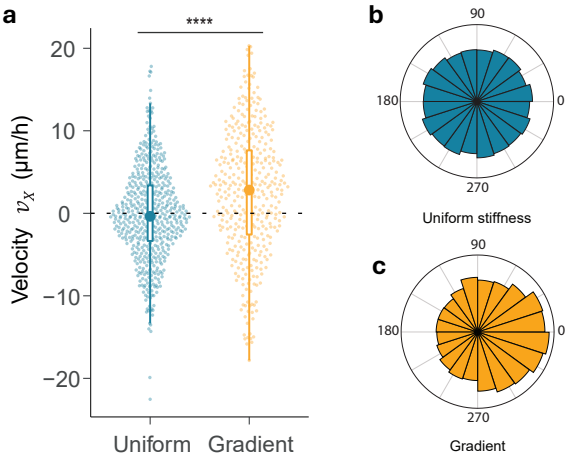

Figure 3.6: Clusters on stiffness-gradient gels perform durotaxis. a, Cluster velocity along the direction of the gradient on uniform (6 kPa) and stiffness-gradient gels, where small dots represent individual clusters and the central dot the median ($n = 527$ clusters for the uniform case, and $n = 366$ for the gradient case), with ****p-value<0.0001. **b,c,** Distribution of the angle between the instantaneous velocity vector and the x axis, on uniform (**b**) and gradient (**c**) gels.

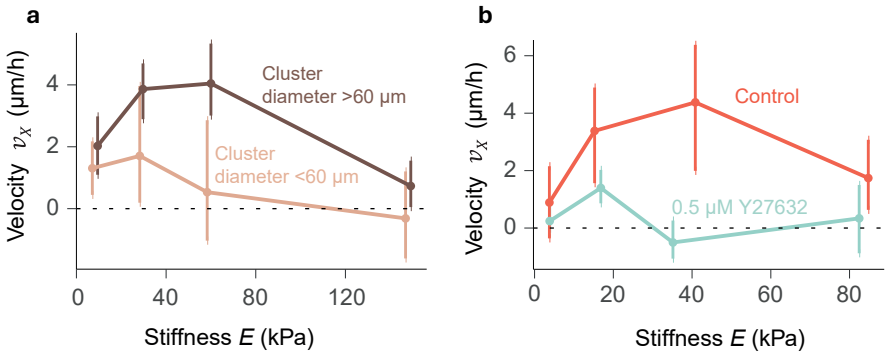

Figure 3.7: Durotactic velocity is non-monotonic with stiffness. a, Durotactic velocity as a function of stiffness for small (diameter < 60 μm) and large (diameter > 60 μm) clusters. **b,** Durotactic velocity in control clusters and in clusters treated with Y27632 (0.5 μM). Data include only clusters > 60 μm. In both, data are median $\pm$ 95% CI.

To characterize durotaxis, the role of cluster size, cell contractility, and stiffness gradient is studied. Large clusters (diameter > 60 μm) are more durotactic than smaller ones (Fig. 3.7a), and their velocity peaks at higher stiffness. Cell contractility is decreased by treating cells with a low dose (0.5 μM) of Y-27632, which is a ROCK (Rho-associated protein kinase) inhibitor substance. ROCK is an enzyme that plays a key role in regulating the cytoskeleton, cell shape, motility, and contraction. It is crucial for the formation of focal adherens junctions [Huveneers2012] and for the recruitment of myosin at the cell-cell junctions [Smutny2010]. Its inhibition decreases thus cell contractility and traction forces [Oakes2012, Sunyer2016, Al-Rekabi2019, Gavara2006, Stricker2013], which decreases durotaxis, with a shifted peak towards lower stiffness (Fig. 3.7b). Finally, different stiffness profiles can be fabricated in the gels (Fig. 3.8a), and durotaxis is significantly enhanced in steeper stiffness gradients (Fig. 3.8b).

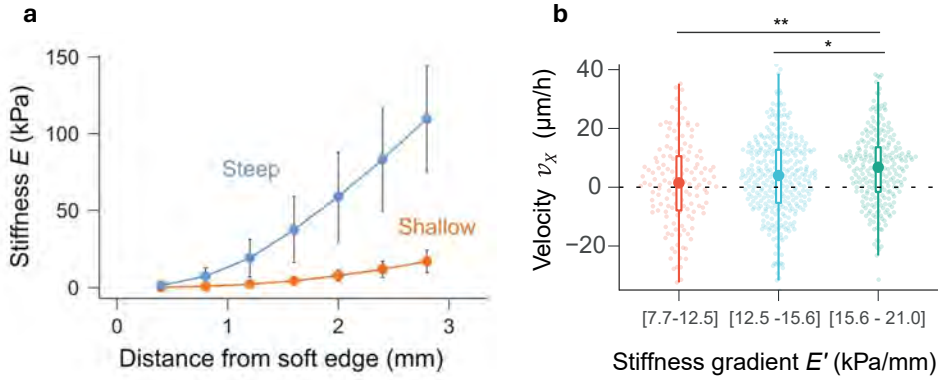

Figure 3.8: Durotactic velocity is larger for steeper stiffness gradients. **a,** Stiffness profiles as a function of distance from the soft edge of the gel, for shallow ($n = 12$) and steep ($n = 12$) profiles, where points are the mean and error bars the standard deviation. The stiffness was determined using AFM. **b,** Durotactic velocity for different stiffness gradients for a fixed starting stiffness $E = 18 \pm 5$ kPa. Clusters on steeper gradients show significantly more durotaxis than those on shallower ones (permutation t-test (two-tailed), **p-value<0.0026, *p-value<0.0463). Each data point represents a displacement and the central dot is the median. Clusters above the 99.5th percentile are not shown.

These results establish two important points. First, durotaxis is not restricted to integrin-mediated migration on ECM substrates, but it can also be driven through cadherin receptors. Second, durotaxis is optimal in the neutral wetting regime and depends on cluster size, contractility, and stiffness gradient.

However, the mechanisms by which this is done are not clearly understood, and a quantitative model is required to unveil the physics behind this behavior.

3.3 Physical model: 3D active wetting theory

The observation of collective durotaxis described above inspired the development of a physical model to quantitatively understand this phenomenon. The model is actually an extension of that in [Pérez-González2019], where the wetting of cell clusters was already explained in terms of a competition of forces in the cell monolayer, more specifically, between cellular contractility and active traction. Here, despite the migration towards the stiffer regions of the substrate, we also observe different wetting states of the clusters (different contact angles with the substrate), and so we hypothesize that we should be able to explain the present observations with a similar model. A comprehensive study of the phenomenology of a similar model was already done in Chapter 2, but now we want to account as well for the third dimension since the morphology of the clusters might be crucial for studying its dynamics.

To this end, we describe a cell cluster on a substrate as an active fluid droplet that partially wets a solid surface with a contact angle θ (see the sketch in Fig. 3.9). The interface between the cell cluster and the surrounding passive fluid has a surface tension γ, which results from a combination of passive cell-cell adhesion and active cortical tension [Lecuit2007, Manning2010, Guevorkian2010, Maître2011, Ehrig2019]. Averaging out tissue shape fluctuations, we describe the cell cluster as a spherical cap of radius R_{sphere}. We assume that the bulk of the cell cluster is passive and that the dynamics of the droplet are determined by the interplay of its surface tension and the in-plane forces at the basal cell monolayer. As in Chapter 2, we model the basal cell monolayer, of contact radius R, as a 2D active polar fluid, so the main ingredients and equations of the model can be recalled from Section 2.2.

3.3.1 Generalized Young-Dupré equilibrium

To extend the theory to 3D clusters, we propose what we call a generalized Young-Dupré force balance that includes the out-of-plane contribution of the surface tension γ of the cell cluster, coupled to the 2D model of the monolayer that we studied in Chapter 2. This new ingredient modifies the contact line dynamics and defines the droplet's dynamic contact angle, thus making the model more realistic by accounting for the aggregate 3D structure. As discussed in Section 2.5, for stress-free boundary conditions, a cell monolayer either spreads or

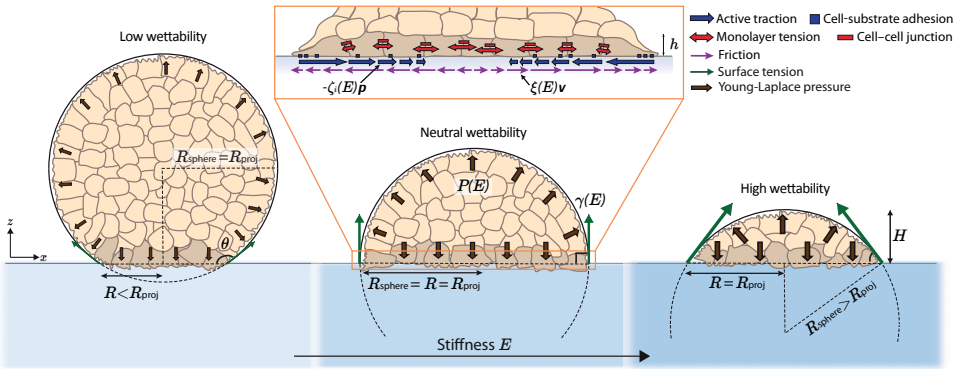

Figure 3.9: Sketch of the model for 3D cell clusters on different stiffness substrates. From experimental observations, the contact angle decreases with the stiffness, and so for a cluster of the same spherical radius R_{sphere} the contact radius R increases with it. R_{proj} is the projected radius of the cell cluster measured in phase-contrast images, which is equal to R_{sphere} when $\theta > 90°$ (low wettability), and to R when $\theta < 90°$ (high wettability). The Young-Laplace pressure in the cluster and the surface tension are mechanosensitive, increasing their magnitude with the stiffness. The inset (same sketch as in the side view of Fig. 2.3), shows a zoom-in of the basal cell monolayer (represented with darker cells) with the cell-substrate forces, transmitted through the cell-substrate adhesions, and the monolayer tension, transmitted throughout the tissue through cell-cell junctions.

retracts indefinitely due to the competition between active traction and contractility. However, for 3D droplets, the surface tension γ introduces an additional force that can either favor spreading or retraction depending on the contact angle θ. For low wettability clusters ($\theta > 90°$), surface tension favors spreading (Fig. 3.9 left), whereas for high wettability ($\theta < 90°$), it favors retraction (Fig. 3.9 right).

In classical wetting theory, the equilibrium contact angle is determined by the Young-Dupré condition, which establishes the balance of the three surface tensions at the contact line. For cell aggregates, a similar energetic approach was proposed to define the wetting conditions in terms of the cell-cell and cell-substrate adhesion energies [Ryan2001,Douezan2011,Douezan2012b,Beaune2014]. This approach, however, did not explicitly account for active cellular forces, which play a key role in tissue wetting [Pérez-González2019]. More recently, in [Zhao2024], they developed a microscopic, mechanical definition of surface tension to build an active Young-Dupré equation, which stabilizes partial wetting. However, we take a different approach. Following [Pérez-González2019], we assume that the surface tension of the interface between the surrounding pas-

sive fluid and the substrate is negligible in front of the active forces. Consistently, our generalized Young-Dupré condition captures a balance of three active forces: active traction and contractility, which are distributed in the polarized layer of the basal cell monolayer, and the cluster's surface tension, which enters as a local force at the contact line. Hence, we include the horizontal component of the surface tension into the monolayer force balance, Eq. 2.25, as a stress boundary condition,

$$n_\alpha(h\sigma^s_{\alpha\beta})n_\beta = -\gamma\cos\theta, \tag{3.1}$$

where n_β is the unit normal vector at the monolayer edge and $\sigma^s_{\alpha\beta}$ the monolayer tension, with h (monolayer height) being there for dimensional reasons. As we argued in Section 2.3, we can reduce the model to an effective 1D system, and so the boundary condition is simply

$$\sigma|^s_{x_\pm} = -\frac{\gamma}{h}\cos\theta. \tag{3.2}$$

In turn, the vertical component of the surface tension is balanced by the Young-Laplace pressure that the cell cluster exerts on the substrate,

$$P = \frac{2\gamma}{R_{\text{sphere}}}. \tag{3.3}$$

This relationship allows us to infer γ from experimental measurements of vertical traction forces on the substrate (Fig. 3.4), which provide a direct measurement of the pressure P (see better in Section 3.3.3). If the surface tension is not large enough, the clusters will tend to either completely wet ($\theta \longrightarrow 0°$) or completely dewet the substrate ($\theta \longrightarrow 180°$), depending on whether the active traction or the cellular contractility prevail [Pérez-González2019]. However, for sufficiently large surface tension, all three active forces may balance, and the droplet can reach a partial wetting state, namely a stable equilibrium with a finite contact angle θ_{eq}.

These states are determined by the roots of the expression of the spreading velocity in Fig. 3.10, and can be observed in the examples of temporal evolutions in Figs. 3.11–3.12.

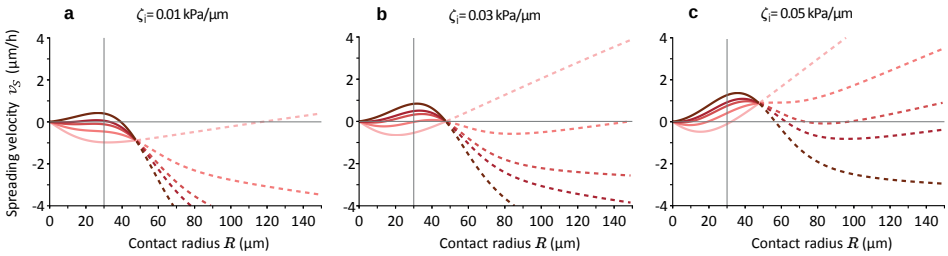

Figure 3.10: Roots of the spreading velocity define the partial wetting state. Spreading velocity of a cluster on top of a uniform-stiffness substrate as a function of the contact radius R, for different active tractions ζ_i (**a-c**) and surface tensions $\gamma = 0, 1.5, 2.5, 3, 4$ mN/m (from lighter to darker red). The volume is constant to $V = 2/3\pi R^{*3}$, being $R^* = 47.6$ μm the radius at the 2D spreading transition for $\zeta_i = 0.03$ kPa/μm. Continuous lines correspond to angles $\theta > 90°$ ($R < R^*$), and dashed ones to $\theta < 90°$ ($R > R^*$), meeting at $\theta = 90°$ ($R = R_{\text{sphere}} = H$). The vertical line shows $R_0 = 30$ μm, initial size chosen in Figs. 3.11–3.12. A cluster converges to the stable fixed point if $v_S(R_0) > 0$ (with roots), it will completely dewets if $v_S(R_0) < 0$, or wets the substrate if $v_S(R_0) > 0$ (no roots).

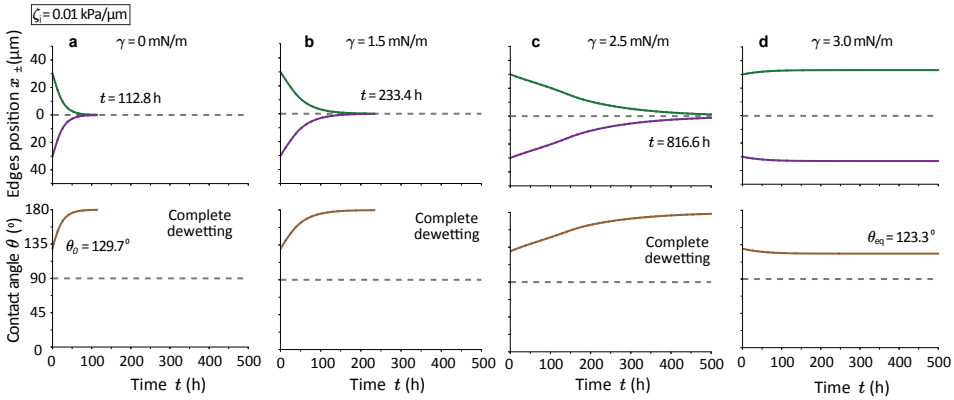

Figure 3.11: Equilibrium partial wetting for sufficiently large surface tension. Evolution of the position of the edges of the basal cell monolayer (green for x_+ and purple for x_-) and the contact angle of a cluster on top of a uniform-stiffness substrate, for $\zeta_i = 0.01$ kPa/μm and increasing γ from left to right. Initially, $R_0 = 30$ μm and $H_0 = 63.9$ μm, giving a volume (kept constant) of $V = 2/3\pi R^{*3}$, with $R^* = 47.6$ μm the radius at the 2D spreading transition for $\zeta_i = 0.03$ kPa/μm. The simulation time is $T = 500$ h and the time step $\Delta t = 6$ min. For $\gamma = 0$ mN/m (**a**), the cluster dewets from the substrate (defined for $R \leq 0.1$ μm) after 112.8 h. It reaches the equilibrium partial wetting state only if γ is large enough, with $\theta_{eq} = 123.3°$ (**d**). The larger γ, the closer is θ_{eq} to 90°.

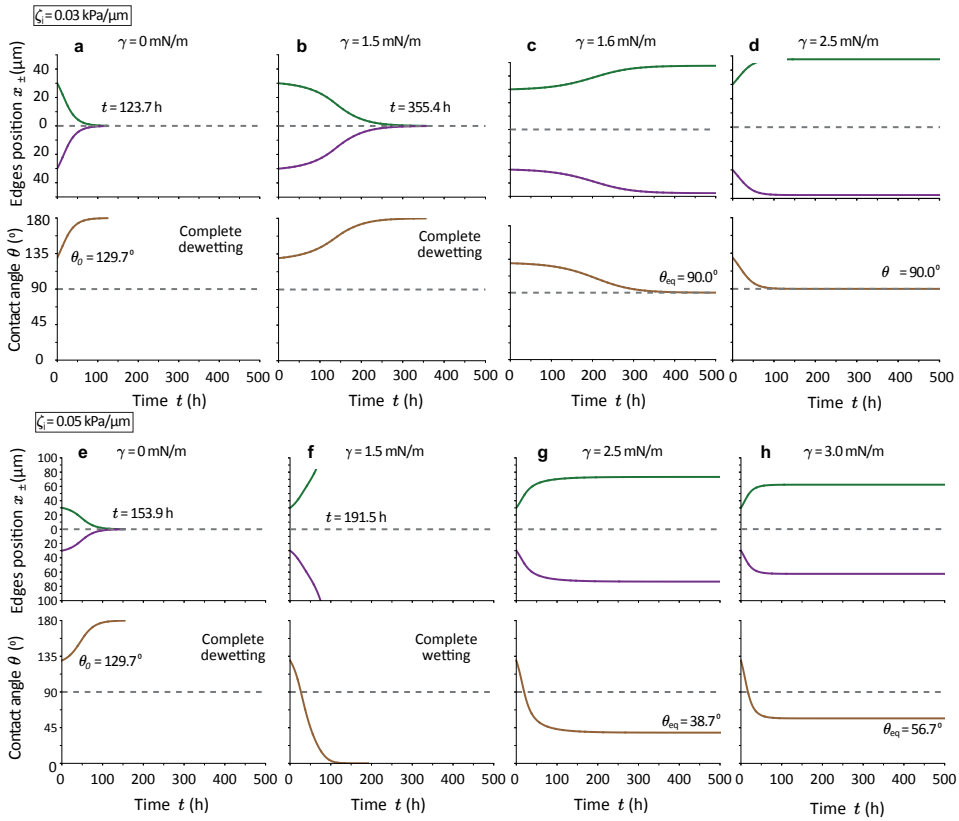

Figure 3.12: Equilibrium partial wetting for sufficiently large surface tension. Same as Fig. 3.11 but with larger active tractions $\zeta_\mathrm{i} = 0.03$ kPa/μm (**b-d**) and $\zeta_\mathrm{i} = 0.05$ kPa/μm (**e-h**). Hence, wetting is reached for lower values of γ. The partial wetting state and the time it takes to reach it depend on the parameters. Again, the larger γ, the closer is θ_eq to 90°.

3.3.2 Stiffness-dependent forces

As explained in Section 2.4, the model parameters that encode tissue-substrate interactions, namely, the passive friction ξ and the active traction ζ_i, depend on the local substrate stiffness and must be determined independently. Consistently with the expressions in Eq. 2.20, we take

$$\zeta_\mathrm{i}(E) = \zeta_\mathrm{i}^\infty \frac{E}{E+E^*}, \quad \xi(E) = \xi^\infty \frac{E}{E+E^*} + \xi_0. \tag{3.4}$$

Moreover, in the experimental measurements, not only radial in-plane tractions but also out-of-plane tractions increase with substrate stiffness (Fig. 3.4). We model this mechanosensitive tissue surface tension response by allowing the pressure $P(E)$ to increase with substrate stiffness. For simplicity, and because there is no experimental evidence of saturation of out-of-plane tractions with stiffness, we assume a linear dependence

$$P(E) = P_0 + s_P E, \tag{3.5}$$

where s_P is called the pressure sensitivity to stiffness. Via the Young-Laplace equation, the pressure dependence with the stiffness gives a stiffness-dependent surface tension

$$\gamma(E) = \frac{R_\mathrm{sphere}}{2} P(E) = \gamma_0 + \ell_\gamma E, \tag{3.6}$$

where $\gamma_0 = P_0 R_\mathrm{sphere}/2$ is the bare surface tension, and $\ell_\gamma = s_P R_\mathrm{sphere}/2$ is called the stiffness response length. Note that when the radius of the spherical cap R_sphere varies, as in dynamical evolutions with constant droplet volume V, γ_0 and ℓ_γ also vary accordingly.

We now need to determine the stiffness profile with the position on the gel. For simplicity, and since the data in Fig. 3.8a is approximately linear, we can consider a linear profile, that is,

$$E(x) = E_0 + E'x, \tag{3.7}$$

where E_0 and E' are the stiffness offset and gradient, respectively. The pressure and surface tension profiles with distance, from Eq. 3.5 and Eq. 3.6, are

$$P(x) = P_{0x} + P'x = (P_0 + s_P E_0) + s_P E'x, \tag{3.8}$$

$$\gamma(x) = \gamma_{0x} + \gamma'x = (\gamma_0 + \ell_\gamma E_0) + \ell_\gamma E'x. \tag{3.9}$$

As we did in Section 2.4.1, to reduce the number of parameters and gain physical insight, we momentarily replace the saturating traction and friction coefficients given in Eq. 3.4 by non-saturating linear functions of substrate stiffness

E, or equivalently, of the position x along the stiffness gradient,

$$\zeta_{\mathrm{i}}(x) = \zeta_{\mathrm{i}}^0 + \zeta_{\mathrm{i}}' x, \quad \xi(x) = \xi_0 + \xi' x, \tag{3.10}$$

where ζ_{i}' and ξ' are the traction and friction gradients, respectively. We can further simplify the problem by taking a uniform friction ($\xi' = 0$), so that the system of equations can be solved analytically to obtain the velocity field. The full solution can be found in Appendix 2.B. Recall the expressions for the dry and wet limits for the center-of-mass or durotactic velocity v_X[1], assuming $L_c \ll R, \lambda$ (Eq. 2.22 and Eq. 2.24),

$$v_X^{\mathrm{dry}} \approx \frac{L_c \lambda}{2\eta} R \zeta_{\mathrm{i}}' = \frac{L_c \lambda}{4\eta} (\zeta_{\mathrm{i}}^+ - \zeta_{\mathrm{i}}^-), \tag{3.11}$$

$$v_X^{\mathrm{wet}} \approx \frac{L_c \lambda^2}{2\eta} \zeta_{\mathrm{i}}' = \frac{L_c \lambda^2}{4\eta} \frac{\zeta_{\mathrm{i}}^+ - \zeta_{\mathrm{i}}^-}{R}, \tag{3.12}$$

where $\zeta_{\mathrm{i}}^{\pm}$ are the local values of the active traction at the respective edges. In both cases, the spreading velocity v_S has the same expression as in uniform-stiffness situations (Eqs. 2.18–2.19), replacing ζ_{i} by the active traction at the center-of-mass $\zeta_{\mathrm{i}}(X)$. In the dry limit, the spreading dynamics are local, with the two edges moving independently, driven only by local forces at the edges. The durotactic velocity is directly proportional to the traction difference across the tissue, and hence to the monolayer size (Eq. 3.11). In contrast, in the wet limit, the two edges are hydrodynamically coupled, and the durotactic velocity depends on the traction difference and inversely on the monolayer size R (Eq. 3.12). Since ζ_{i} is linear, these two dependencies cancel and the durotactic velocity is independent of the monolayer size. In both cases, the durotactic velocity is independent of the traction offset ζ_{i}^0, and hence of the local substrate stiffness. With this simplified version of the 2D model, we cannot explain the non-monotonicity of the durotactic velocity with the substrate stiffness observed in the experiments (Fig. 3.7), hence the need for adding the generalized Young-Dupré contribution and accounting for the third dimension.

3.3.3 Parameter estimates

Values for some parameter estimates are argued in Chapter 2 and also summarized in List of symbols. However, we are missing the surface tension and we need the estimates in the conditions of the present experimental conditions. In Table 3.1, we give estimates of surface tension with stiffness. We can take the

[1]Throughout this chapter the center-of-mass and the spreading velocities are given by v_X and v_S respectively, which were denoted as U and V in Chapter 2.

Stiffness (kPa)	Traction T_r (Pa)	Traction T_z (Pa)	Surface tension γ (mN/m)
1	10	10	0.15
6	40	50	0.75

Table 3.1: Surface tension estimates. Approximate experimental measurements of the radial T_r and vertical T_z components of the traction forces in clusters on top of uniform-stiffness substrates of 1 and 6 kPa (from Fig. 3.4c,d), and surface tension estimates for clusters of an apparent size $R_{\text{sphere}} \approx 30\ \mu$m (from Fig. 3.4a,b).

pressure $P \sim T_z$, and then $\gamma \sim T_z R_{\text{sphere}}/2$. Also $\zeta_{\text{i}} \sim T_r/h$, where h is the height of the basal monolayer, typically $h \sim 5\ \mu$m [Trepat2009, Pérez-González2019]. Although we give specific values in this table, the slopes of these profiles are typically slightly varied to explore a wider range of the phenomenology from the model. Generally, we take $\zeta_{\text{i}}^{\infty} = 0.3$ kPa/μm [Pérez-González2019, Blanch-Mercader2017b], a range of $E^* = (50 - 450)$ kPa, and a range of pressure sensitivity to stiffness of $s_P = (1.0 - 9.1) \cdot 10^{-2}$.

3.4 Non-monotonic durotactic velocity

In this section, we now solve the model and show that the non-monotonicity of the durotactic velocity with substrate stiffness observed in the experiments (Fig. 3.7) arises from a combination of two different effects:

- Both the increase of friction and the saturation of traction with stiffness produce a decrease of durotactic velocity at high stiffness (Section 3.4.1).
- The variation of the dynamic contact angle, which is controlled by the out-of-plane surface tension, produces an increase of durotactic velocity at low stiffness (Section 3.4.2).

The competition of these opposite trends yields a maximal durotactic velocity at an intermediate stiffness, for which durotaxis is optimal. Interestingly, this maximum occurs near the point where the contact angle crosses over 90° (the so-called neutral wetting regime), which separates the conditions of low and high wettability.

To show this, we predict the evolution of the velocity and the shape of a cluster as it migrates towards stiffer regions, numerically integrating the dynamics of a cluster with constant volume. The stiffness is always taken linear with the position on the gel, and the traction, friction, and surface tension are cho-

sen either linear (for simplicity, following Eqs. 3.8–3.10) or saturated (Eq. 3.4), to have more realistic profiles. At each step, the velocity profile is computed solving Eq. 2.25, with the polarization profile from Eq. 2.17 and the boundary conditions from Eq. 3.2. By a simple Euler integration algorithm with a time step Δt, the center-of-mass X and the contact radius R are evolved following

$$X(t+\Delta t) = \frac{1}{2}\big(x_+(t+\Delta t) + x_-(t+\Delta t)\big) = \frac{1}{2}\Big(x_+(t) + v(x_+(t))\Delta t + \big(x_-(t) + v(x_-(t))\Delta t\big)\Big) = X(t) + v_X(t)\Delta t, \tag{3.13}$$

$$R(t+\Delta t) = \frac{1}{2}\big(x_+(t+\Delta t) - x_-(t+\Delta t)\big) = \frac{1}{2}\Big(x_+(t) + v(x_+(t))\Delta t - \big(x_-(t) + v(x_-(t))\Delta t\big)\Big) = R(t) + v_S(t)\Delta t. \tag{3.14}$$

Imposing volume conservation $V_{\text{const}} = \frac{\pi}{6}H(H^2 + 3R^2)$, the new cluster's height $H(t+\Delta t)$ is fixed, and thus, the contact angle is either

$$\begin{cases} \theta = 180 - \operatorname{asin}\left(\frac{R}{R_{\text{sphere}}}\right) \geq 90°, & \text{if } H \geq R, \\ \theta = \operatorname{asin}\left(\frac{R}{R_{\text{sphere}}}\right) \leq 90°, & \text{if } H \leq R. \end{cases} \tag{3.15}$$

In general, the clusters do not strictly follow a quasistatic evolution, defined as a sequence of stages with vanishing spreading velocity. In our present model, the wetting properties are defined globally for the cluster as a whole, so we cannot contemplate contact angle differences at both edges due to different stiffness. In any case, the dominant asymmetry that drives durotaxis is the active traction difference between both edges of the basal monolayer, as seen in Chapter 2 and briefly recalled in Section 3.3.2, so a contact angle asymmetry would enter only as a higher order correction.

3.4.1 Slowdown at high stiffness

The decrease of durotactic velocity at high stiffness is based on the 2D basal cell monolayer dynamics. Obviously, when the friction coefficient ξ increases with substrate stiffness, the durotactic velocity decreases. As shown in Fig. 3.13, the stronger the friction gradient ξ', the stronger the decay of durotactic velocity. Additionally, although an increasing pressure gradient P' yields smaller contact angles and hence faster durotaxis at low stiffness (see more in Section 3.4.2), pressure effects do not produce a velocity decrease at high stiffness; the decrease is only observed when a friction gradient is present.

Regarding the force saturation, active traction forces tend to saturate when stiffness increases, (Fig. 3.14a), and hence the traction difference across the tis-

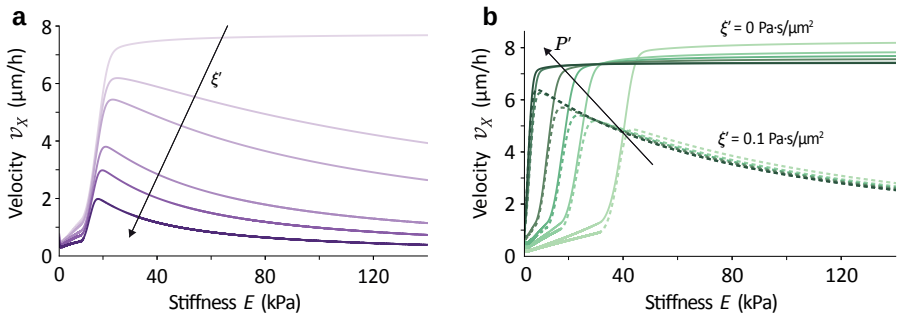

Figure 3.13: Slowdown of the durotactic velocity due to an increase in friction. Cluster's velocity as it moves along a stiffness gradient. Initially, $R_0 = 3.0$ μm, $H_0 = 56.8$ μm and $\theta_0 = 174.0°$ (consistent with Fig. 3.3b), giving a constant volume $V = 92500\pi/3$ μm^3. The initial position is $x_0 = 100$ μm ($E_0 = 3.8$ kPa), and active traction, friction and pressure profiles are linear (Eqs. 3.8–3.10) to show that force saturation is not required for the slowdown of durotaxis at high stiffness. **a.** An increasing friction gradient $\xi' = (0, 0.05, 0.1, 0.3, 0.5, 1.0)$ Pa·s/μm^2 lowers the durotactic velocity at high stiffness. **b,** Increasing pressure gradient $P' = (0.2, 0.4, 0.6, 1.0, 3.0, 4.0)$ Pa/μm, for situations with (continuous lines) and without (dashed lines) friction gradients. $\zeta_i^0 = 0.68$ Pa/μm and $\zeta_i' = 0.05$ Pa/μm^2, and the simulation time-step is $\Delta t = 6$ min.

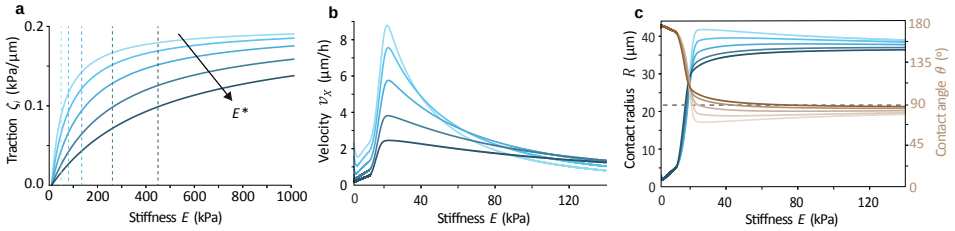

Figure 3.14: Slowdown of the durotactic velocity due to active traction saturation. a, Active traction profiles against stiffness values (Eq. 3.4), whose saturation shifts to higher stiffness when the crossover stiffness E^* increases (with $E^* = 50, 80, 140, 260, 450$ kPa). **b-c,** Evolution of the durotactic velocity (**b**) and shape (**c**) as it moves along a stiffness gradient. As E^* increases, the durotactic velocity and contact angle decrease are less pronounced. Initially, $R_0 = 3.0$ μm, $H_0 = 56.8$ μm and $\theta_0 = 174.0°$ (consistent with Fig. 3.3b), giving a constant volume $V = 92500\pi/3$ μm^3. The initial position is $x_0 = 100$ μm ($E_0 = 3.8$ kPa), and the simulation time-step is $\Delta t = 6$ min.

sue $\Delta\zeta_i \equiv \zeta_i^+ - \zeta_i^-$, decreases (Fig. 3.15a, for a fixed contact radius R). The durotactic velocity increases with the traction difference $\Delta\zeta_i$ (Fig. 3.15b), and

so traction saturation leads to a decrease of durotactic velocity with stiffness (Fig. 3.15c). As force saturation is pushed towards higher stiffness, by increasing the crossover value E^* the slowdown of durotaxis is less pronounced (Fig. 3.14b). In Fig. 3.14c, the slight increase of the contact angle for large stiffness values (and contact radius decrease), comes from the linear increase of the pressure with stiffness (Eq. 3.5), whereas traction and friction saturate. Thus, the surface tension (which is pointing inwards) is capable of causing monolayer retraction. The effect would be further corrected if the pressure also saturated (as in Fig. 3.19) or decreased its value.

Altogether, both the increase in friction and the saturation of active traction lead to slower durotaxis at high stiffness. They are both independent of the 3D shape of the cluster, arising even in the absence of tissue surface tension, as shown in Fig. 3.15.

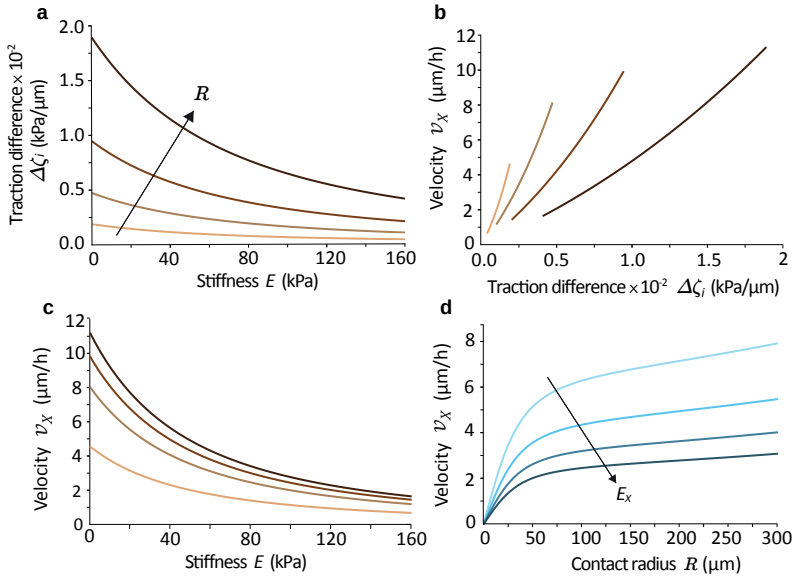

Figure 3.15: Effect of the active traction saturation without surface tension. The figure corresponds to 2D monolayers, in the absence of tissue surface tension $\gamma = 0$. **a,** Because of saturation (Fig. 3.14a), the difference across the monolayer $\Delta\zeta_{\rm i}$ decreases with stiffness, but it increases with size R. In **a-c,** each curve is for a fixed contact radius R, with values $R = 20, 50, 100, 200$ μm. **b-d,** The durotactic velocity increases with traction difference (**b**), and hence it decreases with stiffness (for a fixed R) (**c,d**). Because the active traction difference is larger for larger R, the durotactic velocity increases with contact radius R (for a fixed stiffness E) (**c,d**). In **d**, each curve is for a fixed stiffness, with values $E_X = 25, 50, 75, 100$ kPa.

3.4.2 Speed-up at low stiffness

The increase of durotactic velocity at low stiffness can be explained based on how the 3D shape of the cluster changes with substrate stiffness. From the experimental results (Fig. 3.3b), low stiffness promotes cluster dewetting and hence leads to a high contact angle and low contact radius. This small R yields a small active traction difference across the tissue, which implies a small durotactic velocity (Fig. 3.15c,d). Increasing the stiffness, the contact angle decreases and so R increases (Fig. 3.14c and Fig. 3.16c), producing faster durotaxis. As it affects the contact angle, surface tension γ (and thus pressure P) controls the velocity increase, as shown in Fig. 3.13b and Fig. 3.16a,b.

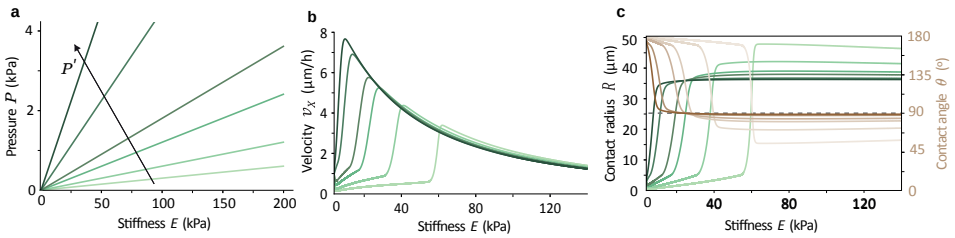

Figure 3.16: Speedup of the durotactic velocity due to an increase in pressure. a, Pressure profiles against stiffness values, changing the pressure gradient ($P' = (0.1, 0.2, 0.4, 0.6, 1.5, 3.0)$ Pa/μm). **b-c,** Evolution of the durotactic velocity (**b**) and shape (**c**) as it moves along a stiffness gradient. As P' increases, the durotactic velocity and contact radius increase happens for lower stiffness values. At high stiffness, the R saturates and the v_X decreases due to the friction increase and the active traction saturation (discussed in (Fig. 3.13) and Fig. 3.14 respectively). Initially, $R_0 = 3.0$ μm, $H_0 = 56.8$ μm and $\theta_0 = 174.0°$ (consistent with Fig. 3.3b), giving a constant volume $V = 92500\pi/3$ μm^3. The initial position is $x_0 = 100$ μm ($E_0 = 3.8$ kPa) and the simulation time-step is $\Delta t = 6$ min.

3.4.3 Dynamic contact angle and optimal durotaxis

The contact angle of the clusters evolving along the stiffness gradient (Fig. 3.14c, Fig. 3.16c, and all those in Section 3.6) does not coincide with the equilibrium solution θ_{eq} at the corresponding stiffness (roots in Fig. 3.10), since the spreading velocity $v_S \neq 0$ in the dynamic evolutions. The relaxation towards the equilibrium solution is slow compared to the time scale at which the cluster moves along the stiffness gradient. Accordingly, the observed contact angle is a dynamic one, and the evolution, except for extremely small stiffness gradients, is not quasistatic. Instead, as it performs durotaxis, the cluster has a positive

spreading velocity ($v_S > 0$), which increases the contact area of the cluster, and consequently the durotactic velocity as well.

The localized peak of $v_S(E)$ in most dynamical evolutions (Fig. 3.19 and Figs. 3.A.1–3.A.3), is related to the non-monotonic behaviour of $v_S(R)$ in a uniform-stiffness substrate (Fig. 3.10). This peak leads to a strong speed-up of the durotactic velocity. When v_S decreases, the velocity increases more slowly, exhibiting an inflection near the v_S peak. Since this region of fast variations is correlated with fast variations of the cosine of θ, which happen precisely at $\theta = 90°$, the maximum durotactic velocity is typically close to $\theta \sim 90°$ (vertical lines in Fig. 3.19). Its exact location along the stiffness axis will depend on the details of the profiles of active traction and friction with stiffness, which control the decrease of the durotactic velocity. For the profiles discussed here, the maximum of the durotactic velocity is indeed close to the peak of spreading velocity and the crossing over 90° of the contact angle. For extreme (and unrealistic) profiles (for instance very small friction gradients), the location of this maximum may in principle depart significantly. Even in such cases, though, the values for this maximum do not differ significantly from those reached past the peak of v_S, as the velocity's dependence on stiffness becomes very flat.

3.5 Effect of cluster size, cellular contractility and stiffness profile

The experimental results in Fig. 3.7 and Fig. 3.8b reveal that the durotactic velocity depends on cluster size, cell contractility, and stiffness gradient. By modifying the corresponding parameters of our model we should capture these results and gain insights into the mechanism at play.

3.5.1 Cluster size

Larger clusters exhibit a higher durotactic velocity, reaching its maximum at higher substrate stiffness (Fig. 3.7a). The model recapitulates these two trends (Fig. 3.17a,d), and can be explained as follows: First, larger clusters have a greater active traction difference across them, which drives faster durotaxis (Fig. 3.15c,d). Second, increasing cluster size favors monolayer wetting [Pérez-González2019], and therefore larger clusters have lower contact angles. At low stiffness, the contact angle is always larger than 90° (Fig. 3.3b), and so decreasing it implies that the horizontal component of the surface tension becomes smaller. As the horizontal component of surface tension is responsible for the durotactic velocity increase at low stiffness (Fig. 3.16), larger clusters have a longer in-

crease of the durotactic velocity with substrate stiffness, and hence they reach their maximum velocity at higher values of the stiffness.

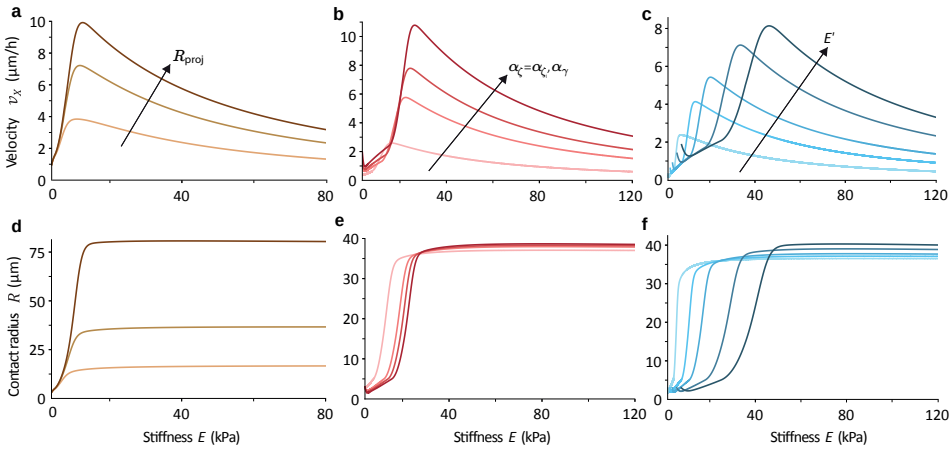

Figure 3.17: Effect of cluster size, cellular contractility, and stiffness gradient. Evolution of the durotactic velocity (**a-c**) and contact radius (**d-f**) as a cluster moves along a stiffness gradient. **a,d,** Increasing the cluster's volume $V = 9250\pi/3, 92500\pi/3, 925000\pi/3$ μm^3 leads to larger contact radius (**d**) and hence faster durotaxis (**a**). **b,e,** Decreasing all the active forces through factors $\alpha_\zeta = \alpha_{\zeta_i} < \alpha_\gamma$ leads to slower durotaxis and a shift of the velocity maximum to smaller stiffness. Here $\alpha_\gamma = 0.7, 1, 1.2, 1.5$ and $\alpha_\zeta = \alpha_{\zeta_i} = 0.4, 1, 1.4, 2$, where a stronger decrease in cellular contractility corresponds to smaller α. **c,f,** Increasing the stiffness gradient $E' = 10, 20, 30, 50, 70$ kPa/mm, produces an increase of durotactic velocity and a displacement of its peak towards stiffer regions. In the light and dark curves from **a** and **d**, initially $R_0 = 3.0$ μm and $H_0 = 26.1, 122.7$ μm, giving $\theta_0 = 166.9°, 177.2°$ respectively. In all the others, $R_0 = 3.0$ μm, $H_0 = 56.8$ μm and $\theta_0 = 174.0°$ (consistent with Fig. 3.3b), giving a constant volume $V = 92500\pi/3$ μm^3. The initial position is $x_0 = 100$ μm ($E_0 = 3.8$ kPa) and the simulation time-step is $\Delta t = 6$ min.

3.5.2 Cellular contractility

Decreasing myosin-generated cellular contractility through the ROCK inhibitor Y-27632 produces slower durotaxis and shifts the maximum of the durotactic velocity towards lower stiffness (Fig. 3.7b). This is recovered in the model by decreasing the magnitude of all the active forces: active traction ζ_i, monolayer contractility $|\zeta|$, and tissue surface tension γ (Fig. 3.17b,e). Specifically, we reduce active forces by multiplying their coefficients by factors $\alpha < 1$: $\zeta^{\text{red}} = \alpha_\zeta \zeta$,

$\zeta_{\mathrm{i}}^{\mathrm{red}} = \alpha_{\zeta_{\mathrm{i}}}\zeta_{\mathrm{i}}$, $\gamma^{\mathrm{red}} = \alpha_\gamma\gamma$. Both monolayer contractility ζ and active traction ζ_{i} are active forces that would vanish completely with no myosin activity. In contrast, tissue surface tension γ has both active and passive contributions [Manning2010]. The passive contribution is due to cell-cell adhesion, which would keep cells adhered and thus produce a tissue surface tension even without myosin activity. Therefore, a reduction of myosin activity, as induced by the Y-27632 treatment, affects ζ and ζ_{i} to a larger extent than γ, and so we take $\alpha_\zeta = \alpha_{\zeta_{\mathrm{i}}} < \alpha_\gamma$. Reducing active forces through these factors, we recover the decrease of durotactic velocity and the shift of its maximum towards lower stiffness.

Decreasing only the monolayer contractility $|\zeta|$ is not enough to explain the experimental results of the Y-27632 treatment. Decreasing the contractility promotes wetting [Pérez-González2019], and therefore it yields a higher contact radius (Fig. 3.18b), shifting the maximum durotactic velocity towards lower stiffness and increasing its magnitude (Fig. 3.18a). Since this increase is opposed to the experimental results (Fig. 3.7b), we corroborate that the decrease of all three active forces (active traction, contractility, and surface tension) is crucial.

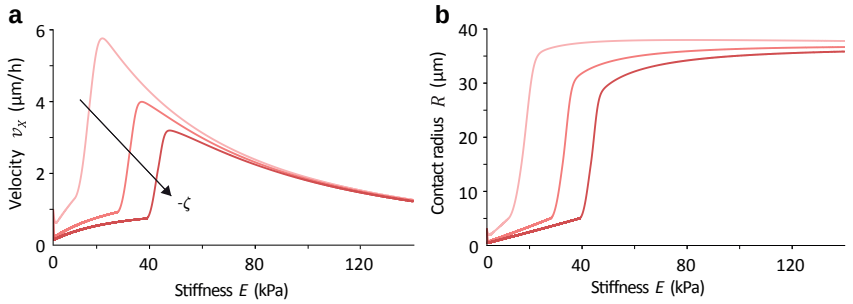

Figure 3.18: Decreasing only monolayer contractility is not enough. Evolution of the durotactic velocity (**a**) and the contact radius (**b**) as a cluster moves along a stiffness gradient. Increasing the contractility $-\zeta = 2, 5, 7$ kPa produces slower durotaxis, and shifts the maximum velocity to higher stiffness (**a**) as it promotes dewetting, i.e., smaller contact radius (**b**). Initially, $R_0 = 3.0$ μm, $H_0 = 56.8$ μm and $\theta_0 = 174.0°$ (consistent with Fig. 3.3b), giving a constant volume $V = 92500\pi/3$ μm^3. The initial position is $x_0 = 100$ μm ($E_0 = 3.8$ kPa), and the simulation time-step is $\Delta t = 6$ min.

3.5.3 Stiffness profile

A higher stiffness gradient produces faster durotaxis (Fig. 3.8b). The model explains these results (Fig. 3.17c,f) since a higher stiffness gradient implies a larger traction difference across the basal monolayer, which drives faster duro-

taxis (Fig. 3.15b). In addition, our predictions reveal that the maximum of the durotactic velocity is shifted towards higher stiffness (Fig. 3.17c) because a higher stiffness gradient yields a lower contact radius R for a fixed stiffness E (Fig. 3.17f), which we have previously shown to shift the optimal durotactic conditions to stiffer substrates (Fig. 3.16b,c).

3.6 Dynamical evolutions in a stiffness gradient

To complete our understanding of the problem, in Fig. 3.19 we finally simulate and track a cluster's migration and morphology change through its evolution up a stiffness gradient. As the cluster moves to stiffer regions, it wets the substrate by decreasing its contact angle, but its durotactic velocity varies non-monotonically,

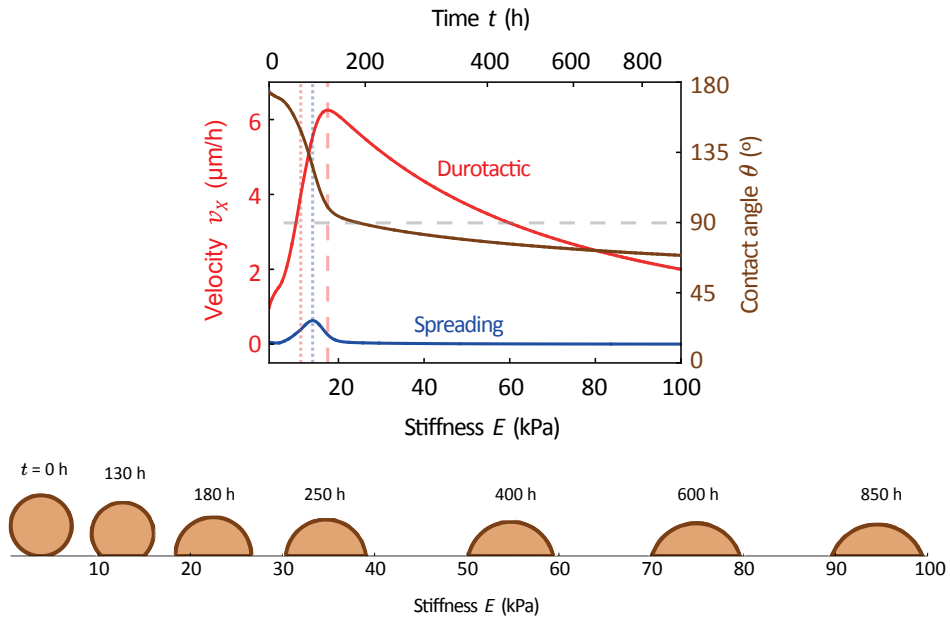

Figure 3.19: Velocity and shape dynamics of a migrating cluster. Non-monotonic dependence of the durotactic velocity v_X with stiffness (in red), the spreading velocity v_S (in blue), and the decrease in the contact angle θ (in brown). Initially, $R_0 = 3.0$ μm, $H_0 = 56.8$ μm and $\theta = 174°$, giving a constant volume $V = 92500\pi/3$ μm^3. The initial substrate stiffness is $E_0 = 3.8$ kPa, and pressure increases and saturates with stiffness, with $P^\infty = 0.6$ kPa and $E_p^* = 10$ kPa (with a similar dependence with stiffness than that for the active traction and the friction in Eq. 3.4). The simulation time step is $\Delta t = 6$ min.

as we have explained above. At low stiffness, the tissue has high contact angles θ (and so low contact radius R). This leads to a small active traction difference across the tissue, and hence a small durotactic velocity. However, the contact angle is large (Fig. 3.3b), and therefore surface tension pulls the cluster edges out (Fig. 3.9 left) and gives rise to a positive spreading velocity. As a result, the contact angle decreases, and the durotactic velocity increases. The speedup of durotaxis at low stiffness is thus favored by surface tension. The positive feedback between spreading and durotaxis produces a fast growth of the durotactic velocity, up to the regions where the surface tension contribution changes sign, at a contact angle of 90° (Fig. 3.9 center). After this point, surface tension points inwards and no longer promotes spreading (Fig. 3.9 right). The spreading velocity therefore decreases, and durotaxis slows down.

All in all, the combined effects of 3D active wetting and the saturation of cellular forces at high stiffness explain why the durotactic velocity first increases and then decreases with substrate stiffness, as observed in the experiments (Fig. 3.7), with a maximum around a contact angle of 90° (Fig. 3.19).

3.7 Limitations of the model and perspectives

We have introduced strong simplifications in the model to reduce the number of parameters and have an effective theory that is amenable to analysis, and that captures the basic physical mechanisms underlying collective durotaxis. Importantly, since we are considering cell clusters as spherical caps, the strong shape fluctuations that are observed in the experiments are not accounted for by the model. Second, the model assumes that surface tension is uniform across the cluster, yielding also a uniform Laplace pressure across the cluster. Therefore, our model does not account for flows driven by Laplace pressure gradients.

Beyond their shape, we describe cell clusters as fluid droplets that are passive in the bulk but active in the basal cell monolayer. We include three active forces: traction, tissue contractility, and surface tension. Traction and contractility are distributed in a boundary layer of finite thickness L_c at the edge of the basal cell monolayer. In contrast, we assume that surface tension is localized strictly at the tissue edge, entering as a boundary condition at the contact line. Therefore, the model does not account for the radial profile of the vertical component of traction forces measured in the experiments (Fig. 3.4d).

For the same reason, we cannot capture the profile of the in-plane traction T_r near the monolayer edge, as can be observed in the fit of the experimental data in Fig. 3.20. To obtain the best possible fit of the model parameters we choose the range of experimental data (dots in Fig. 3.20) that decreases with

the distance from the edge, a bit further away from this edge. Then, the fit is performed with the analytical expression for the traction, $T_x = -f_x h = h\partial_x \sigma^s_{xx}$ (Eq. 2.10), and the boundary condition for the stress with the surface tension $\sigma^s_{xx}(\pm R) = -\gamma/h \cos\theta$ (Eq. 3.2).

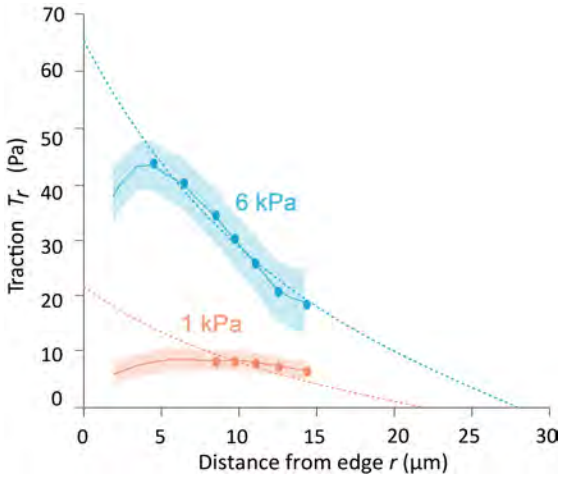

Figure 3.20: Comparison of radial traction forces in experiments and theory. Fits of the theoretically-predicted radial traction profiles (dashed lines) to the experimental data (dots) from Fig. 3.4c. A least-squares minimization method is used, obtaining $L_c = 13.86$ μm, $\zeta_{i1} = 3.75$ Pa/μm and $\zeta_{i6} = 12.6$ Pa/μm, and the sum of the squared residuals being 14.0 Pa^2 and 7.1 Pa^2 for 1 and 6 kPa substrates, respectively. Contact angles of the clusters are chosen to be $\theta_1 = 134°$ for the 1 kPa gel and $\theta_6 = 112°$ for the 6 kPa (Fig. 3.3b). Since in both cases $\theta > 90°$, the apparent cluster's size observed in the experiments corresponds to R_{sphere}, which we estimate to be $R_{\text{sphere}} = 30$ μm (Fig. 3.4a,b). The cluster's contact radius is then $R = R_{\text{sphere}} \sin(\pi - \theta)$, which gives $R_1 = 21.6$ μm and $R_6 = 27.8$ μm. From the vertical traction measurements (Fig. 3.4d), we take $P_1 = 10$ Pa and $P_6 = 50$ Pa. The friction at 1 kPa and 6 kPa is taken from the function $\xi(E)$ (Eq. 3.10), yielding screening lengths of $\lambda_1 = 134$ μm and $\lambda_6 = 130$ μm. Results from the fits are not very sensitive to the choice of all these parameter values.

3.8 Discussion and conclusions

In this chapter, we have studied collective durotaxis of cell clusters with a continuum model, generalizing the theory of active wetting [Pérez-González2019] to 3D clusters, describing them as spherical caps of an active polar fluid. The dynamics are dominated by the active forces at the contact monolayer with the substrate, together with in-plane and out-of-plane components of the surface

tension force exerted by the spherical surface at the contact line. Combining the dependence on the contact angle and the sensitivity of traction forces to the substrate stiffness is essential to explain the interplay between durotaxis and wetting, and consequently to account for the non-monotonic behavior of the durotactic velocity with substrate stiffness.

As predicted in previous theoretical work from [Alert2019b], and further studied in Chapter 2, the experimental results from this chapter demonstrate a mode of durotaxis in which cell clusters move as a whole, with the front and rear edges displacing in the same direction. This behavior is different from that observed in earlier studies of collective durotaxis using flat monolayers, which showed asymmetric spreading, rather than directed migration [Sunyer2016, Martinez2016]. Here, clusters perform cohesive durotactic migration as their interface advances on the stiff side and retracts from the soft side. The durotactic velocity is a non-monotonic function of local substrate stiffness, peaking at an intermediate stiffness, that can be shifted to higher or lower stiffness by tuning cluster size and active forces. As such, clusters display low motility on the soft and stiff regions of the substrate, where they fully dewet and wet the surface, respectively. At intermediate stiffness, close to the crossover between low and high wettability, cell clusters are maximally motile on uniform-stiffness substrates and exhibit optimal durotaxis on gradient-stiffness ones. Therefore, the existence of an optimal stiffness for collective durotaxis is connected to the wetting properties of the droplet, which ultimately depend on the stiffness.

Moreover, we recover all the behaviors with the model about how collective durotaxis depends on the physical properties of the cluster (size, 3D shape, and contractility) and of the substrate (local stiffness and stiffness gradient). The interplay between cell contractility, cluster size, stiffness, and cell traction forces can position clusters near contact angles of $\theta = 90°$, and thus provide them with a sweet spot where cluster durotaxis is maximal.

The finding of an optimal regime for collective durotaxis provides a new approach for controlling directed cell migration *in vivo*. By tuning the local stiffness of a substrate or the active properties of a cluster, organisms could trigger and regulate this directed migration [Barriga2018]. On the other hand, abnormal tissue stiffening or softening, or changes in the active or mechanical properties of cell clusters, may hinder physiological migration or trigger undesired durotaxis, like the movement of clusters during cancer invasion and metastasis. Although measuring mechanical gradients *in vivo* is technically very challenging [Shellard2021b], collective durotaxis is becoming more widely acknowledged as a major mechanism guiding directed cell migration in development [Zhu2020, Shellard2021a] and disease [Haeger2015, DuChez2019]. Our study provides a general

physical framework to address and interpret the mechanisms underlying collective durotaxis.

Contributions and acknowledgements

The work described in this chapter was a close collaboration between theory and experiments. The majority of the experiments were performed by Macià-Esteve Pallarès in the "Integrative cell and tissue dynamics" group led by Xavier Trepat (IBEC, Barcelona). Additionally, Isabela Corina Fortunato (IBEC, Barcelona) performed experiments in fibronectin-coated gels and studied the effect of increasing contractility, and Valeria Grazú in the group led by Jesús Martínez de la Fuente (Instituto de Nanociencia y Materiales de Aragón, INMA, Zaragoza), contributed in technical expertise for the E-cadherin coated gels. Raimon Sunyer (IBEC, Barcelona) assisted in the experiments throughout the project, and together with Manuel Gómez-González developed the analysis software.

With the help of Jaume Casademunt and Ricard Alert (Max Planck Institute for the Physics of Complex Systems, MPI-PKS, Dresden), I developed the model and performed the theoretical analysis. Therefore, Macià-Esteve Pallarès and Raimon Sunyer prepared all the figures in Section 3.2 (Figs. 3.2–3.8) and I prepared all the others from the model (Figs. 3.9–3.20), as well as those in Appendix 3.A.

I want to thank all the members in the groups of Xavier Trepat and Pere Roca-Cusachs, for useful discussions during their group meetings. Specially, thanks to Macià Esteve-Pallarès for his patience explaining to me all the biology that I could not understand, and for the fruitful discussions about the project.

Appendices

3.A Effects of other parameters in the dynamics

We analyze the effects of various model parameters in the dynamical evolutions, such as the initial stiffness E_0 (Fig. 3.A.1), the contractility $|\zeta|$ (Fig. 3.A.2a,b), the pressure offset P_0 (Fig. 3.A.2c,d), and the pressure gradient P' (Fig. 3.A.3). In all the situations, the cell cluster starts with a high contact angle θ on the soft region of the substrate. As it advances towards stiffer regions, the cluster increases its wettability, lowering its contact angle θ and so expanding its contact radius R. As a result, the cluster increases its durotactic velocity, speeding up. Eventually, when it reaches sufficiently stiff substrates, the friction increases, and the active traction saturation slows down the cluster's motion.

In many cases, however, there is an initial decrease of the durotactic velocity, corresponding to a decrease in the contact radius R. This initial slowdown happens when the cluster starts under conditions of dewetting, i.e., with a negative spreading velocity $v_S < 0$. In these situations, the contact radius initially decreases and the contact angle increases, as illustrated in Figs. 3.A.1–3.A.3, in which the initial contact angle is $\theta_0 = 136.4° > 90°$. In a softer initial position (Fig. 3.A.1), with higher contractility (Fig. 3.A.2a-c), or with smaller values of the pressure and thus the surface tension (Fig. 3.A.3), this early-stage effect is accentuated, since all these parameters favor cluster dewetting. Instead, a larger pressure diminishes this effect because it favors the expansion of R at the initial stages and when $\theta > 90°$.

Finally, if the pressure does not increase with stiffness (Fig. 3.A.2d,e), surface tension offers a lower opposition to cluster spreading in low contact angle conditions ($\theta < 90°$). As a result, the contact radius keeps increasing significantly even at high stiffness. Nevertheless, the durotactic velocity still decreases due to the increase in friction.

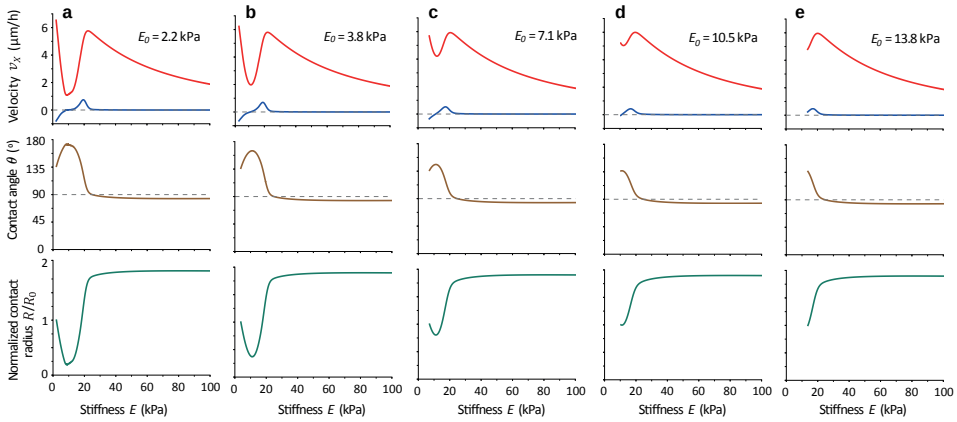

Figure 3.A.1: Effect of the initial substrate stiffness in the dynamics. Evolution of cluster motion and shape as it moves along a stiffness gradient, with saturated traction and friction and linear pressure profiles. In the velocity plots, we show both the durotactic velocity (in red) and the spreading velocity (in blue). Initially, $R_0 = 20.0$ μm, $H_0 = 50.0$ μm and $\theta_0 = 136.4°$, giving a constant $V = 92500\pi/3$ μm^3. We change the initial position to $x_0 = 50, 100, 200, 300, 400$ μm, corresponding to $E_0 = 2.2, 3.8, 7.1, 10.5, 13.8$ kPa. The simulation time-step is $\Delta t = 6$ min.

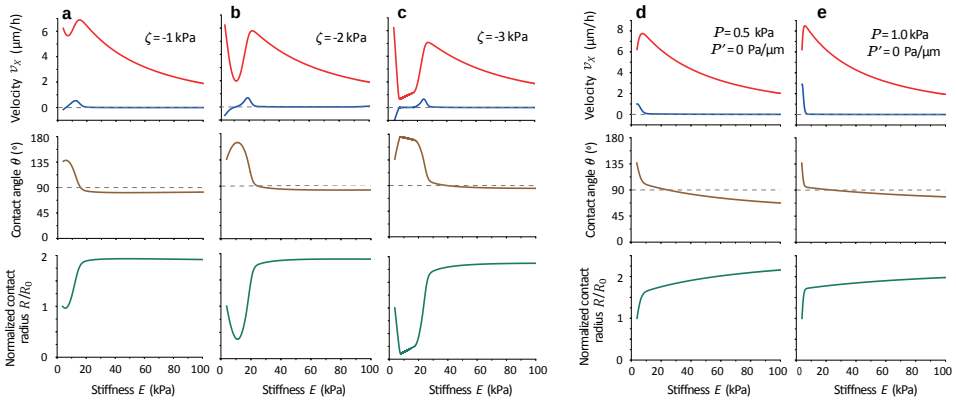

Figure 3.A.2: Effect of the contractility and the pressure offset in the dynamics. Same as Fig. 3.A.1, with initial position $x_0 = 100$ μm ($E_0 = 3.8$ kPa). In **a-c,** we change the contractility to $-\zeta = 1, 2, 3$ kPa, with a linear pressure profile $P_{0x} = 4.2$ Pa and $P' = 0.6$ Pa/μm. In **d** and **e,** we take a uniform pressure of $P = 0.5$ and 1.0 kPa respectively, with a fixed contractility $\zeta = -2$ kPa.

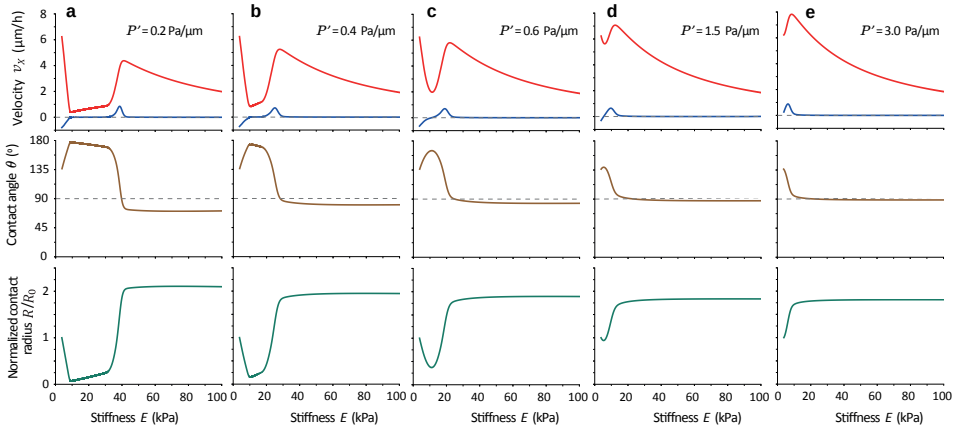

Figure 3.A.3: Effect of the pressure gradient in the dynamics. Same as Fig. 3.A.1, with initial position $x_0 = 100$ μm ($E_0 = 3.8$ kPa), and changing the pressure gradient to $P' = (0.2, 0.4, 0.6, 1.5, 3.0)$ Pa/μm.

Chapter 4

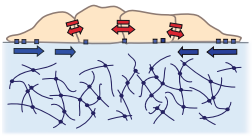

Traction bistability on strain-stiffening substrates

4.1 Introduction

Studying the myriad interactions between cells and the extracellular matrix (ECM) is crucial for many processes in tissue development, repair, and disease progression. For instance, the relationship between traction forces and the orientational order of the matrix could affect the tissue architecture, or the numerous biochemical processes, such as matrix degradation by metalloproteases, may further modulate the physical and mechanical environment of cells. This, in turn, may impact on their migration behavior. In this chapter, we focus specifically on the feedback between traction forces exerted by cells and the stiffness of the ECM. As we have argued in Chapter 2 and Chapter 3, this interaction is particularly relevant in durotaxis, where cells sense and respond to substrate stiffness, guiding their migration towards stiffer regions.

Traction forces are influenced by the properties of the cell's environment, particularly by mechanical properties. For *in vitro* tissues in the laboratory, these forces are inferred from displacements of fluorescent beads embedded in the substrate through a technique called Traction Force Microscopy (TFM, Fig. 4.1). Force-induced deformations of the substrate are measured, which allows to reconstruct cellular forces based on continuum mechanical principles. They are usually found to be larger on stiffer substrates [Discher2005, Saez2005,

Ghibaudo2008, Saez2010, Ladoux2012, Trichet2012, Elosegui-Artola2014, Li2015, Gupta2015, Gupta2016, Pallarès2023]. Therefore, it is well established that the stiffness of a tissue's surroundings influences the active traction forces it exerts, affecting its collective migration. However, whether changes in traction forces can, in turn, alter the stiffness of the environment, remains unexplored.

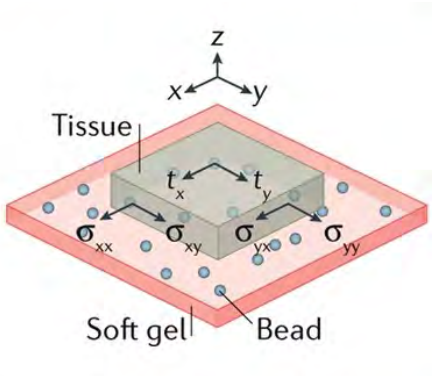

Figure 4.1: Traction measurements in TFM experiments. Cell traction forces, t_x and t_y, are inferred from the beads displacements. Using force balance, the intercellular stresses are computed. They can be tensile or compressive, σ_{xx} and σ_{yy}, in the normal direction of the intercellular junctions or correspond to shear forces, σ_{xy} and σ_{yx}, in the tangential direction. Adapted from [Ladoux2017].

Polyacrylamide (PAA) gels are frequently used as substrates in the laboratory since they are linear elastic materials, displaying a constant elastic modulus for a large range of applied strains [Kandow2007, Storm2005] (see the fabrication protocol in Section 5.3.2). This linearity facilitates robust and computationally inexpensive methods for force inference [Butler2002, Sabass2008, Bergert2016, Bauer2021]. However, biopolymer networks, such as crosslinked actin filaments, collagen, fibrin, or vimentin, are nonlinear elastic materials, displaying strain-stiffening responses: their shear modulus increases abruptly after a certain critical strain [Gardel2004, Storm2005, Pollard2009, Münster2013] (Fig. 4.2). This may have a physiological relevance as a means to prevent damage from exposure to large deformations [Storm2005]. The force reconstruction problem becomes much more difficult in 3D and in these nonlinear materials, but several successful methods have been developed [Steinwachs2016, Toyjanova2014, Dong2017, Song2020, Böhringer2024].

In vivo, changes in stiffness may play a crucial role in modulating traction forces, thereby influencing the collective migration of cells in tissues. The goal of this chapter is to explore the feedback loop between cellular traction forces and substrate stiffness. To this end, we model the substrates used in TFM as 2D elastic materials and examine their interaction with active tractions. While previous models have treated the substrates as linearly elastic materials [Trepat2009], we introduce a nonlinear component to capture the strain-stiffening response present in biopolymer networks. The details of this model are explained in Section 4.2, and its solutions and implications are discussed in Sections 4.3–4.5.

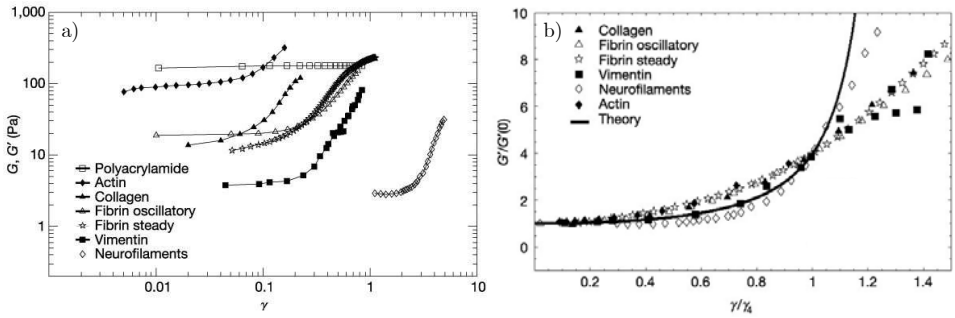

Figure 4.2: Strain-stiffening of biopolymer networks. a, Dynamic shear storage moduli measured at different strain amplitudes γ for a series of crosslinked biopolymer networks. The real part G', reduces to the shear modulus G at zero frequency. The shown data is G for fibrin and neurofilaments, and G' (at 10 rad·s^{-1}) for the others. **b,** Scaled shear modulus by the value at zero strain versus normalized strain, with $G(\gamma_4) = 4G(0)$. The black line is the universal theoretical curve, obtained assuming a uniform distribution of filament lengths averaged for all the orientations. Adapted from [Storm2005].

4

4.2 Nonlinear elastic model for the substrate in TFM

Consider the soft gel depicted in Fig. 4.1 as the substrate for a tissue. Given the symmetry in the x and y directions, we simplify the system by reducing its dimensionality to a 2D substrate, infinite in the x coordinate and with a fixed height $z = h$. Therefore, instead of modeling a monolayer, we are modeling a substrate with 1D multicellular trains on top, where traction forces are exerted solely along the x-axis, denoted by T_x. We will consider the feedback loop between the stiffness of the substrate and the magnitude of the traction forces, which has been mentioned in the introduction and is depicted in Fig. 4.3.

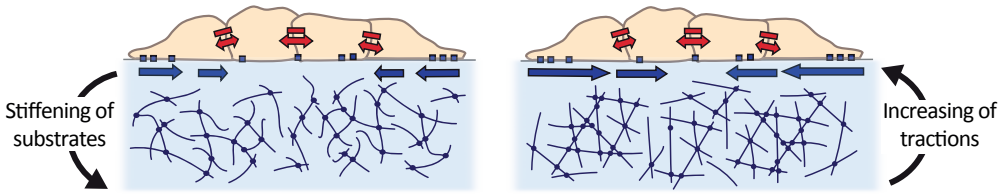

Figure 4.3: Sketch of the model for strain-stiffening substrates. The stiffness of the substrate influences traction forces (blue arrows) that cells exert on it (right), but these tractions produce different deformations on the substrate, influencing the crosslinking of the biopolymer network and thus its stiffness (left).

We adopt a model for the substrate similar to that in [Trepat2009], but adding a nonlinear response. Let u_i be the displacements of the deformations, γ the strain, and σ the stress tensors. For a linear elastic material with shear modulus G and bulk modulus K, we have [Landau1959],

$$\gamma_{ij} = \frac{1}{2}\left(\partial_i u_j + \partial_j u_i\right), \tag{4.1}$$

$$\sigma_{ij} = 2G\left(\gamma_{ij} - \frac{1}{3}\gamma_{kk}\delta_{ij}\right) + K\gamma_{kk}\delta_{ij}, \tag{4.2}$$

where δ_{ij} is the Kronecker delta. Written in component form,

$$\sigma_{xx} = \left(K + \frac{4G}{3}\right)\gamma_{xx} + \left(K - \frac{2G}{3}\right)\gamma_{zz}, \tag{4.3}$$

$$\sigma_{xz} = 2G\gamma_{xz} = 2G\gamma_{zx} = \sigma_{zx}, \tag{4.4}$$

$$\sigma_{zz} = \left(K - \frac{2G}{3}\right)\gamma_{xx} + \left(K + \frac{4G}{3}\right)\gamma_{zz}, \tag{4.5}$$

where $\gamma_{xx} = \partial_x u_x$, $\gamma_{xz} = \frac{1}{2}\left(\partial_x u_z + \partial_z u_u\right) = \gamma_{zx}$, and $\gamma_{zz} = \partial_z u_z$. The equations of equilibrium in the absence of external forces in the bulk of the system, which is the case, are simply $\nabla \cdot \sigma = 0$, so[1]

$$\partial_x \sigma_{xx} + \partial_z \sigma_{xz} = 0, \tag{4.6}$$

$$\partial_x \sigma_{zx} + \partial_z \sigma_{zz} = 0. \tag{4.7}$$

At the bottom plane ($z = 0$), we assume a no-slip condition since the gel is attached to the bottom glass dish. Instead, at the cell/gel interface ($z = h$), we consider zero (or negligible) normal stress and shear stress given by $T = T_x$, which is indeed the traction that the tissue is exerting on the gel. Thus,

$$u_x\big|_{z=0} = 0, \quad u_x\big|_{z=0} = 0 \tag{4.8}$$

$$\sigma_{zz}\big|_{z=h} = 0, \quad \sigma_{xz}\big|_{z=h} = T = 2G\gamma_{xz}\big|_{z=h}. \tag{4.9}$$

To account for the nonlinearity of the substrate due to the strain-stiffening response in a simple way, we consider the shear modulus to be a piecewise function of the shear strain, $G(\gamma_{xz})$. For strains lower than a critical one, we consider that the shear modulus is a constant value G_0 (linear response), while

[1] Do not confuse these equations with Eq. 2.10 and Eq. 2.11, since before the stress was the one of the monolayer, whereas now we are modeling the substrate.

for larger strains we assume a power law function with coefficient α (nonlinear response) [Gardel2004, Storm2005],

$$G(\gamma_{xz}) = \begin{cases} G_0, & \gamma_{xz} \leq \gamma_{xz,\text{crit}}, \\ G_1 \gamma_{xz}^{\alpha}, & \gamma_{xz} > \gamma_{xz,\text{crit}}. \end{cases} \tag{4.10}$$

We call the coefficient G_1 the nonlinear shear modulus, with $G_0 = G_1 \gamma_{xz,\text{crit}}^{\alpha}$ for continuity (Fig. 4.4).

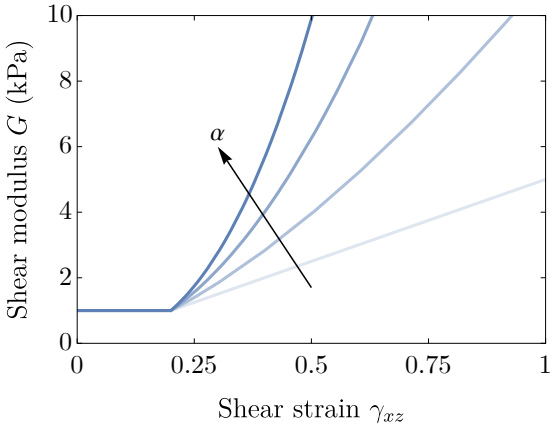

Figure 4.4: Shear modulus as a function of the shear strain. The shear modulus is a piecewise function of the shear strain (Eq. 4.10). Here $\gamma_{xz,\text{crit}} = 0.2$, $G_0 = 1$ kPa and $\alpha = 1, 1.5, 2, 2.5$. Therefore, $G_1 = G_0 \gamma_{xz,\text{crit}}^{-\alpha}$ changes for every curve. Note that since typically the strains are $\gamma_{xz} < 1$, then values for $G_1 \gg G$, and a greater α implies a lower shear modulus G, if G_1 is kept constant. The units of both are the same since the strain is dimensionless.

Furthermore, we assume that for each value of the shear modulus, cells aim to exert a corresponding desired traction value, which we refer to as the target traction. This concept was previously discussed in Section 2.4 or Section 3.3.2, where parameters encoding cell-substrate interactions were modeled as increasing and saturating functions of the substrate's Young's modulus E. Now we consider the shear modulus G, but since both E and G are related (see Section 4.2.1), the underlying reasoning remains consistent. Consequently, we define the target traction as a function of the shear modulus evaluated at $z = h$, denoted as $T_{\text{target}}(G\big|_{z=h})$, since traction occurs solely at this upper surface of the substrate. While we could use the same functional forms as outlined in Eq. 2.20, which are Hill functions of coefficient one, we consider two alternatives for greater insight into the model's predictions: a simple power law with respect to G, or, for

generality, a Hill function of coefficient β,

$$T_{\text{target-PL}}(G) = T_0 G^{\beta}, \tag{4.11}$$

$$T_{\text{target-Hill}}(G) = T^{\infty} \frac{G^{\beta}}{G^{\beta} + (G^*)^{\beta}}, \tag{4.12}$$

where G^* is the characteristic shear modulus of the traction saturation, and T^{∞} is the value of the traction at this saturation (for large G).

The actual traction field T, however, does not instantaneously reach this target traction; rather, it approaches it over a certain time scale τ. This timescale is associated with the time that cells need to adapt their linkers to the substrate to be able to exert different tractions on it. Writing the explicit dependencies, we formulate the simple dynamical equation as follows,

$$\partial_t T = -\frac{1}{\tau}\big(T - T_{\text{target}}(G(\gamma_{xz}\big|_{z=h}))\big). \tag{4.13}$$

Experimentally, the variables most likely to be manipulated are the shear modulus G (changing the substrate's material or polymer concentration, for instance) and T^{∞} (changing the cell line or using drug treatments to modify their contractility and traction). Consequently, most of the plots presented in the following sections are functions of one or the other.

4.2.1 Parameter estimates

The relations between the shear modulus G, the bulk modulus K, the Young's modulus E and the Poisson's ratio ν are [Landau1959],

$$G = \frac{E}{2(1+\nu)}, \quad K = \frac{E}{3(1-2\nu)}, \quad E = \frac{9KG}{3K+G}, \quad \nu = \frac{3K-2G}{2(3K+G)}. \tag{4.14}$$

Since the Poisson's ratio must be $0 < \nu < 0.5$, then $G < 3K/2$. In fact, $\nu \approx 0.48$ in PAA gels [Boudou2009], which implies

$$3K(1-2\nu) = 2G(1+\nu) \longrightarrow K = \frac{2(1+\nu)}{3(1-2\nu)} G \approx \frac{2.96}{0.12} G \approx 24.7G. \tag{4.15}$$

Although TFM experiments are typically conducted with PAA gels, a biopolymer network is used to coat the gel, facilitating cell adhesion, which might exhibit strain-stiffening. While the Poisson's ratio in biopolymer networks is generally smaller than that of PAA gels, its value provides a useful reference for estimating reasonable ranges, for instance, for Young's modulus E, which is the commonly reported measure in experiments. In Table 4.1 we summarize values for some parameters, which would be useful for the numerical simulations. However, the simulations are not included in this thesis, and for the analytical results, only G needs to be estimated.

G (kPa)	K (kPa)	E (kPa)	ν
1	25	3.0	0.48
2	20	5.8	0.45
10	100	29.0	0.45
20	90	55.9	0.40

Table 4.1: Parameter values. Combinations of shear modulus G and bulk modulus K, that give reasonable Young's modulus E and Poisson's ratio for modeled substrates.

4.3 Stationary states

Let T^0 and γ^0_{xz} be the stationary states of the model, fulfilling $\partial_t T = 0$. From Eq. 4.13, $T^0 = T_{\text{target}}(G(\gamma^0_{xz}\big|_{z=h}))$, where T_{target} can be either a power law (Eq. 4.11) or a Hill function (Eq. 4.12) of the shear modulus G. This G, in turn, is a piecewise function of the shear strain γ_{xz} (Eq. 4.10), displaying a linear and a nonlinear regime. In this section, we give the expressions for these stationary states in both of them.

4.3.1 Linear regime

In the linear regime, $G = G_0$ is constant and so T^0 is also constant. Thus, the solution of the system of equations Eqs. 4.6–4.9 is simply a linear x-displacement with z ($u^0_x(z) = cz$, c constant) and no z-displacement ($u^0_z(z) = 0$), giving a constant shear strain $\gamma^0_{xz} = \frac{1}{2}(\partial_x u^0_z + \partial_z u^0_x) = c/2$ [Trepat2009]. Hence, $\gamma^0_{xz} = \gamma^0_{xz}\big|_{z=h}$ and $\gamma^0_{xx} = \gamma^0_{zz} = 0$. From the boundary condition for the shear stress and the traction at the top surface of the gel (Eq. 4.9), the solution is

$$\gamma^0_{xz} = \frac{T_{\text{target}}(G_0)}{2G_0} = \begin{cases} \frac{T_0}{2} G_0^{\beta-1}, & \text{power law,} \\ \frac{T^\infty}{2} \frac{G_0^{\beta-1}}{G_0^\beta + (G^*)^\beta}, & \text{Hill function.} \end{cases} \tag{4.16}$$

We can see that for the power law target traction, if $\beta > 1$ the deformation γ^0_{xz} increases monotonously with the shear modulus G_0, whereas it decreases (also monotonously) for $\beta < 1$ (Fig. 4.5). Thus, even though a stiffer substrate (greater G_0) should be more difficult to deform (and so γ^0_{xz} should decrease), greater tractions also imply greater deformations, and so if the target traction increases sufficiently fast with G_0 (which happens for $\beta > 1$), this yields an increasing γ^0_{xz}.

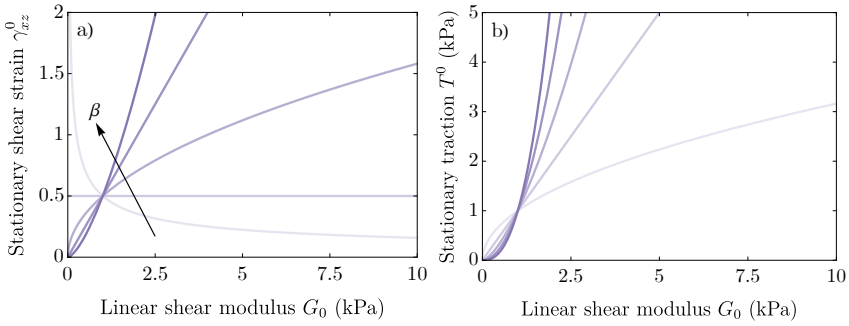

Figure 4.5: Stationary states in the linear regime for a power law target traction. Stationary shear strain γ^0_{xz} (**a**) and traction T^0 (**b**) as a function of the linear shear modulus G_0 in the linear regime and for a power law target traction (Eq. 4.16), with $T_0 = 1$ kPa, and $\beta = 0.5, 1, 1.5, 2, 2.5$.

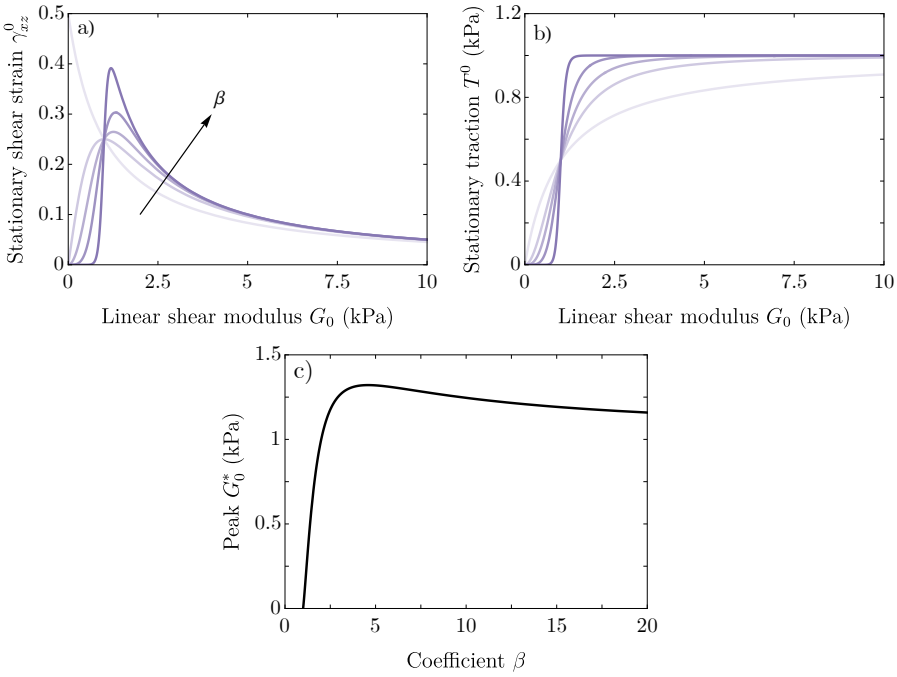

Figure 4.6: Stationary states in the linear regime for a Hill function target traction. Same as Fig. 4.5 but for a Hill function target traction, with $T^\infty = 1$ kPa, $G^* = 1$ kPa, and $\beta = 1, 2, 3, 5, 15$. In **c,** G_0 that gives the peak of the stationary shear strain γ^0_{xz} in Fig. 4.6a, as a function of β (Eq. 4.17).

In contrast, for the Hill function target traction, γ^0_{xz} is non-monotonic with G_0 for $\beta > 1$ (Fig. 4.6a,b), with its peak at (Fig. 4.6c)

$$G_0 = G^*(\beta - 1)^{1/\beta}. \tag{4.17}$$

This non-monotonicity is due to a competition of two effects, actually related to the argument for the power law from before:

- The stiffer the substrate (greater G_0), the larger the traction, and since larger force generates greater deformation, γ^0_{xz} increases. This occurs in a regime where traction can increase sufficiently (small G_0's in Fig. 4.5b and for $\beta > 1$).
- But also, the greater G_0, the stiffer the substrate and the harder to deform it, causing γ^0_{xz} to decrease. This occurs in a regime where traction is already saturating or does not increase sufficiently (high G_0's in Fig. 4.5b or $\beta < 1$).

4.3.2 Nonlinear regime

In the nonlinear regime, $G = G_1\gamma^\alpha_{xz}$ is not constant anymore, but for continuity the solution of the system of Eqs. 4.6–4.9, has again the same dependency as in the linear regime, that is, a uniform traction in x and a constant shear strain for all the z coordinate, $\gamma^0_{xz} = \gamma^0_{xz}\big|_{z=h}$ (and $\gamma^0_{xx} = \gamma^0_{zz} = 0$). From the boundary condition on the cell/gel interface (Eq. 4.9), now

$$(\gamma^0_{xz})^{\alpha+1} = \frac{T_{\text{target}}(G_1(\gamma^0_{xz})^\alpha)}{2G_1} = \begin{cases} \frac{T_0}{2}G_1^{\beta-1}(\gamma^0_{xz})^{\alpha\beta}, & \text{power law,} \\ \frac{T^\infty}{2}\frac{G_1^{\beta-1}(\gamma^0_{xz})^{\alpha\beta}}{(G_1^\beta(\gamma^0_{xz})^{\alpha\beta}+(G^*)^\beta}, & \text{Hill function.} \end{cases} \tag{4.18}$$

In both, we recover Eq. 4.16 for the linear case $\alpha = 0$ (and replacing $G_1 \to G_0$). We can explicitly write the solution for the power law $\gamma^0_{xz\text{-PL}}$ and the corresponding stationary traction, $T^0_{\text{PL}} = T_0(G_1(\gamma^0_{xz\text{-PL}})^\alpha)^\beta$, yielding

$$\gamma^0_{xz\text{-PL}} = \left(\frac{T_0}{2}G_1^{\beta-1}\right)^{\frac{1}{\alpha+1-\alpha\beta}}, \tag{4.19}$$

$$T^0_{\text{PL}} = T_0 G_1^\beta\left(\frac{T_0}{2}G_1^{\beta-1}\right)^{\frac{\alpha\beta}{\alpha+1-\alpha\beta}} = \left(\frac{T_0^{\alpha+1}G_1^\beta}{2^{\alpha\beta}}\right)^{\frac{1}{\alpha+1-\alpha\beta}}. \tag{4.20}$$

In this case, if $1 < \beta < (\alpha+1)/\alpha$, the shear strain $\gamma^0_{xz\text{-PL}}$ increases monotonously with the nonlinear shear modulus G_1, whereas if it is lower or higher, it decreases with G_1 (Fig. 4.7a). The stationary traction T^0_{PL} decreases with G_1

for $\beta > (\alpha+1)/\alpha$ (Fig. 4.7b). One should not be confused by the fact that G_1 is related to the modulus of the substrate but is not the modulus itself. In fact, if $\beta > (\alpha+1)/\alpha$, then $G = G_1(\gamma^0_{xz\text{-PL}})^\alpha$ decreases as well even though G_1 increases, because $\gamma^0_{xz\text{-PL}}(G_1)$ decreases faster. Consequently, both $\gamma^0_{xz\text{-PL}}(G)$ and $T^0_{\text{PL}}(G)$ increase, giving a behavior similar to that of the linear regime (Fig. 4.5). Changing α, which controls the strain-stiffening, we would get the same behavior, since even though $\gamma^0_{xz\text{-PL}}(G_1)$ decreases for $\alpha > 1/(\beta-1)$, it always increases when plotted as a function of the shear modulus G. All in all, if the traction increases sufficiently fast with the shear modulus G (for $\beta > 1$), it is capable of deforming further the substrate even though the latter is getting stiffer, and so $\gamma^0_{xz\text{-PL}}$ increases. Otherwise, if traction does not increase sufficiently ($\beta < 1$), then stiffening overcomes traction deformation, and $\gamma^0_{xz\text{-PL}}$ decreases because the substrate is more difficult to deform.

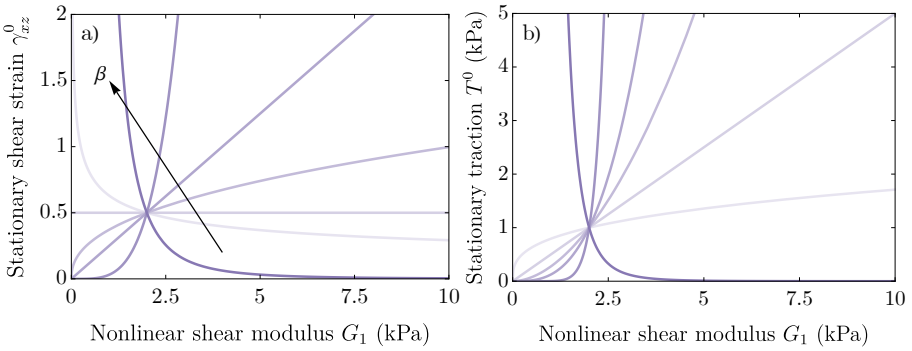

Figure 4.7: Stationary states in the nonlinear regime for a power law target traction. Stationary shear strain γ^0_{xz} (**a**) and traction T^0 (**b**) as a function of the nonlinear shear modulus G_1 in the nonlinear regime and for a power law target traction (Eq. 4.19 and Eq. 4.20). $T_0 = 1$ kPa, $\alpha = 1$ and $\beta = 0.5, 1, 1.3, 1.5, 1.8, 2.5$. Thus, for $1 < \beta < 1.5$, $\gamma^0_{xz}(G_1)$ increases.

For the Hill function target traction, $\gamma^0_{xz\text{-Hill}}$ cannot be found analytically, as it is defined implicitly as the solution of $f(\gamma^0_{xz\text{-Hill}}) = 0$, where

$$\begin{aligned} f(\gamma_{xz}) &\equiv G_1^\beta \gamma_{xz}^{\alpha\beta} - \frac{T^\infty}{2} G_1^{\beta-1} \gamma_{xz}^{\alpha\beta-\alpha-1} + (G^*)^\beta \\ &= G_1^{\beta-1} \gamma_{xz}^{\alpha\beta-\alpha-1} \left(G_1 \gamma_{xz}^{\alpha+1} - \frac{T^\infty}{2} \right) + (G^*)^\beta. \end{aligned} \tag{4.21}$$

The stationary solutions for $\gamma^0_{xz\text{-Hill}}$ and T^0_{Hill} are marked as circles in Fig. 4.8. There are typically two solutions, and both are uniform in space. We will see in

Section 4.4.2 that perturbations of the traction around one of them are unstable (empty circles), and around the other (filled circles) are stable. In this figure, we can observe a non-monotonous behavior of the stable solution $\gamma^0_{xz\text{-Hill}}(G_1)$, although recall that it does not correspond to the shear modulus of the substrate G. In Fig. 4.9, instead of varying G_1 we change the coefficients controlling the target traction growth (β) or the strain-stiffening (α), and we see that in some cases there is only one solution.

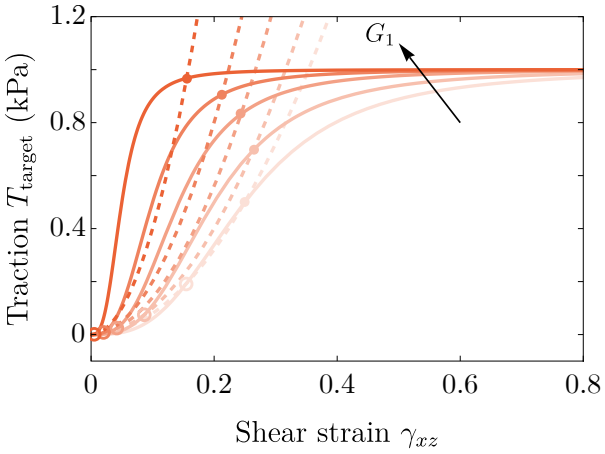

Figure 4.8: Target traction and stationary states in the nonlinear regime. Continuous lines are $T_{\text{target-Hill}}(G_1\gamma^\alpha_{xz})$, and dashed lines $2G_1\gamma^{\alpha+1}_{xz}$, and so the intersection gives the stationary shear strain γ^0_{xz} (Eq. 4.18), which is also solution of $f(\gamma^0_{xz}) = 0$, being f in Eq. 4.21. Parameters are $\alpha = 1$, $\beta = 3$, $G^* = 1$ kPa and $T^\infty = 1$ kPa, and we change $G_1 = 4, 5, 7, 10, 20$ kPa, which corresponds to $G_0 = 0.8, 1, 1.4, 2, 4$ kPa, with $\gamma_{xz,\text{crit}} = 0.2$.

From Eq. 4.21, for small G^*, implying an abrupt increase of the target traction with G, there are two solutions. The first one is $\gamma^0_{xz\text{-Hill,Lim1}} \approx 0$, which cannot be reached since these very small strains belong to the linear regime ($\gamma_{xz} < \gamma_{xz,\text{crit}}$), so the solution will be that of Eq. 4.16. The second is

$$\gamma^0_{xz\text{-Hill,Lim2}} \approx \left(\frac{T^\infty}{2G_1}\right)^{\frac{1}{\alpha+1}}. \tag{4.22}$$

This last one corresponds simply to the solution when the target traction has already saturated to T^∞, and so we recover the same expression by just putting $T_{\text{target}} = T^\infty$ in the first equality of Eq. 4.18.

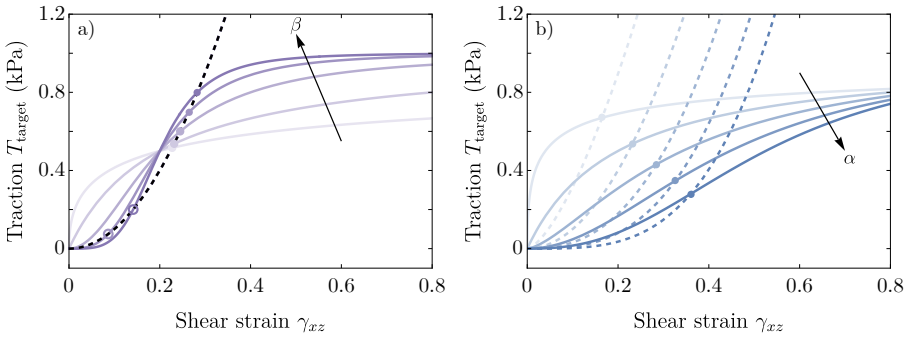

Figure 4.9: Target traction and stationary states in the nonlinear regime. Same as Fig. 4.8 with $G_1 = 5$ kPa. In **a**, $\alpha = 1$ and $\beta = 0.5, 1, 2, 3, 4$. In **b**, $\beta = 1$ and $\alpha = 0.5, 1, 1.5, 2, 2.5$.

4.4 Linear stability analysis of stationary solutions

The stationary states in the nonlinear regime were found assuming that the solution has the same dependency as in the linear regime, that is, uniform traction, a linear $x-$displacement with z and no $z-$displacement (and hence a constant shear strain γ_{xz}). We now discuss the linear stability of the solutions of the nonlinear problem. For a small traction perturbation δT, we linearize the equations around the stationary state γ^0_{xz} to find the growth rate of the perturbation. From Eq. 4.13,

$$\partial_t \delta T = -\frac{1}{\tau}\left[\delta T - \left(\frac{\partial T_{\text{target}}}{\partial \gamma_{xz}}\right)\Big|_{\gamma^0_{xz}} \delta\gamma_{xz}\big|_{z=h}\right], \tag{4.23}$$

and the growth rate of a perturbation of wavenumber q reads,

$$\omega(q) = \frac{1}{\tau}\left[\left(\frac{\partial T_{\text{target}}}{\partial \gamma_{xz}}\right)\Big|_{\gamma^0_{xz}} \frac{\delta\hat{\tilde{\gamma}}_{xz}\big|_{z=h}}{\delta\hat{\tilde{T}}} - 1\right]. \tag{4.24}$$

If $\omega(q) > 0$, the perturbation grows exponentially, and the state is unstable, whereas if the growth rate is negative, it decays, and the state is stable under that perturbation. An imaginary part would imply an oscillatory dynamics of the perturbation. The linearized system of equations and its resolution is explained in detail in Appendix 4.A. Importantly, it directly follows from the boundary condition for the shear stress on the cell/gel interface (Eq. 4.9 right), that the perturbation in the strain only depends on q through the traction perturbation

(Eq. 4.A.22),

$$\delta\hat{\tilde{\gamma}}_{xz}\big|_{z=h} \equiv \frac{1}{2}\left[iq\delta\hat{\tilde{u}}_z + \partial_z(\delta\hat{\tilde{u}}_x)\right]\big|_{z=h} = \frac{\delta\hat{\tilde{T}}}{2G_1(\gamma^0_{xz})^\alpha(\alpha+1)} = \frac{\delta\hat{\tilde{T}}}{2C_2}, \tag{4.25}$$

and so, even though $\delta\hat{\tilde{\gamma}}_{xz}$ may depend explicitly on q, when evaluated at $z = h$ it does not (Fig. 4.10). The expression of the growth rate (also Eq. 4.A.30), reads

$$\omega = \frac{1}{\tau}\left[\left(\frac{\partial T_{\text{target}}}{\partial\gamma_{xz}}\right)\Big|_{\gamma^0_{xz}} \frac{1}{2G_1(\gamma^0_{xz})^\alpha(\alpha+1)} - 1\right]. \tag{4.26}$$

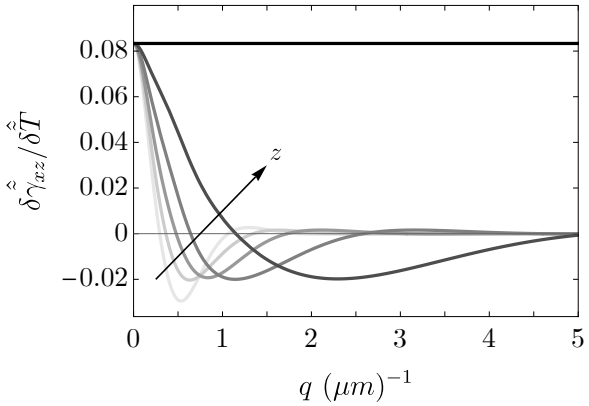

Figure 4.10: Strain perturbation as a function of the wavenumber. Plot of $\delta\hat{\tilde{\gamma}}_{xz}/\delta\hat{\tilde{T}}$ as a function of q, for different values of $z = 0, 1, 2, 3, 4, 5$. For $z = h$ it is independent of q. Parameters are $\alpha = 2$, $h = 5$ μm, $\delta\hat{\tilde{T}} = 1$ kPa·μm·h, $K = 20$ kPa and $G_1\gamma^0_{xz} = 2$ kPa.

This ω does not depend on q, because we are assuming that the top plane is not deforming in z. The full expression for ω has to be determined with a specific profile for the target traction. In the linear regime, this perturbation is always stable since T_{target} does not depend on γ_{xz} ($G = G_0$ is constant) and so $\omega = -1/\tau < 0$. In the nonlinear regime, however, the stability depends on parameter values. We compute it in the following subsections.

4.4.1 Power law target traction

The derivative of the target traction with respect to the shear strain reads

$$\frac{\partial T_{\text{target-PL}}}{\partial\gamma_{xz}} = \frac{\partial T_{\text{target-PL}}}{\partial G}\frac{\partial G}{\partial\gamma_{xz}} = T_0\beta G^{\beta-1}G_1\alpha\gamma_{xz}^{\alpha-1} = T_0\alpha\beta G_1^\beta\gamma_{xz}^{\alpha\beta-1}, \tag{4.27}$$

so plugging it into Eq. 4.26, and evaluating $\gamma^0_{xz} = \gamma^0_{xz\text{-PL}}$ (Eq. 4.19), the expression for the growth rate is greatly simplified, obtaining

$$\omega = \frac{1}{\tau}\left(\frac{\alpha\beta}{\alpha+1} - 1\right). \tag{4.28}$$

Therefore, the exponents α and β are the parameters that control the stability, with $\omega > 0$ occurring for $\beta > \frac{\alpha+1}{\alpha}$ (Fig. 4.11). To have positive feedback, we need a sufficiently strong increase of the target traction with the shear modulus (controlled by β) to compensate for the substrate stiffening encoded in α. By contrast, if the traction does not increase sufficiently (following the target traction), the enhanced resistance to deformation due to the stiffening overcomes the enhanced deformation due to the traction increase and the perturbation decays.

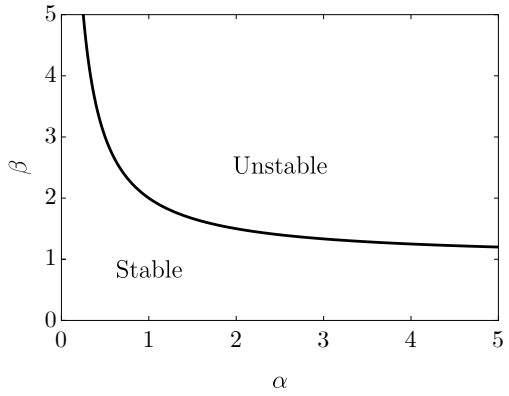

Figure 4.11: Phase diagram for the stability of the perturbation. $\beta(\alpha)$ giving unstable perturbation for a power law target traction.

4.4.2 Hill function target traction

Now, the derivative of the target traction with respect to the shear strain reads

$$\begin{aligned}\frac{\partial T_{\text{target-Hill}}}{\partial \gamma_{xz}} &= \frac{\partial T_{\text{target-Hill}}}{\partial G}\frac{\partial G}{\partial \gamma_{xz}} = T^\infty \frac{(G^*)^\beta \beta G^{\beta-1}}{(G^\beta + (G^*)^\beta)^2} G_1 \alpha \gamma_{xz}^{\alpha-1} \\ &= \frac{T^\infty \alpha\beta G_1^\beta (G^*)^\beta \gamma_{xz}^{\alpha\beta-1}}{(G_1^\beta \gamma_{xz}^{\alpha\beta} + (G^*)^\beta)^2}.\end{aligned} \tag{4.29}$$

Plugging it into Eq. 4.26 and evaluating at γ^0_{xz}, we obtain

$$\omega = \frac{1}{\tau}\left[\frac{T^\infty \alpha\beta G_1^{\beta-1}(G^*)^\beta (\gamma^0_{xz})^{\alpha\beta-\alpha-1}}{2(\alpha+1)[G_1^\beta (\gamma^0_{xz})^{\alpha\beta} + (G^*)^\beta]^2} - 1\right]. \tag{4.30}$$

Since we do not have analytical solutions for $\gamma^0_{xz} = \gamma^0_{xz\text{-Hill}}$ for all the parameters (see Section 4.3.2), we cannot have a general explicit expression for this growth rate ω. For small values of the exponents we obtain that the state is stable:

- $\alpha = 1, \beta = 1$: The stationary shear strain is solution of $G_1\gamma_{xz}^2 + (G^*)\gamma_{xz} - T^\infty/2 = 0$ (Eq. 4.21), and so (taking the positive solution from the second order equation to have $\gamma^0_{xz} > 0$),

$$\gamma^0_{xz} = \frac{1}{2G_1}(-G^* + \sqrt{(G^*)^2 + 2G_1T^\infty}), \tag{4.31}$$

  which is positive since $2G_1T^\infty > 0$. The growth rate gets simplified to

$$\omega = -\frac{1}{\tau}\frac{1}{\left(1 + \frac{G^*}{\sqrt{(G^*)^2+2G_1T^\infty}}\right)} < 0. \tag{4.32}$$

- $\alpha = 1, \beta = 2$: The stationary shear strain is solution of $G_1^2\gamma_{xz}^2 - G_1T^\infty/2 + (G^*)^2 = 0$, and so

$$\gamma^0_{xz} = \frac{\sqrt{G_1T^\infty - 2(G^*)^2}}{\sqrt{2}G_1}. \tag{4.33}$$

  To have a real solution, the parameters should fulfil $G_1T^\infty > 2(G^*)^2$, which yields a negative growth rate,

$$\omega = \frac{1}{\tau}\frac{2(G^*)^2 - G_1T^\infty}{G_1T^\infty} < 0. \tag{4.34}$$

For larger or other combinations of the coefficients, the solution for γ^0_{xz} and ω must be found numerically, solving $f(\gamma^0_{xz}) = 0$, where f is in Eq. 4.21, and choosing the real and positive roots of the function, since only those have physical meaning. We see that when β is large, so the target traction grows fast with the shear modulus G, it is possible to find a parameter region where the stationary state is unstable ($\omega > 0$). This happens when we have more than one real and positive solution for γ^0_{xz}. In this case, the instability of the perturbation around each of the stationary solutions changes, being the smaller solution unstable, and the larger one stable.

In Fig. 4.8 we saw an example for $\alpha = 1$ and $\beta = 3$. The stationary solutions for γ^0_{xz} are plotted as circles in the $T_{\text{target}}(\gamma_{xz})$ curve. For each curve, the smaller solution (empty circle) gives unstable states, that is, with $\omega > 0$, because it is in a region where T_{target} increases more rapidly, with a similar tendency than the power law (and indeed, in Eq. 4.28 we saw that the power law target traction yields a positive growth rate for $\alpha = 1$ and $\beta = 3$). On the contrary, the larger

solution (filled circle), gives stable states, that is, with $\omega < 0$, because the target traction is closer to the saturation, and so it does not increase sufficiently fast with the shear modulus G. We also observe this behavior for other combinations of α and β (like in Fig. 4.9), including also non-integer values.

4.4.3 Adding a diffusive spatial coupling

We now extend the traction dynamics Eq. 4.13 to spatially non-uniform states, introducing a simple diffusive coupling, to account, for instance, for the coupling between the polarity and the traction of cells with their neighbors,

$$\partial_t T = -\frac{1}{\tau}\big(T - T_{\text{target}}(G(\gamma_{xz}\big|_{z=h})) - D\nabla^2 T\big), \tag{4.35}$$

where $[D] = L^2$. Now the growth rate is a decreasing function of q, and using that $\omega(D=0)$ is the growth rate from Eq. 4.26, then

$$\omega(q) = \omega(D=0) - \frac{D}{\tau}q^2, \tag{4.36}$$

being $q^* \equiv \sqrt{\frac{\omega(D=0)\tau}{D}}$ (such that $\omega(q^*) = 0$), the cut-off between a regime of unstable perturbations (for $q < q^*$) and stable ones (for $q > q^*$), as can be seen in Fig. 4.12. Taking realistic values for the parameters, as in the figure, unstable perturbations may take place for wavelengths of a few micrometers ($2.8\ \mu\text{m} < \lambda^* < 9.7\ \mu\text{m}$), and so visible in the tissue length scales, and may last a few hours (up to $\omega^{-1} \sim 2$ h).

4.5 Non-monotonicity and bistability of the solutions

In Section 4.3.1, we observed a non-monotonic behavior of the strain as a function of the substrate's shear modulus in the linear regime and with a Hill function target traction (Fig. 4.6). We explained it as a competition between two effects: on the one hand, an increase in traction with shear modulus leads to a greater deformation, while on the other hand, the stiffening of the substrate makes it more resistant to deformation. In Fig. 4.13 we see that this non-monotonicity is also recovered in the nonlinear regime, both when γ^0_{xz} is plotted as a function of the nonlinear shear modulus G_1 (Fig. 4.13a,b) or the actual shear modulus G (Fig. 4.13c,d, computing G with Eq. 4.10), for different constant T^∞ values. Conversely, in Fig. 4.16, the solutions are plotted versus T^∞, for different constant G_1 values (Fig. 4.16). Here this non-monotonicity is not expected, because by increasing T^∞ we are only increasing the traction but not stiffening the

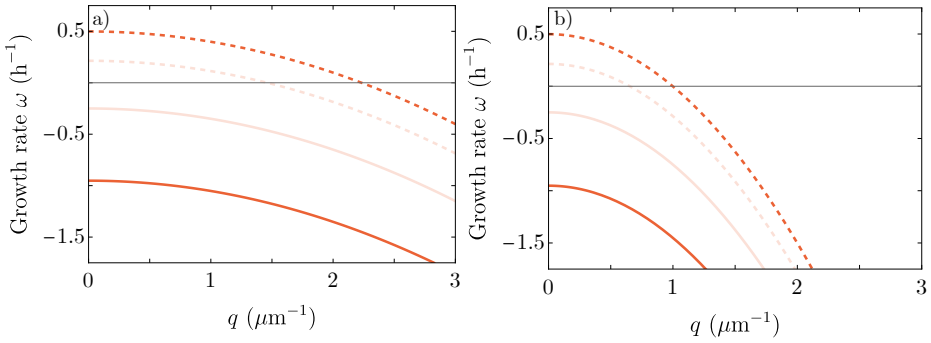

Figure 4.12: Dispersion relation of the perturbation. $\omega(q)$ for $D = 0.1$ μm^2 (**a**) and $D = 0.5$ μm^2 (**b**), where continuous lines correspond to stable points from Fig. 4.8 (same parameters), and dashed ones to unstable points. For $G_1 = 4$ kPa (light curves), $\gamma^0_{xz} = 0.25 \rightarrow \omega(D = 0) = -0.25$ (stable) and $\gamma^0_{xz} = 0.15 \rightarrow \omega(D = 0) = 0.21$ (unstable). In this last case, $q^* = 1.46$ μm^{-1} (**a**) and $q^* = 0.65$ μm^{-1} (**b**). For $G_1 = 20$ kPa (dark curves), $\gamma^0_{xz} = 0.16 \rightarrow \omega(D = 0) = -0.95$ (stable) and and $\gamma^0_{xz} = 0.005 \rightarrow \omega(D = 0) = 0.50$ (unstable). In this last case, $q^* = 2.24$ μm^{-1} (**a**) and $q^* = 1.00$ μm^{-1} (**b**).

substrate, and so the stable solutions are monotonously increasing. However, the non-monotonicity with G_1 can also be observed by looking at the different curves, mainly in the linear regime.

In some regimes, we observe bistability of the solutions and the presence of hysteresis. When G_1 is considered (Fig. 4.13a,b), for small values of G_1, the linear solution (below the black horizontal dashed line that represents $\gamma_{xz,\text{crit}}$), which is stable, and the stable one in the nonlinear regime (continuous line above $\gamma_{xz,\text{crit}}$), may coexist. In a typical hysteresis loop, the system starts with the solution in the linear regime and jumps to the stable one in the nonlinear regime as the nonlinear shear modulus is increased. If it is decreased again, it will fall back to the linear solution at a point past the first jump. An equivalent plot of Fig. 4.13a is shown in Fig. 4.14, for only one value of T^∞, to distinguish the solutions in the different regimes and better observe the bistability. The effect of $\gamma_{xz,\text{crit}}$ is illustrated in Fig. 4.15. If larger strains are needed to enter the nonlinear regime (increasing the critical strain), the linear regime is enlarged, and if big enough, the unstable solution will cease to exist. Instead, we will only have the linear regime solution, which is stable, and the discontinuous behavior (and the bistability) of the stationary solutions is lost.

Although G is not a parameter of the model, it is the experimentally measured shear modulus of the substrate, whereas the coefficient G_1 is more difficult to obtain. Thus, if we plot the stationary states as a function of G instead of

G_1 (Fig. 4.13c,d), we see that this bistability is not manifest and the same solutions as in the linear regime are obtained, but with $G_0 \to G$, from Eq. 4.16. This happens because the unstable solutions in the nonlinear regime when G_1 is considered (dotted lines in Fig. 4.13a,b), decrease for an increasing G_1 (which is also observed in the empty circles in Fig. 4.8). This decrease implies a decrease in $G = G_1(\gamma^0_{xz})^\alpha$, even though G_1 is increasing, which yields the increasing solutions for an increasing G. In this case, it is not possible to have two stable solutions for the same value of shear modulus G, regardless of the saturating traction value, but the non-monotonicity is still recovered.

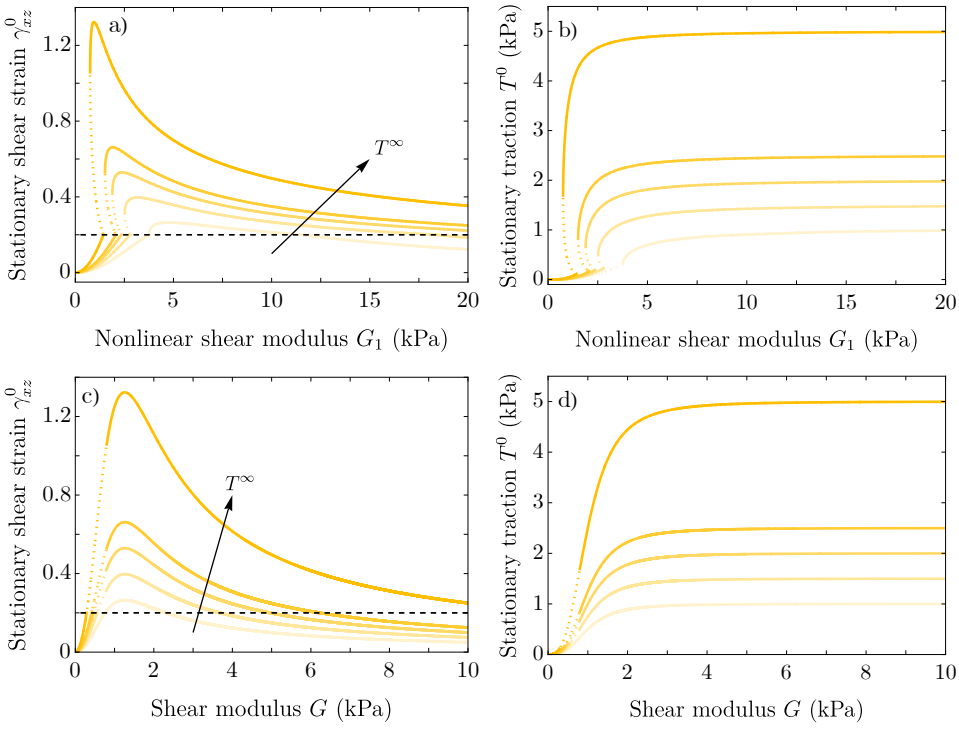

Figure 4.13: Stationary states in the nonlinear regime for a Hill function target traction. a,b, Stationary solutions for γ^0_{xz} (**a**) and T^0 (**b**) as a function of G_1, changing $T^\infty = 1, 1.5, 2, 2.5, 5$ kPa. **c,d,** γ^0_{xz} and T^0 as a function of G. In all, $\alpha = 1, \beta = 3$, $G^* = 1$ kPa and $\gamma_{xz,\text{crit}} = 0.2$ (horizontal dashed line in **a** and **c**). Continuous lines show stable solutions (both in the linear and the nonlinear regimes) and dotted lines show unstable solutions in the nonlinear regime.

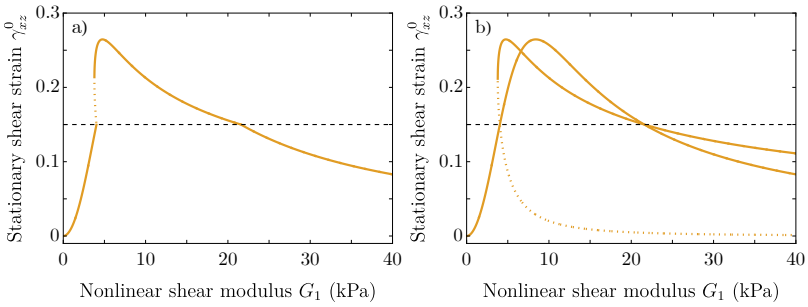

Figure 4.14: Regimes of the stationary shear strain. In **a**, only the solution for the corresponding regime is chosen, whereas in **b** all are plotted. Continuous lines show stable solutions (both in the linear and the nonlinear regimes) and dotted lines the unstable ones in the nonlinear regime. Parameters are $\gamma_{xz,\mathrm{crit}} = 0.15$ (horizontal dashed line), and $\alpha = 1$, $\beta = 3$, $T^\infty = 1$ kPa, $G^* = 1$ kPa.

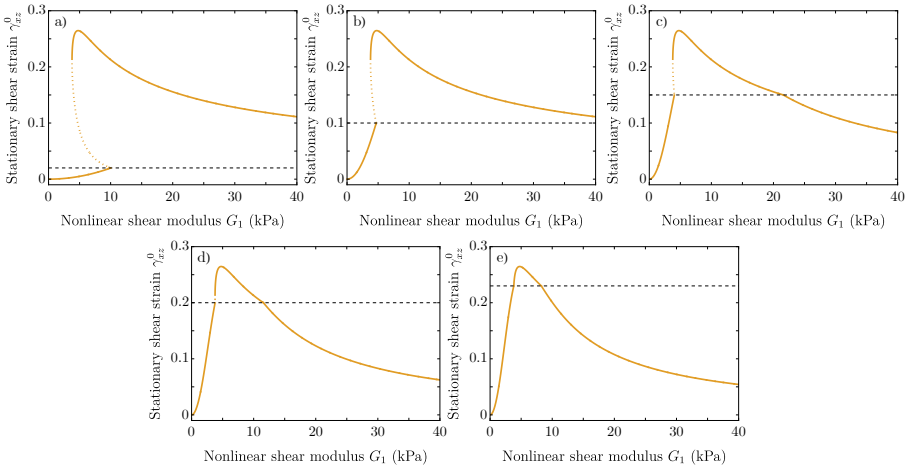

Figure 4.15: Effect of the critical shear strain. Same as Fig. 4.14a, increasing $\gamma_{xz,\mathrm{crit}} = 0.02, 0.1, 0.15, 0.2, 0.23$ from **a** to **e**. If it is large enough, the unstable solution in the nonlinear regime does not exist anymore.

Finally, when plotting the stationary solutions versus the traction saturation value T^∞ (Fig. 4.16), the bistability of the solutions is still present. This tells us that in some regimes of T^∞, two stable solutions may coexist, jumping from the linear to the nonlinear one when T^∞ is increased, and going back, following a hysteresis cycle, when it is decreased. These predictions could be potentially tested in the experiments, which is discussed in the conclusions section.

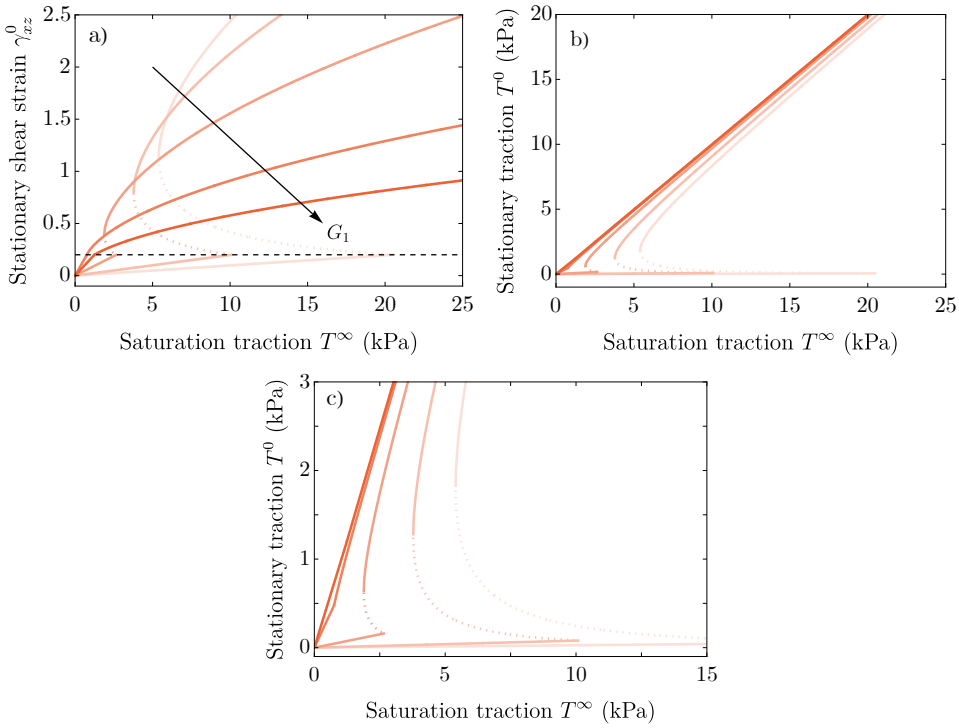

Figure 4.16: Stationary states in the nonlinear regime for a Hill function target traction. a,b, Stationary solutions for γ^0_{xz} (**a**) and T^0 (**b** and **c**, being **c** a zoom-in of **b**) as a function of T^∞, changing $G_1 = 0.7, 1, 2, 6, 15$ kPa. Continuous lines show stable solutions (both in the linear and the nonlinear regimes) and dotted lines show unstable solutions in the nonlinear regime.

4.6 Discussion and conclusions

In this chapter, we have investigated the feedback mechanisms between cellular traction forces and the stiffness of the extracellular matrix. Our study highlights the role of strain-stiffening of the extracellular environment in regulating tissue dynamics, particularly the traction forces and their impact on spreading and migration.

One key finding is the bistable nature of the solutions, both for the substrate's strain and the cellular tractions, in certain regimes of the model parameters, especially regarding the nonlinear shear modulus and the traction saturation value. Near these regimes, a slight increase of either parameter would trigger a discontinuous transition to much higher traction values—from the linear stable solution

to the nonlinear stable solution—enabling tissues to overcome intercellular contractility and facilitating the spreading transition. Although both active forces—traction and contractility—are driven by myosin activity, they evolve distinctly due to the feedback loop between substrate stiffness and traction forces, leaving contractility unaffected. Thus, this transition could be a triggering mechanism for the spreading of a tissue, because leaving contractility unaffected, the higher traction values (and higher stiffness of the substrate) induce the spreading of the tissue [Alert2019b]. The accompanying hysteresis cycle ensures stability.

These predictions could be potentially tested in epithelial migration assays, by either modifying the substrate's stiffness (and so impacting the coefficient G_1) or the traction saturation values (changing T^∞). In *in vitro* experiments, typically, PAA gels coated with a biopolymer network are used as substrates, and once they are prepared, it is difficult to tune their stiffness *in situ* during the experiment. Adjusting polymer concentration once the cells are migrating may be an option to test, but we suspect it would not be a very clean experiment. However, the traction saturation value is easier to modify. By treatments impacting on the myosin phosphorylation, like human epidermal growth factor (hEGF), which increases contractility [Chan2021,Iwabu2004], or Y-27632 ROCK inhibitor or blebbistatin that completely or partially inhibit it [Pérez-González2019], the traction saturation value would be increased or decreased, respectively. By measuring substrate deformation and inferring the traction forces from it, it should be possible to test whether these discontinuous transitions to higher or lower traction states take place.

These findings have potential implications for processes requiring tissue spreading, such as wound healing and epithelial migration. By increasing myosin phosphorylation levels, cells can enhance their traction forces. Because of the ECM stiffening, cells may then get to a higher-traction state, aiding the spreading process. These insights could also have implications for tumor progression. During tumor development, increased intracellular contractility, often due to elevated myosin levels, directly affects the parameter of traction saturation (T^∞) in our model. Consequently, the surrounding ECM (stroma) gets rigidified. By modeling this stiffening through the substrate's nonlinear behavior, we predict that once contractility surpasses a certain threshold, cells can transition from a low-traction to a high-traction state. This shift may correspond to the initiation of tumor spreading.

In addition to increasing contractility, another pathway to achieving a higher-traction state involves stiffening the ECM itself. By secreting and accumulating matrix components, tissues may enhance the stiffness of their environment, promoting a similar transition. This mechanism is observed in several

biological processes, including embryonic development (such as *Xenopus laevis* mesoderm stiffening, essential for triggering migration and coordinating morphogenesis [Barriga2018]), wound healing (through cortical and matrix deposition [Enoch2008, Vasudevan2023]), or tumor progression (via matrix deposition by fibroblasts around the tumor [Ronnov-Jessen1996, Shekhar2003, vanKempen2003, Schedin2004]).

In summary, our findings underscore the intricate interplay between tissue mechanics and the nonlinear properties of the surrounding substrate or ECM, revealing how strain-stiffening can drive transitions that promote tissue spreading and migration. This study enhances our understanding of how tissues interact with and modify their environment, suggesting new avenues to explore—such as the potential explanation of traction bursts in dense ECM regions observed by [Böhringer2024]—through this feedback mechanism between stiffness and traction.

Contributions and acknowledgements

The work described in this chapter was initiated during a stay of three months at the Max Planck Institute for the Physics of Complex Systems (MPI-PKS), the Center for Systems Biology Dresden (CSBD), and the Max Planck Institute of Molecular Cell Biology and Genetics (MPI-CBG), in Dresden, at the "The Physics of Living Matter" group led by Ricard Alert. He proposed the project, and we developed it during and after the stay.

I want to thank specially Ashot Matevosyan for his tips in the analytical resolution of the system for the linear perturbation analysis (from Appendix 4.A), and Ahandeep Manna for his constant help and ideas with the model, as well with the FEniCS Project for the numerical simulations with finite elements (although they are not included in the thesis).

Appendices

4.A Linearization and solution of the system

The system of equations Eqs. 4.6–4.9 cannot be solved analytically in the nonlinear regime ($G = G_1\gamma_{xz}^{\alpha}$) for an arbitrary traction T. If we assume $T = T^0 + \delta T$, being T^0 uniform, then we can take the linearized quantities $\gamma = \gamma^0 + \delta\gamma$ and $\sigma = \sigma^0 + \delta\sigma$, where γ^0 and σ^0 are the stationary solutions in the nonlinear regime for a uniform traction T^0 (Section 4.3.2). Eqs. 4.3–4.5 translate to

$$\sigma_{xx}^0 + \delta\sigma_{xx} = \left(K + \frac{4G_1(\gamma_{xz}^0 + \delta\gamma_{xz})^{\alpha}}{3}\right)(\gamma_{xx}^0 + \delta\gamma_{xx}) + \left(K - \frac{2G_1(\gamma_{xz}^0 + \delta\gamma_{xz})^{\alpha}}{3}\right)(\gamma_{zz}^0 + \delta\gamma_{zz}), \tag{4.A.1}$$

$$\sigma_{xz}^0 + \delta\sigma_{xz} = 2G_1(\gamma_{xz}^0 + \delta\gamma_{xz})^{\alpha+1} \tag{4.A.2}$$

$$\sigma_{zz}^0 + \delta\sigma_{zz} = \left(K - \frac{2G_1(\gamma_{xz}^0 + \delta\gamma_{xz})^{\alpha}}{3}\right)(\gamma_{xx}^0 + \delta\gamma_{xx}) + \left(K + \frac{4G_1(\gamma_{xz}^0 + \delta\gamma_{xz})^{\alpha}}{3}\right)(\gamma_{zz}^0 + \delta\gamma_{zz}). \tag{4.A.3}$$

To linear order, $(\gamma_{xz}^0 + \delta\gamma_{xz})^{\alpha} \approx (\gamma_{xz}^0)^{\alpha} + \alpha(\gamma_{xz}^0)^{\alpha-1}\delta\gamma_{xz}$, and since $\gamma_{xx}^0 = \gamma_{zz}^0 = 0$ (Section 4.3.2), this gives

$$\delta\sigma_{xx} \approx C_1\delta\gamma_{xx} + (C_3 - C_2)\delta\gamma_{zz}, \tag{4.A.4}$$

$$\delta\sigma_{xz} \approx 2C_2\delta\gamma_{xz}, \tag{4.A.5}$$

$$\delta\sigma_{zz} \approx (C_3 - C_2)\delta\gamma_{xx} + C_1\delta\gamma_{zz}, \tag{4.A.6}$$

where we have defined the constants $C_1 = K + \frac{4}{3}G_1(\gamma_{xz}^0)^{\alpha}$, $C_2 = G_1(\gamma_{xz}^0)^{\alpha}(\alpha+1)$ and $C_3 = K + G_1(\gamma_{xz}^0)^{\alpha}(\alpha + 1/3)$, so that $C_3 - C_2 = K - \frac{2}{3}G_1(\gamma_{xz}^0)^{\alpha}$. The

linearized system of equations for the perturbations of the stress then, $\partial_x(\delta\sigma_{xx})+\partial_z(\delta\sigma_{xz})=0$ and $\partial_x(\delta\sigma_{xz})+\partial_z(\delta\sigma_{zz})=0$ (Eqs. 4.6–4.9), read

$$C_1\partial_x(\delta\gamma_{xx})+(C_3-C_2)\partial_x(\delta\gamma_{zz})+2C_2\partial_z(\delta\gamma_{xz})=0, \tag{4.A.7}$$
$$2C_2\partial_x(\delta\gamma_{xz})+(C_3-C_2)\partial_z(\delta\gamma_{xx})+C_1\partial_z(\delta\gamma_{zz})=0, \tag{4.A.8}$$
$$u_x\big|_{z=0}=0,\quad u_x\big|_{z=0}=0, \tag{4.A.9}$$
$$\left[(C_3-C_2)\delta\gamma_{xx}+C_1\delta\gamma_{zz}\right]\big|_{z=h}=0, \tag{4.A.10}$$
$$2C_2\delta\gamma_{xz}\big|_{z=h}=\delta T, \tag{4.A.11}$$

which, substituting for the perturbations of the displacements, $\delta\gamma_{xx}=\partial_x(\delta u_x)$, $\delta\gamma_{xz}=\frac{1}{2}(\partial_x(\delta u_z)+\partial_z(\delta u_x))$ and $\delta\gamma_{zz}=\partial_z(\delta u_z)$,

$$C_1\partial_x^2(\delta u_x)+(C_3-C_2)\partial_x\partial_z(\delta u_z)+C_2(\partial_z\partial_x(\delta u_z)+\partial_z^2(\delta u_x))=0, \tag{4.A.12}$$
$$C_2(\partial_x^2(\delta u_z)+\partial_x\partial_z(\delta u_x))+(C_3-C_2)\partial_z\partial_x(\delta u_x)+C_1\partial_z^2(\delta u_z)=0, \tag{4.A.13}$$
$$u_x\big|_{z=0}=0,\quad u_x\big|_{z=0}=0, \tag{4.A.14}$$
$$\left[(C_3-C_2)\partial_x(\delta u_x)+C_1\partial_z(\delta u_z)\right]\big|_{z=h}=0, \tag{4.A.15}$$
$$C_2\left[\partial_x(\delta u_z)+\partial_z(\delta u_x)\right]\big|_{z=h}=\delta T. \tag{4.A.16}$$

In Fourier space for $x\to q$ and Laplace for times $t\to\omega$,

$$-C_1q^2\delta\hat{\hat{u}}_x+C_2\partial_z^2(\delta\hat{\hat{u}}_x)+iqC_3\partial_z(\delta\hat{\hat{u}}_z)=0, \tag{4.A.17}$$
$$C_1\partial_z^2(\delta\hat{\hat{u}}_z)-C_2q^2\delta\hat{\hat{u}}_z+iqC_3\partial_z(\delta\hat{\hat{u}}_x)=0, \tag{4.A.18}$$
$$\delta\hat{\hat{u}}_x\big|_{z=0}=0,\quad \delta\hat{\hat{u}}_z\big|_{z=0}=0, \tag{4.A.19}$$
$$\left[(C_3-C_2)iq\delta\hat{\hat{u}}_x+C_1\partial_z(\delta\hat{\hat{u}}_z)\right]\big|_{z=h}=0, \tag{4.A.20}$$
$$C_2\left[iq\delta\hat{\hat{u}}_z+\partial_z(\delta\hat{\hat{u}}_x)\right]\big|_{z=h}=\delta\hat{\hat{T}}. \tag{4.A.21}$$

Note that from this last equation, which comes from the boundary condition for the shear stress in the cell/gel interface, we have that $\delta\hat{\hat{\gamma}}_{xz}$ does not depend on q when evaluated at $z=h$ (same result as we briefly stated in Eq. 4.25),

$$\delta\hat{\hat{\gamma}}_{xz}\big|_{z=h}\equiv\frac{1}{2}\left[iq\delta\hat{\hat{u}}_z+\partial_z(\delta\hat{\hat{u}}_x)\right]\big|_{z=h}=\frac{\delta\hat{\hat{T}}}{2C_2}. \tag{4.A.22}$$

The solution for this system, Eq. 4.A.21, will be a combination of exponentials, $\delta\hat{\hat{u}}_x=\sum_{i=1}^4 A_ie^{\lambda_i z}$ and $\delta\hat{\hat{u}}_z=\sum_{i=1}^4\mu_iA_ie^{\lambda_i z}$, with λ_i and μ_i functions of

C_1, C_2, C_3 and q[1]. We get

$$\lambda_1 = -\lambda_2 = -f_1(C_1, C_2, C_3)q \tag{4.A.23}$$
$$\lambda_3 = -\lambda_4 = -f_2(C_1, C_2, C_3)q \tag{4.A.24}$$
$$\mu_1 = -\mu_2 = if_1(C_1, C_2, C_3)g_1(C_1, C_2, C_3) \equiv ih_1(C_1, C_2, C_3) \tag{4.A.25}$$
$$\mu_3 = -\mu_4 = if_2(C_1, C_2, C_3)g_2(C_1, C_2, C_3) \equiv ih_2(C_1, C_2, C_3) \tag{4.A.26}$$

being $h_i \equiv f_i g_i$ (with $i = 1, 2$) and

$$f_{\substack{1\\2}} = \sqrt{\frac{C_1^2 + C_2^2 - C_3^2 \mp \sqrt{k}}{2C_1C_2}}, \quad g_{\substack{1\\2}} = \frac{C_1^2 - C_2^2 - C_3^2 \pm \sqrt{k}}{2C_2C_3} \tag{4.A.27}$$

where $k = (C_1-C_2-C_3)(C_1+C_2-C_3)(C_1-C_2+C_3)(C_1+C_2+C_3)$. Substituting C_i with the according expressions with the bulk and the shear modulus K and G, this gives $k = -\frac{16}{9}G_1^2(\gamma_{xz}^0)^{2\alpha}(G_1(\gamma_{xz}^0)^\alpha + 3K)\alpha[3K + G_1(\gamma_{xz}^0)^\alpha(4+3\alpha)]$, and so it is negative since $G_1, K, \alpha, \gamma_{xz}^0 > 0$. Therefore, the functions f_1 and f_2, related to the length scale in the exponentials, are imaginary. Writing explicitly $\delta\hat{\tilde{u}}_x$ and $\delta\hat{\tilde{u}}_x$,

$$\begin{aligned}
\delta\hat{\tilde{u}}_x &= A_1e^{-f_1qz} + A_2e^{f_1qz} + A_3e^{-f_2qz} + A_4e^{f_2qz} \\
&= (-A_1 + A_2)\sinh(f_1qz) + (A_1 + A_2)\cosh(f_1qz) \\
&\quad + (-A_3 + A_4)\sinh(f_2qz) + (A_3 + A_4)\cosh(f_2qz) \\
&\equiv B_1\sinh(f_1qz) + B_2\cosh(f_1qz) \\
&\quad + B_3\sinh(f_2qz) + B_4\cosh(f_2qz),
\end{aligned} \tag{4.A.28}$$

$$\begin{aligned}
\delta\hat{\tilde{u}}_z &= ih_1(A_1e^{-f_1qz} - A_2e^{f_1qz}) + ih_2(A_3e^{-f_2qz} - A_4e^{f_2qz}) \\
&= ih_1(-A_1 - A_2)\sinh(f_1qz) + ih_1(A_1 - A_2)\cosh(f_1qz) \\
&\quad + ih_2(-A_3 - A_4)\sinh(f_2qz) + ih_2(A_3 - A_4)\cosh(f_2qz) \\
&\equiv -i\Big[h_1\big(B_2\sinh(f_1qz) + B_1\cosh(f_1qz)\big) + \\
&\quad h_2\big(B_4\sinh(f_2qz) + B_3\cosh(f_2qz)\big)\Big],
\end{aligned} \tag{4.A.29}$$

where $B_i(C_1, C_2, C_3, q, \delta\hat{\tilde{T}}, h)$ are determined with the boundary conditions of Eq. 4.A.21. We see that $\delta\hat{\tilde{u}}_x$ is real and $\delta\hat{\tilde{u}}_z$ imaginary. Hence, $\delta\hat{\tilde{\gamma}}_{xz} = \frac{1}{2}[\partial_z(\delta\hat{\tilde{u}}_x) +$

[1]The linear case ($\alpha = 0$) would need of another term in the ansatz, $ze^{\lambda z}$ because the system in this case is degenerate, since $C_1 - C_2 - C_3 = 0$, with $C_1 = K + \frac{4}{3}G_0$, $C_2 = G_0$ and $C_3 = K + \frac{G_0}{3}$). Therefore, we only have two solutions for λ_i, μ_i (that is, $\lambda = \pm q$ and $\mu = \pm i$), but since it is a second-order system of two equations, we need four solutions.

$iq\delta\hat{\tilde{u}}_z]$, is real, and so is the growth rate of the perturbation ω (Eq. 4.24). Finally, substituting Eq. 4.A.22 there, we get the result in Eq. 4.26,

$$\begin{aligned}\omega &= \frac{1}{\tau}\left[\left(\frac{\partial T_{\text{target}}}{\partial \gamma_{xz}}\right)\Big|_{\gamma^0_{xz}} \frac{1}{2C_2} - 1\right] \\ &= \frac{1}{\tau}\left[\left(\frac{\partial T_{\text{target}}}{\partial \gamma_{xz}}\right)\Big|_{\gamma^0_{xz}} \frac{1}{2G_1(\gamma^0_{xz})^\alpha(\alpha+1)} - 1\right],\end{aligned} \tag{4.A.30}$$

and so ω does not depend on the traction perturbation.

Chapter 5

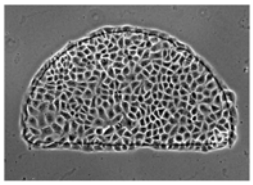

Experiments on shape-sensing motility of monolayer clusters

5.1 Introduction

The relationship between movement and morphology across biological systems has been extensively studied. For instance, keratocyte lamellar fragments, lacking nuclei and most organelles, exhibit directional motility by retracting the rear edge, which has actin and myosin accumulation [Verkhovsky1998, Pollard2003] (Fig. 5.1a,b,d), despite the absence of a larger-scale machinery regulating the global polarization of the full keratocyte. Phenomenological models show that these lamellar fragments may become motile through a morphological instability that couples shape to movement via polymerization forces at the boundary and the actin hydrodynamics, even without molecular motors [Blanch-Mercader2013].

The question that now arises is whether, at larger scales, cell monolayers can also exhibit spontaneous motility driven by morphological symmetry breaking. An indication of this has been observed in [Beaune2018] with the so-called giant keratocytes (Fig. 5.1c). In those experiments, a monolayer becomes morphologically unstable. Still, the motility is achieved through the formation of a large 3D structure that implies a global polarization of the system, akin to unicellular keratocytes. Whether an arbitrarily shaped monolayer can be spontaneously motile without a global polarization, such as in the case of the previously mentioned lamellar fragments, is a nontrivial question. The physics of monolayers

is fundamentally different from that of lamellar fragments, which is driven by actin polymerization. Unlike actin gels, monolayers involve supra-cellular organization and coordination among cells within the tissue. Without the global head-tail polarization of giant keratocytes, it remains unclear whether cells in a monolayer, following only the endogenous cues that impose outward orientation at the periphery, can sense the overall shape of the monolayer cluster and coordinate their motion to generate sustained motion.

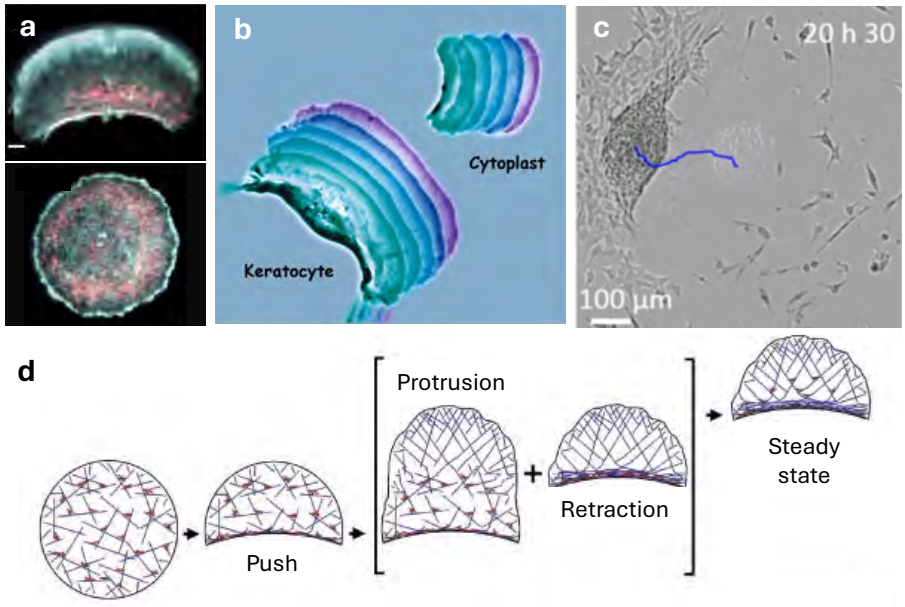

Figure 5.1: Examples of spontaneous motility. a Fluorescence image of the cytoskeletal organization of a moving (top) and a stationary (bottom) fish erpidermal keratocyte fragment, where myosin II distribution is labeled in red and actin in cyan. Scale bar, 2 μm. From [Verkhovsky1998]. **b,** Overlays of phase contrast images taken every 15 s showing the motility of a keratocyte and a cytoplast (keratocyte fragment lacking the nucleus). Time from turquoise to violet. From [Pollard2003]. **c,** Trajectory of an aggregate of murine sarcoma cells expressing E-cadherins at their surface, from [Beaune2018]. **d,** Model for the polarization and propagation of directional locomotion. A discoid, non-polarized cytoplast is pushed at one side, which results in the accumulation of actin filaments and clusters of myosin filaments into a bundle along the deformed edge. This favors its retraction, but protrusion continues at the opposite edge, reinforcing functional asymmetry. Protrusion and retraction occur simultaneously at opposite edges in the steady state. From [Verkhovsky1998].

Directed collective migration may naturally emerge if some external symmetry-breaking process generates a preferential direction, and if the dynamics tend to at least maintain or reinforce it. As explained in the general introduction (Section 1.1.2 and Section 1.2.2), this symmetry breaking can happen through the interaction with an external field, like the morphogen concentration in chemotaxis, or the substrate rigidity in durotaxis. Otherwise, it can be generated intrinsically, through concentration gradients inside the tissue, or via shape asymmetries. Given that monolayer edges are morphologically unstable, spontaneous morphological symmetry breaking might be expected in the presence of noise. However, under what circumstances the cell interactions alone may themselves transmit information on the cluster shape so that an organized global motion is sustained remains unclear. We note that in contrast to the guidance of an external field, which typically acts individually on each cell, shape-sensing motility, in this case, would be an inherently collective phenomenon.

All in all, this chapter aims to explore how morphological symmetry breaking can drive collective migration in cell monolayers, identifying the shapes and conditions that optimize this behavior. To this end, we perform experiments tracking the migration of monolayers, patterned with different initial configurations. Monolayers are modeled as active polar fluids under the same framework of previous chapters, and predictions from the theory, developed by Joan Térmens in our group (UB, Barcelona), are explained in Section 5.2. They motivated the search for this phenomenon in the experiments. In Section 5.3 we outline the experimental protocol, to then focus on the results and comparison between both in Section 5.4.

5.2 Spontaneous motility of monolayer clusters

Building on the same active matter framework as in Chapters 2–3, cell monolayers are modeled as continuous active polar fluids, coarse-grained at scales larger than the cell size. The ingredients of the model can be recalled in Section 2.2, but now, instead of the symmetric monolayers, like the circles or stripes in previous chapters, we want to consider the shape perturbations of a circle. Any small linear perturbation can be classified according to its Fourier mode (Fig. 5.2). In our active drop model, the zeroth mode captures the spreading-retraction dynamics, the first mode describes a displacement of the circle and is thus marginal—consistently with translational invariance—, and the second and higher-order modes may be unstable, as shown in [Pérez-González2019]. However, only the first mode (displacement) has a single symmetry axis, as required to define a preferred direction. Since this mode is marginal, the only way to gen-

erate motion must involve the coupling of different modes, which can only occur at the nonlinear level. Accordingly, the possible instability of circles into motile shapes is necessarily nonlinear, as in the case of lamellar fragments [Blanch-Mercader2013]. We will not pursue here an extension of the weakly nonlinear analysis of [Blanch-Mercader2013]. Instead, we will consider large perturbations deeply in the nonlinear regime. Specifically, on circles cut out on one side with chords of different lengths and rounded edges (Fig. 5.3).

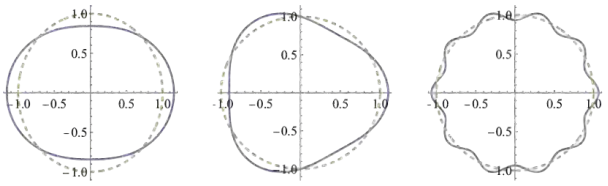

Figure 5.2: Linear perturbations of a circle. Second, third, and tenth modes of linear perturbations of the circle, with $\delta R = \lambda/2, \lambda/3, \lambda/10$ respectively. The zeroth mode corresponds to modifying the area of the circle, the first to translations of the circle's center, and the following ones to periodic deformations: the second mode gives ellipses, the third one shapes with 3-fold symmetry, etc.

In Chapter 2 (Section 2.3.1), we reduced the system to an effective 1D setup because the goal was to study the effect of a stiffness gradient in one direction. Now, however, we want to elucidate the relationship between the shape of the monolayer cluster and its spontaneous migration, so we must keep the two dimensions. The model equations have been presented in Eq. 2.6, Eq. 2.9, Eq. 2.14 and Eq. 2.15, but we recall them again here. For a simply connected domain, $\Omega(t)$, the evolving polarization p_α and velocity v_α fields must fulfil for all times,

- Polarization: $L_c^2 \nabla^2 p_\alpha = p_\alpha$. (5.1)
- Force balance: $\partial_\beta \sigma^s_{\alpha\beta} + f_\alpha = 0$. (5.2)
- Stress tensor: $\sigma^s_{\alpha\beta} = \eta(\partial_\alpha v_\beta + \partial_\beta v_\alpha) - \zeta p_\alpha p_\beta$. (5.3)
- External force density: $f_\alpha = -\xi v_\alpha + \zeta_i p_\alpha$. (5.4)

Because the edges are free to deform and move, the problem at hand is a free boundary problem. Being $\hat{n}_\alpha$ the unit (outward) normal vector along the boundary of the domain, $\partial\Omega(t)$, the boundary conditions for all times read,

- Normal polarization: $p_\alpha = \hat{n}_\alpha$. (5.5)
- Stress-free: $\hat{n}_\alpha \sigma^s_{\alpha\beta} = 0$. (5.6)
- Kinetic condition: $v_{\alpha,n} = v_\alpha \hat{n}_\alpha$. (5.7)

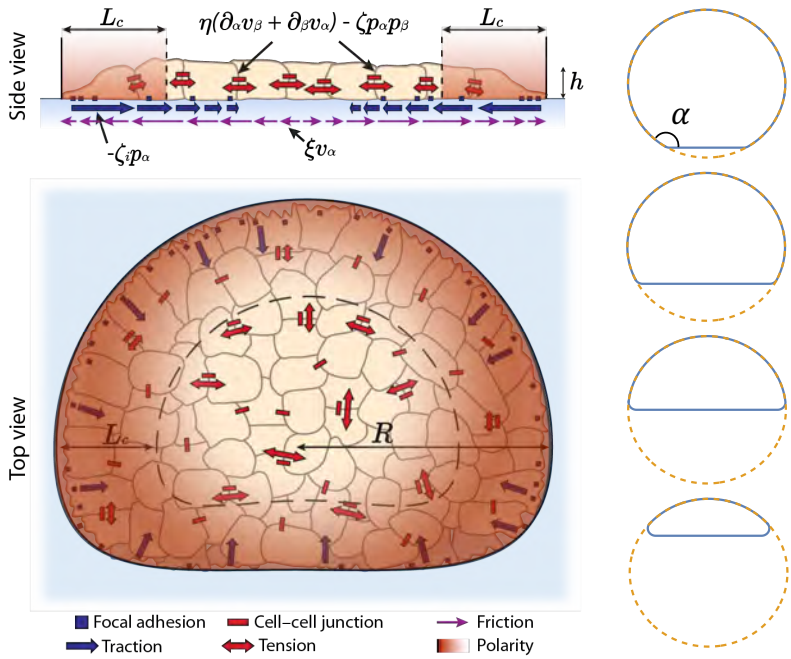

Figure 5.3: Sketch of the model for uniaxial monolayers. Active polar fluid model for the considered uniaxial monolayer clusters, with the same ingredients as in Fig. 2.3. Adapted from [Pérez-González2019]. On the right, the angle defining the cut on one side of the circle is $\alpha = 150, 120, 90, 60°$ (from top to bottom).

For simplicity, we are neglecting a possible contribution due to surface tension. This could be easily incorporated in Eq. 5.6. The kinetic or continuity condition (Eq. 5.7) allows us to relate the boundary velocity of the monolayer with the normal component of the velocity profile at that boundary, and thus defines the motion of the edge. This same model was well studied in a 2D circular monolayer of radius R in [Pérez-González2019]. There, assuming radial symmetry, the model was analytically treatable, and a transition between monolayer spreading and retraction—or wetting and dewetting—was defined, as explained in Section 1.3.2 from the general introduction. However, in the current asymmetrical shapes, both the polarization p_α and the velocity v_α fields cannot be solved analytically.

A numerical approach based on finite-element techniques is used for the simulations. The cluster domain is represented by an unstructured triangular mesh that is denser at the boundary layer (width of approximately L_c from the boundary) and more sparse at the center, in order to handle the curved and sharp

boundaries better. The iteration consists on:

1. Solve a weak form for the polarization (Eq. 5.1 and Eq. 5.5, with a fine implementation of the Dirichlet condition).
2. Solve a weak form for the velocity (Eqs. 5.2–5.4 and Eq. 5.6, substituting the polarization field from step 1).
3. Compute the next boundary configuration, by applying the kinetic condition (Eq. 5.7) to the vertices of the actual one and interpolating with splines. Then, generate a new adaptive mesh and go back to step 1.

By selecting the initial monolayer shape and a range of model parameters, we can obtain their time evolutions, which enables us to classify the modes of migration based on the different conditions. While some aspects of these dynamics are shown and discussed in Section 5.2.2, the key to understanding the mechanism of the spontaneous migration lies in analyzing the center-of-mass velocity, which is addressed in the following section.

5.2.1 Center-of-mass velocity

We describe monolayer clusters as 2D shapes and represent vectors using bold symbols to simplify the notation. To describe the spontaneous migration we are primarily interested in the center-of-mass velocity, $\mathbf{V_{CM}} \equiv \dot{\mathbf{R}}_{\mathbf{CM}}$, where $\mathbf{R_{CM}} \equiv \frac{1}{A}\int_\Omega \mathbf{r}\, dS$. Since the total area $A \equiv \int_\Omega dS$ changes, at any time instant the center-of-mass velocity is given by the exact expression[1]

$$\mathbf{V_{CM}} = \frac{1}{A}\left[\int_\Omega \mathbf{v}\, dS + \int_\Omega (\mathbf{r} - \mathbf{R_{CM}})\,(\nabla\cdot\mathbf{v})\; dS\right]. \tag{5.8}$$

The first term of the rhs is actually the integral of the polarization field, since using the divergence theorem when integrating Eq. 5.2 over the domain, and with the stress-free boundary conditions (Eq. 5.6), we get

$$\int_\Omega (\nabla\cdot\sigma^{\mathbf{s}})\; dS = \int_{\partial\Omega} (\sigma^{\mathbf{s}}\cdot\hat{\mathbf{n}})\; dS = 0 \rightarrow \int_\Omega \mathbf{f}\, dS = 0. \tag{5.9}$$

With Eq. 5.4 we have,

$$\int_\Omega \mathbf{v}\, dS = \frac{\zeta_{\mathrm{i}}}{\xi}\int_\Omega \mathbf{p}\, dS. \tag{5.10}$$

[1] The derivation of this formula is obtained by using the divergence theorem $\int_\Omega \nabla\cdot\mathbf{F}\, dS = \int_{\partial\Omega}\mathbf{F}\cdot\hat{\mathbf{n}}\, dS$ (being $\mathbf{F}$ a continuous differentiable vector field), and also that $\frac{d}{dt}\int_\Omega \mathbf{F}\, dS = \int_{\partial\Omega}\mathbf{F}(\mathbf{v}\cdot\hat{\mathbf{n}})\, dS$. Therefore, the change of the area is given by $\frac{dA}{dt} = \frac{d}{dt}\int_\Omega dS = \int_\Omega(\nabla\cdot\mathbf{v})\, dS$.

Plugging it in Eq. 5.8, we obtain

$$\mathbf{V_{CM}} = \frac{1}{A}\left[\frac{\zeta_\mathrm{i}}{\xi}\int_\Omega \mathbf{p}\, dS + \int_\Omega (\mathbf{r} - \mathbf{R_{CM}})\,(\nabla\cdot\mathbf{v})\; dS\right]. \tag{5.11}$$

Recalling that the polarization field is given by Eq. 5.1 (with the boundary condition from Eq. 5.5), Eq. 5.11 immediately provides some insights in simple cases. For instance, for an incompressible flow ($\nabla\cdot\mathbf{v} = 0$) or for a spreading flow at a uniform rate ($\nabla\cdot\mathbf{v} = \alpha(t)$[1]), the second term of the rhs of Eq. 5.11 vanishes. In general, the second term is also relatively small in situations where the area is not changing significantly, such as close to the active spreading transition. Since the correction due to the second term is more difficult to interpret, for the purpose of discussion and analysis, it is useful to consider the first term as a good estimate of the center-of-mass velocity. In this approximation, the center-of-mass velocity is basically proportional to the integral of the polarization, and so the whole domain moves as if the total traction was pulling against a global friction coefficient $A(t)\xi$.

However, whether or not the integral of Eq. 5.10 is finite is not trivial, since it depends on the domain shape. Because $\int_{\partial\Omega}\hat{\mathbf{n}}\; ds = 0$, if L_c is very small—representing a thin peripheral boundary layer where polarization, and thus traction, is localized—, there is no significant movement of the center of mass ($\lim_{L_c\to 0}\mathbf{V_{CM}} = 0$, including also the second term, since in this limit $\nabla\cdot\mathbf{v} = \alpha$). To have a finite velocity, we need both a finite L_c, smaller but comparable to the characteristic size of the shape, and an asymmetry in the shape that can establish a head-tail polarity. If both conditions are achieved, contour lines along the polarized boundary layer with constant $|\mathbf{p}|$ will have a non-normal component of $\mathbf{p}$, and contour lines that are normal to $\mathbf{p}$ will have non-constant $|\mathbf{p}|$. Therefore, one may expect a non-zero value of the total traction force, and thus a positive center-of-mass velocity, $\mathbf{V_{CM}} \neq 0$. The mechanism for the motility is better explained in the next section, with the classification of the migratory modes.

We note that $\mathbf{V_{CM}} \neq 0$ for a given shape does not imply that the motion will be sustained since the shape will also evolve, and it can do so in the direction to either increase or decrease the speed. This will depend on the dynamical equations and on the model parameters. In Fig. 5.4, we show two examples of dynamical evolutions where the shape feedback is positive, yielding an accelerating motion.

[1] Which would correspond to a uniform thinning of the monolayer $\dot{h}/h = -\alpha(t)/2$.

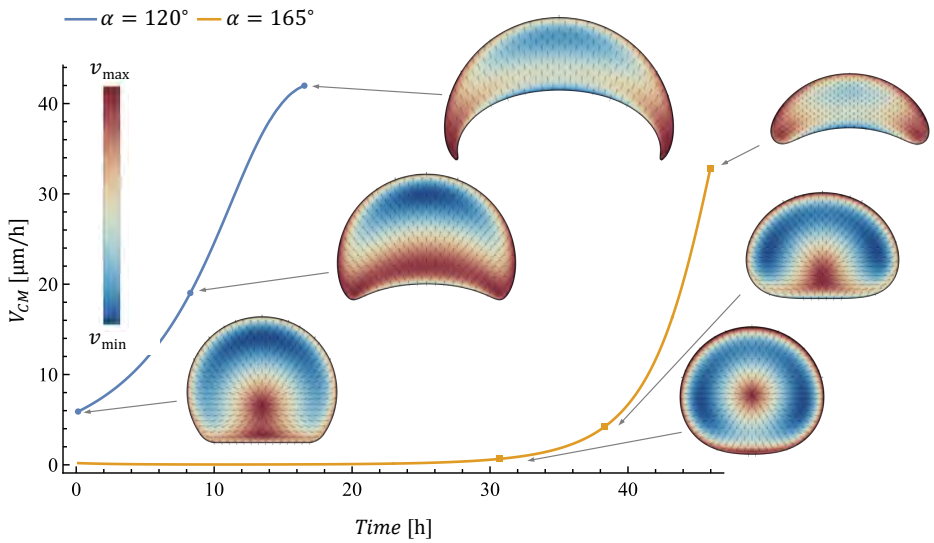

Figure 5.4: Temporal evolution and spontaneous motility of monolayers. Evolution of the center-of-mass velocity and shape of the monolayer in two initial configurations, with angles $\alpha = 120°$ and $165°$, and effective radii (radius that a circle of the same area would have) of $R_0 = 166.6$ μm and 145 μ respectively. These were finely tuned to ensure that the simulations stayed close to the spreading-retraction transition during the initial stages. The color map and the black arrows represent the velocity field. Parameters lie within the ranges estimated in [Pérez-González2019], with $h = 5$ μm, $\eta = 25$ MPa·s, $\xi = 0.1$ kPa·s/μm^2, $\zeta_i = 0.1$ kPa/μm, $\zeta = -20$ kPa. $L_c = R_0/4$ to simplify the simulations, and simulation time is $\Delta t = 200$ s.

5

5.2.2 Collective migration modes

In addition to the prediction of a finite $\mathbf{V_{CM}}$, we are interested in knowing the evolution of the shape to elucidate whether this provides a positive feedback that sustains or even accelerates the motion. To do so we will characterize the different propagation modes that are compatible with a given center-of-mass velocity. By performing multiple simulations, we see that spontaneous motility is indeed generic. The symmetry-breaking shapes that have a larger effect in terms of the motion of the center of mass are the ones with $\alpha \geq 90°$ (as in Fig. 5.4), since those with $\alpha < 90°$ are closer to ellipses and end up triggering the second mode of the linear perturbations, with clusters elongating more than collectively migrating. A fine-tuning of the parameters of the model is needed to get simulations in which the area of the clusters does not change much because if it does, the other effects get hindered (L_c is every time smaller compared to the

size and the center-of-mass velocity decreases). Four modes of collective motility are identified and depicted in Fig. 5.5.

In the absence of contractility $\zeta = 0$ and with a very small L_c, the clusters either display a constant front velocity (in the dry regime[1], Fig. 5.5a) or an isotropic spreading (in the wet regime, Fig. 5.5b), but their center of mass remains stationary ($\mathbf{V_{CM}} = 0$). Both situations are quite trivial: In the dry limit, cells at the edge are insensitive to the cluster's shape and $\mathbf{v} \approx 0$ in the bulk, and so despite the change in shape and size, the center of mass is not displaced because the total traction force vanishes. In the wet limit, the cells' behavior depends solely on their relative position to the center of mass, and since the shape is preserved, with $\nabla \cdot \mathbf{v} = \alpha(t)$, the center of mass does not move.

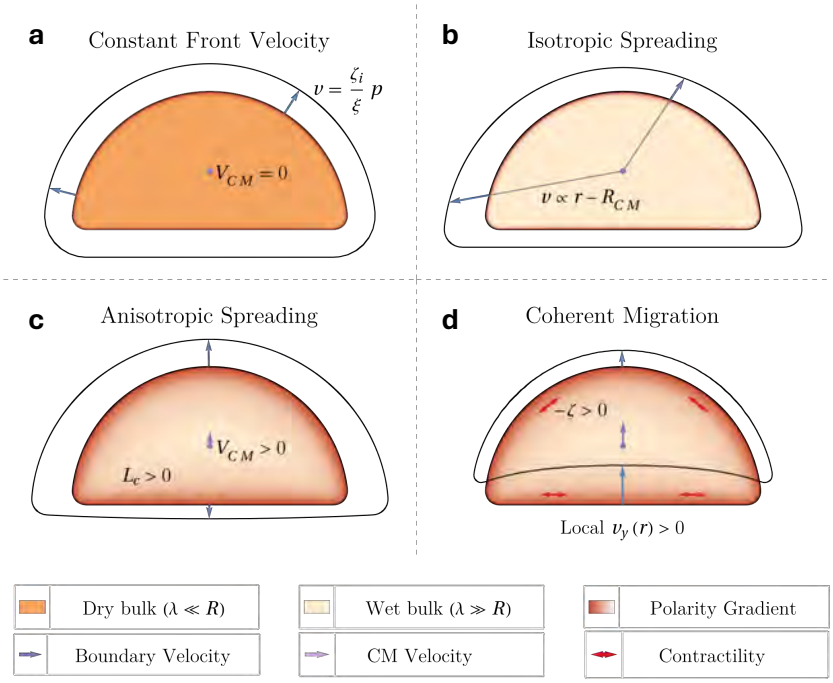

Figure 5.5: Classification of migration modes. Four types of collective migration are identified depending on the model parameters. If L_c is very small, $\mathbf{V_{CM}} = 0$ both in the dry (**a**) and wet regimes (**b**). In the dry regime, the front velocity is constant, whereas in the wet regime, the expansion preserves the cluster's shape. In the wet regime and for larger L_c, then $\mathbf{V_{CM}} > 0$, yielding to anisotropic spreading when the contractility is not sufficient (**c**), or to coherent migration when this contractility is larger (**d**).

[1]Recall the definitions of dry and wet regimes in Section 2.3.1.

As L_c increases within the wet regime, but still in the absence of contractility, the center-of-mass velocity becomes positive ($\mathbf{V_{CM}} \neq 0$), with $\nabla \cdot \mathbf{v}$ not uniform (Fig. 5.5c). The cells now respond to non-local hydrodynamic interactions and non-local alignment interactions, and the velocity profile along the edge is sensitive to the overall shape. Vortices of opposite directions appear at the bottom corners (Fig. 5.6(1)), which generically generate a net displacement if there is a global head-tail asymmetry. In the polarized boundary layer, velocity and polarization are aligned ($\mathbf{v} \cdot \mathbf{p} > 0$), and the front and rear spread at different velocities, which gives place to anisotropic spreading.

Lastly, coherent migration of the entire cluster (Fig. 5.5d) only occurs when contractility is large enough to be close to the spreading transition (defined in Section 1.3.2) so that the area is not changing significantly. The combination of both active forces—active traction and contractility—in the boundary layer, produces an overall displacement of the cluster, with the rear edge retracting because the velocity and the polarization are antiparallel ($\mathbf{v} \cdot \mathbf{p} < 0$), in contrast to the previous mode of anisotropic spreading. This reversal of the rear velocity comes from a reversal of the sense of rotation of the vortex couple at the bottom corners (Fig. 5.6(2)), which happens near the spreading transition. This coherent migration is not a flocking transition because the system remains unpolarized in the bulk, and although the velocity field is globally oriented, the polarization field is not, remaining oriented towards the exterior of the boundary everywhere. This is a remarkable new form of self-organization in which there is some long-range orientational order for the velocity field but not for the polarization.

Finally, although different migration modes were found for semicircles, simulations were conducted using initial shapes other than the uniaxial cut circles to explore the full range of dynamic behaviors. An example is presented in Fig. 5.7, where the clusters exhibit rotation rather than spontaneous motility. These results motivated to include rotation patterns in the experiments, although they were finally not analyzed.

In summary, the theoretical predictions reveal a strong link between morphology and collective migration in cell monolayers that are not globally polarized. This connection arises from the interaction between cluster morphology (both shape and size), active forces, and an anisotropic velocity field. We emphasize that, besides the morphological asymmetry, a finite range of the aligning interactions (finite L_c) is necessary to generate global motion. These results provide a clear motivation for experiments, aimed at validating the presence of this rich migratory phenomenology. The distinction between the isotropic and the anisotropic spreading will be the focus of attention in the experimental sections, as discussed below.

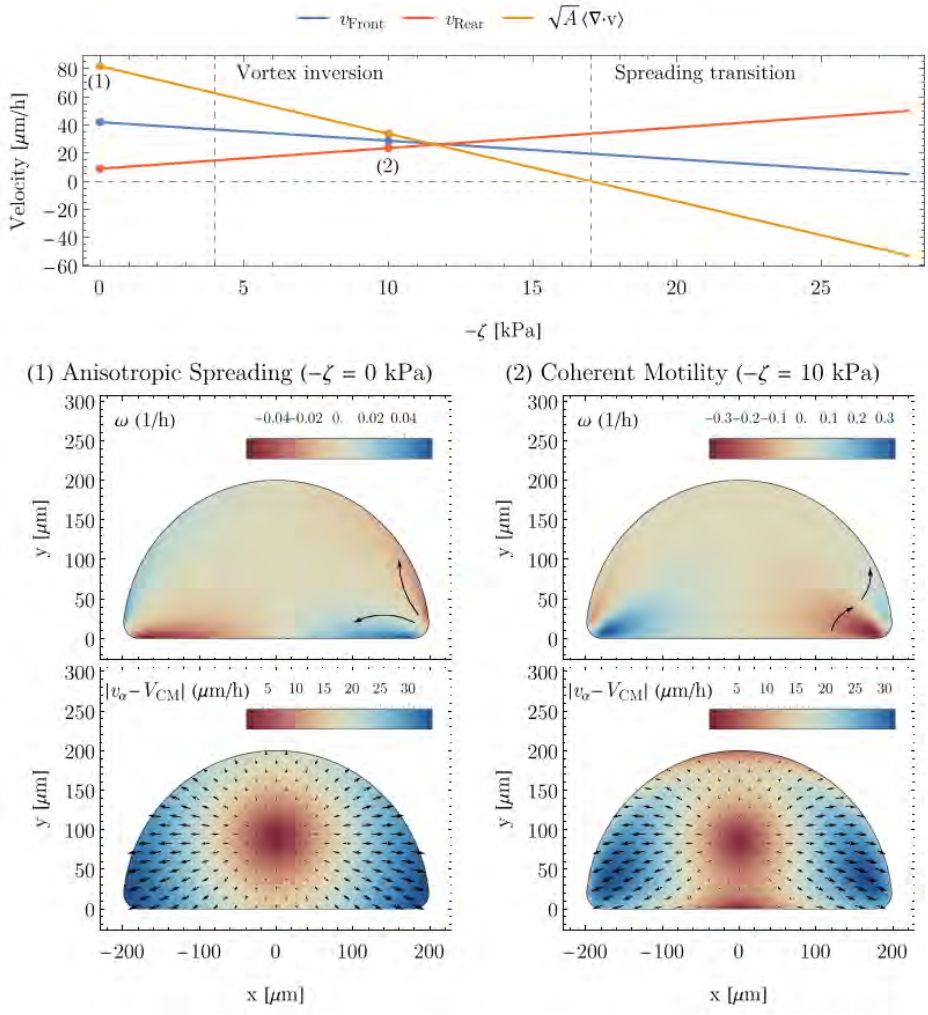

Figure 5.6: Effect of contractility in the migration modes. Front, rear, and spreading velocity as a function of contractility. The yellow line shows the evolution of the area, since $\sqrt{A}\langle\nabla\cdot\mathbf{v}\rangle \equiv \sqrt{A}\int_\Omega(\nabla\cdot\mathbf{v})dS = \sqrt{A}\dot{A}$. When contractility is increased, the sense of direction of the bottom vortices is reversed (vorticity ω shown in the top snapshots of panels (1) and (2)), bringing the anisotropic spreading mode (1) to a coherent migration mode (2), in which the rear edge retracts instead of spreading (velocity corrected with the CM velocity in the bottom snapshots). For even larger contractilities, the spreading transition is achieved and the area starts decreasing, shown when the yellow line in the plot becomes negative.

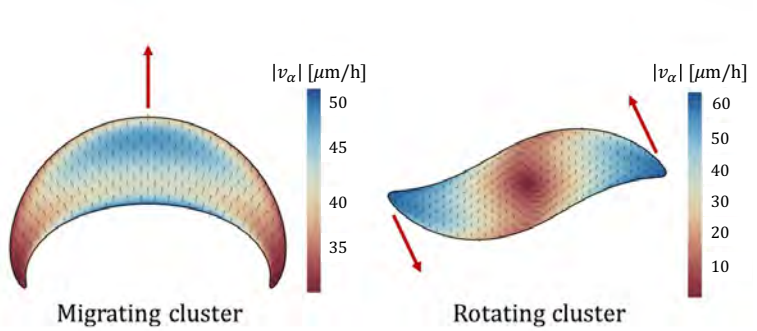

Figure 5.7: Design of migrating and rotating clusters. Different shapes that give either migrating or rotating dynamics. The color code shows the magnitude of the velocity field, and the black lines represent the velocity vectors.

5.3 Materials and methods

The goal is to pattern cell monolayers with shapes similar to those used in the simulations, exhibiting asymmetry along the front-rear axis while maintaining left-right symmetry. A widely used method for cell patterning involves polydimethylsiloxane (PDMS) membranes or stencils, as employed in several previous studies [Wang2002, Poujade2007] and extensively used within our group [Serra-Picamal2012, Sunyer2016, Uroz2018]. These membranes feature some designed empty regions where cells adhere, confining the initial monolayer shapes to the desired geometry. Once the membranes are removed, cells are free to migrate (Fig. 5.9). In this section, we outline the experimental protocol used to conduct these experiments and detail the methods for analyzing the resulting data.

5

5.3.1 Fabrication of PDMS membranes

To fabricate the PDMS membranes, a master mold with the desired raised structures is created using soft photolithography. First, a thin layer of SU-8 negative photoresist is spun onto a glass wafer. The desired features are designed and printed onto an acetate mask (ordered from JD-Photodata, layout in Fig. 5.8). This mask is aligned with the SU-8-coated wafer and exposed to UV light. The regions exposed to UV undergo cross-linking and remain attached to the glass slide, while the unexposed areas remain soluble and are washed away during the development process. The resulting master wafer contains raised cross-linked photoresist structures, which can be reused multiple times with proper cleaning and storage. This process is performed by the MicroFabSpace service at IBEC's

Core Facilities.

Next, uncured PDMS, mixed in a 10:1 ratio of base to cross-linker, is poured onto the master and spin-coated to a thickness below the height of the SU-8 features (∼100 μm), in order to produce the stencils. We use a single step of 1 minute at 600 rpm for spinning. The coated masters are left overnight and then cured for one hour at 95°C. For thinner membranes (∼45 μm), a thicker PDMS border is sometimes applied along the edges for easier handling. Once cured, the membranes are peeled off using tweezers and stored in ethanol until use. There were no significant differences in the experimental outcome between using different thickness stencils.

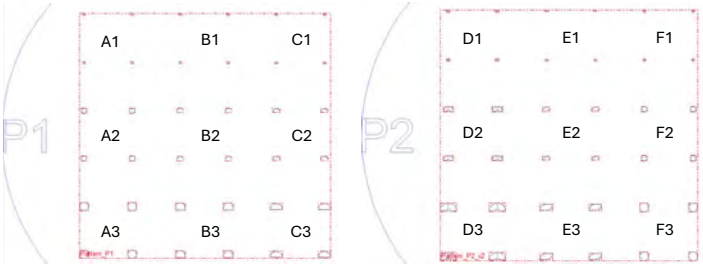

Figure 5.8: Patterns' layout in the PDMS fabricated membranes. Properties of the A-D shapes are summarized in Table 5.1. Although we ended up not analyzing neither F or E shapes, F are circles and E rotating patterns as in Fig. 5.7.

5.3.2 Preparation of PAA gels

Polyacrylamide (PAA) gels are commonly used for collective cell migration experiments due to their suitability for traction force microscopy measurements (TFM) [Kandow2007], and because they offer a more physiological environment than glass substrates. Their main advantage is that they are linear elastic materials [Storm2005], with easily tunable stiffness, which can be adjusted by varying the concentration of acrylamide and bis-acrylamide monomers [Yeung2005]. Although TFM was not performed in this study, we initially considered it, and together with the physiological relevance we opted to conduct the experiments on PAA substrates.

The preparation of PAA gels was adapted from previous protocols [Yeung2005, Kandow2007]. First, glass-bottom dishes are activated with a solution of acetic acid, bind-silane (M6514, Sigma), and ethanol, in a 1:1:14 ratio, for one hour. The dishes are washed twice with ethanol and dried via aspiration. Glass coverslips of 18 mm in diameter are treated with Repel Silane (General Electric, USA) for one hour, and then washed thoroughly in ethanol and Milli-Q water

before being air-dried. This process ensures that the gels adhere firmly to the glass-bottom dishes but not to the coverslips, making them easier to remove.

A stock solution containing a concentration of 5.5% acrylamide, 0.09% bisacrylamide, 0.5% ammonium persulphate (APS) and 0.05% tetramethylethylenediamine (TEMED) is prepared to produce 5 kPa gels. TEMED must be added last since it triggers polymerization. While different Young's moduli can be achieved by adjusting the concentrations, as detailed in [Tse2010], all the present experiments are conducted at 5 kPa because varying the stiffness is not the focus of this study. A 22.5 μl drop of the solution, to have gels approximately 100 μm thick, is placed on the center of the glass-bottom dishes. The solution is then covered with glass coverslips to evenly distribute the gel and create a flat surface. After polymerization (about one hour), the gels are immersed in phosphate-buffered saline (PBS) for several minutes, and the coverslips are carefully removed with tweezers. The gels are washed again in PBS and stored at 4°C until use.

Since PAA gels are inert materials, before using a gel for an experiment it has to be functionalized with ECM proteins to allow cell attachment and migration across it. Thus, before placing the PDMS membranes, they are incubated with a 2 mg·ml^{-1} solution of Sulfo-SANPAH in Milli-Q water under UV light (365 nm wavelength, at a distance of $\sim$ 5 cm) for 7.5 min. Excess Sulfo-SANPAH is removed with three consecutive washes of 2.5 min each: two with HEPES and one with PBS. After drying for 5 min, the gels are incubated overnight at 4°C with 100 μl of rat tail type I collagen solution (0.1 mg·ml^{-1}, Millipore). They are then UV-sterilized before cell seeding.

5.3.3 Cell culture techniques

Both MDCK (epithelial cells from the kidney tubule of an adult Cocker Spaniel dog) and MCF-10A cells (human epithelial cells from the fibrocystic breast of an adult female) are used for the study. They are cultured in Dulbecco's Modified Eagle's Medium containing high glucose and pyruvate (11995, Thermofisher) supplemented with 10% fetal bovine serum (FBS, Gibco), 1% penicillin and 1% streptomycin. Cells are maintained at 37°C in a humidified atmosphere containing 5% CO_2.

5.3.4 Cell patterning on the gels

Before performing the experiment, the PDMS stencils are passivated to prevent disruption of the protein coating on the gel during stencil removal. They are air-dried and then incubated in a 2% Pluronic acid F-127 solution in PBS for one hour. After incubation, they are washed twice in PBS and dried thoroughly

for 20 min. Meanwhile, the collagen-coated PAA gels are washed twice with PBS and completely dried by aspiration for no more than 8 min. Passivated PDMS stencils are carefully placed on the center of the gels, as seen in the first step of the schematics of the procedure in Fig. 5.9. Then, little drops with densities around $750 \cdot 10^3$ cells/ml are placed on top of the stencils, trying to remove the air bubbles from the openings. After 30 min, the unattached cells are washed away and fresh medium is added. Cells settle into the patterns and attach to the gel only at the openings of the stencils. Once they reach confluence (typically between 10 and 20 h), the stencil is peeled off, allowing the cells to migrate freely over the surrounding space.

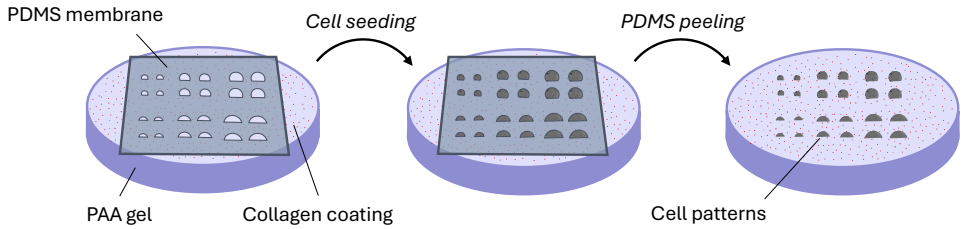

Figure 5.9: Steps of the PDMS membrane patterning assay. Inspired by the schematic figures in [Serra-Picamal2012, Pérez-González2019].

5.3.5 Time-lapse microscopy

As soon as the confinement is released, the samples are transferred to the microscope, and time-lapse imaging typically begins about an hour after the release. Multidimensional acquisition routines are carried out on an automated inverted microscope (Nikon Eclipse Ti) equipped with thermal, CO_2, and humidity control, operating with the MetaMorph software. The image acquisition interval is set to 15 min, with each experiment typically running for at least 14 h. Images are captured using a 10X 0.3 NA objective, and an automated stage is employed to capture multiple positions, selecting only the good monolayer patterns. Phase contrast images of the migration of the monolayers are then saved for subsequent analysis.

5.3.6 Analysis techniques

Custom-made MATLAB scripts, integrated with Fiji software plug-ins, are used to process phase contrast images. The analysis pipeline proceeds as follows:

1. **Selection of the good samples**: Several samples, despite being imaged, are not suitable for analysis due to various experimental issues. One of the main encountered problems is significant peeling of the collagen layer after the PDMS stencil is removed, even with the passivation treatment. This peeling directs the migration of the monolayers toward regions with collagen, making it difficult to associate the migration patterns with the intended shape asymmetry.

   Another issue arises from the varying sizes of the shapes in the stencils. Typically, the smaller shapes become too crowded when the larger ones reach confluence and are ready for imaging. As a result, many of these shapes form 3D clusters rather than 2D monolayers, adding complexities that cannot be compared to the 2D continuous model described in Section 5.2. Additionally, some shapes remain non-confluent, with gaps or denser cell concentrations at the pattern boundaries, which act as barriers to migration. Rotation patterns are also excluded, as rotation is not observed in the experiments, and these patterns are not consistent with the front-rear displacement differences seen in the simulations for the anisotropic spreading mode.

   Finally, in some cases, the initial shape of the monolayer is lost quickly after the confinement is released, which contrasts with the behavior observed in the model. This is primarily due to cell lamellipodia guiding migration in small regions, resulting in excessive fingering and significant shape deformation.

   Examples of such discarded patterns can be found in Appendix 5.A, and the statistics for the selected samples corresponding to each pattern are presented in Table 5.1.

2. **Registration, rotation, and translation of images**: To correct for camera movement, most image stacks are registered using the "StackReg" plug-in from Fiji, with the translation mode. For samples where this yields unsatisfactory results, the "Correct3Ddrift" plug-in in the xy plane and the "DescriptorBased" plug-in with the Rigid 2D mode are applied.

   Rotation and translation of the images are performed using a custom-made MATLAB code, which identifies the center and the straight line of each shape, and then rotates them so that this line is horizontal. This ensures that the patterns are centered in the images, with their axis of mirror symmetry aligned along the vertical y-axis. An example can be found in Fig. 5.10.

3. **Segmentation**: At each time point, cell islands are semi-automatically segmented using the "EGT_Segmentation" function, developed at the National Institute of Standards and Technology. Any errors in the automatic segmentation are manually corrected by creating a mask in Fiji.

4. **Displacement computation**: As illustrated in Fig. 5.11, to average out details in both front and rear regions, we compute the area enclosed by the boundary at time t and the initial boundary at $t = 0$ h. This area is then divided by the width of the considered region (x in Fig. 5.11b), and the averaged y displacement at time t (y in Fig. Fig. 5.11b) is obtained.

Pattern type	L_x (μm)	# MDCK	# MCF-10A
A3 	202.95	3	6
B1 	96.55	3	3
B2 	241.38	8	7
B3 	386.21	13	9
C1 	141.42	3	3
C2 	353.55	5	2
C3 	565.66	7	4
D1 	183.31	2	2
D2 	458.28	7	2
D3 	733.26	6	2

Table 5.1: Statistics of the selected and analyzed patterns. Number of different patterns analyzed for each cell line (total: $N = 57$ MDCK and $N = 40$ MCF-10A). The effective radii are $R_{\text{eff}} = 50, 125, 200$ μm for sizes 1, 2, and 3 respectively. L_x refers to the length of the straight bottom line in the x direction (from the lowest left to the lowest right points). No samples were selected for the A1 and A2 patterns.

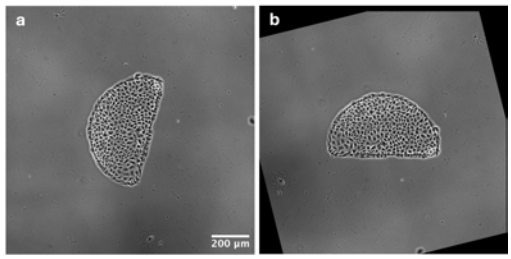

Figure 5.10: Example of the registration, rotation, and translation of samples. a, First time point of the original phase-contrast image taken of a C3 MDCK sample. **b,** Registered, rotated, and translated monolayer.

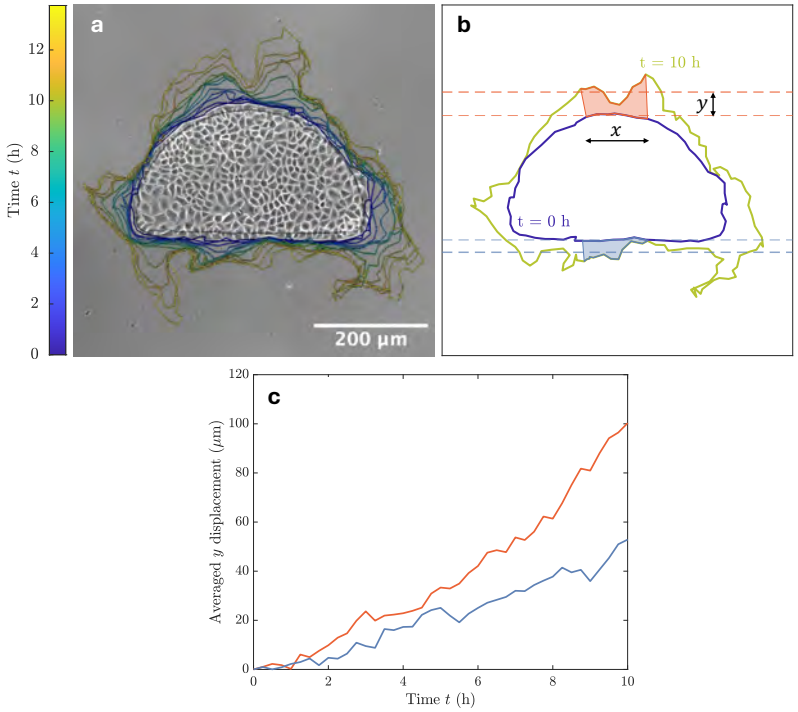

Figure 5.11: Computation of the front and rear averaged displacements. a, Phase-contrast image of an MDCK monolayer (C3 pattern), showing the evolution of the segmented mask boundaries with a color code for time (lines are every hour). **b,** Boundaries of the monolayer at $t = 0$ h and $t = 10$ h, and shaded area that is used for computing the averaged y displacement of the front and the rear. **c,** Front (red) and rear (blue) averaged y displacements over time.

After these steps, we obtain plots of the averaged y displacements in the front and rear regions for all the selected samples. These are then averaged within each pattern and cell type to calculate the displacements Δy shown in Fig. 5.12 and Fig. 5.13, as well as in all the corresponding data from Appendix 5.B.

5.4 Results: anisotropic spreading in experiments

Coherent migration of the entire tissues, with the retracting rear edge (Fig. 5.5d, with two dynamical examples in Fig. 5.4), is not observed in our experiments with prescribed shapes. A possible explanation is that the monolayers in our experiments are too far from the spreading transition, exhibiting low contractility or being too large, such that spreading always dominates over the retraction of the rear edge. To address this problem, we attempted to use other cell lines, hoping for higher contractility, and tested to enhance it with hEGF (human epidermal growth factor). However, we could not bring the monolayers closer to the spreading transition, and due to time constraints, further optimization or investigation was not possible. As a result, this mode of collective tissue migration was not observed in our controlled experiments. However, examples of this mode have been observed revisiting other experiments on durotaxis, shown in Fig. 5.14 in the discussion section.

However, we systematically observed the anisotropic spreading mode from Fig. 5.5c. Even though the isotropic spreading mode also exhibits a differential front-rear velocity, we have used our theoretical model to fit the parameter L_c, which provides the unequivocal distinction between isotropic and anisotropic spreading as defined. Indeed, our data in Fig. 5.12 shows finite values of $L_c = (35 \pm 10)$ μm, which are only consistent with anisotropic spreading, that is, with a finite center-of-mass velocity. This analysis is shown for the C3 patterns (larger semicircles) of MDCK cells, as they provide the best comparison with the simulations, both in terms of statistical consistency and the well-defined initial shapes of the 2D monolayers. Plus, among the experimental possible patterns, the semicircles were the more motile ones, according to model predictions.

In Fig. 5.13, we show the temporal evolution of the front and rear displacements when all patterns and sizes are combined, for both MDCK and MCF-10A cell lines. This approach provides improved statistics, and although the effect is reduced, a significant positive spreading displacement is still observed in both cases during the first few hours of evolution, demonstrating the anisotropic spreading mode. Note that the averaging of different shapes and sizes precludes the fitting of L_c. However, given the systematic difference between the front and rear velocity, and assuming that L_c is itself insensitive to size and shape, once

this has been unequivocally determined, we conclude that all cases correspond to anisotropic spreading. The effect is somewhat smaller in the MCF-10A samples, which we attribute to their higher surface tension, causing the monolayers to quickly lose their original shape as they attempt to revert to a circular form.

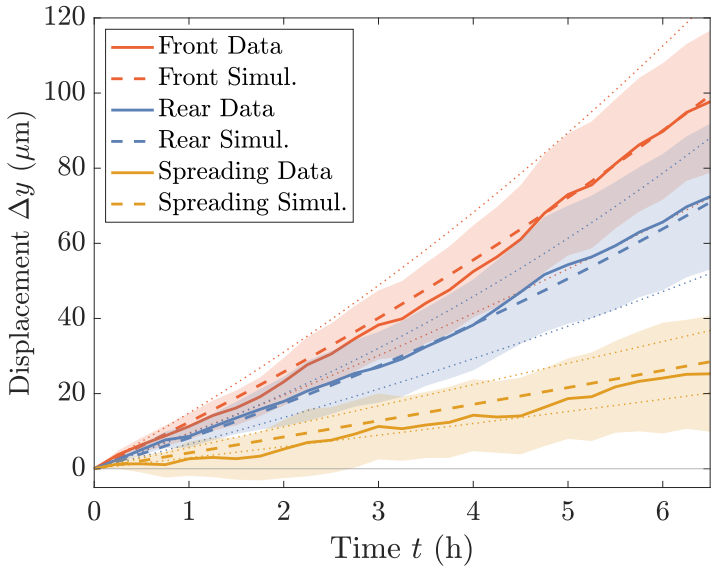

Figure 5.12: Theoretical fits for the C3 MDCK samples. Theoretical results (dashed lines) of the temporal evolution of the front (red), rear (blue), and spreading (yellow, front−rear) averaged displacements, which best fit the C3 MDCK data. Continuous lines are the experimental mean ($N = 7$), with the shaded area indicating the Standard Error of the Mean (SEM). The model parameters, $L_c = 35$ μm and $\eta = 10$ MPa·s, are selected from the theoretical curves that fit better the experimental data. Dotted lines indicate the lower and upper bounds of the theoretical fits, plotted with $L_c = 25, 45$ μm, respectively. Individual patterns and temporal evolutions for each sample are in Figs. 5.B.1–5.B.3.

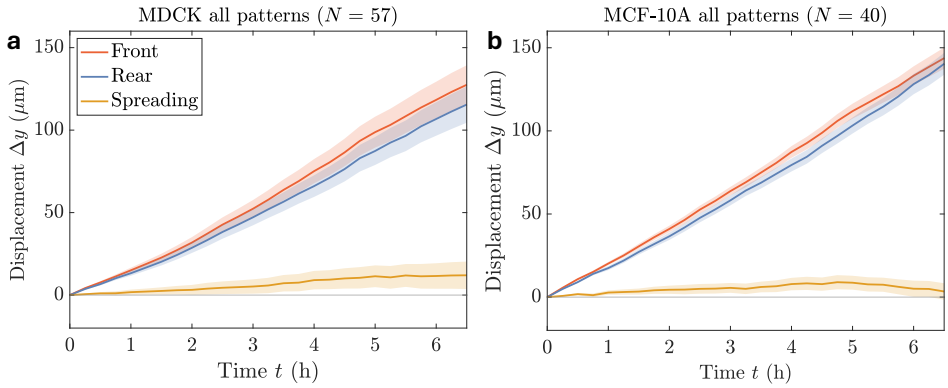

Figure 5.13: Temporal evolutions of the averaged displacements for the combined patterns. Front (red), rear (blue), and spreading (yellow, front-rear) averaged displacements when all the patterns and sizes are combined, for MDCK (**a**) and MCF-10A cell lines (**b**).

Videos 5.1: Migration of the selected samples displaying anisotropic migration. Migration of the monolayers with the segmented masks, for the MDCK and the MCF10A cell lines. To watch the videos, click here or scan the QR-code in List of videos.

5.5 Discussion and conclusions

In this chapter, we have explored the relationship between morphology and motility in cell monolayers using a model of active polar media to describe cell clusters that lack global polarization. The theory predicts several modes of spontaneous migration driven by shape-induced symmetry breaking, including steady front movement, isotropic spreading that preserves the shape, anisotropic spreading with a positive center-of-mass velocity, and coherent migration with rear-edge retraction. However, our experiments basically revealed anisotropic spreading in the monolayers. We have shown a positive spreading velocity (or displacement) and a good fit with the theory for a finite L_c, both when analyzing the semicircle patterns for MDCK cells (which closely compare with the theoretical predictions), and when combining all the pattern types and sizes.

While not aiming for a quantitative comparison with the theory, but rather as a proof of concept, in A431 clusters (human epidermoid carcinoma cells) we identified instances of spontaneous migration associated with the rear-edge retraction. In these experiments, the clusters were formed by seeding $5 \cdot 10^3$

cells in low attachment wells with starvation media for 24 h and treated with 1 ng/ml of hEGF to increase their cellular contractility. Then, they were seeded as clusters without any shape patterning. The examples shown in Fig. 5.14 correspond to clusters with initial shapes similar to those in our controlled experiments, although smaller in size. They likely exhibit increased contractility due to the preparation protocol, which may explain the observed coherent migration, potentially linked to the shape asymmetry. However, additional controlled experiments would be necessary to verify this rear retraction mode and to fully characterize other potential migratory behaviors linked to shape asymmetry in cohesive tissues.

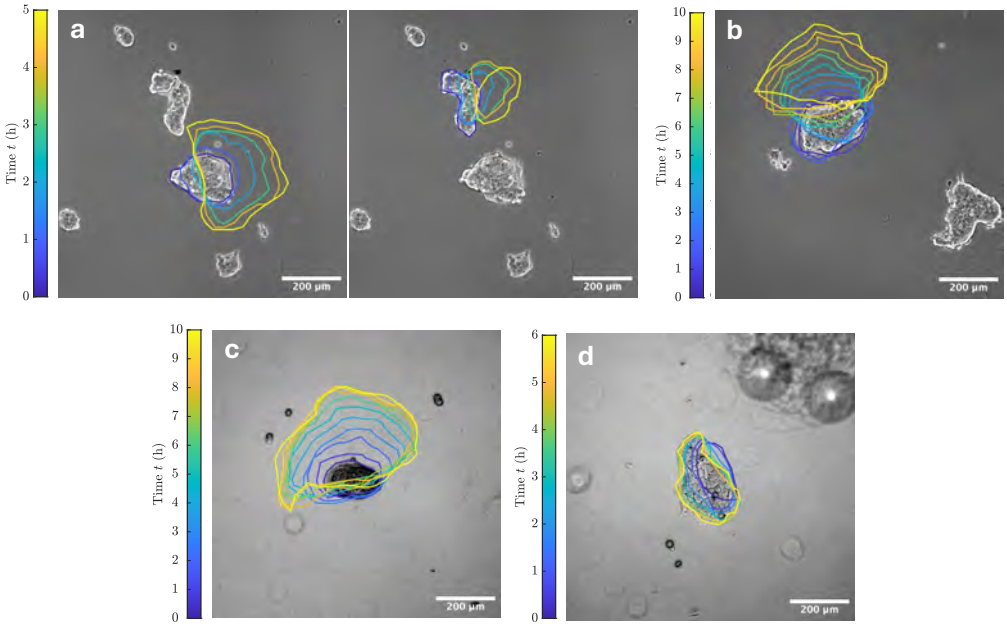

Figure 5.14: Coherent migration of A431 clusters. Phase-contrast images of A431 clusters seeded on PAA gels, showing the evolution of the manually segmented mask boundaries with a color code for time (lines are every hour). **a,b** PAA gels have a stiffness gradient increasing towards the left, but since the clusters move towards the right (**a**) or upwards (**b**), the stiffness is not directing the motion. **c,d** PAA gels have a uniform stiffness of 30 kPa. Images courtesy of Isabela Corina Fortunato, from experiments conducted in [Pallarès2023].

Videos 5.2: Migration of the A431 clusters displaying coherent migration. Migration of the A431 clusters from Fig. 5.14. To watch the videos, click here or scan the QR-code in List of videos.

Our results suggest that spontaneous migration in cell monolayers can indeed be driven by shape asymmetry, supporting the idea that cells can sense shape through the transmission of both alignment and hydrodynamic forces, without requiring any external guidance or a global polarization of the tissue. This insight has broader implications for understanding collective cell migration beyond specific cases, like the keratocytes discussed in the introduction. By elucidating when and how monolayers exhibit spontaneous motility, we better understand the underlying biophysical principles governing collective migration in epithelial tissues, which may play a fundamental role in various biological processes. In particular, in cases with external symmetry breaking, such as in durotaxis, the endogenous cues defined by the outward polarization of peripheral cells will compete with the exogenous ones defined by the external guidance due to the stiffness gradient. It is thus expected that the shape-induced motility of deformable clusters will modify or even overcome durotaxis and other guided migration modes. An example of asymmetric clusters moving against a durotactic signal is actually shown in Fig. 5.14a. This work paves the way for future studies to explore the conditions under which spontaneous migration emerges and how it interferes with external cues, contributing to the understanding of the physical mechanisms driving tissue organization and dynamics.

Contributions and acknowledgements

The work described in this chapter was a collaboration between theory and experiments. The theory development and simulations were done by Joan Térmens in our group in the Physics faculty of the UB, under the supervision of Jaume Casademunt. Ido Lavi (Biophysical Modeling, Flatiron Institute) assisted with the numerical simulations and the development of the theory.

With the help of Marija Matejčić from the "Integrative cell and tissue dynamics" group led by Xavier Trepat (IBEC, Barcelona), I conducted all the experiments and did the analysis. Therefore, Joan Térmens prepared all the figures in Section 5.2 (Figs. 5.2–5.7) and I prepared all the others from the experiments and comparison with the model (Figs. 5.8–5.13), as well as those in Appendix 5.A and Appendix 5.B. In Fig. 5.12, the theoretical fits were provided by Joan Térmens. I also prepared Fig. 5.14, but the experiments and images were courtesy of Isabela Corina Fortunato, also from Xavier Trepat's group.

I want to thank all the members in Xavier Trepat's and Pere Roca-Cusachs' groups, for all their help and expertise in the laboratory, and their interesting discussions during their group meetings. Especially, thanks to Marija Matejčić who taught me the experimental techniques and assisted in all the experiments.

Appendices

5.A Examples of discarded samples

As explained in Section 5.3.6, we discarded samples for the analysis due to various experimental issues. In Fig. 5.A.1 we show one example of each.

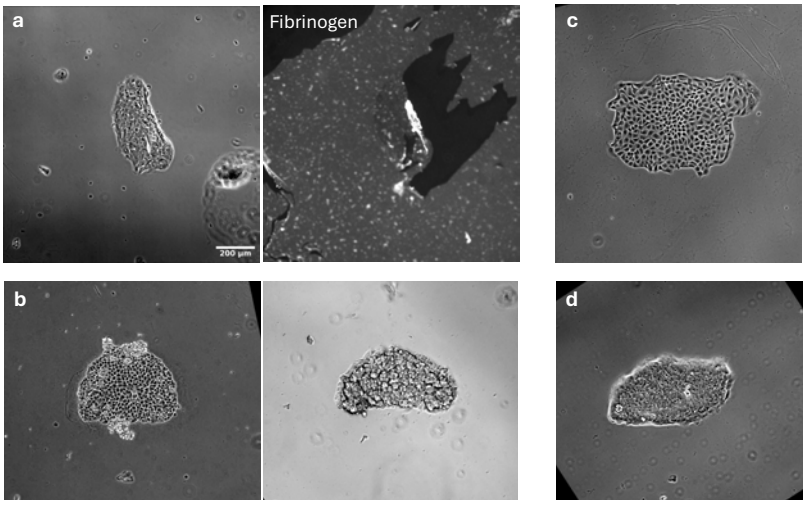

Figure 5.A.1: Examples of discarded samples. **a,** Phase contrast image of an MCF-10A sample (left) and fibrinogen fluorescence (right), which is a signature of the collagen distribution on the PAA gel. We can observe the peeling of collagen after the removal of the PDMS stencil, on the right side of the tissue. **b,** Bad initial shapes (3D and too crowded), for two MDCK samples. **c,** Bad shape evolution (fast fingering appearing, observed on the top right of the tissue), for a MDCK sample. The snapshot is at $t = 2$ h after imaging starts. **d,** Rotating pattern of a MCF-10A sample. The scale bar applies to all the images.

5.B Extended selected data

Here we show all the selected samples for the analysis. The C3 MDCK selected ones are shown in Fig. 5.B.1 and Fig. 5.B.2, and the temporal evolutions of the averaged displacements together in the same plot can be found in Fig. 5.B.3. These are the ones used in Fig. 5.12 for the fitting of the theoretical predictions.

In Fig. 5.B.4 and Fig. 5.B.5, we show the temporal evolutions of the averaged displacements for the MDCK and MCF-10A cell lines, respectively, with each panel corresponding to a different initial configuration (of shape and size). To recall the description of each pattern see the designs in Table 5.1. Averaging the data in all the panels, we obtain the evolutions displayed in Fig. 5.13.

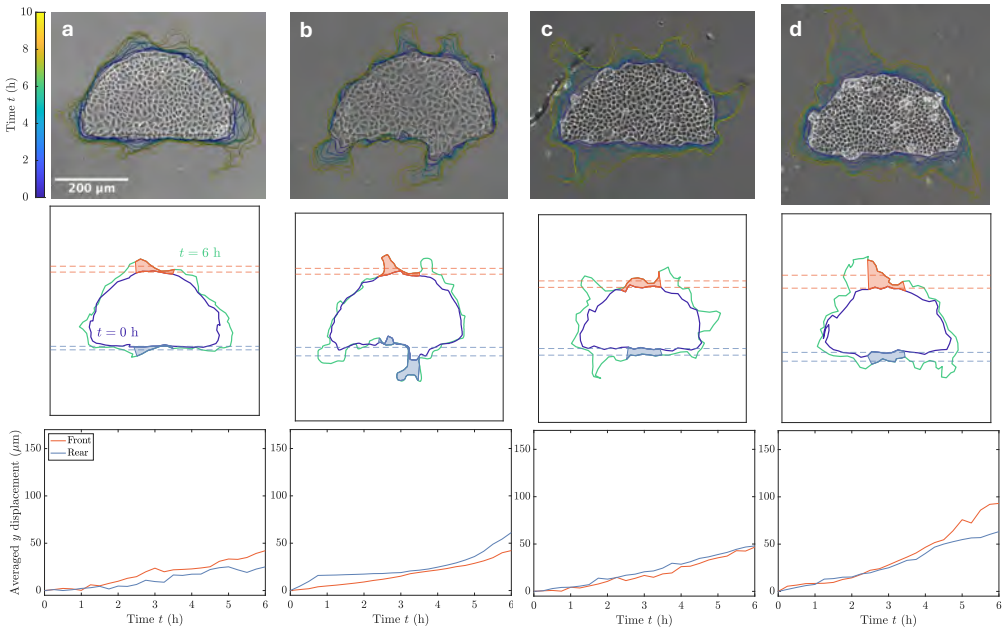

Figure 5.B.1: Selected C3 MDCK samples. Phase contrast images (first row), segmented masks at $t = 6$ h (second row), and temporal evolutions of the front (red) and rear (blue) averaged y displacements (third row). The color code in the phase contrast images represents time (lines are every hour). The three remaining selected samples are in Fig. 5.B.2.

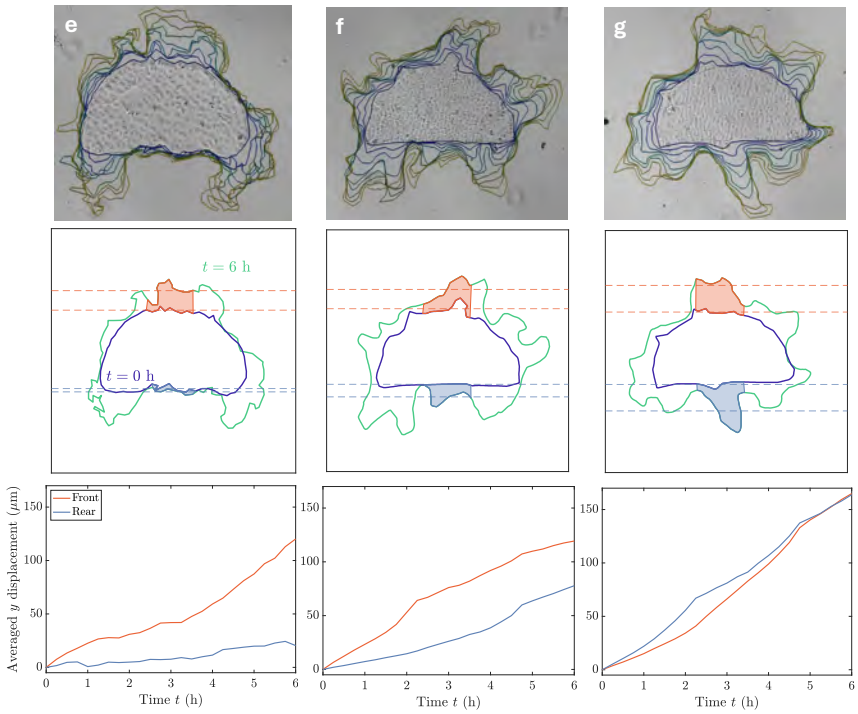

Figure 5.B.2: Selected C3 MDCK samples. Same as Fig. 5.B.1, for the three remaining selected samples.

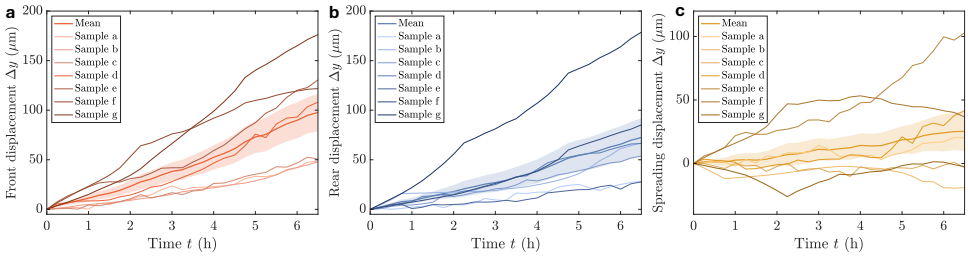

Figure 5.B.3: Detailed temporal evolutions for the C3 MDCK samples. Temporal evolution of the front (**a**), rear (**b**) and spreading (**c**) averaged displacements for the $N = 7$ selected C3 MDCK samples, which correspond to those in Fig. 5.B.1 and Fig. 5.B.2. Thicker lines represent the experimental mean, and the shaded area corresponds to the Standard Error of the Mean (SEM). It is the same data as in Fig. 5.12, but displayed in three different plots to highlight the individual evolutions of the different samples.

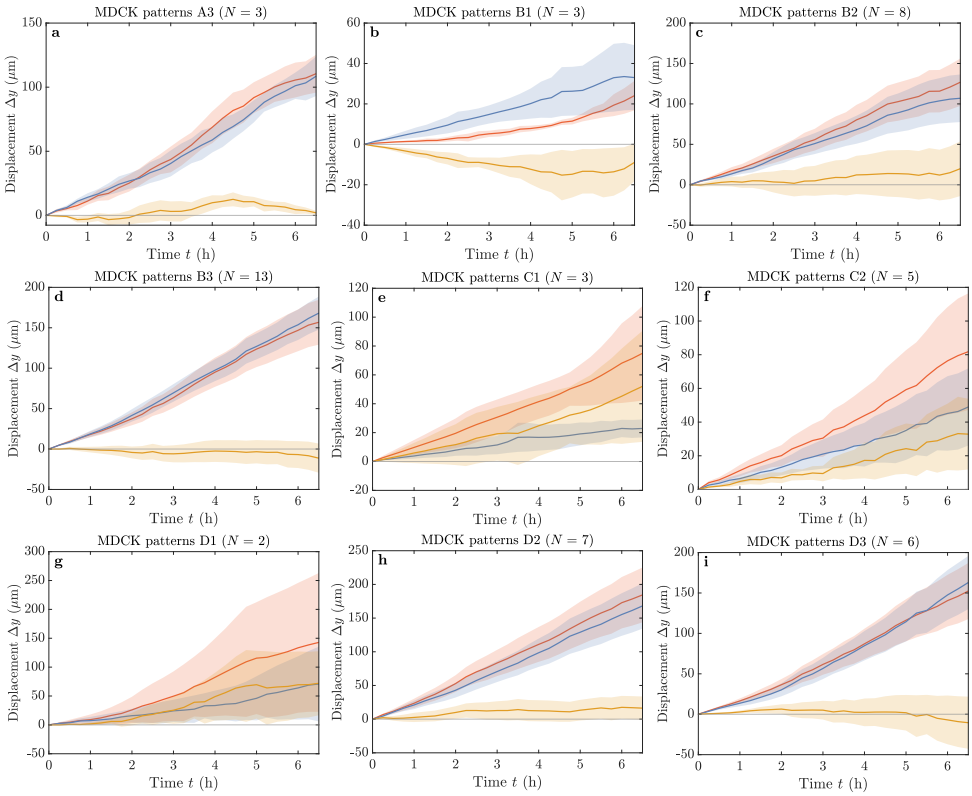

Figure 5.B.4: Temporal evolutions of the averaged displacements for MDCK patterns. Averaged front (red), rear (blue), and spreading (yellow) displacements over time, showing the mean (thick lines) and SEM (shaded area). Each plot represents a different pattern type (as indicated in the titles). The C3 patterns are omitted here, as they have already been presented separately in Fig. 5.B.3.

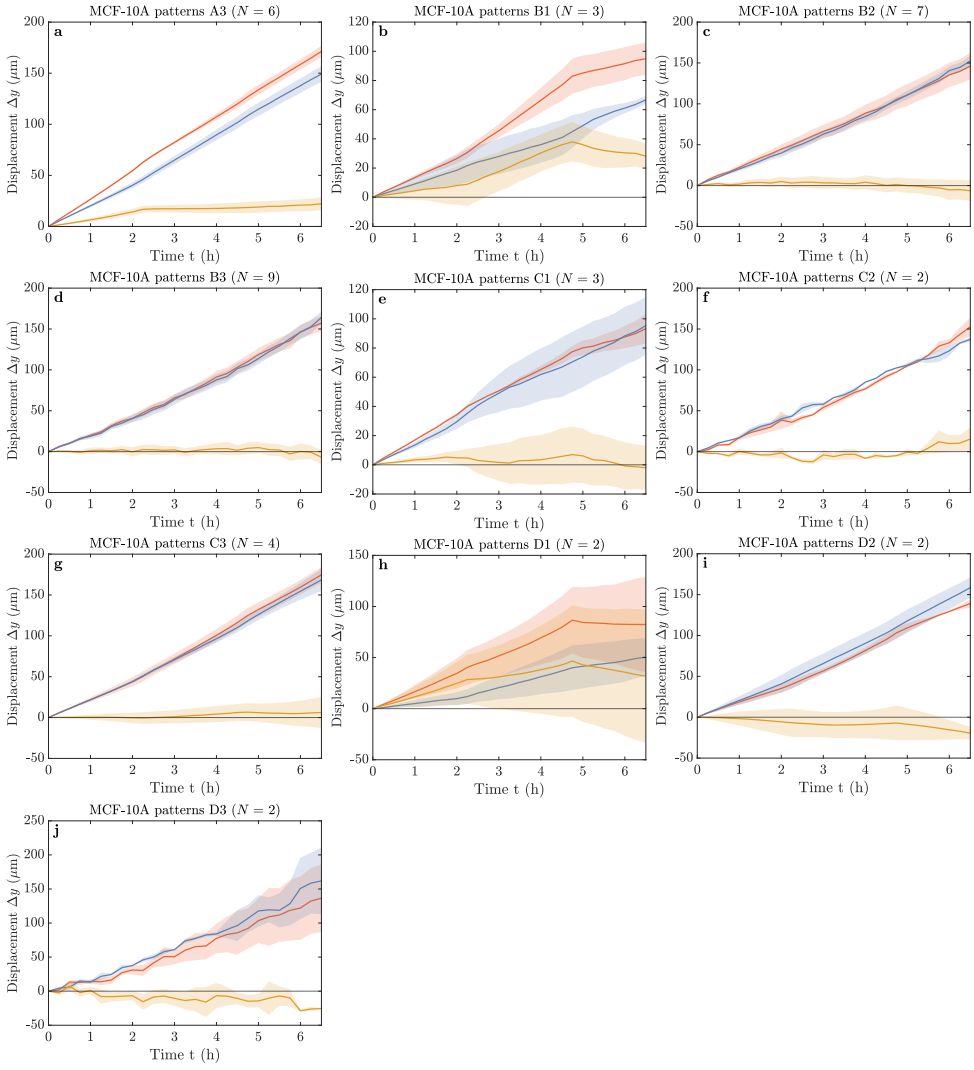

Figure 5.B.5: Temporal evolutions of the averaged displacements for MCF-10A patterns. Averaged front (red), rear (blue), and spreading (yellow) displacements over time, showing the mean (thick lines) and SEM (shaded area). Each plot represents a different pattern type (as indicated in the titles).

Chapter 6

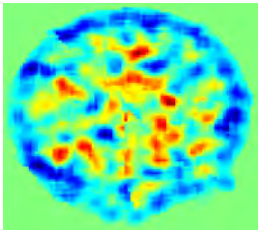

Continuum stochastic model for cell monolayers

6.1 Introduction

Throughout the previous chapters, we have exploited the hydrodynamic approach to model living tissues as active polar fluids. However, we have not accounted for the inherent randomness of biological systems, which is very apparent in the monolayer experiments here considered, both in the behavior of bulk fields and in the dynamics of tissue edges, as clearly manifest in the fingering instabilities encountered in the preceding chapter. Several authors have already developed more or less general formulations of continuum models with explicit fluctuations in the context of confluent tissues, such as in [Killeen2022, Armengol2024]. This chapter addresses the formulation of different phenomenological Langevin-like stochastic models as a first step towards a fluctuating hydrodynamic theory of tissues. At this stage, our approach is adapted to the type of *in vitro* experiments that we have already modeled throughout this thesis and their precedents, for which we have the raw data from traction measurements, so that we can directly test the different stochastic models and try to infer the noise parameters from specific experiments.

We note that in the absence of shape fluctuations, such as in the 1D case or for non-deformable circular shapes, the active polar model for an epithelial cell monolayer explained in Section 2.2 of Chapter 2, and also applied to cellular

clusters in Chapter 3, gives no mean velocity of the clusters for homogeneous external conditions. This results from symmetry considerations, but we can also see it explicitly for a 1D system, integrating the main equation throughout the system in $x \in [x_-, x_+]$ (which comes from force balance and constitutive equations Eq. 2.9, Eq. 2.14 and Eq. 2.15), with stress-free boundary conditions, $\sigma^s(x_\pm) = 0$.

$$\partial_x \sigma^s = \xi v - \zeta_{\mathrm{i}} p, \tag{6.1}$$

$$\int_{x_-}^{x_+} \partial_x \sigma^s = \sigma^s(x_+) - \sigma^s(x_-) = 0 = \int_{x_-}^{x_+} (\xi(x) v(x) - \zeta_{\mathrm{i}}(x) p(x)) dx. \tag{6.2}$$

Then, assuming a constant friction $\xi(x) = \xi$, the mean velocity is

$$\bar{v} \equiv \frac{1}{2L} \int_{x_-}^{x_+} v(x) dx = \frac{1}{2L\xi} \int_{x_-}^{x_+} \zeta_{\mathrm{i}}(x) p(x) dx. \tag{6.3}$$

Note that this velocity is the center-of-mass velocity v_{CM} only when the system's size is not changing, $\dot{L} = 0$. Otherwise, we would have a second term, analogous to that of the divergence of the velocity field calculated in the expression of the center-of-mass of a 2D monolayer in Eq. 5.8. The polarization field at equilibrium, which comes from the solution of Eq. 2.6 with the quasistatic approximation, $\partial_t p_\alpha = 0$, is written in Eq. 2.17 for a 1D system, being

$$p(x) = \frac{\sinh\left((x - X)/L_c\right)}{\sinh\left(L/L_c\right)}, \tag{6.4}$$

where $X \equiv (x_+ + x_-)/2$ is its center-of-mass position, $L \equiv (x_+ - x_-)/2$ the monolayer half-width, and L_c the nematic length, characterizing the decay between maximal polarization at the edge, and vanishing polarization at the center of the monolayer. For uniform substrate conditions, and thus constant $\zeta_{\mathrm{i}}(x) = \zeta_{\mathrm{i}}$, we see from Eq. 6.3 that the mean velocity vanishes since the polarization from Eq. 6.4 is an odd function.

However, this is not realistic. In monostiffness substrates, even clusters that do not have significant shape fluctuations exhibit strong fluctuations of observables, such as cluster velocity (Fig. 6.1) or traction forces exerted on the substrate (Fig. 6.2) [Trepat2009, Serra-Picamal2012, Pallarès2023]. The goal of this chapter, thus, is to include stochastic terms in our continuum model to account for these fluctuations and see what we can learn from them through their implications on the observed fluctuations of physical observables.

To this end, we have several ways of introducing noise in our continuum model: In Section 6.2, we add it as an internal noise in the dynamics of the

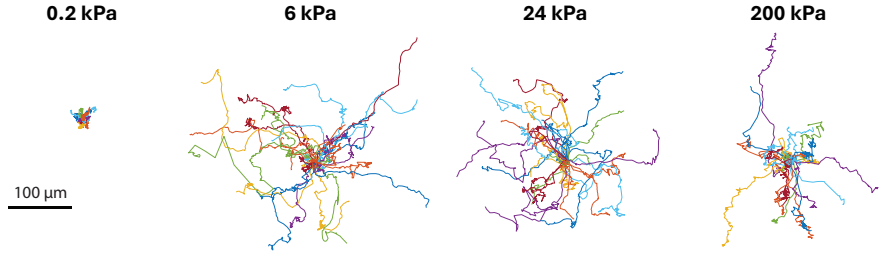

Figure 6.1: Random motion of cell clusters on uniform stiffness gels. Representative trajectories of A431 cell clusters migrating on gels of different uniform stiffness. It corresponds to the same data as in Fig. 3.3a. From [Pallarès2023].

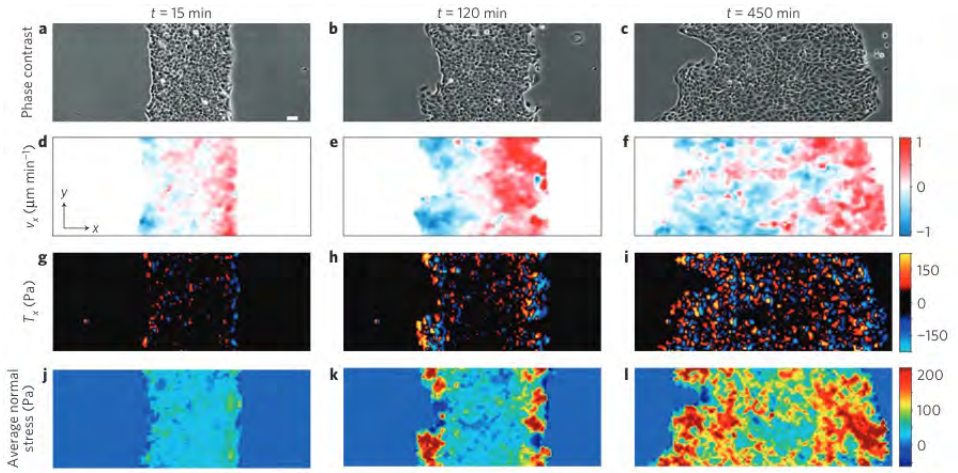

Figure 6.2: Maps of cell velocity, cell-substrate reactions, and monolayer stresses. Phase-contrast images (**a**–**c**), velocity v_x (**d**–**f**), tractions T_x (**g**–**i**), average normal stress σ (**j**–**l**) at 15 min, 120 min and 450 min after removing a PDMS membrane with an opening used to pattern rectangular monolayers. Scale bar, 50 μm. From [Serra-Picamal2012].

polarity, in such a way that the number of additional parameters is minimal. This can be done additively (Section 6.2.1) or multiplicatively (Section 6.2.2), implying different spatial distribution of the fluctuations in the system. For simplicity, the calculations for the additive noise case are more detailed, and we leave a deeper study of the multiplicative case for future work. Another way to introduce fluctuations is by adding noise in the active traction parameter, done in Section 6.3, which accounts for an external noise related to the attachment and detachment kinetics of the substrate adhesions with the cells in the mono-

layer. In this chapter, we give the predictions and consequences of each type of noise and try to distinguish which is the most relevant type through comparison with experimental data, analyzed from [Uroz2018] and [Pérez-González2019] in Section 6.4. Although the data analysis is not completely conclusive and, in reality, all these noise sources (and possibly others) will be present, with this simplified model we can already draw some conclusions and estimate some useful parameters related to fluctuations, such as diffusion coefficients. Our model is based on some assumptions and cannot capture all the richness of the problem. We will also discuss some limitations in fitting real data, concerning for instance the spatial correlation functions, which opens directions for future work.

In Appendix 6.A, we justify better the weak noise approximation for accounting for the noise term in an easy way. Definitions of Fourier transforms and Dirac delta functions used for the calculations throughout the chapter are in Appendix 6.B, and other calculations, not strictly necessary for the progression of the ideas in the chapter, in Appendix 6.C and Appendix 6.D. In Appendix 6.E, we detail the methodology for the autocorrelation function analysis with the experimental data.

6.2 Internal noise: polarity dynamics

The full equation for the polarity dynamics was given in Eq. 2.1 from Chapter 2. There, we neglected polarity advection and co-rotation, flow alignment, and active spontaneous polarization effects ($\bar{\nu}_1, \nu_1, \epsilon \to 0$), getting the simplified relaxational polarity dynamics from Eq. 2.5 used throughout the thesis,

$$\partial_t p_\alpha = -\frac{1}{\gamma_1}\left(a p_\alpha - K\nabla^2 p_\alpha\right). \tag{6.5}$$

In addition, a quasi-static approximation was assumed to account for the fast relaxation of the polarization compared to velocity, taking $\partial_t p_\alpha = 0$. Since we now need to introduce noise terms, which in principle contain all time scales, we need to keep the time derivative in Eq. 6.5. Then, it is not obvious whether the other neglected terms can now be neglected. In Appendix 6.A, we justify for the additive case, when it is possible to neglect advection and co-rotation, in the context of a weak noise approximation.

We explore two ways of adding this noise: If additive (Section 6.2.1), the noise in the polarization field contributes equally everywhere in the system. If multiplicative (Section 6.2.2), the fluctuations are larger where the polarization is also larger, which happens in regions up to a distance of L_c from the monolayer edges. We give the majority of the results in an arbitrary and very large

$d-$dimensional system, being $\mathbf{r} \in L^d$ the positional coordinate, but we also show some for a 1D system for simplicity, and for a 2D one for comparison with the experimental data.

6.2.1 Additive noise

In this case, we add a white noise ψ_α in the polarity dynamics,

$$\partial_t p_\alpha = -\frac{1}{\gamma_1}\left(a p_\alpha - K\nabla^2 p_\alpha\right) + \psi_\alpha, \tag{6.6}$$

with $\langle \psi_\alpha(\mathbf{r},t)\psi_\beta(\mathbf{r}',t')\rangle = 2\epsilon\delta(\mathbf{r}-\mathbf{r}')\delta(t-t')\delta_{\alpha\beta}$, where ϵ is the noise intensity. Introducing small-amplitude perturbations δp around the equilibrium state p^0_α, we can write $p_\alpha = p^0_\alpha + \delta p_\alpha$. Since p^0_α fulfills Eq. 6.5, we can actually write the dynamics in terms of the perturbations,

$$\partial_t \delta p_\alpha = -\frac{1}{\gamma_1}\left(a\delta p_\alpha - K\nabla^2 \delta p_\alpha\right) + \psi_\alpha. \tag{6.7}$$

The assumption of weak noise is implicit in the fact that the fluctuations in the polarization are decoupled from those in the velocity. The nonlinear coupling due to the advection is not present if we keep only linear orders in the perturbations of the equilibrium state (Appendix 6.A). In this subsection, we will compute the autocorrelation function for the polarization fluctuations, the structure factor, and the power spectral density, which will allow us to get estimates for an effective temperature and relations between the model parameters when comparing to experimental data in Section 6.4. We will also obtain an estimate for the diffusion coefficient for a 1D monolayer, although we leave the comparison to experimental data for future work.

6.2.1.1 Autocorrelation functions

In Fourier space for the position ($\delta p_\alpha(\mathbf{r},t) \to \delta\hat{p}_\alpha(\mathbf{q},t)$), we get from Eq. 6.7

$$\partial_t \delta\hat{p}_\alpha(\mathbf{q},t) = -\omega(\mathbf{q})\delta\hat{p}_\alpha(\mathbf{q},t) + \hat{\psi}_\alpha(\mathbf{q},t), \tag{6.8}$$

where $\omega(\mathbf{q})$ is the dispersion relation, defined as

$$\omega(\mathbf{q}) \equiv \frac{1}{\gamma_1}\left(a + K\mathbf{q}^2\right) = \frac{1}{\tau}\left(1 + L_c^2\mathbf{q}^2\right), \tag{6.9}$$

where $\tau \equiv \gamma_1/a$ and $L_c \equiv \sqrt{K/a}$. Solving this differential equation in time[1],

$$\delta\hat{p}_\alpha(\mathbf{q},t) = e^{-\omega(\mathbf{q})t}\int_{-\infty}^{t} e^{\omega(\mathbf{q})t'}\hat{\psi}_\alpha(\mathbf{q},t')dt'. \tag{6.10}$$

Then, using $\langle\hat{\psi}_\alpha(\mathbf{q},t)\hat{\psi}_\beta(\mathbf{q}',t')\rangle = 2\epsilon(2\pi)^d\delta(\mathbf{q}+\mathbf{q}')\delta(t-t')\delta_{\alpha\beta}$ (see Eq. 6.B.5 in Appendix 6.B), and that the dispersion relation fulfills $\omega(-\mathbf{q}) = \omega(\mathbf{q})$, the autocorrelation function in Fourier space for the polarization fluctuations is

$$\begin{aligned}
&\langle\delta\hat{p}_\alpha(\mathbf{q},t)\delta\hat{p}_\beta(\mathbf{q}',t')\rangle = \\
&= e^{-\omega(\mathbf{q})t-\omega(\mathbf{q}')t'}\int_{-\infty}^{t}dt_1\int_{-\infty}^{t'}dt_2 e^{\omega(\mathbf{q})t_1+\omega(\mathbf{q}')t_2}\langle\hat{\psi}_\alpha(\mathbf{q},t_1)\hat{\psi}_\beta(\mathbf{q}',t_2)\rangle \\
&= 2\epsilon(2\pi)^d\delta(\mathbf{q}+\mathbf{q}')e^{-\omega(\mathbf{q})(t+t')}\int_{-\infty}^{t}dt_1\int_{-\infty}^{t'}dt_2 e^{\omega(\mathbf{q})(t_1+t_2)}\delta(t_1-t_2)\delta_{\alpha\beta} \\
&= 2\epsilon(2\pi)^d\delta(\mathbf{q}+\mathbf{q}')e^{-\omega(\mathbf{q})(t+t')}\delta_{\alpha\beta}\int_{-\infty}^{\min(t,t')}dt_1 e^{2\omega(q)t_1} \\
&= \frac{\epsilon(2\pi)^d\delta(\mathbf{q}+\mathbf{q}')\delta_{\alpha\beta}}{\omega(\mathbf{q})}e^{-\omega(\mathbf{q})|t-t'|}.
\end{aligned} \tag{6.11}$$

Then, $\langle|\delta\hat{p}(\mathbf{q},t)|^2\rangle \equiv \langle\delta\hat{p}_\alpha(\mathbf{q},t)\delta\hat{p}_\alpha(\mathbf{q},t)^*\rangle = \langle\delta\hat{p}_\alpha(\mathbf{q},t)\delta\hat{p}_\alpha(-\mathbf{q},t)\rangle$, where we use the Einstein summation convention over repeated greek indices. With $t' = t$ and $\mathbf{q}' = -\mathbf{q}$, and using $\delta(\mathbf{0}) = L^d/(2\pi)^d$ to account for the finite system size (see Eq. 6.B.4 in Appendix 6.B), we obtain

$$\langle|\delta\hat{p}(\mathbf{q},t)|^2\rangle = \frac{\epsilon d L^d}{\omega(\mathbf{q})}. \tag{6.12}$$

Now, also in Fourier space for the time ($\delta p_\alpha(\mathbf{r},t) \to \delta\hat{\tilde{p}}_\alpha(\mathbf{q},\omega)$), from Eq. 6.7

$$\delta\hat{\tilde{p}}_\alpha(\mathbf{q},\omega) = \frac{\hat{\tilde{\psi}}_\alpha(\mathbf{q},\omega)}{-i\omega+\omega(\mathbf{q})}, \tag{6.13}$$

being $\omega(\mathbf{q})$ the dispersion relation defined in Eq. 6.9, not to be confused with the frequency ω. Using $\langle\hat{\tilde{\psi}}_\alpha(\mathbf{q},\omega)\hat{\tilde{\psi}}_\beta(\mathbf{q}',\omega')\rangle = 2\epsilon(2\pi)^d\delta(\mathbf{q}+\mathbf{q}')2\pi\delta(\omega+\omega')\delta_{\alpha\beta}$

[1] A differential equation $\frac{dg(q,t)}{dt} = -\omega(q,t)g(q,t)+h(q,t)$ can be solved by the integrating factor $\mu(q,t)$, so that $\frac{d\mu(q,t)}{dt} = \omega(q,t)\mu(q,t) \to \mu(q,t) = e^{\int\omega(q)dt}$, and then $g(q,t) = \frac{1}{\mu(q,t)}\int\mu(q,t')h(q,t')dt'+c$, where $c=0$ if we choose properly the integration limits.

(see Eq. 6.B.6 in Appendix 6.B), the autocorrelation function both in Fourier space for time and position yields

$$\langle \delta\hat{\tilde{p}}_\alpha(\mathbf{q},\omega)\delta\hat{\tilde{p}}_\beta(\mathbf{q}',\omega')\rangle = \frac{2\epsilon(2\pi)^d\delta(\mathbf{q}+\mathbf{q}')2\pi\delta(\omega+\omega')\delta_{\alpha\beta}}{(-i\omega+\omega(\mathbf{q}))(-i\omega'+\omega(\mathbf{q}'))}. \tag{6.14}$$

Like before, $\langle|\delta\hat{\tilde{p}}(\mathbf{q},\omega)|^2\rangle \equiv \langle\delta\hat{\tilde{p}}_\alpha(\mathbf{q},\omega)\delta\hat{\tilde{p}}_\alpha(\mathbf{q},\omega)^*\rangle = \langle\delta\hat{\tilde{p}}_\alpha(\mathbf{q},\omega)\delta\hat{\tilde{p}}_\alpha(-\mathbf{q},-\omega)\rangle$, summing every component. With $\omega' = -\omega$ and $\mathbf{q}' = -\mathbf{q}$ in, and using $\delta(\mathbf{0}) = L^d/(2\pi)^d$ in space and $\delta(0) = T/(2\pi)$ in time (Eq. 6.B.4 in Appendix 6.B), we obtain

$$\langle|\delta\hat{\tilde{p}}(\mathbf{q},\omega)|^2\rangle = \frac{2\epsilon d L^d T}{\omega^2+\omega^2(\mathbf{q})}. \tag{6.15}$$

From Eq. 6.11, we can compute the spatial autocorrelation function in real space in both one and 2D systems, for $t' = t$ and using the inverse Fourier transform definitions (see Appendix 6.B).

- **1D**: The inverse Fourier transform $\mathcal{F}^{-1}[\cdot]$ of a Lorentzian function in one dimension is an exponential, and so we obtain

$$\begin{aligned}\langle\delta p(x,t)\delta p(x',t)\rangle &= \frac{1}{(2\pi)^2}\int_{-\infty}^{\infty}dq\int_{-\infty}^{\infty}dq' e^{iqx}e^{iq'x'}\langle\delta\hat{p}(q,t)\delta\hat{p}(q',t)\rangle \\ &= \frac{1}{(2\pi)^2}\int_{-\infty}^{\infty}dq\int_{-\infty}^{\infty}dq' e^{iqx+iq'x'}\frac{2\pi\epsilon\delta(q+q')}{\omega(q)} = \frac{\epsilon}{2\pi}\int_{-\infty}^{\infty}dq\frac{e^{iq(x-x')}}{\omega(q)} \\ &= \frac{\epsilon\tau}{2\pi}\int_{-\infty}^{\infty}dq\frac{e^{iq(x-x')}}{1+L_c^2q^2} = \epsilon\tau\mathcal{F}^{-1}_{x-x'}\left[\frac{1}{1+L_c^2q^2}\right] = \frac{\epsilon\tau}{2L_c}e^{-|x-x'|/L_c}.\end{aligned} \tag{6.16}$$

  The second moment of the fluctuations of the polarization, with $x' = x$, is thus

$$\langle\delta p^2\rangle = \frac{\epsilon\tau}{2L_c}. \tag{6.17}$$

- **2D**: The inverse Fourier transform $\mathcal{F}^{-1}[\cdot]$ of the Lorentzian function in two dimensions is a modified Bessel function of the second kind $K_0(\cdot)$ (see Eq. 6.C.1 from Appendix 6.C, with $c = L_c^{-1}$), giving

$$\begin{aligned}\langle\delta p_\alpha(\mathbf{r},t)\delta p_\alpha(\mathbf{r}',t)\rangle &= \frac{1}{(2\pi)^4}\int_{\mathbb{R}^2}d\mathbf{q}\int_{\mathbb{R}^2}d\mathbf{q}' e^{i\mathbf{q}\cdot\mathbf{r}}e^{i\mathbf{q}'\cdot\mathbf{r}'}\langle\delta\hat{p}_\alpha(\mathbf{q},t)\delta\hat{p}_\alpha(\mathbf{q}',t)\rangle \\ &= \frac{2\epsilon\tau}{(2\pi)^2}\int_{\mathbb{R}^2}d\mathbf{q}\frac{e^{i\mathbf{q}\cdot(\mathbf{r}-\mathbf{r}')}}{1+L_c^2\mathbf{q}^2} = \frac{2\epsilon\tau}{L_c^2}\mathcal{F}^{-1}_{\mathbf{r}-\mathbf{r}'}\left[\frac{1}{L_c^{-2}+\mathbf{q}^2}\right] \\ &= \frac{\epsilon\tau}{\pi L_c^2}K_0\left(\frac{|\mathbf{r}-\mathbf{r}'|}{L_c}\right),\end{aligned} \tag{6.18}$$

  where the 2 in the second equality appears because of the contribution of both coordinates.

6.2.1.2 Structure factor and energy equipartition

The static structure factor $S(\mathbf{q})$ is the Fourier transform of the spatial correlation function $C(\mathbf{r})$, thus characterizing the structure of correlations throughout the system. The step-by-step calculation can be found in Eq. 6.C.3 from Appendix 6.C, obtaining for the polarization fluctuations,

$$C(\mathbf{r}) \equiv \left\langle \frac{1}{L^d} \int_{L^d} \delta p_\alpha(\mathbf{r}', t) \delta p_\alpha(\mathbf{r}' + \mathbf{r}, t) d\mathbf{r}' \right\rangle, \tag{6.19}$$

$$S(\mathbf{q}) \equiv \int_{L^d} C(\mathbf{r}) e^{-i\mathbf{q}\cdot\mathbf{r}} d\mathbf{r} = \frac{1}{L^d} \langle |\delta \hat{p}(\mathbf{q}, t)|^2 \rangle = \frac{\epsilon d}{\omega(\mathbf{q})}, \tag{6.20}$$

where Eq. 6.12 is used in the last equality. The integral of the structure factor gives the second moment (see Eq. 6.C.4),

$$\langle \delta p^2 \rangle \equiv \langle \delta p_\alpha \delta p_\alpha \rangle \equiv C(\mathbf{0}) = \frac{1}{(2\pi)^d} \int_{\Omega^d} S(\mathbf{q}) d\mathbf{q} = \frac{\epsilon d}{(2\pi)^d} \int_{\Omega^d} \frac{d\mathbf{q}}{\omega(\mathbf{q})}. \tag{6.21}$$

Let's explicitly compute the integral in one and two dimensions.

- **1D**: We recover the same result as in Eq. 6.17,

$$\langle \delta p^2 \rangle = \frac{\epsilon\tau}{2\pi} \int_{-\infty}^{\infty} \frac{dq}{1 + L_c^2 q^2} = \frac{\epsilon\tau}{2\pi} \left[\frac{\arctan(L_c q)}{L_c} \right]_{-\infty}^{\infty} = \frac{\epsilon\tau}{2L_c}. \tag{6.22}$$

- **2D**: Using $\mathbf{dq} = 2\pi q dq$, where q is the modulus, we define a cutoff $q_{\max}$, necessary to avoid divergence of the integral and because of the experimental resolution of the traction measurements. Then,

$$\begin{aligned} \langle \delta p^2 \rangle &= \frac{2\epsilon\tau}{(2\pi)^2} \int_{\mathbb{R}^2} \frac{d\mathbf{q}}{1 + L_c^2 \mathbf{q}^2} = \frac{2\epsilon\tau}{(2\pi)^2} \int_0^{q_{\max}} \frac{2\pi q}{1 + L_c^2 q^2} dq \\ &= \frac{\epsilon\tau}{2\pi L_c^2} \ln\left(1 + L_c^2 q_{\max}^2\right). \end{aligned} \tag{6.23}$$

The energy equipartition theorem at equilibrium states that each component and mode $\mathbf{q}$ of the free energy contributes with half a $k_B T$, $\langle \hat{F}_\mathbf{q} \rangle = \frac{1}{2} k_B T d$. Although our system is not at equilibrium, we can use the theorem to estimate an effective temperature and see relations between the model parameters. Recall the simplified Frank elastic free energy[1] from Eq. 2.4, written here for the polarization fluctuations around a uniform, non-polarized equilibrium,

$$F = \int_{L^d} \left[\frac{a}{2} \delta p_\alpha \delta p_\alpha + \frac{K}{2} (\partial_\alpha \delta p_\beta)(\partial_\alpha \delta p_\beta) \right] d\mathbf{r}. \tag{6.24}$$

[1] Note that the parameters a and K will take different values and dimensions depending on the dimensions of Ω.

Using the inverse Fourier transform definitions, it reads

$$F = \frac{1}{2(2\pi)^d} \int_{\Omega^d} \left(a + K\mathbf{q}^2\right) |\delta\hat{p}(\mathbf{q},t)|^2 d\mathbf{q}$$
$$F = \frac{1}{2L^d} \sum_{\mathbf{q}\in\Omega^d} \left(a + K\mathbf{q}^2\right) |\delta\hat{p}(\mathbf{q},t)|^2, \tag{6.25}$$

where we discretized by multiplying by $(2\pi)^d/L^d$. Since $F = \sum_{\mathbf{q}} \hat{F}_{\mathbf{q}}$, then

$$\langle |\delta\hat{p}(\mathbf{q},t)|^2 \rangle = \frac{L^d k_B T d}{a + K\mathbf{q}^2} = \frac{L^d k_B T d}{\gamma_1 \omega(\mathbf{q})}, \tag{6.26}$$

being $\omega(\mathbf{q})$ the dispersion relation from Eq. 6.9. Finally, with $\langle |\delta\hat{p}(\mathbf{q},t)|^2 \rangle = \epsilon d L^d/\omega(\mathbf{q})$ (Eq. 6.12), we get an equivalence between the noise intensity, the rotational viscosity, and an effective temperature of the system,

$$\epsilon\gamma_1 = k_B T. \tag{6.27}$$

6.2.1.3 Power spectrum and fluctuation-dissipation relation

The dynamic structure factor $S(\mathbf{q},\omega)$ is the Fourier transform of the spatiotemporal correlation function $C(\mathbf{r},t)$. With a very similar procedure to that of the structure factor (see Eq. 6.C.6 in Appendix 6.C), we get

$$C(\mathbf{r},t) \equiv \left\langle \frac{1}{L^d T} \int_{L^d} \int_T \delta p_\alpha(\mathbf{r}',t') \delta p_\alpha(\mathbf{r}'+\mathbf{r}, t'+t) dt' d\mathbf{r}' \right\rangle, \tag{6.28}$$

$$S(\mathbf{q},\omega) \equiv \int_{L^d} \int_T C(\mathbf{r},t) e^{-i\omega t} e^{-i\mathbf{q}\cdot\mathbf{r}} dt d\mathbf{r} = \frac{1}{L^d T} \langle |\delta\hat{\tilde{p}}(\mathbf{q},\omega)|^2 \rangle$$
$$= \frac{2\epsilon d}{\omega^2 + \omega^2(\mathbf{q})}, \tag{6.29}$$

where Eq. 6.15 is used in the last equality. The power spectral density (PSD) $S(\omega)$ is the integral in $\mathbf{q}-$space, which characterizes temporal correlations in the system,

$$S(\omega) \equiv \int_{\Omega^d} S(\mathbf{q},\omega) d\mathbf{q}. \tag{6.30}$$

Let's explicitly compute it in one and two dimensions. Although we do not do it here, it might be useful in the future to compare with spectroscopy experiments of traction fluctuations.

- **1D**: Using the residues theorem,

$$S(\omega) = \int_{-\infty}^{\infty} \frac{2\epsilon\, dq}{\omega^2 + \frac{1}{\tau^2}\left(1 + L_c^2 q^2\right)^2} = \frac{\epsilon\pi\tau^2}{L_c}\sqrt{\frac{1}{(\tau\omega)^3}}\frac{\sec\left(\frac{1}{2}\arctan\left(\tau\omega\right)\right)}{\left(1+\frac{1}{\tau^2\omega^2}\right)^{3/4}}. \quad (6.31)$$

Defining $x \equiv \tau\omega$, the scaling for low ($\omega \to 0$) and high frequencies ($\omega \to \infty$), using $\sec(a+b) = (\cos a \cos b - \sin a \sin b)^{-1}$, gives[1]:

$$\lim_{\omega\to 0} S(\omega) \sim \frac{\epsilon\pi\tau^2}{L_c}\left(1 - \frac{5}{8}(\tau\omega)^2 + \cdots\right), \quad (6.32)$$

$$\lim_{\omega\to \infty} S(\omega) \sim \frac{\epsilon\pi\tau^2}{L_c}\sqrt{\frac{2}{(\tau\omega)^3}}\left(1 - \frac{1}{2\tau\omega} + \cdots\right). \quad (6.33)$$

- **2D**: Using $\mathbf{dq} = 2\pi q dq$, where q is now the modulus, we get

$$S(\omega) = \int_{\mathbb{R}^2} \frac{4\epsilon\, d\mathbf{q}}{\omega^2 + \frac{1}{\tau^2}\left(1 + L_c^2\mathbf{q}^2\right)^2} = 8\pi\epsilon\tau^2\int_0^{\infty}\frac{q\, dq}{\tau^2\omega^2 + \left(1 + L_c^2 q^2\right)^2}$$
$$= \frac{4\pi\epsilon\tau^2}{L_c^2}\frac{1}{\tau\omega}\left(\frac{\pi}{2} - \arctan\left(\frac{1}{\tau\omega}\right)\right). \quad (6.34)$$

The limits for low and high frequencies give

$$\lim_{\omega\to 0} S(\omega) \sim \frac{4\pi\epsilon\tau^2}{L_c^2}\left(1 - \frac{1}{3}(\tau\omega)^2 + \cdots\right), \quad (6.35)$$

$$\lim_{\omega\to \infty} S(\omega) \sim \frac{4\pi\epsilon\tau^2}{L_c^2}\frac{1}{\tau\omega}\left(\frac{\pi}{2} - \frac{1}{\tau\omega} + \cdots\right). \quad (6.36)$$

The PSD in the 2D system case (Fig. 6.3b), is the most relevant one for comparison with typical experiments, and could be useful for inferring model parameters, like τ, L_c, and ϵ.

The fluctuation-dissipation theorem relates the thermodynamic fluctuations and the linear response in equilibrium systems. Even though our system is not at equilibrium, we can obtain a formal analogy to the fluctuation-dissipation theorem with an effective temperature, given that in our weak noise approximation,

[1] For $x \to 0$: $\arctan(x) \approx x - \frac{x^3}{3} + \theta\left(x^5\right)$, $\cos(x) \approx 1 - \frac{x^2}{2} + \theta(x^4)$, $\sin(x) \approx x - \frac{x^3}{6} + \theta(x^5)$, $(1+\frac{1}{x^2})^{3/4} \approx \frac{1}{x^{3/2}} + \frac{3}{4}x^{1/2} + \theta(x^{5/2})$ and $\frac{1}{1-\frac{x^2}{2}} \approx 1 + \frac{x^2}{2} + \theta(x^3)$. For $x \to \infty$: $\arctan(x) \approx \frac{\pi}{2} - \frac{1}{x} + \frac{1}{3x^3} + \theta\left(1/x^5\right)$, $(1+\frac{1}{x^2})^{3/4} \approx 1 + \frac{3}{4x^2} + \theta(1/x^3)$ and $\frac{1}{1+\frac{1}{2x}} \approx 1 - \frac{1}{2x} + \frac{1}{4x^2} + \theta(1/x^3)$.

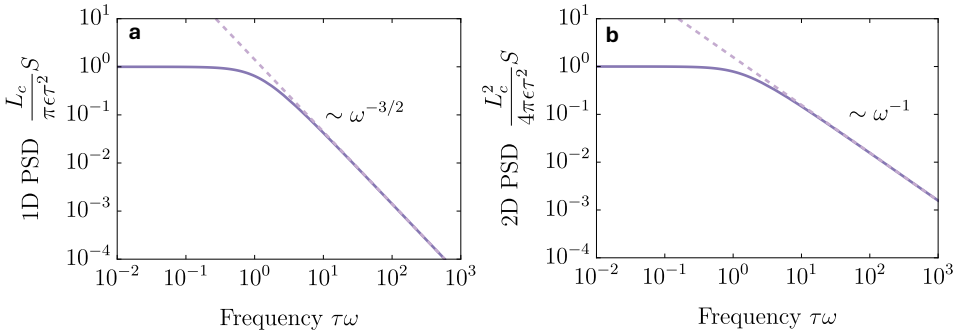

Figure 6.3: Power spectral density for an additive noise in the polarity dynamics. Dimensionless PSD as a function of a dimensionless frequency $\tau\omega$, for a 1D (**a**) and a 2D system (**b**). Continuous lines are the full expressions obtained in Eq. 6.31 and Eq. 6.34, and dashed lines are the corresponding power-law decays coming from the limit at large frequencies, obtained in Eq. 6.33 and Eq. 6.36 respectively.

the dynamics of the polarity is linear. The linear response function or susceptibility $\chi_{\alpha\beta}(\mathbf{r},t)$, is defined by $\langle\delta\hat{\tilde{p}}_\alpha(\mathbf{q},\omega)\rangle \equiv \hat{\tilde{\chi}}_{\alpha\beta}(\mathbf{q},\omega)\hat{\tilde{G}}_\beta(\mathbf{q},\omega)$, being $G_\alpha(\mathbf{r},t)$ an external force. If instead of Eq. 6.7 we write the dynamics of the polarity with this $G_\alpha(\mathbf{r},t)$,

$$\partial_t\delta p_\alpha = -\frac{1}{\gamma_1}\left(a\delta p_\alpha - \nabla^2\delta p_\alpha - G_\alpha\right) + \psi_\alpha, \tag{6.37}$$

then, the average of the Fourier transform in time and space reads

$$\langle\delta\hat{\tilde{p}}_\alpha(\mathbf{q},\omega)\rangle = \frac{\hat{\tilde{G}}_\alpha(\mathbf{q},\omega)}{\gamma_1(-i\omega+\omega(\mathbf{q}))} \equiv \hat{\tilde{\chi}}_{\alpha\beta}(\mathbf{q},\omega)\hat{\tilde{G}}_\alpha(\mathbf{q},\omega), \tag{6.38}$$

where we used that $\langle\hat{\tilde{G}}_\alpha(\mathbf{q},\omega)\rangle = \hat{\tilde{G}}_\alpha(\mathbf{q},\omega)$ because the external force is not noise-dependent and $\langle\hat{\tilde{\psi}}_\alpha(\mathbf{q},\omega)\rangle = 0$. Thus, the susceptibility $\chi_{\alpha\beta}(\mathbf{r},t)$ verifies

$$\hat{\tilde{\chi}}_{\alpha\beta}(\mathbf{q},\omega) \equiv \frac{\delta_{\alpha\beta}}{\gamma_1(-i\omega+\omega(\mathbf{q}))} = \frac{\omega(\mathbf{q})+i\omega}{\gamma_1(\omega^2+\omega^2(\mathbf{q}))}\delta_{\alpha\beta}, \tag{6.39}$$

where the imaginary part is the dissipative response. Then, with Eq. 6.29, but taking into account only one component (and so writing the indices $\alpha\beta$ instead of the contracted indices, and $d=1$), then

$$S_{\alpha\beta}(\mathbf{q},\omega) = \frac{2\epsilon\gamma_1}{\omega}\,\mathrm{Im}(\hat{\tilde{\chi}}_{\alpha\beta}(\mathbf{q},\omega)), \tag{6.40}$$

because $(\omega^2+\omega^2(\mathbf{q}))^{-1} = \frac{\gamma_1}{\omega}\,\mathrm{Im}(\hat{\tilde{\chi}}_{\alpha\beta}(\mathbf{q},\omega))$. This result has the same structure as the fluctuation-dissipation theorem if we map the prefactor to $2k_BT/\omega$, yielding

$$\frac{2\epsilon\gamma_1}{\omega} = \frac{2k_BT}{\omega} \longrightarrow \epsilon\gamma_1 = k_BT, \tag{6.41}$$

so we retrieve the result we obtained from the energy equipartition argument in Eq. 6.27. We will use these results to characterize the fluctuations of real traction data in terms of an effective temperature in Section 6.4.

6.2.1.4 Cluster diffusion coefficient

Now we consider a 1D system, $x \in [x_-, x_+]$, to get simplified results. Like in Chapter 2 (Section 2.3), this is an effective setup that models non-deformable circular clusters. We assume a uniform stiffness substrate and thus a constant active traction parameter, $\zeta_{\mathrm{i}}(x) = \zeta_{\mathrm{i}}$, and we write the polarization field to linear order in the perturbations, $p(x,t) = p_0(x) + \delta p(x,t)$, being p_0 the expression in Eq. 6.4. Then, from Eq. 6.3, the integral is just that of the polarization fluctuations since p_0 is odd,

$$\bar{v}(t) = \frac{\zeta_{\mathrm{i}}}{2L\xi}\int_{x_-}^{x_+} \delta p(x,t)dx. \tag{6.42}$$

The mean displacement,

$$\bar{x}(t) = \int_0^t \bar{v}(t')dt' = \frac{\zeta_{\mathrm{i}}}{2L\xi}\int_0^t dt' \int_{x_-}^{x_+} \delta p(x',t')dx', \tag{6.43}$$

and the mean squared displacement of the center-of-mass of the cluster, assuming L constant and so that $\bar{v} \equiv v_{CM}$ (see detailed calculation in Eq. 6.C.7 from Appendix 6.C), is

$$\begin{aligned}\langle \bar{x}(t)^2\rangle = &\left(\frac{\zeta_{\mathrm{i}}}{2L\xi}\right)^2 \frac{\epsilon}{2\pi}\int_{x_-}^{x_+} dx' \int_{x_-}^{x_+} dx'' \int_{-\infty}^{\infty} dq e^{iq(x'-x'')} \\ &\cdot \frac{2}{\omega^2(q)}\left(t + \frac{1}{\omega(q)}\left(e^{-\omega(q)t} - 1\right)\right).\end{aligned} \tag{6.44}$$

In general, L should be time-dependent. Consequently, our calculation is valid in parameter regions close to the active spreading transition, where the system size does not change significantly. In other regimes, one should determine the mean spreading velocity from the deterministic model, but then the calculation becomes more involved.

If the long-time asymptotics is diffusive, then the diffusion coefficient is obtained from $\langle \bar{x}(t)^2 \rangle = 2tD_{\text{diff}} + f(t)$, where $f(t)/t$ decays to zero at long times. We thus have, in the constant L approximation,

$$\begin{aligned} D_{\text{diff}} &= \left(\frac{\zeta_{\text{i}}}{2L\xi}\right)^2 \frac{\epsilon}{2\pi} \int_{x_-}^{x_+} dx' \int_{x_-}^{x_+} dx'' \int_{-\infty}^{\infty} dq e^{iq(x'-x'')} \frac{1}{\omega^2(q)} \\ &= \left(\frac{\zeta_{\text{i}}}{2L\xi}\right)^2 \epsilon\tau^2 \int_{x_-}^{x_+} dx' \int_{x_-}^{x_+} dx'' \mathcal{F}^{-1}_{x-x'} \left[\frac{1}{(1+L_c^2 q^2)^2}\right] \\ &= \left(\frac{\zeta_{\text{i}}}{2L\xi}\right)^2 \epsilon\tau^2 \int_{x_-}^{x_+} dx' \int_{x_-}^{x_+} dx'' \frac{1}{4L_c} \left(1 + \frac{|x'-x''|}{L_c}\right) e^{-|x'-x''|/L_c} \\ &= \left(\frac{\zeta_{\text{i}}}{2L\xi}\right)^2 \frac{\epsilon\tau^2 L_c}{2} \left(\frac{4L}{L_c} - 3 + e^{-2L/L_c}\left(\frac{2L}{L_c} + 3\right)\right), \end{aligned} \tag{6.45}$$

or, in terms of the variance of the polarization fluctuations $\langle \delta p^2 \rangle$ instead of the noise intensity ϵ (both related by Eq. 6.17 for one dimension),

$$D_{\text{diff}} = \left(\frac{\zeta_{\text{i}}}{2L\xi}\right)^2 \langle \delta p^2 \rangle \tau L_c^2 \left(\frac{4L}{L_c} - 3 + e^{-2L/L_c}\left(\frac{2L}{L_c} + 3\right)\right). \tag{6.46}$$

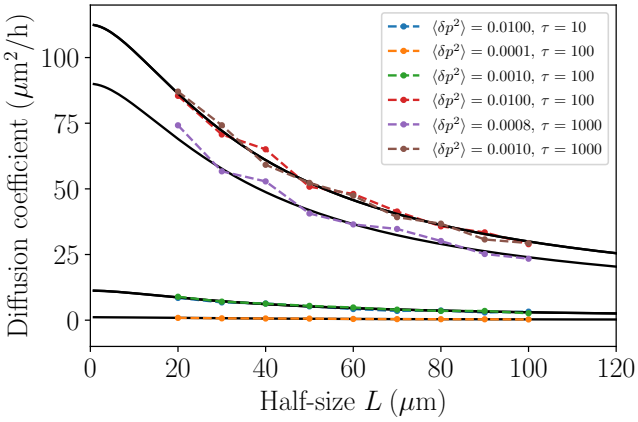

Figure 6.4: Diffusion coefficient for an additive noise in the polarity dynamics. Numerical simulations (dashed colored points) and analytical predictions (black lines) for the diffusion coefficient as a function of the half-size of the monolayer, for the different parameters shown in the legend. Other parameters are $L_c = 15\ \mu$m, $\zeta_{\text{i}} = 0.05$ kPa/μm, $\zeta = -2$ kPa, $\xi = 0.2$ kPa s/μm^2, $\eta = 20$ MPa s.

We perform numerical simulations of the problem by simulating a 1D system, with the polarization given in Eq. 6.4 and noise in its dynamics following Eq. 6.6 [García-Ojalvo1992]. We assume periodic boundary conditions, but in order to avoid spurious correlations between the two edges, we simulate this polarization in a space that is extended by $3L_c$ beyond each side of the monolayer. With Eq. 6.3, we obtain the mean velocity $\bar{v}(t)$ by integrating the polarization field and with $L(t) = (x_+(t) - x_-(t))/2$, and we then evolve the edges by writing $x_\pm(t + \Delta t) = x_\pm(t) + \bar{v}(t)\Delta t$. In this way, we obtain the new $L(t + \Delta t)$ and simulate again the polarization field with additive noise, checking that in all the cases, the changes in L are not very significant and so the assumption that it is constant is justified. The coefficient diffusion is measured from the mean squared displacement $\langle \bar{x}(t)^2 \rangle$ over time.

In Fig. 6.4 we see that the analytical prediction matches well with the simulations. However, experimental diffusion coefficients of monolayers were difficult to analyze, and we leave the study for further work.

6.2.2 Multiplicative noise

In this case, we add a scalar white noise ψ multiplying the polarization field in the polarity dynamics, in such a way that

$$\partial_t p_\alpha = -\frac{1}{\gamma_1}(a p_\alpha - K\nabla^2 p_\alpha) + p_\alpha^0 \psi, \tag{6.47}$$

with $\langle \psi(\mathbf{r}, t)\psi(\mathbf{r}', t') \rangle = 2\epsilon\delta(\mathbf{r} - \mathbf{r}')\delta(t - t')$, where ϵ is again the noise intensity. The equation actually comes from adding a noise term in the a parameter, by $\partial_t p_\alpha = -\frac{1}{\gamma_1}(a(1 + \psi)p_\alpha - K\nabla^2 p_\alpha) = -\frac{1}{\gamma_1}(a p_\alpha - K\nabla^2 p_\alpha) - \frac{a}{\gamma_1}\psi p \approx \frac{1}{\gamma_1}(a p_\alpha - K\nabla^2 p_\alpha) - \frac{a}{\gamma_1} p_\alpha^0 \psi$, neglecting second order terms $\delta p_\alpha \psi$ and redefining a/γ_1 inside of the noise intensity ϵ. This approximation is also valid for sufficiently weak noise. The terms considered correspond to the leading order within an expansion on the noise intensity around the deterministic dynamics. To linear order, $p_\alpha = p_\alpha^0 + \delta p_\alpha$ and since p_α^0 fulfills Eq. 6.5, we can thus write the dynamics in terms of the perturbations,

$$\partial_t \delta p_\alpha = -\frac{1}{\gamma_1}(a\delta p_\alpha - K\nabla^2 \delta p_\alpha) + p_\alpha^0 \psi. \tag{6.48}$$

The main difference between the additive and the multiplicative approach is that in the former case, the noise has the same intensity throughout the system, whereas in the latter it is stronger where the polarization is also stronger, which happens near the boundaries. Since the effect of the multiplicative noise on the diffusion of clusters is typically much smaller than that of the additive noise, and

also being mathematically more involved, we will not pursue the multiplicative case in detail, neither analytically nor numerically. If present, multiplicative noise is expected to coexist with additive noise, hence providing a relatively small correction to that case. In the following section we discuss a simple argument in 1D to justify how the effect of the multiplicative noise scales with the system size, and yields typically smaller diffusion coefficients than the additive noise.

6.2.2.1 Diffusion coefficient estimate

The diffusion coefficient in the multiplicative case is less dependent on the size of the system than on the additive noise. Here, we give a heuristic argument for the 1D system. Assuming that $p(x_\pm) = \pm 1$, and $p \approx 0$ elsewhere, we can consider a system with N elements of size L_c, having in total a length $2L = NL_c$. Then only the x_+ and x_- elements have non zero polarization, yielding

$$\delta\bar{p}(t) = \frac{1}{2L}\int_{x_-}^{x_+} \delta p(x,t)dx \approx \frac{1}{N}(\delta p(x_+) + \delta p(x_-)) \sim \pm\frac{\sqrt{2\langle\delta p^2\rangle}}{N}. \tag{6.49}$$

Then, the mean velocity for a constant friction is (Eq. 6.42)

$$\bar{v}(t) = \frac{\zeta_\mathrm{i}}{\xi}\delta\bar{p}(t) \sim \pm\frac{\zeta_\mathrm{i}}{\xi}\frac{\sqrt{2\langle\delta p^2\rangle}}{N}, \tag{6.50}$$

and the diffusion coefficient, using that $D \propto (\bar{v}\tau)^2/\tau = \bar{v}^2\tau$,

$$D \sim \frac{\zeta_\mathrm{i}^2}{\xi^2}\langle\delta p^2\rangle\frac{L_c^2}{2L^2}\tau. \tag{6.51}$$

Note that with this same argument, for an additive noise, all the intervals contribute to the calculus of the mean polarization fluctuations, $\delta\bar{p} = \sum_{i=1}^{N}\delta p_i/N \sim \sqrt{\langle\delta p^2\rangle/N}$, and then,

$$D \sim \frac{\zeta_\mathrm{i}^2}{\xi^2}\langle\delta p^2\rangle\frac{L_c}{2L}\tau, \tag{6.52}$$

which is in accordance with the first term of the exact relation found in Eq. 6.46. Consequently, the diffusion coefficient for the multiplicative noise decreases with a stronger inverse power of system size, namely as L^{-2} instead of L^{-1}.

6.3 External noise: maximal-traction fluctuations

For the additive internal noise in the polarity dynamics, the relaxation time is given by $\omega(\mathbf{q})^{-1}$ (Eq. 6.11), and so it is different for every mode $\mathbf{q}$, as a

consequence of the dynamical equation for the polarity. Instead, an external noise in the traction will reflect different physics associated with the kinetic processes of the linkers with the substrate. A detailed modeling of these processes would define the statistics of such fluctuations. However, we will not pursue such detailed modeling here and assume for simplicity that the traction fluctuations exhibit one single characteristic time scale, irrespective of the spatial Fourier mode, and a single characteristic length scale. These noise parameters will not be related to those associated with the polarity dynamics. We thus consider an external noise in the active traction parameter ζ_i to account for fluctuations originated in the attachment and detachment of the adhesions of the monolayer with the substrate. For simplicity, we write the formalism for a 1D system, but it could easily be translated to higher dimensions. The main model equation Eq. 6.1 has now an active traction such that

$$\zeta_\mathrm{i}(x,t) = \zeta_\mathrm{i}^0(1+\alpha\psi(x,t)), \tag{6.53}$$

being ψ the noise term and α a parameter controlling the noise intensity. We want ψ to be a colored noise, exponentially correlated in time and space. Being λ the correlation length, τ the correlation time and ϵ the noise intensity,

$$\langle\psi(x',t')\psi(x'+x,t'+t)\rangle = \frac{\epsilon}{2\lambda\tau}e^{-|x|/\lambda}e^{-|t|/\tau}, \tag{6.54}$$

which gives way to a white noise in the limit of $\lambda,\tau\to 0$, $\langle\psi(x,t)\psi(x',t')\rangle \to 2\epsilon\delta(x-x')\delta(t-t')$. Since the system is finite and because we now want a unique relaxation time for all the modes q, we write ψ as a decomposition of N Fourier modes, being $2L$ the system's size (see the step-by-step generation of the noise as this decomposition in Appendix 6.D). This decomposition is also useful for numerical implementation and gives

$$\psi(x,t) = \sum_{n=0}^{N}\left(a_n(t)\cos\left(\frac{2\pi n}{2L}x\right) + b_n(t)\sin\left(\frac{2\pi n}{2L}x\right)\right). \tag{6.55}$$

To have the exponential decay in the spatial correlation function, we need the amplitudes of all the modes to be normal (Gaussian) independent variables $a_n, b_n \sim \mathcal{N}(0, \sqrt{\langle a_n^2\rangle})$, with variances

$$\langle a_n^2\rangle = \langle b_n^2\rangle = \begin{cases} \frac{\epsilon}{L} & n=0 \\ \frac{\epsilon}{L}\frac{2}{1+\lambda^2\left(\frac{\pi n}{L}\right)^2} & n=1,\dots,N. \end{cases} \tag{6.56}$$

To have as well an exponential decay in the temporal correlation function, the amplitudes must follow an Ornstein-Uhlenbeck process, such that

$$\frac{da_n}{dt} = -\frac{1}{\tau}a_n + \frac{1}{\tau}\eta(t), \tag{6.57}$$

where $\eta(t)$ is a white noise, with $\langle \eta(t)\eta(t')\rangle = 2\mu_n\delta(t-t')$. This way,

$$\langle a_n(t')a_n(t'+t)\rangle = \frac{\mu_n}{\tau}e^{-|t|/\tau} = \langle a_n^2\rangle e^{-|t|/\tau}, \tag{6.58}$$

and the same for b_n, where we used that for $t=0$, $\langle a_n(0)^2\rangle = \langle a_n^2\rangle$ and so $\mu_n = \tau\langle a_n^2\rangle$ (variances in Eq. 6.56). Summarizing, in space and time (see Eq. 6.D.3 and Eq. 6.D.7), we get

$$\langle \psi(x',t)\psi(x'+x,t)\rangle = \frac{\epsilon}{L}\left(1+\sum_{n=1}^{N}\frac{2}{1+\lambda^2\left(\frac{\pi n}{L}\right)^2}\cos\left(\frac{\pi n}{L}x\right)\right) \approx \frac{\epsilon}{\lambda}e^{-|x|/\lambda}, \tag{6.59}$$

$$\langle \psi(x,t')\psi(x,t'+t)\rangle = \frac{\epsilon}{L}\left(1+\sum_{n=1}^{N}\frac{2}{1+\lambda^2\left(\frac{\pi n}{L}\right)^2}\right)e^{-|t|/\tau} \equiv \frac{\mu}{\tau}e^{-|t|/\tau}, \tag{6.60}$$

being $\mu \equiv \sum_{n=0}^{N}\mu_n = \sum_{n=0}^{N}\langle a_n^2\rangle\tau$.

6.3.1 Diffusion coefficient

Taking the active traction parameter from Eq. 6.53, and the polarity from Eq. 6.4, then the mean velocity (Eq. 6.3) is

$$\begin{aligned}\bar{v}(t) &= \frac{1}{2L\xi}\int_{x_-}^{x_+}\zeta_{\mathrm{i}}^0(1+\alpha\psi(x,t))p(x)dx = \frac{\zeta_{\mathrm{i}}^0\alpha}{2L\xi}\int_{x_-}^{x_+}\psi(x,t)p(x)dx \\ &= \frac{\zeta_{\mathrm{i}}^0\alpha}{2L\xi}\int_{x_-}^{x_+}\psi(x,t)\frac{\sinh\left((x-X)/L_c\right)}{\sinh\left(L/L_c\right)}dx,\end{aligned} \tag{6.61}$$

where in the first equality we have used that p is an odd function. The mean displacement and the mean squared displacement give

$$\begin{aligned}\bar{x}(t) &= \int_0^t \bar{v}(t')dt' \\ &= \frac{\zeta_{\mathrm{i}}^0\alpha}{2L\xi\sinh\left(L/L_c\right)}\int_0^t dt'\int_{x_-}^{x_+}\psi(x',t')\sinh\left(\frac{x'-X}{L_c}\right)dx',\end{aligned} \tag{6.62}$$

$$\begin{aligned}\langle\bar{x}(t)^2\rangle = &\left(\frac{\zeta_{\mathrm{i}}^0\alpha}{2L\xi\sinh\left(L/L_c\right)}\right)^2\int_0^t dt'\int_0^t dt''\int_{x_-}^{x_+}dx'\int_{x_-}^{x_+}dx'' \\ &\cdot\langle\psi(x',t')\psi(x'',t'')\rangle\sinh\left(\frac{x'-X}{L_c}\right)\sinh\left(\frac{x''-X}{L_c}\right),\end{aligned} \tag{6.63}$$

and since $\langle \bar{x}(t)^2 \rangle = 2tD_{\text{diff}}$ for long times, we can obtain the diffusion coefficient by substituting the noise correlation function. As before, we are assuming a colored noise defined by the correlation function in Eq. 6.54, and we get

$$\langle \bar{x}(t)^2 \rangle = \left(\frac{\zeta_{\text{i}}^0 \alpha}{L\xi} \right)^2 \frac{\epsilon}{8\lambda\tau \sinh^2(L/L_c)} F(t)G(L), \tag{6.64}$$

where the functions $F(t)$ and $G(L)$ are given by

$$F(t) = 2\tau \left(t + \tau(e^{-t/\tau} - 1) \right), \tag{6.65}$$

$$\begin{aligned} G(L) = \frac{L_c}{\lambda} \frac{1}{(1/\lambda^2 - 1/L_c^2)} \left(\sinh\left(\frac{2L}{L_c}\right) - \frac{2L}{L_c} \right) \\ + \frac{4e^{-L/\lambda}}{(1/L_c^2 - 1/\lambda^2)^2} \left(\frac{1}{L_c} \cosh\left(\frac{L}{L_c}\right) + \frac{1}{\lambda} \sinh\left(\frac{L}{L_c}\right) \right) \\ \cdot \left(\frac{1}{L_c} \cosh\left(\frac{L}{L_c}\right) \sinh\left(\frac{L}{\lambda}\right) - \frac{1}{\lambda} \sinh\left(\frac{L}{L_c}\right) \cosh\left(\frac{L}{\lambda}\right) \right). \end{aligned} \tag{6.66}$$

Therefore, the exact solution for the diffusion coefficient reads

$$D_{\text{diff}} = \left(\frac{\zeta_{\text{i}}^0 \alpha}{L\xi} \right)^2 \frac{\epsilon}{8\lambda \sinh^2(L/L_c)} G(L). \tag{6.67}$$

For a very small correlation length $\lambda \ll L_c$ (limit of spatially white noise), we obtain a simplified expression using $G(L) \approx \lambda L_c \left(\sinh\left(\frac{2L}{L_c}\right) - \frac{2L}{L_c} \right)$,

$$D_{\text{diff}} \approx \left(\frac{\zeta_{\text{i}}^0 \alpha}{L\xi} \right)^2 \frac{\epsilon L_c}{8 \sinh^2(L/L_c)} \left(\sinh\left(\frac{2L}{L_c}\right) - \frac{2L}{L_c} \right). \tag{6.68}$$

If we take a strictly white noise in both time and space, with $\langle \psi(x,t)\psi(x',t') \rangle = 2\epsilon\delta(x-x')\delta(t-t')$, from Eq. 6.63 we get

$$\begin{aligned} \langle \bar{x}(t)^2 \rangle &= \left(\frac{\zeta_{\text{i}}^0 \alpha}{2L\xi \sinh(L/L_c)} \right)^2 2\epsilon t \int_{x_-}^{x_+} dx' \sinh^2\left(\frac{x' - X}{L_c} \right) \\ &= \left(\frac{\zeta_{\text{i}}^0 \alpha}{L\xi} \right)^2 \frac{\epsilon L_c t}{4 \sinh^2(L/L_c)} \left(\sinh\left(\frac{2L}{L_c}\right) - \frac{2L}{L_c} \right), \end{aligned} \tag{6.69}$$

yielding the same diffusion coefficient as in Eq. 6.68.

The full expression for the colored noise (continuous lines in Fig. 6.5a) gives an interesting non-monotonic behavior, where at the limit of small system sizes ($L \to 0$), $D_{\text{diff}} \approx \frac{8L}{15\lambda} + \theta(L^2)$, and so the diffusion coefficient increases with system size until a maximum at L^*, plotted in Fig. 6.5b as a function of the noise correlation length λ. After the peak, the diffusion coefficient decreases with size. There are thus two effects at play: On the one hand, for enough small systems, if L is smaller or comparable to λ, then this correlation throughout the system enhances the overall motion, since a value taken by the noise persists in the entire system and for the correlation time, thus increasing the diffusion coefficient. This effect is less pronounced for larger systems, which generically average out fluctuations, leading to a decreasing diffusion coefficient with system size. For white noise or in the small correlation length limit $\lambda \ll L_c$ (dashed lines in Fig. 6.5a), the diffusion coefficient already decreases with the size, since at $L \to 0$, $D_{\text{diff}} \approx \frac{4\lambda}{3L} + \theta(L)$. This is because now $\lambda \to 0$, and only the decreasing effect due to an increase in system size is at play.

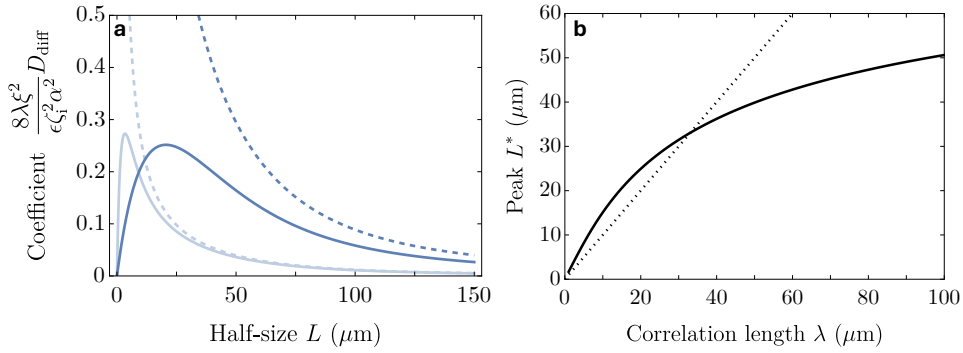

Figure 6.5: Diffusion coefficient for an external noise in the active traction. a, Analytical predictions for a dimensionless diffusion coefficient as a function of the half-size of the monolayer, for a noise correlation length of $\lambda = 2$ μm (light blue) and $\lambda = 15$ μm (dark blue), being $L_c = 30$ μm. The continuous line is the full expression (Eq. 6.67), whereas the dashed line is the limit for $\lambda \ll L_c$ (Eq. 6.68), which is a better approximation for the $\lambda = 2$ μm case. **b,** Half-size L^* that gives the peak for the diffusion coefficient in **a**, as a function of the noise correlation length (continuous line). The dotted line shows the $L^* = \lambda$ curve.

These results could be interesting for comparison with experimental measurements of diffusion coefficients of cellular clusters. A measured non-monotonic behavior could thus be a signature of external noise such as the one here modeled and would provide us with a way of inferring the noise correlation length.

6.4 Experimental data analysis

To compare the theoretical predictions from the previous chapters with experiments, and to try to infer the noise parameters, in this chapter we analyze data of traction force measurements in epithelial monolayers, from [Uroz2018] for the spreading of rectangular monolayers of MDCK cells, and from [Pérez-González2019] for confined circular monolayers of MDA-MB-231 cells. In this last experiment, the cells were genetically engineered to have an inducible promoter of the gene responsible for the expression of E-cadherin by adding dexamethasone. Therefore, E-cadherin expression increases with time, and so we cannot do temporal averages since the conditions, and hence parameters, are changing. Nevertheless, it is useful to analyze the data and focus on given time points. With this analysis, we argue to what extent the data can inform us about the noise origin, and use the theory (mainly for the additive noise in the polarity dynamics) to obtain some parameter estimates.

6.4.1 Noise origin

The experimental data has a subcellular resolution, but since our model is not intended to capture subcellular scales of the traction fluctuations, we apply a coarse-graining of the data to eliminate these fluctuations. We average windows of $w \times w$ traction values that should be comparable to the size of a cell, with w being odd integers so that the averaged value remains in the center of the window. For experiments in rectangular geometry, 1 bright field pixel ~ 0.16 μm and each traction value corresponds to 16 pixels ~ 2.56 μm. Since cells are around $\sim 100-200$ pixels ($16-32$ μm), we take $w = 7, 9, 11, 13$. In the circular monolayers, we have less resolution, 1 bright field pixel ~ 0.32 μm, but also each traction value corresponds to 16 pixels ~ 5.12 μm. Cells are similar sizes as in the rectangular case, so the sliding window is taken as the half, $w = 3, 5, 7$. In any case, we have checked that the results are not very sensitive to this parameter.

In Fig. 6.6 we plot the average kymographs for the rectangular and the circular monolayers. As expected, the horizontal traction T_x (Fig. 6.6b) and the radial traction T_r (Fig. 6.6e) (in the rectangular and circular cases respectively), are larger near the boundaries and point inwards, whereas the vertical traction T_y (Fig. 6.6c) and the tangential traction T_t (Fig. 6.6f) average to zero.

In Fig. 6.7, we plot the traction values and standard deviations as a function of the distance to the edge (either with the horizontal coordinate x for the rectangular case, or the radial coordinate r in the circular case). For the rectangular geometry, the fit for the traction in cartesian coordinates is exponential (only

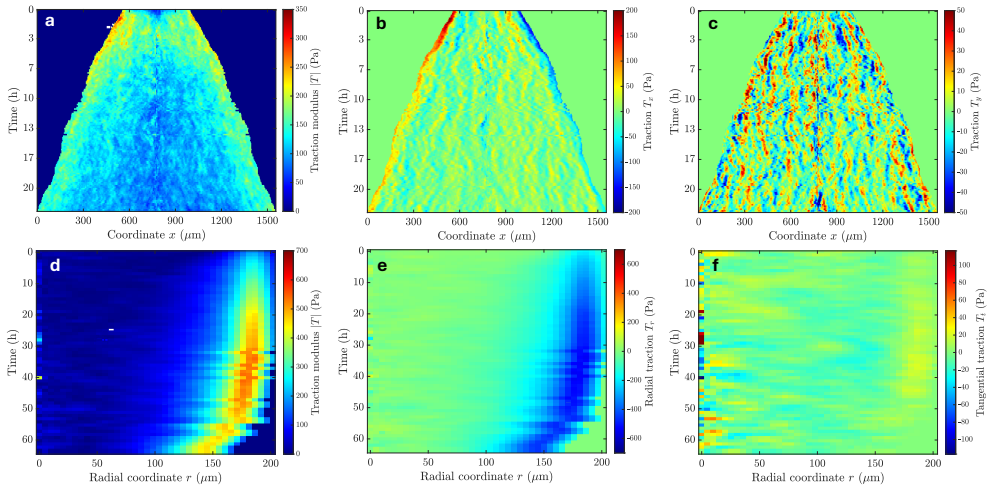

Figure 6.6: Traction kymographs. a-c, Traction kymographs of rectangular monolayers, averaging data from 3 experiments of MDCK cells from [Uroz2018], with a coarse-graining parameter of $w = 11$. Traction modulus (**a**), traction in the x direction (**b**, parallel to the direction of motion of the cells), and traction in the y direction (**c**, transversal to the direction of motion). **d-f,** Traction kymographs of circular confined monolayers of 200 μm of radii of MDA-MB-231 cells, and a 100 μg/ml collagen density in the coating solution. Data is averaged from 15 experiments, from [Pérez-González2019], with a coarse-graining parameter of $w = 5$. Traction modulus (**d**), traction in the radial direction (**e**), and traction in the tangential direction (**f**). Note the scale of the color bar is different in all the plots.

one side of the sinh from Eq. 6.4), so we can write

$$T_x(x) = T_0 e^{-x/L_c}, \tag{6.70}$$

whereas for the circular geometry, in polar coordinates, is [Pérez-González2019]

$$T_r(r) = T_0 \frac{I_1((R-r)/L_c)}{I_1(R/L_c)}, \tag{6.71}$$

being R the radius of the monolayer and I_1 the modified Bessel function of the first kind and first order. Here r is the distance from the edge, instead of the radial coordinate from the center to the edge. The first increase of traction very close to the edge in Fig. 6.7b is not captured by the model. Presumably, this may be a spurious effect due to fluctuations of the position of the edge. After this initial increase, the decrease is reasonably well fitted by this Bessel function. In both Fig. 6.7a and Fig. 6.7b, the standard deviation of the traction

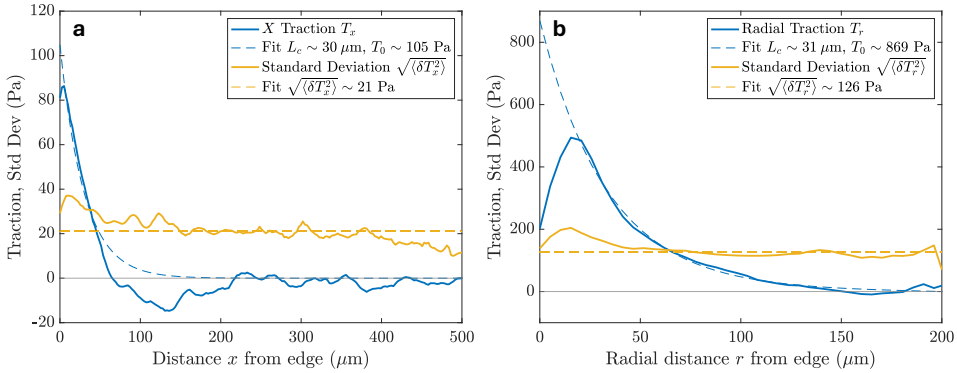

Figure 6.7: Traction as a function of the distance from the edge. a, Data of the X traction, T_x, and its standard deviation averaging both right and left edges. The fit (Eq. 6.70) gives $L_c \sim 30$ μm (about $2-3$ cells) and $T_0 \sim 105$ Pa, and the estimate for the standard deviation far from the edge is $\sqrt{\langle \delta T_x^2 \rangle} \sim 21$ Pa. Same data as in Fig. 6.6a-c, also with a coarse-graining of $w = 11$ but averaged in time to improve the statistics. **b,** Data of the traction in the radial direction, T_r, and its standard deviation, averaging radially. Same data as in Fig. 6.6d-f, also with a coarse-graining of $w = 5$, for the time point $t = 30$ h. The fit (Eq. 6.71) gives $L_c \sim 31$ μm and $T_0 \sim 869$ Pa, and $\sqrt{\langle \delta T_r^2 \rangle} \sim 126$ Pa.

measurements is larger near the edge, but still significantly large deep inside the monolayer, where we fit a horizontal line to estimate $\sqrt{\langle \delta T_\alpha^2 \rangle}$. This is a signature that both multiplicative noise (larger fluctuations where tractions are larger) and additive noise (homogeneous fluctuations throughout the system) coexist in the real tissue. The plot in Fig. 6.7b for the circular geometry is for a fixed time point since, in those experiments, the conditions change with time, and therefore, we cannot do temporal averages. However, we obtain good fits in all the time points, allowing us to plot the evolution of the fitted parameters in Fig. 6.8.

The experiments of circular confined monolayers were performed for three different collagen densities (1, 10, and 100 μg/ml) in the solution for the substrate coating. Since this density influences the number of cell-substrate adhesion ligands, we hypothesize that a difference in the fluctuations measurements could be interpreted as a signature of external noise in the active traction parameter. However, in Fig. 6.9 no significant differences are observed in the standard deviation fit far from the edge of the monolayer. Therefore we conclude that, within our modeling framework, the external noise is not as important as the internal one, that is, the noise in the polarity dynamics.

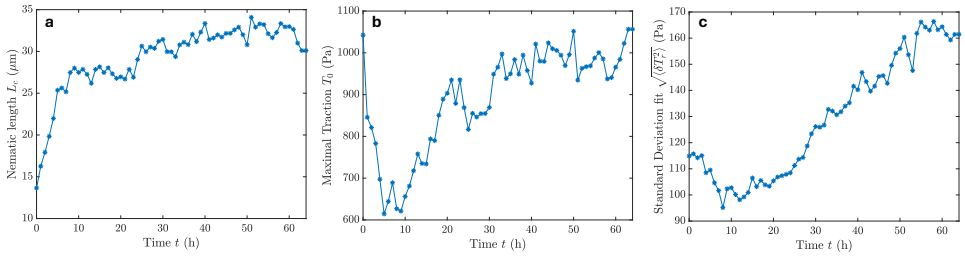

Figure 6.8: Evolution in time of the fitted parameters in circular monolayers. Evolution for the parameters L_c and T_0 obtained from fitting the radial traction T_r from Fig. 6.6d-f with Eq. 6.71, and $\langle \delta T_r^2 \rangle$ with a horizontal line far from the edge. They increase with time because the values of the tractions are also larger due to a greater E-cadherin expression. The values from Fig. 6.7b correspond to the $t = 30$ h time point.

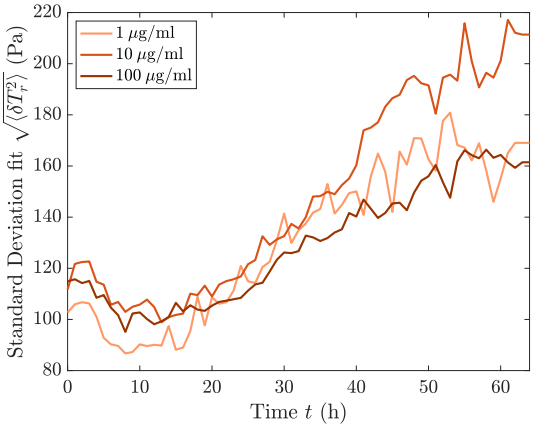

Figure 6.9: Effect of the coating density in circular monolayers. Standard deviation fits of the radial traction T_r with time, for different coating densities (1, 10, and 100 μg/ml). The last corresponds to the data in Fig. 6.6d-f, Fig. 6.7b and Fig. 6.8.

Moreover, although the multiplicative and the additive noise in the polarity coexist (as seen in Fig. 6.7), the plateau far from the edge remains larger than the increase in the edge, and so we conclude that the additive noise should be more significant than the multiplicative one. Both for this reason and for simplicity, in the following sections we focus on the analysis and comparison of the experimental data with the predictions of an additive noise in the polarity dynamics.

6.4.2 Estimation of an effective non-equilibrium temperature

Although the system is not at equilibrium, in Section 6.2.1.3 we saw that, in the approximation where the polarity dynamics is linear and decoupled from the velocity, a formal analogy with the fluctuation-dissipation theorem holds with an effective temperature. From this result, and to the extent that fluctuations in the system are consistent with those of the model, we can use the data to assign an effective temperature to the system. Since both the rectangular and circular geometry experiments are effectively 2D systems, we can obtain the variance of the polarization fluctuations through the integral of the structure factor in Eq. 6.23. However, note that there $\langle \delta p^2 \rangle \equiv \langle \delta p_x^2 + \delta p_y^2 \rangle \equiv \langle \delta p_r^2 + \delta p_t^2 \rangle$, but in Fig. 6.7 we plot only one component. Therefore, we divide the result of Eq. 6.23 by 2. Using $\epsilon\gamma_1 = k_B T$ (Eq. 6.27) and $\tau \equiv \gamma_1/a$, we get

$$\langle \delta p_\alpha^2 \rangle = \frac{k_B T}{4\pi a L_c^2} \ln\left(1 + L_c^2 q_{\max}^2\right). \tag{6.72}$$

Here, both a and K correspond to the 2D free energy, but from the literature, we typically have values in a volume, that is, in three dimensions. Therefore, we must convert this a to the typical 3D one by multiplying by the height of the monolayer h, $a = h a_{3D}$, since we integrate over the vertical dimension of the system. The effective equilibrium temperature thus reads

$$k_B T = \frac{4\pi h a_{3D} L_c^2 \langle \delta p_\alpha^2 \rangle}{\ln\left(1 + L_c^2 q_{\max}^2\right)}, \tag{6.73}$$

where the cutoff $q_{\max} = 2\pi/\lambda_{\min}$ comes from the coarse-graining in the data analysis. As explained in Section 6.4.1, we have taken values of the coarse-graining w such that we average approximately the size of a cell, and so $\lambda_{\min} \sim (16 - 32)$ μm[1]. We also need to relate $\langle \delta p_\alpha^2 \rangle$ to experimental observables. From the experimental data we get values of the variance of the traction force measurements $\langle \delta T_\alpha^2 \rangle$, which are related to the polarization through force balance $T_\alpha = -h f_\alpha = h(\xi v_\alpha - \zeta_{\mathrm{i}} p_\alpha)$ (Eq. 2.15). Then,

$$\begin{aligned} \langle \delta T_\alpha^2 \rangle &= \langle (T_\alpha - \langle T_\alpha \rangle)^2 \rangle = h^2 \langle (\xi \delta v_\alpha - \zeta_{\mathrm{i}} \delta p_\alpha)^2 \rangle = h^2 \big(\xi^2 \langle \delta v_\alpha \rangle^2 \\ &+ \zeta_{\mathrm{i}}^2 \langle \delta p_\alpha \rangle^2 - 2\xi\zeta_{\mathrm{i}} \langle \delta v_\alpha \delta p_\alpha \rangle \big) \approx h^2 \left(\xi^2 \langle \delta v_\alpha \rangle^2 + \zeta_{\mathrm{i}}^2 \langle \delta p_\alpha \rangle^2 \right), \end{aligned} \tag{6.74}$$

where we have assumed first order in the fluctuations, $\langle \delta v_\alpha \delta p_\alpha \rangle = \langle v_\alpha p_\alpha \rangle - \langle v_\alpha \rangle \langle p_\alpha \rangle \approx 0$. By definition, $T_0 \equiv h\zeta_{\mathrm{i}}$ is the maximal traction stress in the

[1] To be more precise, $\lambda_{\min} = 2.56w$ μm for the rectangular geometry and $\lambda_{\min} = 5.12w$ μm for the circular one.

experiments, and so

$$\langle \delta p_\alpha^2 \rangle \approx \frac{1}{h^2 \zeta_\mathrm{i}^2} \big(\langle \delta T_\alpha^2 \rangle - h^2 \xi^2 \langle \delta v_\alpha^2 \rangle \big) \approx \frac{1}{T_0^2} \big(\langle \delta T_\alpha^2 \rangle - h^2 \xi^2 \langle \delta v_\alpha^2 \rangle \big). \tag{6.75}$$

Moreover, taking realistic estimated values from experiments, we see that the term containing the friction and the velocity fluctuations can be neglected. A realistic range for the friction parameter is $\xi \sim (100 - 600)$ Pa $\cdot$ s/μm^2 $\sim (0.03 - 0.2)$ Pa $\cdot$ h/μm^2 [Pérez-González2019], and we take $\sqrt{\langle \delta v_x^2 \rangle} \sim 5$ μm/h for the fluctuations in the velocity (Fig. 6.10). Thus, assuming a typical monolayer height of $h \sim 5$ μm, the friction term is of the order of $h^2 \xi^2 \langle \delta v_x^2 \rangle \sim (0.6 - 25)$ Pa^2. Considering that the fluctuations of the traction are $\langle \delta T_x \rangle^2 \sim 21^2$ Pa^2 $= 441$ Pa^2 (Fig. 6.7a), the friction term is between one and three orders of magnitude smaller and can thus be neglected. Therefore,

$$\langle \delta p_\alpha \rangle^2 \approx \frac{\langle \delta T_\alpha^2 \rangle}{T_0^2}. \tag{6.76}$$

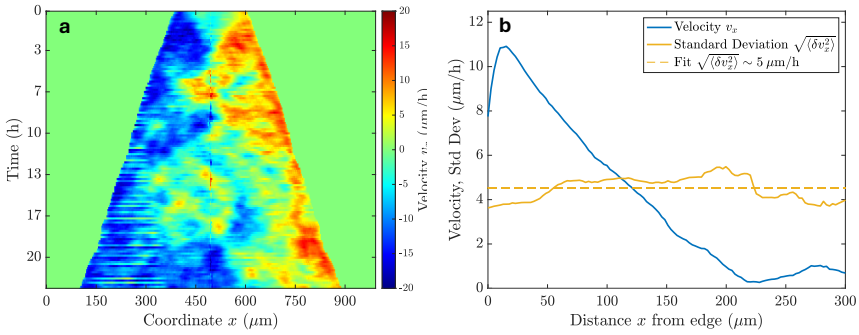

Figure 6.10: Velocity in rectangular monolayers. a, Kymograph of the X velocity, v_x for a rectangular monolayer. **b,** v_x as a function of distance from the edge, averaging both edges (changing the sign of the velocity on the left edge). We estimate from here $\sqrt{\langle \delta v_x^2 \rangle} \sim 5$ μm/h. Data is from only one experiment of MDCK cells from [Uroz2018], with a coarse-graining parameter of $w = 11$.

Let's now give values in the two different geometries. It is important to note that the coarse-graining parameter w does not change the order of magnitude of the results, because although q_max decreases if w increases, also $\langle \delta p_\alpha^2 \rangle$ decreases since the traction fluctuations are averaged on a larger window (Fig. 6.11c), while both L_c and T_0 remain very similar for different coarse-graining parameters (Fig. 6.11a,b). Therefore, we just show the estimates for the coarse-graining

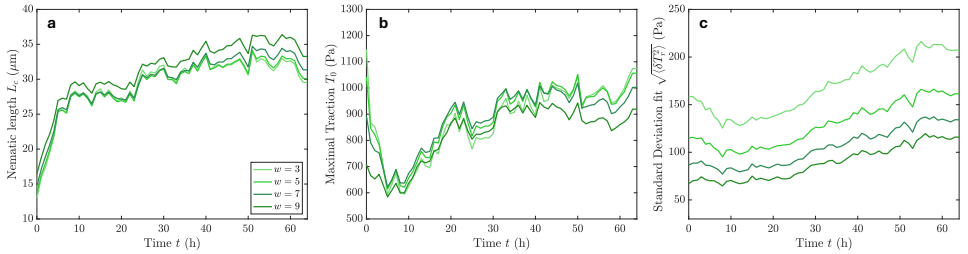

Figure 6.11: Effect of the coarse-grainig in circular monolayers. Evolution in time for the parameters L_c and T_0 obtained from fitting the radial traction T_r with Eq. 6.71, and $\langle \delta T_r^2 \rangle$ with a horizontal line far from the edge. Data comes from the kymographs of circular monolayers but with different coarse-graining parameters ($w = 3, 5, 7, 9$, from light to dark green). The $w = 11$ case corresponds to the same curves as in Fig. 6.8.

parameters already chosen in Fig. 6.6 and Fig. 6.7. Taking $a_{3D} \sim (1 - 20)$ Pa and $h \sim 5$ μm [Blanch-Mercader2017a, Pérez-González2019], then:

- **Rectangular monolayers**: From Fig. 6.7a (coarse-graining $w = 11 \rightarrow \lambda_{\min} \sim 28$ μm), we take $L_c \sim 30$ μm, $T_0 \sim 105$ Pa and $\sqrt{\langle \delta T_x^2 \rangle} \sim 21$ Pa. From Eq. 6.76, $\langle \delta p_x^2 \rangle \sim 0.04$, and so using Eq. 6.73, we get

$$k_B T \approx 4\pi \frac{5 \cdot a_{3D} \cdot 30^2 \cdot 0.04}{\ln\left(1 + 30^2 \cdot \left(\frac{2\pi}{28}\right)^2\right)} \approx (0.6 - 11.8) \cdot 10^3 \text{ Pa} \cdot \mu\text{m}^3,$$

  which is $k_B T \approx (0.6 - 11.8) \cdot 10^6$ pN $\cdot$ nm $\approx (0.15 - 2.9) \cdot 10^6$ $k_B T^*$ (at room temperature $T^* = 298$ K, we know $k_B T^* = 4.11$ pN$\cdot$nm).

- **Circular monolayers**: From Fig. 6.7b (coarse-graining $w = 5 \rightarrow \lambda_{\min} \sim 26$ μm), we take $L_c \sim 31$ μm, $T_0 \sim 869$ Pa and $\sqrt{\langle \delta T_r^2 \rangle} \sim 126$ Pa. From Eq. 6.76, $\langle \delta p_r^2 \rangle \sim 0.02$, and so using Eq. 6.73, we get

$$k_B T \approx 4\pi \frac{5 \cdot a_{3D} \cdot 31^2 \cdot 0.02}{\ln\left(1 + 31^2 \cdot \left(\frac{2\pi}{26}\right)^2\right)} \approx (0.3 - 6.0) \cdot 10^3 \text{ Pa} \cdot \mu\text{m}^3,$$

  which is $k_B T \approx (0.3 - 6.0) \cdot 10^6$ pN $\cdot$ nm $\approx (0.07 - 1.5) \cdot 10^6$ $k_B T^*$.

Summarizing, we get an effective temperature around $10^5 - 10^6$ $k_B T^*$. This is quite big, because the fluctuations in the system are indeed macroscopic, and energetically significant at the characteristic energy scale of the polarization,

$aL_c^2 = K$. We can compare this energy scale of fluctuations with an estimation based on cell mechanics in the tissue. Considering the typical traction force per unit area of a cell as $\sim (10 - 100)$ Pa (standard deviation in the center of the monolayer in Fig. 6.7) and its typical length as ~ 10 μm, then the typical force scale is $\sim (1 - 10) \cdot 10^3$ Pa$\cdot\mu$m^2 $= (1 - 10)$ nN. The lamellipodia has turnover times in the order of 30 seconds to a few minutes. Taking ~ 1 min, and with a velocity of $\sim 5 \cdot \mu$m/h (standard deviation in Fig. 6.10), this gives a displacement of ~ 0.1 μm. Then, the work is $\sim (0.1 - 1)$ nN$\cdot\mu$m $= 10^5 - 10^6$ pN$\cdot$nm. This is the same order of magnitude as what we obtained above. So we can argue that the energy of the fluctuations is comparable to the scale of the mechanical energy generated by the cells. Therefore, the fluctuations originate from the cell machinery itself.

6.4.3 Autocorrelation functions

In Section 6.2.1.1 we predicted the autocorrelation functions for the polarization fluctuations, both spatially and temporally (Eq. 6.11 and Eq. 6.18 for a 2D system). Mapping the traction with the polarization, we expect the autocorrelation of the traction fluctuations to have the same dependence. Therefore, for the X traction T_x in the rectangular geometry, and for the radial traction T_r in the radial geometry, we expect a temporal correlation function $\langle \delta T_\alpha(t) \delta T_\alpha(t') \rangle \propto e^{-|t-t'|/\tau}$, and a spatial correlation function $\langle \delta T_\alpha(\mathbf{r}) \delta T_\alpha(\mathbf{r}') \rangle \propto K_0(|\mathbf{r} - \mathbf{r}'|/L_c)$. In Fig. 6.12 we plot the spatial and temporal autocorrelation functions in the two experimental datasets. The data analysis method is explained in Appendix 6.E.

We can see that an exponential function fits well the temporal correlation functions (Fig. 6.12b,d), giving correlation times of $\tau \sim 0.6$ h for the rectangular geometry, and $\tau \sim 0.8$ h for the circular one. However, a clear discrepancy exists between the experimental data and the theoretical fits for the spatial correlation functions (Fig. 6.12a,c). Instead, at least for the rectangular geometry Fig. 6.12a, we see a negative autocorrelation at lengths of about 30 μm, between one and two cells, which could be a signature of the internal structure of cells, which exhibit anticorrelation at the cell scale due to the dipolar force distribution. The inner force distribution at this single-cell scale is clearly not captured by our model, which is designed to describe supracellular structures. However, in other experiments that do not reflect such internal structure, we could still expect to observe the behavior predicted by our theory of additive noise in the polarity dynamics. For instance, this might be the case of [Saraswathibhatla2021], where the spatial traction autocorrelation decays to zero over a distance of two cell diameters. Whether those data can be fitted with our theory will be discussed elsewhere.

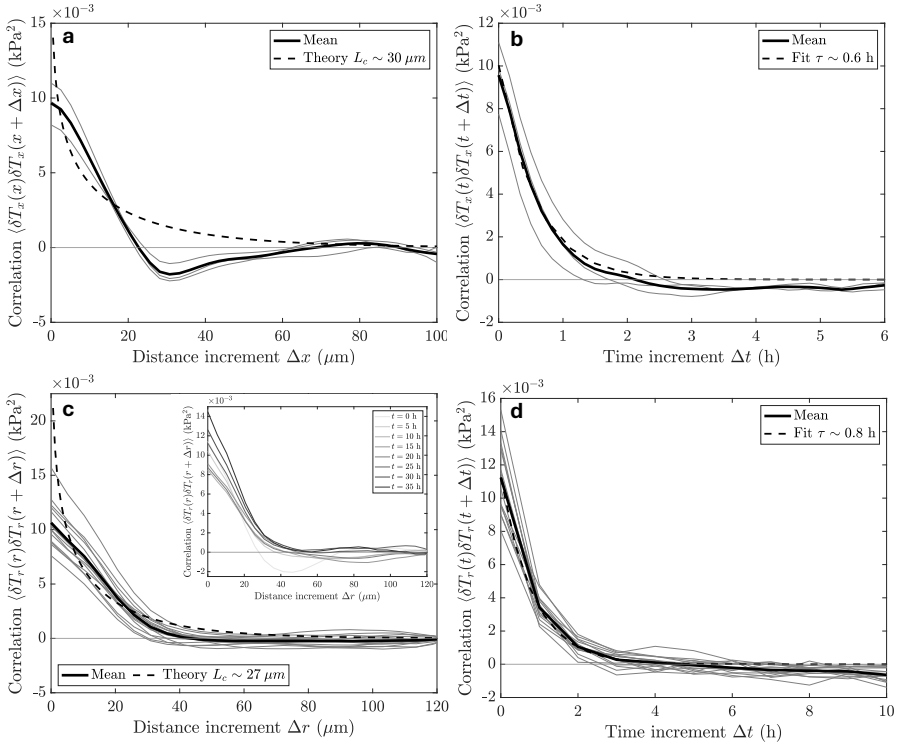

Figure 6.12: Autocorrelation functions of the traction fluctuations. a,b, Spatial (**a**) and temporal (**b**) autocorrelation of the X traction δT_x in rectangular monolayers, from the same data as in Fig. 6.6a-c, also with a coarse-graining of $w = 11$ and averaged in time. **c,d,** Spatial (**c**) and temporal (**d**) autocorrelation of the radial traction δT_r in circular monolayers, from the same data as in Fig. 6.6d-f, also with a coarse-graining of $w = 5$. The spatial correlation is very similar at different time-points (**inset, c**), and so in **c** we plot the time average up to 36 h. The black continuous line is the mean of all the experiments (which are represented in the grey thin lines), and the dashed line is the theoretical fit, taking L_c either from Fig. 6.7a or averaging Fig. 6.8a for the considered times.

In addition to the discrepancies between our model and real data due to the data's subcellular resolution, there is yet another general limitation that must always be considered with care, namely, the assumption of weak noise. This has allowed us to decouple the polarization field from the velocity (see Appendix 6.A) and thus largely simplify the analysis. However, we have seen that fluctuations are relatively large, compared to the typical energy scales associated with cell polarization. It is thus possible that the coupling between velocity and polarization is relevant in some cases, requiring a more general treatment of

noise. Overall, in the simplicity of our model resides the power to make strong and useful predictions in many situations. A model with full nonlinear couplings is expected to be more accurate but would lack some of the insights and predictive power of our simplified version.

6.5 Discussion and conclusions

In this chapter, we have proposed three different ways to introduce stochastic terms in our continuum model of epithelial monolayers, accounting for the inherent randomness of biological systems, and we have compared the predictions with experimental data of traction force fluctuations.

We first modeled an internal noise coming from the tissue by introducing noise in the polarity dynamics. We considered cases of both additive and multiplicative noise. We focused mostly on the additive one for simplicity and because it was observed in the experimental data that it was the most relevant noise source. We obtained theoretical predictions for the diffusion coefficient of a cell cluster for both cases, also showing that the multiplicative noise case was subdominant for large systems. For the additive noise, we computed the correlation functions and the power spectral densities. These observables can be compared with existing data, except for the diffusion coefficient, for which no sufficient data was available. For the correlation functions, we obtained that the temporal correlation was well captured by the model, and could give estimates for the correlation time. The spatial correlation function, however, featured effects not included in our model, possibly related to internal structure at the subcellular scale. The discrepancies can also be attributed partly to the weak noise approximation assumed in the model, which excludes correlations between polarization and velocity fluctuations. The results obtained for the power spectral density and the diffusion coefficient could also be useful to fit experimental data and infer model parameters, which we defer to future work.

Another possible noise source we have considered is that of an external noise coming from the adhesion with the substrate, through the ligand kinetics. This was modeled by adding noise to the active traction parameter. In this case, the diffusion coefficient gives a non-monotonic dependency with the monolayer cluster size, which we did not observe when adding noise in the polarity dynamics. Therefore, if this behavior was observed in experimental data, it could be a signature of the presence of this type of external noise.

The proposed formalism also gave us a way to characterize the noise statistics in terms of an effective, nonequilibrium temperature in the tissue. From the experimental data, we could get values of the effective energy scale k_BT which

are large, consistent with the macroscopic character of the fluctuations at the cell scale, which is consistent with estimates based on the inner mechanical processes that generate the polarization fluctuations.

All in all, this new formalism gives us the possibility to model more realistic situations that account for the randomness of living systems, and a powerful tool to get information about the system through the fluctuations of some variables, in this case, the traction forces. Our model is a first step towards a theory of fluctuating hydrodynamics of tissues. The next step to improve our approach must include the coupling of polarization and velocity fluctuations in the bulk as well as the fluctuations of the boundary.

Acknowledgements

I want to thank Ricard Alert for some discussions during the development of the theory and more specifically for the comparison with experimental data.

Appendices

6.A Weak noise approximation

The full equation for the polarity dynamics was given in Eq. 2.1 from Chapter 2. Neglecting flow alignment and active spontaneous polarization effects ($\bar{\nu}_1, \nu_1, \epsilon \to 0$), but keeping the advection and co-rotation terms, it reads

$$(\partial_t + v_\beta \partial_\beta) p_\alpha + \omega_{\alpha\beta} p_\beta = -\frac{1}{\gamma_1} \left(a p_\alpha - K \nabla^2 p_\alpha \right) + \psi_\alpha, \tag{6.A.1}$$

where we have added a noise term ψ_α. We can also write the force balance equation, which comes from Eq. 2.9, Eq. 2.14 and Eq. 2.15, being

$$\eta \nabla^2 v_\alpha - \xi v_\alpha = -\zeta_\mathrm{i} p_\alpha - \zeta \partial_\beta (p_\alpha p_\beta). \tag{6.A.2}$$

To linear order in the perturbations, and so assuming a weak noise approximation, the solutions for the polarization and velocity can be written as $p_\alpha = p^0_\alpha + \delta p_\alpha$ and $v_\alpha = v^0_\alpha + \delta v_\alpha$, where p^0_α and v^0_α are the respective fields at equilibrium. Then, the dynamics of the polarity perturbations reads

$$\begin{aligned} \partial_t \delta p_\alpha + v^0_\beta \partial_\beta \delta p_\alpha + \delta v_\beta \partial_\beta p^0_\alpha + \omega^0_{\alpha\beta} \delta p_\beta + \delta \omega_{\alpha\beta} p^0_\beta = \\ = -\frac{1}{\gamma_1} \left(a \delta p_\alpha - K \nabla^2 \delta p_\alpha \right) + \psi_\alpha. \end{aligned} \tag{6.A.3}$$

In the central region of the system ($r < R - L_c$ for a circular monolayer), we can assume that $p^0_\alpha \approx 0$, and with a small friction ($\xi \to 0$), we get $v^0_\alpha \sim (\zeta_\mathrm{i} L_c / \eta) r_\alpha$ from Eq. 6.A.2. This gives $\omega^0_{\alpha\beta} \approx 0$. Thus the equation for the polarity perturbations gets greatly simplified,

$$\partial_t \delta p_\alpha + v^0_\beta \partial_\beta \delta p_\alpha \approx -\frac{1}{\gamma_1} \left(a \delta p_\alpha - K \nabla^2 \delta p_\alpha \right) + \psi_\alpha. \tag{6.A.4}$$

Assuming that $\partial_\beta \delta p_\alpha \sim \delta p_\alpha / L_c$, we see that the term $v_\beta^0 \partial_\beta \delta p_\alpha$ can be neglected in front of $a\delta p_\alpha/\gamma_1$ if

$$\frac{\zeta_\mathrm{i} L_c R}{\eta} \frac{\delta p_\alpha}{L_c} \ll \frac{a}{\gamma_1} \delta p_\alpha \longrightarrow \frac{\zeta_\mathrm{i} R}{\eta} \ll \frac{a}{\gamma_1} \equiv \tau^{-1} \longrightarrow \tau \ll \frac{\eta}{\zeta_\mathrm{i} R}. \tag{6.A.5}$$

The advection term can thus be neglected as long as the relaxation of the polarity field is sufficiently fast compared to other processes in the system. Equivalently, this implies that the shear viscosity is much larger than the rotational viscosity, satisfying $\frac{\gamma_1}{\eta} \ll \frac{a}{\zeta_\mathrm{i} R}$. If this applies, we get

$$\partial_t \delta p_\alpha \approx -\frac{1}{\gamma_1} \left(a\delta p_\alpha - K\nabla^2 \delta p_\alpha \right) + \psi_\alpha, \tag{6.A.6}$$

This is the main equation we use throughout the chapter, introduced in Eq. 6.7. In general, if the noise is strong, and/or if the above condition is not satisfied, a stochastic model for the two coupled equations for velocity and polarity must be considered.

6.B On Fourier transforms and Dirac delta functions

Given a function $f(\mathbf{r},t)$, $\mathbf{r}\in\mathbb{R}^d$, the Fourier transform in space is defined as

$$\hat{f}(\mathbf{q},t)=\int_{\mathbb{R}^d} f(\mathbf{r},t)e^{-i\mathbf{q}\cdot\mathbf{r}}d\mathbf{r}, \tag{6.B.1}$$

while given $\hat{f}(\mathbf{q},t)$, the inverse Fourier transform is

$$f(\mathbf{r},t)=\frac{1}{(2\pi)^d}\int_{\mathbb{R}^d}\hat{f}(\mathbf{q},t)e^{i\mathbf{q}\cdot\mathbf{r}}d\mathbf{q}. \tag{6.B.2}$$

The Fourier transform in time is equally defined but for the integration limits in a 1D space. The Dirac Delta function is

$$\delta(\mathbf{r})=\frac{1}{(2\pi)^d}\int_{\mathbb{R}^d}e^{i\mathbf{p}\cdot\mathbf{r}}d\mathbf{p}, \tag{6.B.3}$$

and it is an even function, since $\delta(-\mathbf{r})=\delta(\mathbf{r})$. We see from the definition that, for $\mathbf{p}$ in a spatial domain $\mathbf{p}\in L^d$, or in a temporal domain $p\in T$, then

$$\delta(\mathbf{0})=\frac{1}{(2\pi)^d}\int_{\mathbb{R}^d}e^{i\mathbf{p}\cdot\mathbf{0}}d\mathbf{p}=\frac{L^d}{(2\pi)^d},\quad \delta(0)=\frac{1}{2\pi}\int_{\mathbb{R}}e^{ip\cdot 0}dp=\frac{T}{2\pi}. \tag{6.B.4}$$

Being $\langle\psi_\alpha(\mathbf{r},t)\psi_\beta(\mathbf{r}',t')\rangle=2\epsilon\delta(\mathbf{r}-\mathbf{r}')\delta(t-t')\delta_{\alpha\beta}$ the autocorrelation function for a vectorial noise ψ_α, then in Fourier space for the position, it reads

$$\begin{aligned}\langle\hat{\psi}_\alpha(\mathbf{q},t)\hat{\psi}_\beta(\mathbf{q}',t')\rangle&=\int_{\mathbb{R}^d}d\mathbf{r}\int_{\mathbb{R}^d}d\mathbf{r}'e^{-i\mathbf{q}\cdot\mathbf{r}}e^{-i\mathbf{q}'\cdot\mathbf{r}'}\langle\psi_\alpha(\mathbf{r},t)\psi_\beta(\mathbf{r}',t')\rangle\\&=\int_{\mathbb{R}^d}d\mathbf{r}\int_{\mathbb{R}^d}d\mathbf{r}'e^{-i\mathbf{q}\cdot\mathbf{r}-i\mathbf{q}'\cdot\mathbf{r}'}2\epsilon\delta(\mathbf{r}-\mathbf{r}')\delta(t-t')\delta_{\alpha\beta}\\&=2\epsilon\int_{\mathbb{R}^d}d\mathbf{r}e^{-i(\mathbf{q}+\mathbf{q}')\cdot\mathbf{r}}\delta(t-t')\delta_{\alpha\beta}=2\epsilon(2\pi)^d\delta(\mathbf{q}+\mathbf{q}')\delta(t-t')\delta_{\alpha\beta}.\end{aligned} \tag{6.B.5}$$

And also in Fourier space for the time,

$$\begin{aligned}\langle\hat{\tilde{\psi}}_\alpha(\mathbf{q},\omega)\hat{\tilde{\psi}}_\beta(\mathbf{q}',\omega')\rangle&=\int_{\mathbb{R}^d}d\mathbf{r}\int_{\mathbb{R}^d}d\mathbf{r}'\int_{-\infty}^{\infty}dt\int_{-\infty}^{\infty}dt'e^{-i\mathbf{q}\cdot\mathbf{r}-i\omega t}e^{-i\mathbf{q}'\cdot\mathbf{r}'-i\omega' t'}.\\&\cdot\langle\psi_\alpha(\mathbf{r},t)\psi_\beta(\mathbf{r}',t')\rangle=\int_{\mathbb{R}^d}d\mathbf{r}\int_{\mathbb{R}^d}d\mathbf{r}'\int_{-\infty}^{\infty}dt\int_{-\infty}^{\infty}dt'e^{-i\mathbf{q}\cdot\mathbf{r}-i\mathbf{q}'\cdot\mathbf{r}'}e^{-i\omega t-i\omega' t'}.\\&\cdot 2\epsilon\delta(\mathbf{r}-\mathbf{r}')\delta(t-t')\delta_{\alpha\beta}=2\epsilon\int_{\mathbb{R}^d}d\mathbf{r}e^{-i(\mathbf{q}+\mathbf{q}')\cdot\mathbf{r}}\int_{-\infty}^{\infty}dte^{-i(\omega+\omega')t}\\&=2\epsilon(2\pi)^d\delta(\mathbf{q}+\mathbf{q}')2\pi\delta(\omega+\omega')\delta_{\alpha\beta}.\end{aligned} \tag{6.B.6}$$

6.C Additive polarity calculations

Using polar coordinates (r and q are the moduli), we compute the inverse Fourier transform of a Lorentzian function in two dimensions,

$$\mathcal{F}^{-1}\left[\frac{1}{c^2+\mathbf{q}^2}\right] = \frac{1}{(2\pi)^2}\int_{\mathbb{R}^2}\frac{e^{i\mathbf{q}\cdot\mathbf{r}}}{c^2+\mathbf{q}^2}d\mathbf{q} = \frac{1}{(2\pi)^2}\int_0^\infty\int_0^{2\pi}\frac{e^{iqr\cos\theta}}{c^2+q^2}qdqd\theta$$
$$= \frac{1}{(2\pi)^2}\int_0^\infty\frac{qdq}{c^2+q^2}\int_0^{2\pi}e^{iqr\cos\theta}d\theta = \frac{1}{2\pi}\int_0^\infty\frac{qJ_0(qr)}{c^2+q^2}dq = \frac{K_0(cr)}{2\pi}, \quad (6.C.1)$$

where J_0 is the Bessel function of the first kind and K_0 is the modified Bessel function of the second kind, both of zeroth-order.

Using the definition for the correlation function of the polarization fluctuations in a $d-$dimensional domain L^d,

$$C(\mathbf{r}) \equiv \left\langle \frac{1}{L^d}\int_{L^d}\delta p_\alpha(\mathbf{r}',t)\delta p_\alpha(\mathbf{r}'+\mathbf{r},t)d\mathbf{r}'\right\rangle, \quad (6.C.2)$$

with a change of variables $\mathbf{s} = \mathbf{r}' + \mathbf{r}$, the static structure factor is

$$S(\mathbf{q}) \equiv \int_{L^d}C(\mathbf{r})e^{-i\mathbf{q}\cdot\mathbf{r}}d\mathbf{r} = \frac{1}{L^d}\left\langle\int_{L^d}\int_{L^d}\delta p_\alpha(\mathbf{r}',t)\delta p_\alpha(\mathbf{r}'+\mathbf{r},t)e^{-i\mathbf{q}\cdot\mathbf{r}}d\mathbf{r}'d\mathbf{r}\right\rangle$$
$$= \frac{1}{L^d}\left\langle\int_{L^d}\int_{L^d}\delta p_\alpha(\mathbf{r}',t)\delta p_\alpha(\mathbf{s},t)e^{-i\mathbf{q}\cdot(\mathbf{s}-\mathbf{r}')}d\mathbf{r}'d\mathbf{s}\right\rangle$$
$$= \frac{1}{L^d}\left\langle\int_{L^d}\delta p_\alpha(\mathbf{r}',t)e^{-i(-\mathbf{q})\cdot\mathbf{r}'}d\mathbf{r}'\int_{L^d}\delta p(\mathbf{s},t)e^{-i\mathbf{q}\cdot\mathbf{s}}d\mathbf{s}\right\rangle$$
$$= \frac{1}{L^d}\langle\delta\hat{p}_\alpha(-\mathbf{q},t)\delta\hat{p}_\alpha(\mathbf{q},t)\rangle = \frac{1}{L^d}\langle|\delta\hat{p}(\mathbf{q},t)|^2\rangle. \quad (6.C.3)$$

The autocorrelation, which is the correlation function for $\mathbf{r}=0$, reads

$$\langle\delta p^2\rangle \equiv C(\mathbf{0}) = \left\langle\frac{1}{L^d}\int_{L^d}\delta p_\alpha(\mathbf{r})\delta p_\alpha(\mathbf{r})d\mathbf{r}\right\rangle = \frac{1}{L^d}\left\langle\int_{L^d}d\mathbf{r}\frac{1}{(2\pi)^d}\right.$$
$$\left.\int_{\Omega^d}\delta\hat{p}_\alpha(\mathbf{q},t)e^{i\mathbf{q}\cdot\mathbf{r}}d\mathbf{q}\frac{1}{(2\pi)^d}\int_{\Omega^d}\delta\hat{p}_\alpha(\mathbf{q}',t)e^{i\mathbf{q}'\cdot\mathbf{r}}d\mathbf{q}'\right\rangle$$
$$= \frac{1}{L^d(2\pi)^d}\int_{\Omega^d}\int_{\Omega^d}\langle\delta\hat{p}_\alpha(\mathbf{q},t)\delta\hat{p}_\alpha(\mathbf{q}',t)\rangle\,\delta(\mathbf{q}+\mathbf{q}')d\mathbf{q}d\mathbf{q}'$$
$$= \frac{1}{L^d(2\pi)^d}\int_{\Omega^d}\langle|\delta\hat{p}(\mathbf{q},t)|^2\rangle d\mathbf{q} = \frac{1}{(2\pi)^d}\int_{\Omega^d}S(\mathbf{q})d\mathbf{q}, \quad (6.C.4)$$

because $\langle|\delta\hat{p}(\mathbf{q},t)|^2\rangle = L^dS(\mathbf{q})$ has just been computed in Eq. 6.C.3.

Now, if the signal evolves with time, then the correlation function is

$$C(\mathbf{r},t) \equiv \left\langle \frac{1}{L^d T} \int_{L^d} \int_T \delta p_\alpha(\mathbf{r}',t') \delta p_\alpha(\mathbf{r}'+\mathbf{r}, t'+t) dt' d\mathbf{r}' \right\rangle. \tag{6.C.5}$$

With a change $\mathbf{s} = \mathbf{r}' + \mathbf{r}$ and $\xi = t' + t$, the dynamic structure factor is

$$\begin{aligned}
S(\mathbf{q},\omega) &\equiv \int_{L^d}\int_T C(\mathbf{r},t) e^{-i\omega t} e^{-i\mathbf{q}\cdot\mathbf{r}} dt d\mathbf{r} \\
&= \frac{1}{L^d T}\left\langle \int_{L^d}\int_T \int_{L^d}\int_T \delta p_\alpha(\mathbf{r}',t')\delta p_\alpha(\mathbf{r}'+\mathbf{r},t'+t) e^{-i\mathbf{q}\cdot\mathbf{r}} e^{-i\omega t} dt' d\mathbf{r}' dt d\mathbf{r} \right\rangle \\
&= \frac{1}{L^d T}\left\langle \int_{L^d}\int_T \int_{L^d}\int_T \delta p_\alpha(\mathbf{r}',t')\delta p_\alpha(\mathbf{s},\xi) e^{-i\mathbf{q}\cdot(\mathbf{s}-\mathbf{r}')} e^{-i\omega(\xi-t')} dt' d\mathbf{r}' d\xi d\mathbf{s} \right\rangle \\
&= \frac{1}{L^d T}\Bigg\langle \int_{L^d}\int_T \delta p_\alpha(\mathbf{r}',t') e^{-i(-\mathbf{q})\cdot\mathbf{r}'} e^{-i(-\omega)t'} dt' d\mathbf{r}' \\
&\cdot \int_{L^d}\int_T \delta p_\alpha(\mathbf{s},\xi) e^{-i\mathbf{q}\cdot\mathbf{s}} e^{-i\omega\xi} d\xi d\mathbf{s} \Bigg\rangle = \frac{1}{L^d T}\langle \delta\hat{\tilde{p}}_\alpha(-\mathbf{q},-\omega)\delta\hat{\tilde{p}}_\alpha(\mathbf{q},\omega)\rangle \\
&= \frac{1}{L^d T}\langle |\delta\hat{\tilde{p}}(\mathbf{q},\omega)|^2\rangle.
\end{aligned} \tag{6.C.6}$$

For a 1D system, the mean squared displacement can be computed by plugging the autocorrelation in Fourier space (Eq. 6.11) in the third equality, and also using that $\int_0^t dt' \int_0^t dt'' e^{-|t'-t''|/\beta} = 2\beta\left(t + \beta\left(e^{-t/\beta} - 1\right)\right)$. It gives

$$\begin{aligned}
\langle \bar{x}(t)^2\rangle &= \left(\frac{\zeta_\mathrm{i}}{2L\xi}\right)^2 \int_0^t dt' \int_0^t dt'' \int_{x_-}^{x_+} dx' \int_{x_-}^{x_+} dx'' \langle \delta p(x',t')\delta p(x'',t'')\rangle \\
&= \left(\frac{\zeta_\mathrm{i}}{2L\xi}\right)^2 \int_0^t dt' \int_0^t dt'' \int_{x_-}^{x_+} dx' \int_{x_-}^{x_+} dx'' \frac{1}{(2\pi)^2} \int_{-\infty}^{\infty} dq \int_{-\infty}^{\infty} dq' \\
&\cdot \langle \delta\hat{p}(q,t')\delta\hat{p}(q',t'')\rangle e^{iqx'} e^{iq'x''} = \left(\frac{\zeta_\mathrm{i}}{2L\xi}\right)^2 \int_0^t dt' \int_0^t dt'' \int_{x_-}^{x_+} dx' \int_{x_-}^{x_+} dx'' \\
&\cdot \frac{\epsilon}{2\pi} \int_{-\infty}^{\infty} dq \int_{-\infty}^{\infty} dq' \delta(q+q') \frac{e^{-\omega(q)|t'-t''|}}{\omega(q)} e^{iqx'} e^{iq'x''} \\
&= \left(\frac{\zeta_\mathrm{i}}{2L\xi}\right)^2 \frac{\epsilon}{2\pi} \int_0^t dt' \int_0^t dt'' e^{-\omega(q)|t'-t''|} \int_{x_-}^{x_+} dx' \int_{x_-}^{x_+} dx'' \int_{-\infty}^{\infty} dq \frac{e^{iq(x'-x'')}}{\omega(q)} \\
&= \left(\frac{\zeta_\mathrm{i}}{2L\xi}\right)^2 \frac{\epsilon}{2\pi} \int_{x_-}^{x_+} dx' \int_{x_-}^{x_+} dx'' \int_{-\infty}^{\infty} dq e^{iq(x'-x'')}. \\
&\cdot \frac{2}{\omega^2(q)} \left(t + \frac{1}{\omega(q)}\left(e^{-\omega(q)t} - 1\right)\right).
\end{aligned} \tag{6.C.7}$$

6.D Generating the external noise as a Fourier decomposition

We want to express the noise added in the active traction parameter (Eq. 6.53) as a decomposition in Fourier modes, as written in Eq. 6.55, where a_n, b_n are normal independent variables of mean zero. For this reason, we should find their variances $\langle a_n^2 \rangle$ so that the noise is exponentially correlated both in space and time, with a unique correlation time for all the modes. We use that $\langle a_n a_m \rangle = \langle a_n \rangle \langle a_m \rangle = 0$ for $n \neq m$, (since $\langle a_n \rangle = \langle b_n \rangle = 0$), and the same for the b's. Defining a 1D system from $x_- = X - L$ to $x_+ = X + L$, where X is the center-of-mass and L the half-width of the system, the correlation in space reads

$$
\begin{aligned}
\langle \psi(x',t)\psi(x'+x,t)\rangle &= \frac{1}{2L}\sum_{n=0}^{N}\int_{x_-}^{x_+} dx' \left\langle \psi(x',t)\psi(x'+x,t)\right\rangle \\
&= \frac{1}{2L}\sum_{n=0}^{N}\int_{x_-}^{x_+} dx' \Bigg(\langle a_n(t)^2\rangle \cos\left(\frac{2\pi n}{2L}x'\right)\cos\left(\frac{2\pi n}{2L}(x+x')\right) \\
&+ \langle b_n(t)^2\rangle \sin\left(\frac{2\pi n}{2L}x'\right)\sin\left(\frac{2\pi n}{2L}(x+x')\right)\Bigg) \\
&= \frac{1}{2L}\sum_{n=0}^{N}\Bigg(\langle a_n(t)^2\rangle \int_{x_-}^{x_+} dx' \cos\left(\frac{\pi n}{L}x'\right)\cos\left(\frac{\pi n}{L}(x+x')\right) \\
&+ \langle b_n(t)^2\rangle \int_{x_-}^{x_+} dx' \sin\left(\frac{\pi n}{L}x'\right)\sin\left(\frac{\pi n}{L}(x+x')\right)\Bigg) \\
&= \frac{1}{2L}\sum_{n=0}^{N}(\langle a_n(t)^2\rangle + \langle b_n(t)^2\rangle) L\cos\left(\frac{\pi n}{L}x\right) \\
&= \sum_{n=0}^{N}\langle a_n(t)^2\rangle \cos\left(\frac{\pi n}{L}x\right),
\end{aligned}
\tag{6.D.1}
$$

where we have used that $\langle b_n^2 \rangle = \langle a_n^2 \rangle$. We want an exponential correlation function[1], $\langle \psi(x',t)\psi(x'+x,t)\rangle \equiv C(x) = \frac{\epsilon}{\lambda} e^{-|x|/\lambda}$, that in Fourier space reads

$$
\hat{C}(q) = \int_{-\infty}^{\infty} C(x) e^{-iqx} dx = \frac{\epsilon}{\lambda}\int_{-\infty}^{\infty} e^{-|x|/\lambda - iqx} dx = \frac{2\epsilon}{1+\lambda^2 q^2}. \tag{6.D.2}
$$

[1] So that in the limit for a small correlation length we get a Delta function (and so a white noise): $C(x) = \frac{\epsilon}{\lambda} e^{-|x|/\lambda} \xrightarrow{\lambda \to 0} 2\epsilon\delta(x)$.

Back to real space,

$$C(x) = \frac{1}{2\pi}\int_{-\infty}^{\infty}\hat{C}(q)e^{iqx}dq = \frac{2\epsilon}{2\pi}\int_{-\infty}^{\infty}\frac{e^{iqx}}{1+\lambda^2q^2}dq = \frac{\epsilon}{\pi}\int_{-\infty}^{\infty}\frac{\cos(qx)}{1+\lambda^2q^2}dq$$
$$= \frac{\epsilon}{\pi}\cdot\frac{2\pi}{2L}\left(\frac{\cos(0)}{1+\lambda^2 0^2} + 2\sum_{n=1}^{N}\frac{1}{1+\lambda^2\left(\frac{\pi n}{L}\right)^2}\cos\left(\frac{\pi n}{L}x\right)\right)$$
$$= \frac{\epsilon}{L}\left(1+\sum_{n=1}^{N}\frac{2}{1+\lambda^2\left(\frac{\pi n}{L}\right)^2}\cos\left(\frac{\pi n}{L}x\right)\right), \tag{6.D.3}$$

where we have used that the sin function is odd and so its integral vanishes, and we have then discretized the integral by multiplying it by $\frac{2\pi}{2L}$ and putting $q \equiv \frac{2\pi n}{2L} = \frac{\pi n}{L}$ (where, except for the mode $n = 0$, the modes $n = 1, \dots, N$ should be multiplied by 2). We obtain thus the result in Eq. 6.59. This must be equal to the result obtained in Eq. 6.D.1, and so the variances of the modes are

$$\langle a_0(t)^2\rangle = \frac{\epsilon}{L}, \tag{6.D.4}$$
$$\langle a_n(t)^2\rangle = \frac{\epsilon}{L}\frac{2}{1+\lambda^2\left(\frac{\pi n}{L}\right)^2}, \quad \text{for } n = 1, \dots, N. \tag{6.D.5}$$

which is the result in Eq. 6.56.

The correlation in time, following a similar procedure as before, is

$$\langle\psi(x,t')\psi(x,t'+t)\rangle = \frac{1}{T}\sum_{n=0}^{N}\int_0^T dt'\,\langle\psi(x,t')\psi(x,t'+t)\rangle$$
$$= \frac{1}{T}\sum_{n=0}^{N}\int_0^T dt'\Bigg(\langle a_n(t')a_n(t'+t)\rangle\cos^2\left(\frac{2\pi n}{2L}x\right) +$$
$$+ \langle b_n(t')b_n(t'+t)\rangle\sin^2\left(\frac{2\pi n}{2L}x\right)\Bigg)$$
$$= \frac{1}{T}\sum_{n=0}^{N}\int_0^T dt'\langle a_n(t')a_n(t'+t)\rangle\left(\cos^2\left(\frac{\pi n}{L}x\right) + \sin^2\left(\frac{\pi n}{L}x\right)\right)$$
$$= \frac{1}{T}\sum_{n=0}^{N}\int_0^T dt'\langle a_n^2\rangle e^{-|t|/\tau} = \sum_{n=0}^{N}\langle a_n^2\rangle e^{-|t|/\tau}, \tag{6.D.6}$$

where we have used that $\langle a_n(t')a_n(t'+t)\rangle = \langle b_n(t')b_n(t'+t)\rangle = \frac{\mu_n}{\tau}e^{-|t|/\tau} = \langle a_n^2\rangle e^{-|t|/\tau}$ (Eq. 6.58, since $a_n(t), b_n(t)$ are Ornstein-Uhlenbeck processes). Therefore, plugging the variances of the modes here (Eq. 6.D.4 and Eq. 6.D.5), we get

an exponential function for the correlation in time for the noise,

$$\langle \psi(x,t')\psi(x,t'+t)\rangle = \frac{\epsilon}{L}\left(1+\sum_{n=1}^{N}\frac{2}{1+\lambda^2\left(\frac{\pi n}{L}\right)^2}\right)e^{-|t|/\tau} \equiv \frac{\mu}{\tau}e^{-|t|/\tau}, \quad (6.D.7)$$

with

$$\mu \equiv \sum_{n=0}^{N}\mu_n = \sum_{n=0}^{N}\langle a_n^2\rangle\tau = \frac{\epsilon\tau}{L}\left(1+\sum_{n=1}^{N}\frac{2}{1+\lambda^2\left(\frac{\pi n}{L}\right)^2}\right),$$

attaining the result in Eq. 6.60.

6.E Methods for the experimental data analysis

The spatial and temporal autocorrelation functions plotted in Fig. 6.12 were obtained from the experimental data of fluctuations of the traction forces. In order not to be influenced by the higher values near the edges (Fig. 6.7), we compute in both cases the correlation in a region of the center of the monolayer. In Fig. 6.E.1 and Fig. 6.E.2, we show these regions in the initial time points of the traction maps for the different experimental realizations, both in the rectangular and in the circular geometry.

For the spatial correlation, we average time points separated by more than $\sim \tau$, not to be influenced by the temporal correlation of the data. A maximum distance from the center $r_{\max}$ is selected to define a region (black lines in the figures), and the correlation of all the points in that region is computed and averaged. In the rectangular case, we compute the correlation of a point with that at distance Δx of the same row, and then average for all the rows (that is, average through the coordinate y). We do the same for the circular geometry but taking two points separated by a radial distance Δr, and then averaging for the angular coordinate. In the computation, we always subtract the mean traction, in order to obtain the autocorrelation of the traction fluctuations instead of the traction values themselves.

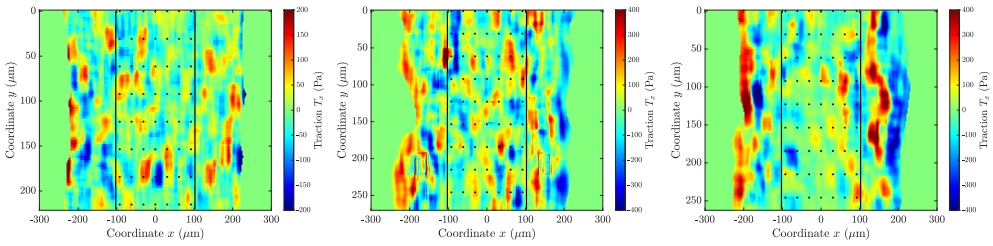

Figure 6.E.1: Autocorrelation computation in rectangular monolayers. X traction colormap in the three analyzed experiments with rectangular geometry from [Uroz2018], for the first time point and with a coarse-graining parameter of $w = 11$. Their temporal sequences give the kymographs in Fig. 6.6a-c.

The temporal correlation is computed in a very similar procedure, but now we select points inside of the central region that are equally spaced and separated by $\sim L_c$ (black dots in the figures), not to be influenced by the spatial correlation of the data. We take those points at a time t and calculate the autocorrelation with the same point at time $t + \Delta t$, also subtracting the mean values to get the autocorrelation of the fluctuations.

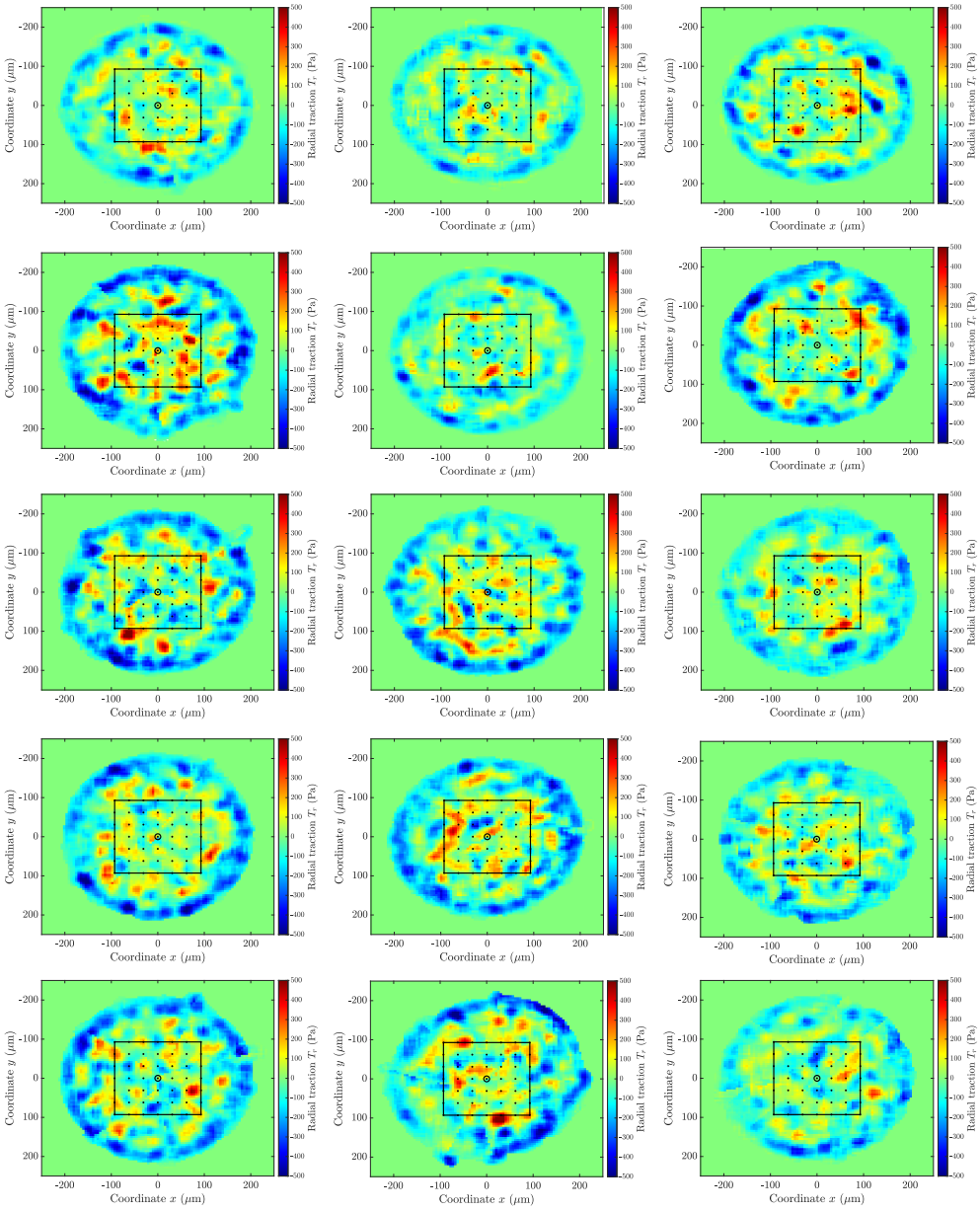

Figure 6.E.2: Autocorrelation computation in circular monolayers. Radial traction colormap in the fifteen analyzed experiments with circular geometry from [Pérez-González2019], for the first time point and with a coarse-graining parameter of $w = 5$. Their temporal sequences give the kymographs in Fig. 6.6d-f.

Chapter 7

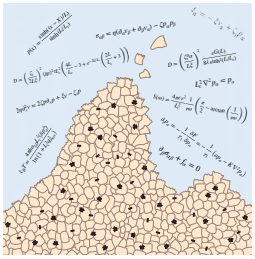

General conclusions

In this thesis we explored several examples of collective cell migration of cell clusters, directed by different forms of symmetry-breaking, either extrinsic, such as external gradients of environmental stiffness, or intrinsic, such as the new phenomenon of shape sensing. We also explored the role of a nontrivial rheology of the substrate in how the collective motion may be triggered. Under the soft active matter physics framework, we examined the extent to which a mechanical description alone can account for observed collective migration phenomena. Here, we summarize our work's main conclusions and the perspectives of future developments derived from it.

The first two chapters establish a general physical framework to describe and understand collective durotaxis in epithelial tissues. In Chapter 2, we extended a continuum model of 2D epithelial monolayers as active, viscous polar systems, and we generalized it to consider 3D cellular aggregates in Chapter 3. Through a comprehensive study of the model phenomenology and comparison with experimental data, the main findings are:

- In the presence of a stiffness gradient of the substrate, 2D monolayers perform durotaxis, and their center-of-mass (or durotactic) velocity increases with the active traction gradient, related to the substrate's stiffness. It also increases for larger tissue sizes, decreases for increased friction or active traction saturation, and is independent of the contractility and the traction offset. The spreading velocity increases with the traction offset, the tissue size, and the hydrodynamic length, but decreases with the con-

tractility and is independent of the active traction gradient if it does not change significantly over the monolayer width.

- Three durotactic regimes emerge: Large monolayers spread indefinitely, small ones contract, and those in an intermediate size range display a non-monotonic evolution whereby they switch from contraction to spreading at a certain time.
- Adding surface tension and elastic resistance is a realistic way to prevent the indefinite spreading, slowing down expansion and accelerating contraction.
- 3D cellular aggregates perform cohesive durotactic migration as their interface advances on the stiff side and retracts from the soft side, and their durotactic velocity is non-monotonic with the local substrate stiffness.
- To explain this non-monotonic behavior, the contribution of the surface tension of the 3D structure on top of the basal monolayer is needed, generalizing the theory of active wetting and connecting the clusters' wetting properties with durotaxis. Clusters display low motility on the soft and stiff regions of the substrate, where they fully dewet and wet the surface, respectively, but at an intermediate stiffness, close to the crossover between low and high wettability, they are maximally motile.
- The optimal stiffness can be shifted to higher or lower stiffness by tuning cluster size and active forces, which could be a way for organisms to trigger and regulate this directed migration.

In the majority of the experiments with 2D monolayers, the tissues expand indefinitely because either contractility is not large enough or active tractions are too large. However, for 3D cellular aggregates, the intermediate mode of coherent migration was observed. Future directions include incorporating more realistic ingredients into the model, such as spatial pressure variations across a cluster, size-dependent surface tension of cell aggregates, elastocapillary effects resulting from substrate deformation, or differences in surface tension across a cluster that could result in different contact angles at the stiff versus the soft side. Additionally, performing more experiments to observe and characterize the full spectrum of dynamical evolutions, and tracking individual clusters during all their migration, would be necessary to fully validate the model predictions.

In Chapter 4, we explored how extracellular matrix (ECM) stiffening interacts with cellular traction forces. Given the strain-stiffening properties of biopolymer networks, we assessed the feedback between substrate stiffness and traction forces. Key points of the results include:

- The strain of the substrate is non-monotonic with its stiffness. On the one hand, greater stiffness provokes an increase in traction, which leads to a greater strain, while on the other hand, the stiffening of the substrate makes it more resistant to deform.

- The bistable nature of the solutions in a certain parameter regime allows a sudden increase in traction forces when the substrate rigidifies, or the contractility or active traction saturation value is increased, enabling tissues to overcome intercellular contractility and potentially triggering the spreading. Bistability also implies the existence of hysteresis.

- This could have implications in contexts where there is an increased intracellular contractility, or where the ECM stiffens by secreting and accumulating matrix components (tumor progression, embryonic development, or wound healing), with a high-traction state that enhances tissue migration.

An interesting follow-up of this project would involve designing experiments that tune substrate stiffness or modulate myosin phosphorylation to observe the discontinuous jump in cellular traction values. Additionally, numerical simulations could validate the analytical findings and characterize the nonlinear transition to the stationary state.

In Chapter 5, experimental work was conducted to test the predictions on the relationship between tissue morphology and motility in globally unpolarized cell clusters without external cues, that is, due to shape asymmetry alone. The theoretical analysis predicts that spontaneous motility of clusters is generically expected if the range of alignment interactions is not too small compared to the system size, and if the screening length that measures the range of hydrodynamic interactions is larger than the system size. Depending on whether contractility is small or large, two different modes of sustained collective migration are identified: anisotropic spreading and coherent migration, both with a finite and sustained velocity of the center of mass. We have designed experiments as a proof of concept for these predictions, which had not been tested before. Specifically, we have found that:

- A systematic study of shapes and sizes shows unequivocally that the phenomenon of shape-sensing motility is present in monolayer clusters.

- The experiments allow us to measure the crucial parameter of the range of alignment forces, L_c. This measurement confirms that the observed migration mode, the anisotropic spreading, is clearly distinguished from the case of isotropic spreading, which would not involve a center of mass speed.

- Once a finite L_c is measured, our data proves that the phenomenon is generic, as long as a systematic front-rear velocity difference is observed. We check this through the statistical analysis of different shapes and sizes, and different cell lines.

- The coherent migration mode predicted for large contractility is not observed in our series of experiments because the used cells did not exhibit sufficient contractility. However, by revisiting data from previous experiments designed for other purposes, we have identified a few cases where coherent migration is, in fact, observed. These observations also indicate that the effect of shape-sensing motility may be larger than durotactic cues and could thus overcome durotaxis.

These results prove experimentally for the first time that cell clusters can effectively sense their global shape and thus, without other external clues, drive the collective migration of the cluster. In this scenario, cells obtain positional information from force transmission through the cluster. Further controlled experiments are needed to verify more systematically the coherent migration mode with rear-edge retraction and to thoroughly characterize other migratory behaviors related to shape asymmetry in cohesive tissues. Another potential extension of this work would be to couple the shape-sensing mechanism with externally guided migratory processes, such as durotaxis, exploring the complex, interconnected nature of collective cell migration in real biological environments. The combined use of durotaxis and shape-sensing experiments could also provide an alternative procedure to prepare asymmetric initial conditions in a less aggressive way than the mask peeling we have used in this work, and allow a more precise testing of all predictions.

In Chapter 6, we extended the hydrodynamic model to include fluctuations of different origins. Experiments and measurements on variables such as traction and velocity show large fluctuations. In some cases, such as in the presence of fingering instabilities, fluctuations must be incorporated explicitly. As a first step towards a fluctuating hydrodynamics theory of tissues, we have proposed, analyzed, and simulated different stochastic equations to account for internal or external noise sources.

- An internal noise, added in the polarity dynamics, accounts for stochasticity in the cells' cytoskeleton and yields predictions for different observables, such as the diffusion coefficient of the finite cell clusters, the power spectral density, and the correlation function of traction measurements. Noise can be introduced additively or multiplicatively, yielding different predictions that can be experimentally tested.

- An external noise, added in the active traction parameter, accounts for the noise coming from the attachment and detachment kinetics of ligands between the cells and the substrate, giving a non-monotonic diffusion coefficient with the monolayer size, absent in the internal noise models.
- Our results for additive noise, which turn out to be the most adequate formulation of traction fluctuations at the inner, unpolarized regions of the tissue, allow us to characterize them in terms of an effective temperature of the system, through the formulation of an effective, non-equilibrium fluctuation-dissipation relation.
- Analyzing experimental data of traction fluctuations, we observe that the additive noise in the polarity dynamics is the most relevant in the system. The model predicts temporal correlation functions accurately, but deviates on the spatial correlation, possibly reflecting a subcellular structure and the limitations of a weak noise approximation.

Future work should involve further analysis of additional experiments to compare and fit our theoretical predictions, such as power spectral density and diffusion coefficients of cell clusters. For example, observing a non-monotonic diffusion coefficient with the monolayer size could indicate the significance of external noise over internal noise in tissue dynamics.

In summary, developing effective theoretical models for complex systems like cells and tissues deepens our understanding of the biophysical principles underlying collective migration. Specifically, continuum models of tissues have proven insightful and predictive, often describing phenomena only observed in experiments *a posteriori*. These models not only shed light on the underlying physics of fundamental biological processes but also inspire new experimental designs, allowing for a close and fruitful integration between theory and experiments in our quest to explain nature.

Resum en català

Migració cel·lular dirigida: forces, formes i fluctuacions en teixits. De la hidrodinàmica activa als experiments.

Paraules clau: Matèria condensada tova, matèria activa, teixits, mecànica, migració cel·lular col·lectiva, durotaxi.

Aquesta tesi està dedicada a estudiar la migració cel·lular col·lectiva en teixits epitelials, sota el marc de la física de la matèria tova activa. Modelitzem els teixits epitelials com fluids polars actius, ja que els seus components, les cèl·lules, tenen una font interna d'energia i s'alineen, polaritzant-se, per tal de generar el moviment. Tot i la miríada d'interaccions químiques i cascades de senyalització extremadament complexes dins de les cèl·lules, en última instància el moviment ha d'estar governat per les lleis més bàsiques de la física. L'enfocament d'aquesta tesi, doncs, és utilitzar models fenomenològic simples, codificant totes aquestes complexes interaccions en termes de les forces físiques i paràmetres materials del teixit. Això ens permet, de manera molt simplificada però efectiva, tenir un model genèric per a modelitzar diversos escenaris rellevants en migració cel·lular col·lectiva.

L'escenari més estudiat, especialment als Capítols 2–3, és el de la durotaxi col·lectiva, que consisteix en la migració dirigida del teixit per factors mecànics externs a les cèl·lues. S'observa quan l'entorn de les cèl·lules—en el cas dels experiments *in vitro*, el substrat, típicament un gel de poliacrilamida recobert amb proteïna de la matriu extracel·lular—, presenta un gradient de rigidesa. Estudiem a fons un model d'una monocapa epitelial basat en la teoria de gels actius, desenvolupat prèviament al grup, i l'estenem per tal d'explicar resultats experimentals de durotaxi col·lectiva d'agregats cel·lulars.

Al Capítol 2 ens centrem en un model per a monocapes bidimensionals, classificant les dinàmiques d'escampament o contracció segons la mida del tei-

xit. Solucionem el model analíticament en casos simples però rellevants, per tal d'obtenir una idea clara de la fenomenologia i dels mecanismes de la migració pels diferents règims dels paràmetres del model. Al Capítol 3, desenvolupem i generalitzem el model per tal de tenir en compte l'estructura tridimensional d'un agregat cel·lular, per tal de comparar amb experiments de durotaxi col·lectiva. La tensió superficial i les propietats de mullat de l'agregat són crucials per explicar el comportament no monòton, observat als experiments, de la velocitat de durotaxi amb la rigidesa local del substrat. Per zones molt toves o molt rígides, els agregats o bé es contrauen del tot, formant angles de contacte molt grans amb el substrat, o bé fan un escampament total mullant-lo completament, amb angles de contacte molt petits. Entremig, un angle de contacte finit, acoblat amb l'augment de les forces de tracció amb la rigidesa, fa que motilitat dels agregats augmenti, donant lloc a una rigidesa òptima per la qual la velocitat de durotaxi és màxima.

En conjunt, el fenomen de la durotaxi podria tenir implicacions en processos biològics fonamentals on hi ha moviment dirigit de cèl·lules, ja sigui en desenvolupament embrionari—com ja s'ha observat en estudis amb *Xenopus laevis*—o metàstasi cancerígena. Desxifrar els mecanismes físics subjacents d'aquest moviment, és doncs molt important per entendre millor aquests processos biològics.

Seguint en la línia d'estudiar les interaccions entre el teixit i el seu entorn extracel·lular, al Capítol 4 examinem la influència de les forces de tracció en la rigidesa del substrat. Que la rigidesa de l'entorn afecta les forces de tracció que fan les cèl·lules és conegut i incorporat en molts models, però aquí explorem com aquestes forces, alhora, afecten la rigidesa del substrat. Típicament, les xarxes biopolimèriques són materials elàstics no lineals que s'endureixen amb la deformació, és a dir, quanta més deformació se'ls hi aplica més rígides es tornen. Per tant, a més força de tracció, més deformació i més rígids són els substrats, recoberts d'aquestes xarxes biopolimèriques. Incorporant aquesta retroalimentació al model, veiem que existeix una biestabilitat per algunes solucions de la tracció, cosa que podria ser rellevant per desencadenar la migració al saltar a un estat de tracció més elevada. Aquest resultat podria ser aplicable en la progressió d'un tumor, on les cèl·lules passarien a un estat de més alta tracció a mesura que l'estroma es rigidifica i la seva contractilitat augmenta.

Al Capítol 5, investiguem la migració dirigida per la forma dels teixits enlloc de la rigidesa de l'entorn. No només factors externs a les cèl·lules poden generar un moviment dirigit, sinó que l'asimetria en la forma del teixit també podria provocar aquest moviment espontani, col·lectiu i dirigit. És diferent al comportament d'estol en el sentit que aquí el teixit no està polaritzat globalment, però el trencament de simetria provoca un desequilibri de forces que genera el movi-

ment. Motivats per la teoria, duem a terme experiments per tal d'analitzar el moviment de teixits epitelials dels quals imposem la forma inicial. Amb els experiments, principalment podem distingir el mode d'escampament anisotròpic, ja que estem massa lluny de les condicions en què podríem observar migració coherent de tot el teixit, amb l'extrem posterior retractant-se. La cerca d'aquest mode en els experiments és per un futur estudi, però els resultats del capítol suporten la idea que la migració cel·lular col·lectiva pot emergir de mecanismes purament físics sense necessitat d'una polarització global del teixit.

Finalment, per tal de modelitzar situacions més realistes, al Capítol 6 estenem el model hidrodinàmic d'un teixit per incloure-hi soroll, tenint en compte l'estocasticitat inherent dels sistemes biològics. Afegim soroll intern a la dinàmica de la polaritat, o bé extern al paràmetre de tracció activa, per tal de modelitzar el soroll del còrtex d'actomiosina cel·lular o la cinètica d'adhesió entre les cèl·lules i el substrat, respectivament. Comparant amb dades experimentals de les fluctuacions de les forces de tracció, podem veure quin tipus de soroll és més adequat i ens dona unes prediccions més encertades, així com ajustar els paràmetres del model. Varis dels resultats teòrics, com els coeficients de difusió o la densitat espectral de potències, poden servir com a bases per a dissenyar futurs experiments.

En conclusió, amb aquesta tesi contribuïm al coneixement dels mecanismes físics subjacents a la migració cel·lular col·lectiva en teixits, en relació amb la interacció dels teixits amb el seu entorn i en l'organització i coordinació de com emergeix la migració espontània o dirigida. L'estudi és rellevant ja que la migració cel·lular col·lectiva és present en diversos processos biològics, ja sigui en desenvolupament embrionari, metàstasi cancerígena, regeneració de teixits o tancament de ferides. El desenvolupament de models teòrics simples però efectius, no només il·lumina la física subjacent a aquests processos, sinó que també pot inspirar nous dissenys experimentals, permetent una integració fructífera entre teoria i experiments en la nostra recerca per explicar la natura.

List of symbols

	Description [Units]	Estimate	References
$\sigma_{\alpha\beta}$	Stress tensor $[ML^{-1}T^{-2}]$		
f_α	Force density $[ML^{-2}T^{-2}]$		
T_α	Traction force $[ML^{-1}T^{-2}]$		
p_α	Polarity $[\cdot]$		
v_α	Velocity $[LT^{-1}]$		
X	Center-of-mass, CM $[L]$		
L	Half-width $[L]$		
R	Contact radius $[L]$		
U, v_X	CM velocity $[LT^{-1}]$		
V, v_S	Spreading velocity $[LT^{-1}]$	$1-20$ Pa	
K	Frank constant $[MLT^{-2}]$	$2-10$ nN	
a	Restoring coefficient $[ML^{-1}T^{-2}]$		
h	Monolayer height $[L]$	5 μm	[Trepat2009, Pérez-González2019, Blanch-Mercader2017b]
L_c	Nematic length $[L]$	25 μm (15 μm)	—"—, $\sqrt{K/a}$
ζ	Contractility $[ML^{-1}T^{-2}]$	-20 kPa (-2 kPa)	—"—
η	Viscosity $[ML^{-1}T^{-1}]$	80 MPa·s (20 MPa·s)	—"—

	Description [Units]	Estimate	References
γ_1	Rotational viscosity $[ML^{-1}T^{-1}]$		
λ	Hydrodynamic length $[L]$	300 μm (420 μm)	$\sqrt{2\eta/\xi}$
L_p	Active polar length $[L]$	200 μm	$\lvert\zeta\rvert/(2\zeta_\mathrm{i})$
ζ_i^0	Active traction offset $[ML^{-2}T^{-2}]$	0.05 kPa/μm	[Sunyer2016, Alert2019b, Douezan2012a]
ζ_i'	Active traction gradient $[ML^{-3}T^{-2}]$	0.08 Pa/μm^2	
ζ_i^∞	Active traction saturation $[ML^{-2}T^{-2}]$	0.3 kPa/μm	[Trepat2009, Pérez-González2019, Blanch-Mercader2017b]
ξ_0	Friction offset $[ML^{-3}T^{-1}]$	0.22 kPa·s/μm^2	
ξ^∞	Friction saturation $[ML^{-3}T^{-1}]$	0.5 kPa·s/μm^2	[Cochet-Escartin2014]
E_0	Substrate's softest stiffness $[ML^{-1}T^{-2}]$	0.5 kPa	Fig. 3.5, Fig. 3.8a
E'	Stiffness gradient $[ML^{-2}T^{-2}]$	33 kPa/mm	—"—
E^*	Characteristic stiffness of saturation $[ML^{-1}T^{-2}]$	140 kPa	[Douezan2012b]
P_{0x}	Pressure offset $[ML^{-1}T^{-2}]$	4.2 Pa	
s_P	Pressure sensitivity to stiffness $[\cdot]$	0.018	
γ	Surface tension $[MT^{-2}]$	1-10 mN/m	[Foty1994, Forgacs1998, Guevorkian2010, Stirbat2013, Cochet-Escartin2014, Nier2015]

Unless otherwise specified in the captions, these values are used in Chapter 2 and those in the parenthesis in Chapter 3. These symbols are also for Chapters 5–6.

List of figures

List of tables

List of videos

The link to the videos can be accessed by scanning the following QR-code or by clicking here.

Bibliography

[Al-Rekabi2019] Al-Rekabi, Z., Fura, A. M., Juhlin, I., Yassin, A., Popowics, T. E. & Sniadecki, N. J. Hyaluronan-CD44 interactions mediate contractility and migration in periodontal ligament cells. *Cell Adhes. Migr.* **13**, 138–150 (2019). (Cited on page 63.)

[Alberts2002] Alberts, B., Johnson, A., Lewis, J., Raff, M., Roberts, K. & Walter, P. *Molecular Biology of the Cell* (Garland Science, New York, 2002), 4th edn. (Cited on pages 4 and 5.)

[Alert2019a] Alert, R., Blanch-Mercader, C. & Casademunt, J. Active Fingering Instability in Tissue Spreading. *Phys. Rev. Lett.* **122**, 088104 (2019). (Cited on pages 17, 25, 28, 29, 31, 32, and 33.)

[Alert2019b] Alert, R. & Casademunt, J. Role of Substrate Stiffness in Tissue Spreading: Wetting Transition and Tissue Durotaxis. *Langmuir* **35**, 7571–7577 (2019). (Cited on pages 23, 25, 28, 29, 31, 32, 35, 49, 58, 82, 109, and 196.)

[Alert2020] Alert, R. & Trepat, X. Physical Models of Collective Cell Migration. *Annu. Rev. Condens. Matter Phys.* **11**, 77–101 (2020). (Cited on pages 8 and 17.)

[Amiri2022] Amiri, A., Mueller, R. & Doostmohammadi, A. Unifying polar and nematic active matter: emergence and co-existence of half-integer and full-integer topological defects. *J. Phys. A: Math. Theor.* **55**, 094002 (2022). (Cited on page 14.)

[Ananthakrishnan2007] Ananthakrishnan, R. & Ehrlicher, A. The Forces Behind Cell Movement. *Int. J. Biol. Sci.* **3**, 303–317 (2007). (Cited on page 5.)

[Angelini2011] Angelini, T. E., Hannezo, E., Trepat, X., Marquez, M., Fredberg, J. J. & Weitz, D. A. Glass-like dynamics of collective cell migration. *PNAS* **108**, 4714–4719 (2011). (Cited on page 27.)

[Arciero2011] Arciero, J. C., Mi, Q., Branca, M. F., Hackam, D. J. & Swigon, D. Continuum Model of Collective Cell Migration in Wound Healing and Colony Expansion. *Biophys. J.* **100**, 535–543 (2011). (Cited on page 14.)

[Armengol2023] Armengol-Collado, J., Carenza, L., Eckert, J. *et al.* Epithelia are multiscale active liquid crystals. *Nat. Phys.* **19**, 1773–1779 (2023). (Cited on page 15.)

[Armengol2024] Armengol-Collado, J.-M., Carenza, L. N. & Giomi, L. Hydrodynamics and multiscale order in confluent epithelia. *eLife* **13**, e86400 (2024). (Cited on pages 15 and 145.)

[Babb2004] Babb, S. G. & Marrs, J. A. E-cadherin regulates cell movements and tissue formation in early zebrafish embryos. *Dev. Dyn.* **230**, 263–277 (2004). (Cited on page 57.)

[Balcioglu2020] Balcioglu, H. E., Balasubramaniam, L., Stirbat, T. V., Doss, B. L., Fardin, M. A., Mège, R. M. & Ladoux, B. A subtle relationship between substrate stiffness and collective migration of cell clusters. *Soft Matter* **16**, 1825–1839 (2020). (Cited on page 12.)

[Bambardekar2015] Bambardekar, K., Clement, R., Blanc, O., Chardes, C. & Lenne, P. F. Direct laser manipulation reveals the mechanics of cell contacts in vivo. *PNAS* **112**, 1416–1421 (2015). (Cited on page 11.)

[Banerjee2019] Banerjee, S. & Marchetti, M. C. *In Cell Migrations: Causes and Functions. In Cell Migrations: Causes and Functions.* edited by La Porta, C. & Zapperi, S., 45–66 (Springer, Cham, Switzerland, 2019). (Cited on page 17.)

[Baptista2019] Baptista, D., Teixeira, L., van Blitterswijk, C., Giselbrecht, S. & Truckenmüller, R. Overlooked? Underestimated? Effects of Substrate Curvature on Cell Behavior. *Trends Biotechnol.* **37**, 838–854 (2019). (Cited on page 6.)

[Barriga2018] Barriga, E. H., Franze, K., Charras, G. & Mayor, R. Tissue stiffening coordinates morphogenesis by triggering collective cell migration in vivo. *Nature* **554**, 523–527 (2018). (Cited on pages 82 and 110.)

[Barry2014] Barry, A. K., Tabdili, H., Muhamed, I., Wu, J., Shashikanth, N., Gomez, G. A., Yap, A. S., Gottardi, C. J., Rooij, J. D., Wang, N. & Leckband, D. E. α-Catenin cytomechanics - role in cadherin-dependent adhesion and mechanotransduction. *J. Cell Sci.* **127**, 1779–1791 (2014). (Cited on page 61.)

[Basu2008] Basu, A., Joanny, J., Jülicher, F. & Prost, J. Thermal and non-thermal fluctuations in active polar gels. *Eur. Phys. J. E* **27**, 149–160 (2008). (Cited on page 17.)

[Bauer2021] Bauer, A. *et al.* pyTFM: a tool for traction force and monolayer stress microscopy. *PLoS Comput. Biol.* **17**, e1008364 (2021). (Cited on page 90.)

[Beaune2018] Beaune, G., Blanch-Mercader, C., Douezan, S., Dumond, J., González-Rodríguez, D., Cuvelier, D., Ondarçuhu, T., Sens, P., Dufour, S., Murrell, M. P. & Brochard-Wyart, F. Spontaneous migration of cellular aggregates from giant keratocytes to running spheroids. *PNAS* **115**, 12926–12931 (2018). (Cited on pages 14, 58, 115, and 116.)

[Beaune2014] Beaune, G., Stirbat, T. V., Khalifat, N., Cochet-Escartin, O., Garcia, S., Gurchenkov, V. V., Murrell, M. P., Dufour, S., Cuvelier, D. & Brochard-Wyart, F. How cells flow in the spreading of cellular aggregates. *PNAS* **111**, 8055–8060 (2014). (Cited on pages 58 and 65.)

[BenAmar2016] Ben Amar, M. & Bianca, C. Onset of nonlinearity in a stochastic model for auto-chemotactic advancing epithelia. *Sci. Rep.* **6**, 33849 (2016). (Cited on page 17.)

[Bergert2016] Bergert, M. *et al.* Confocal reference free traction force microscopy. *Nat. Commun.* **7**, 12814 (2016). (Cited on page 90.)

[Blanch-Mercader2017b] Blanch-Mercader, C., Vincent, R., Bazellières, E., Serra-Picamal, X., Trepat, X. & Casademunt, J. Effective viscosity and dynamics of spreading epithelia: a solvable model. *Soft Matter* **13**, 1235–1243 (2017). (Cited on pages 17, 24, 28, 29, 32, 34, 71, 195, and 196.)

[Blanch-Mercader2013] Blanch-Mercader, C. & Casademunt, J. Spontaneous Motility of Actin Lamellar Fragments. *Phys. Rev. Lett.* **110**, 1–5 (2013). (Cited on pages 115 and 118.)

[Blanch-Mercader2017a] Blanch-Mercader, C. & Casademunt, J. Hydrodynamic instabilities, waves and turbulence in spreading epithelia. *Soft Matter* **13**, 6913–6928 (2017). (Cited on pages 29, 32, and 170.)

[Blanchoin2014] Blanchoin, L., Boujemaa-Paterski, R., Sykes, C. & Plastino, J. Actin Dynamics, Architecture, and Mechanics in Cell Motility. *Physiol. Rev.* **94**, 235–263 (2014). (Cited on pages 2 and 3.)

[Boudou2009] Boudou, T., Ohayon, J., Picart, C., Pettigrew, R. & Tracqui, P. Nonlinear elastic properties of polyacrylamide gels: implications for quantification of cellular forces. *Biorheology* **46**, 191–205 (2009). (Cited on page 94.)

[Brückner2024] Brückner, D. B. & Hannezo, E. Tissue Active Matter: Integrating Mechanics and Signaling into Dynamical Models. *Cold Spring Harb. Perspect. Biol.* **a041653** (2024). (Cited on page 14.)

[Butler2002] Butler, J. P., Tolic-Norrelykke, I. M., Fabry, B. & Fredberg, J. J. Traction fields, moments, and strain energy that cells exert on their surroundings. *Am. J. Physiol. Cell Physiol.* **282**, C595–C605 (2002). (Cited on page 90.)

[Böhringer2024] Böhringer, D., Cóndor, M., Bischof, L., Czerwinski, T., Gampl, N., Ngo, P. A., Bauer, A., Voskens, C., López-Posadas, R., Franze, K., Budday, S., Mark, C., Fabry, B. & Gerum, R. Dynamic traction force measurements of migrating immune cells in 3D biopolymer matrices. *Nat. Phys.* **20**, 1816–1823 (2024). (Cited on pages 90 and 110.)

[Cai2014] Cai, D., Chen, S. C., Prasad, M., He, L., Wang, X., Choesmel-Cadamuro, V., Sawyer, J. K., Danuser, G. & Montell, D. J. Mechanical Feedback through E-Cadherin Promotes Direction Sensing during Collective Cell Migration. *Cell* **157**, 1146–1159 (2014). (Cited on page 57.)

[Camley2016] Camley, B. A., Zimmermann, J., Levine, H. & Rappel, W. J. Emergent Collective Chemotaxis without Single-Cell Gradient Sensing. *Phys. Rev. Lett.* **116**, 1–6 (2016). (Cited on page 12.)

[Campas2014] Campàs, O., Mammoto, T., Hasso, S. *et al.* Quantifying cell-generated mechanical forces within living embryonic tissues. *Nat. Methods* **11**, 183–189 (2014). (Cited on page 11.)

[Chan2021] Chan, G. K., McGrath, J. A. & Parsons, M. Spatial activation of ezrin by epidermal growth factor receptor and focal adhesion kinase coordinates epithelial cell migration. *Open Biol.* **11**, 210166 (2021). (Cited on page 109.)

[Chiang2024] Chiang, M., Hopkins, A., Loewe, B., Marchetti, M. C. & Marenduzzo, D. Intercellular friction and motility drive orientational order in cell monolayers. *PNAS* **121**, e2319310121 (2024). (Cited on page 15.)

[Chugh2018] Chugh, P. & Paluch, E. K. The actin cortex at a glance. *J. Cell Sci.* **131**, jcs186254 (2018). (Cited on page 3.)

[Coburn2016] Coburn, L., Lopez, H., Caldwell, B. J., Moussa, E., Yap, C., Priya, R., Noppe, A., Roberts, A. P., Lobaskin, V., Yap, A. S., Neufeld, Z. & Gomez, G. A. Contact inhibition of locomotion and mechanical crosstalk between cell–cell and cell–substrate adhesion determine the pattern of junctional tension in epithelial cell aggregates. *Mol. Biol. Cell* **27**, 3436–3448 (2016). (Cited on page 27.)

[Cochet-Escartin2014] Cochet-Escartin, O., Ranft, J., Silberzan, P. & Marcq, P. Border Forces and Friction Control Epithelial Closure Dynamics. *Biophys. J.* **106**, 65–73 (2014). (Cited on page 196.)

[Copenhagen2020] Copenhagen, K., Alert, R., Wingreen, N. S. & Shaevitz, J. W. Topological defects promote layer formation in Myxococcus xanthus colonies. *Nat. Phys.* **17**, 211–215 (2021). (Cited on pages 13 and 14.)

[Cortese2014] Cortese, B., Palamà, I. E., D'Amone, S. & Gigli, G. Influence of electrotaxis on cell behaviour. *Integr. Biol.* **6**, 817–830 (2014). (Cited on page 6.)

[Costigliola2017] Costigliola, N. *et al.* Vimentin fibers orient traction stress. *PNAS* **114**, 5195–5200 (2017). (Cited on page 4.)

[Cote2022] Cote, L. E. & Feldman, J. L. Won't You be My Neighbor: How Epithelial Cells Connect Together to Build Global Tissue Polarity. *Front. Cell Dev. Biol.* **10** (2022). (Cited on page 9.)

[Dai2020] Dai, W., Guo, X., Cao, Y., Mondo, J. A., Campanale, J. P., Montell, B. J., Burrous, H., Streichan, S., Gov, N., Rappel, W.-J. & Montell, D. J. Tissue topography steers migrating Drosophila border cells. *Science* **370**, 987–990 (2020). (Cited on page 57.)

[DeGennes1993] De Gennes, P.-G. & Prost, J. *The Physics of Liquid Crystals* (Oxford University Press, 1993). (Cited on pages 17, 28, and 29.)

[deMercado2024] de Mercado, R. R., Beslmüller, K., Vorselen, D., Danen, E. H. & Schmidt, T. Single-Cell Local Stress Analysis in Tumoroids. *bioRxiv* (2024). (Cited on page 11.)

[Deng2021] Deng, Y., Levine, H., Mao, X. & Sander, L. M. Collective motility and mechanical waves in cell clusters. *Eur. Phys. J. E* **44**, 137 (2021). (Cited on page 23.)

[Discher2005] Discher, D. E., Janmey, P. & Wang, Y.-L. Tissue cells feel and respond to the stiffness of their substrate. *Science* **310**, 1139–43 (2005). (Cited on page 89.)

[Dombrowski2004] Dombrowski, C., Cisneros, L., Chatkaew, S., Goldstein, R. E. & Kessler, J. O. Self-Concentration and Large-Scale Coherence in Bacterial Dynamics. *Phys. Rev. Lett.* **93**, 098103 (2004). (Cited on page 13.)

[Dominguez2011] Dominguez, R. & Holmes, K. C. Actin Structure and Function. *Annu. Rev. Biophys.* **40**, 169–186 (2011). (Cited on page 2.)

[Dong2017] Dong, L. & Oberai, A. A. Recovery of cellular traction in three-dimensional nonlinear hyperelastic matrices. *Comput. Methods Appl. Mech. Eng.* **314**, 296–313 (2017). (Cited on page 90.)

[Doostmohammadi2018] Doostmohammadi, A., Ignés-Mullol, J., Yeomans, J. *et al.* Active nematics. *Nat. Commun.* **9**, 3246 (2018). (Cited on page 14.)

[Dorrell2002] Dorrell, M. I., Aguilar, E. & Friedlander, M. Retinal Vascular Development Is Mediated by Endothelial Filopodia, a Preexisting Astrocytic Template and Specific R-Cadherin Adhesion. *Invest. Ophthalmol. Visual Sci.* **43**, 3500–10 (2002). (Cited on page 57.)

[Douezan2012b] Douezan, S. & Brochard-Wyart, F. Spreading dynamics of cellular aggregates confined to adhesive bands. *Eur. Phys. J. E* **35**, 116 (2012). (Cited on pages 58, 65, and 196.)

[Douezan2012a] Douezan, S., Dumond, J. & Brochard-Wyart, F. Wetting transitions of cellular aggregates induced by substrate rigidity. *Soft Matter* **8**, 4578–4583 (2012). (Cited on pages 18 and 196.)

[Douezan2011] Douezan, S., Guevorkian, K., Naouar, R., Dufour, S., Cuvelier, D. & Brochard-Wyart, F. Spreading dynamics and wetting transition of cellular aggregates. *PNAS* **108**, 7315–20 (2011). (Cited on pages 18, 58, and 65.)

[DuChez2019] DuChez, B. J., Doyle, A. D., Dimitriadis, E. K. & Yamada, K. M. Durotaxis by Human Cancer Cells. *Biophys. J.* **116**, 670–683 (2019). (Cited on pages 6, 7, 12, and 82.)

[Duclos2017] Duclos, G., Erlenkämper, C., Joanny, J. F. & et al. Topological defects in confined populations of spindle-shaped cells. *Nat. Phys.* **13**, 58–62 (2017). (Cited on pages 14 and 17.)

[Duclos2018] Duclos, G., Blanch-Mercader, C., Yashunsky, V. *et al.* Spontaneous shear flow in confined cellular nematics. *Nat. Phys.* **14**, 728–732 (2018). (Cited on page 14.)

[Duclos2014] Duclos, G., Garcia, S., Yevick, H. G. & Silberzan, P. Perfect nematic order in confined monolayers of spindle-shaped cells. *Soft Matter* **10**, 2346–2353 (2014). (Cited on page 14.)

[Dufort2011] Dufort, C. C., Paszek, M. J. & Weaver, V. M. Balancing Forces: Architectural Control of Mechanotransduction. *Nat. Rev. Molec. Cell Biol.* **12**, 308–319 (2011). (Cited on page 9.)

[Eckert2021] Eckert, J., Abouleila, Y., Schmidt, T. & Mashaghi, A. Single Cell Micro-Pillar-Based Characterization of Endothelial and Fibroblast Cell Mechanics. *Micro* **1**, 242–249 (2021). (Cited on page 11.)

[Ehrig2019] Ehrig, S., Schamberger, B., Bidan, C. M., West, A., Jacobi, C., Lam, K., Kollmannsberger, P., Petersen, A., Tomancak, P., Kommareddy, K., Fischer, F. D., Fratzl, P. & Dunlop, J. W. C. Surface tension determines tissue shape and growth kinetics. *Sci. Adv.* **5**, 9394–9405 (2019). (Cited on page 64.)

[Elosegui-Artola2014] Elosegui-Artola, A., Bazellières, E., Allen, M. D., Andreu, I., Oria, R., Sunyer, R., Gomm, J. J., Marshall, J. F., Jones, J. L., Trepat, X. & Roca-Cusachs, P. Rigidity sensing and adaptation through regulation of integrin types. *Nat. Mater.* **13**, 631–7 (2014). (Cited on page 89.)

[Elosegui-Artola2016] Elosegui-Artola, A., Oria, R., Chen, Y., Kosmalska, A., Pérez-González, C., Castro, N., Zhu, C., Trepat, X. & Roca-Cusachs, P. Mechanical regulation of a molecular clutch defines force transmission and transduction in response to matrix rigidity. *Nat. Cell Biol.* **18**, 540–548 (2016). (Cited on page 61.)

[Enoch2008] Enoch, S. & Leaper, D. J. Basic science of wound healing. *Surgery (Oxford)* **26**, 31–37 (2008). (Cited on page 110.)

[Escribano2018] Escribano, J., Sunyer, R., Sánchez, M. T., Trepat, X., Roca-Cusachs, P. & García-Aznar, J. A hybrid computational model for collective cell durotaxis. *Biomech. Model. Mechano.* **17**, 1037–1052 (2018). (Cited on pages 23 and 48.)

[Evans2013] Evans, N. D., Oreffo, R. O., Healy, E., Thurner, P. J. & Man, Y. H. Epithelial mechanobiology, skin wound healing, and the stem cell niche. *J. Mech. Behav. Biomed. Mater.* **28**, 397–409 (2013). (Cited on page 12.)

[Farooqui2005] Farooqui, R. & Fenteany, G. Multiple rows of cells behind an epithelial wound edge extend cryptic lamellipodia to collectively drive cell-sheet movement. *J. Cell Sci.* **118**, 51–63 (2005). (Cited on pages 11 and 27.)

[Forgacs1998] Forgacs, G., Foty, R. A., Shafrir, Y. & Steinberg, M. S. Viscoelastic Properties of Living Embryonic Tissues: a Quantitative Study. *Biophys. J.* **74**, 2227–2234 (1998). (Cited on pages 29 and 196.)

[Fortunato2022] Fortunato, I. C. & Sunyer, R. The Forces behind Directed Cell Migration. *Biophysica* **2**, 548–563 (2022). (Cited on page 7.)

[Foty1994] Foty, R. A., Forgacs, G., Pfleger, C. M. & Steinberg, M. S. Liquid properties of embryonic tissues: Measurement of interfacial tensions. *Phys. Rev. Lett.* **72**, 2298–2301 (1994). (Cited on page 196.)

[Fournier2010] Fournier, M. F., Sauser, R., Ambrosi, D., Meister, J.-J. & Verkhovsky, A. B. Force transmission in migrating cells. *J. Cell Biol.* **188**, 287–297 (2010). (Cited on page 5.)

[Friedl2009] Friedl, P. & Gilmour, D. Collective cell migration in morphogenesis, regeneration and cancer. *Nat. Rev. Mole. Cell Biol.* **10**, 445–457 (2009). (Cited on page 8.)

[Garcia2019] Garcia-Arcos, J., Chabrier, R., Deygas, M., Nader, G., Barbier, L., Sáez, P., Mathur, A., Vargas, P. & Piel, M. Reconstitution of cell migration at a glance. *J. Cell Sci.* **132**, 225565 (2019). (Cited on page 3.)

[Garcia-Gonzalez2020] Garcia-Gonzalez, D. & Muñoz-Barrutia, A. Computational insights into the influence of substrate stiffness on collective cell migration. *Extreme Mech. Lett.* **40**, 100928 (2020). (Cited on page 23.)

[Garcin2019] Garcin, C. & Straube, A. Microtubules in cell migration. *Essays Biochem.* **63**, 509–520 (2019). (Cited on page 3.)

[García-Ojalvo1992] García-Ojalvo, J., Sancho, J. M. & Ramírez-Piscina, L. Generation af spatiotemporal colored noise. *Phys. Rev. A* **46**, 4670–4675 (1992). (Cited on page 158.)

[Gardel2004] Gardel, M. L., Shin, J. H., MacKintosh, F. C., Mahadevan, L., Matsudaira, P. & Weitz, D. A. Elastic Behavior of Cross-Linked and Bundled Actin Networks. *Science* **304**, 1301–1305 (2004). (Cited on pages 90 and 93.)

[Gardel2010] Gardel, M. L., Schneider, I. C., Aratyn-Schaus, Y. & Waterman, C. M. Mechanical Integration of Actin and Adhesion Dynamics in Cell Migration. *Annu. Rev. Cell Dev. Biol.* **26**, 315–333 (2010). (Cited on pages 4 and 7.)

[Gavara2006] Gavara, N., Sunyer, R., Roca-Cusachs, P., Farré, R., Rotger, M. & Navajas, D. Thrombin-induced contraction in alveolar epithelial cells probed by traction microscopy. *J. Appl. Physiol.* **101**, 512–520 (2006). (Cited on page 63.)

[Ghibaudo2008] Ghibaudo, M., Saez, A., Trichet, L., Xayaphoummine, A., Browaeys, J., Silberzan, P., Buguin, A. & Ladoux, B. Traction forces and rigidity sensing regulate cell functions. *Soft Matter* **4**, 1836–1843 (2008). (Cited on pages 61 and 89.)

[Giannone2009] Giannone, G., Mège, R. M. & Thoumine, O. Multi-level molecular clutches in motile cell processes. *Trends Cell Biol.* **19**, 475–486 (2009). (Cited on page 57.)

[González-Rodríguez2012] González-Rodríguez, D., Guevorkian, K., Douezan, S. & Brochard-Wyart, F. Soft matter models of developing tissues and tumors. *Science* **338**, 910–7 (2012). (Cited on pages 18 and 58.)

[González-Valverde2018] González-Valverde, I. & García-Aznar, J. M. Mechanical modeling of collective cell migration: An agent-based and continuum material approach. *Comput. Methods Appl. Mech. Eng.* **337**, 246–262 (2018). (Cited on pages 23 and 48.)

[Grimaldi2020] Grimaldi, C., Schumacher, I., Boquet-Pujadas, A., Tarbashevich, K., Vos, B. E., Bandemer, J., Schick, J., Aalto, A., Olivo-Marin, J. C., Betz, T. & Raz, E. E-cadherin focuses protrusion formation at the front of migrating cells by impeding actin flow. *Nat. Commun.* **11**, 5397 (2020). (Cited on page 57.)

[Guevorkian2010] Guevorkian, K., Colbert, M. J., Durth, M., Dufour, S. & Brochard-Wyart, F. Aspiration of Biological Viscoelastic Drops. *Phys. Rev. Lett.* **104**, 218101 (2010). (Cited on pages 64 and 196.)

[Gupta2016] Gupta, M., Doss, B., Lim, C. T., Voituriez, R. & Ladoux, B. Single cell rigidity sensing: A complex relationship between focal adhesion dynamics and large-scale actin cytoskeleton remodeling. *Cell Adh. Migr.* **10**, 554–567 (2016). (Cited on page 89.)

[Gupta2015] Gupta, M., Sarangi, B. R., Deschamps, J., Nematbakhsh, Y., Callan-Jones, A., Margadant, F., Mège, R. M., Lim, C. T., Voituriez, R. & Ladoux, B. Adaptive rheology and ordering of cell cytoskeleton govern matrix rigidity sensing. *Nat. Commun.* **6**, 7525 (2015). (Cited on pages 7, 8, 35, and 89.)

[Hadjifrangiskou2023] Hadjifrangiskou, I., Ruske, L. J. & Yeomans, J. M. Active nematics with deformable particles. *Soft Matter* **19**, 6664–6670 (2023). (Cited on page 14.)

[Haeger2015] Haeger, A., Wolf, K., Zegers, M. M. & Friedl, P. Collective cell migration: Guidance principles and hierarchies. *Trends Cell Biol.* **25**, 556–566 (2015). (Cited on pages 12 and 82.)

[Hakim2017] Hakim, V. & Silberzan, P. Collective cell migration: a physics perspective. *Rep. Prog. Phys.* **80**, 076601 (2017). (Cited on pages 8 and 27.)

[Harris2012] Harris, A. R., Peter, J., Bellis, J., Baum, B., Kabla, A. & Charras, G. T. Characterizing the mechanics of cultured cell monolayers. *PNAS* **109**, 16449–16454 (2012). (Cited on page 17.)

[Hartman2016] Hartman, C. D., Isenberg, B. C., Chua, S. G. & Wong, J. Y. Vascular smooth muscle cell durotaxis depends on extracellular matrix composition. *PNAS* **113**, 11190–11195 (2016). (Cited on page 57.)

[Hennig2018] Hennig, K., Wang, I., Moreau, P., Valon, L., DeBeco, S., Coppey, M., Miroshnikova, Y. A., Albiges-Rizo, C., Favard, C., Voituriez, R. & Balland, M. Stick-slip dynamics of cell adhesion triggers spontaneous symmetry breaking and directional migration of mesenchymal cells on one-dimensional lines. *Sci. Adv.* **6**, eaau5670 (2020). (Cited on page 46.)

[Huveneers2012] Huveneers, S., Oldenburg, J., Spanjaard, E., van der Krogt, G., Grigoriev, I., Akhmanova, A., Rehmann, H. & de Rooij, J. Vinculin associates with endothelial VE-cadherin junctions to control force-dependent remodeling. *J. Cell Biol.* **196**, 641–652 (2012). (Cited on page 63.)

[Isenberg2009] Isenberg, B. C., DiMilla, P. A., Walker, M., Kim, S. & Wong, J. Y. Vascular Smooth Muscle Cell Durotaxis Depends on Substrate Stiffness Gradient Strength. *Biophys. J.* **97**, 1313–1322 (2009). (Cited on pages 7 and 57.)

[Iwabu2004] Iwabu, A., Smith, K., Allen, F. D., Lauffenburger, D. A. & Wells, A. Epidermal growth factor induces fibroblast contractility and motility via a protein kinase C delta-dependent pathway. *J. Biol. Chem.* **279**, 14551–14560 (2004). (Cited on page 109.)

[Jacobs2013] Jacobs, C. R., Huang, H. & Kwon, R. Y. *Introduction to cell mechanics and mechanobiology* (Garland Science, 2013). (Cited on page 5.)

[Jin2008] Jin, T., Xu, X. & Hereld, D. Chemotaxis, Chemokine Receptors and Human Disease. *Cytokine* **44**, 1–8 (2008). (Cited on page 6.)

[Joanny2007] Joanny, J., Jülicher, F., Kruse, K. & Prost, J. Hydrodynamic theory for multi-component active polar gels. *New J Phys.* **9**, 422 (2007). (Cited on page 17.)

[Jülicher2011] Jülicher, F. *Active fluids and gels. In New Trends in the Physics and Mechanics of Biological Systems.* edited by Amar, M. B., Goriely, A., Müller, M. M. & Cugliandolo, L., chap. 4 (Oxford University Press, 2011). (Cited on pages 14, 27, and 30.)

[Jülicher2018] Jülicher, F., Grill, S. W. & Salbreux, G. Hydrodynamic theory of active matter. *Rep. Prog. Phys.* **81**, 076601 (2018). (Cited on page 14.)

[Jülicher2007] Jülicher, F., Kruse, K., Prost, J. & Joanny, J. F. Active behavior of the Cytoskeleton. *Phys. Rep.* **449**, 3–28 (2007). (Cited on pages 13, 14, and 17.)

[Kandow2007] Kandow, C. E., Georges, P. C., Janmey, P. A. & Beningo, K. A. Polyacrylamide Hydrogels for Cell Mechanics: Steps Toward Optimization and Alternative Uses. *Methods Cell Biol.* **83**, 29–46 (2007). (Cited on pages 90 and 127.)

[Kawaguchi2017] Kawaguchi, K., Kageyama, R. & Sano, M. Topological defects control collective dynamics in neural progenitor cell cultures. *Nature* **545**, 327–331 (2017). (Cited on pages 14 and 17.)

[Khalilgharibi2016] Khalilgharibi, N., Fouchard, J., Recho, P., Charras, G. & Kabla, A. The dynamic mechanical properties of cellularised aggregates. *Curr. Opin. Cell Biol.* **42**, 113–120 (2016). (Cited on page 30.)

[Khurana2011] Khurana, S. & George, S. P. The role of actin bundling proteins in the assembly of filopodia in epithelial cells. *Cell Adhes. Migr.* **5**, 409–420 (2011). (Cited on page 3.)

[Killeen2022] Killeen, A., Bertrand, T. & Lee, C. F. Polar Fluctuations Lead to Extensile Nematic Behavior in Confluent Tissues. *Phys. Rev. Lett.* **128** (2022). (Cited on page 145.)

[Krause2014] Krause, M. & Gautreau, A. Steering cell migration: lamellipodium dynamics and the regulation of directional persistence. *Nat. Rev. Molec. Cell Biol.* **15**, 577–590 (2014). (Cited on page 3.)

[Kruse2006] Kruse, K., Joanny, J., Jülicher, F. & Prost, J. Contractility and retrograde flow in lamellipodium motion. *Phys. Biol.* **3**, 130 (2006). (Cited on page 17.)

[Kruse2004] Kruse, K., Joanny, J., Jülicher, F., Prost, J. & Sekimoto, K. Asters, Vortices, and Rotating Spirals in Active Gels of Polar Filaments. *Phys. Rev. Lett.* **92**, 078101 (2004). (Cited on pages 14 and 17.)

[Kruse2005] Kruse, K., Joanny, J. F., Jülicher, F., Prost, J. & Sekimoto, K. Generic theory of active polar gels: A paradigm for cytoskeletal dynamics. *Eur. Phys. J. E* **16**, 5–16 (2005). (Cited on pages 13, 14, 27, and 30.)

[Köpf2013] Köpf, M. H. & Pismen, L. M. A continuum model of epithelial spreading. *Soft Matter* **9**, 3727 (2013). (Cited on page 17.)

[Ladoux2017] Ladoux, B. & Mège, R.-M. Mechanobiology of collective cell behaviours. *Nat. Rev. Mol. Cell Biol.* **18**, 743–757 (2017). (Cited on pages 6, 8, 10, and 90.)

[Ladoux2016] Ladoux, B., Mège, R.-M. & Trepat, X. Front-Rear Polarization by Mechanical Cues: From Single Cells to Tissues. *Trends Cell Biol.* **26**, 420–433 (2016). (Cited on pages 7, 8, and 27.)

[Ladoux2012] Ladoux, B. & Nicolas, A. Physically based principles of cell adhesion mechanosensitivity in tissues. *Reports Prog. Phys.* **75**, 116601 (2012). (Cited on page 89.)

[Landau1959] Landau, L. & Lifshitz, E. *Theory of Elasticity* (Pergamon Press, 1959). (Cited on pages 92 and 94.)

[Lecuit2007] Lecuit, T. & Lenne, P. F. Cell surface mechanics and the control of cell shape, tissue patterns and morphogenesis. *Nat. Rev. Mol. Cell Biol.* **8**, 633–644 (2007). (Cited on page 64.)

[Lee2011b] Lee, P. & Wolgemuth, C. Advent of complex flows in epithelial tissues. *Phys. Rev. E Stat. Nonlin. Soft Matter Phys.* **83**, 1–5 (2011). (Cited on pages 14 and 29.)

[Lee2011a] Lee, P. & Wolgemuth, C. W. Crawling Cells Can Close Wounds without Purse Strings or Signaling. *PLoS Comput. Biol.* **7**, e1002007 (2011). (Cited on pages 14, 17, and 29.)

[Li2015] Li, J., Han, D. & Zhao, Y.-P. Kinetic behaviour of the cells touching substrate: the interfacial stiffness guides cell spreading. *Sci. Rep.* **4**, 3910 (2015). (Cited on page 89.)

[Liu2014] Liu, Q. & Song, B. Electric field regulated signaling pathways. *Int. J Biochem. Cell Biol.* **55**, 264–268 (2014). (Cited on page 6.)

[Lo2000] Lo, C.-M., Wang, H.-B., Dembo, M. & li Wang, Y. Cell Movement Is Guided by the Rigidity of the Substrate. *Biophys. J.* **79**, 144–152 (2000). (Cited on pages 6, 7, 23, and 57.)

[Lodish2000] Lodish, H., Berk, A., Zipursky, S. L., Matsudaira, P., Baltimore, D. *et al.* *Molecular Cell Biology* (W. H. Freeman & Company, 2000). (Cited on page 5.)

[Luccardini2013] Luccardini, C., Hennekinne, L., Viou, L., Yanagida, M., Murakami, F., Kessaris, N., Ma, X., Adelstein, R. S., Mège, R. M. & Métin, C. N-Cadherin Sustains Motility and Polarity of Future Cortical Interneurons during Tangential Migration. *J. Neurosci.* **33**, 18149–18160 (2013). (Cited on page 57.)

[Lyon2019] Lyon, J. G., Mokarram, C. & Bellamkonda, R. V. Electrotaxis of Glioblastoma and Medulloblastoma Spheroidal Aggregates. *Sci. Rep.* **9**, 5309 (2019). (Cited on page 12.)

[Maiuri2015] Maiuri, P., Rupprecht, J. F., Wieser, S., Ruprecht, V., Bénichou, O., Carpi, N., Coppey, M., Beco, S. D., Gov, N., Heisenberg, C. P., Crespo, C. L., Lautenschlaeger, F., Berre, M. L., Lennon-Dumenil, A. M., Raab, M., Thiam, H. R., Piel, M., Sixt, M. & Voituriez, R. Actin flows mediate a universal coupling between cell speed and cell persistence. *Cell* **161**, 374–386 (2015). (Cited on page 6.)

[Majumdar2014] Majumdar, R., Sixt, M. & Parent, C. A. New paradigms in the establishment and maintenance of gradients during directed cell migration. *Curr. Opin. Cell Biol.* **30**, 33–40 (2014). (Cited on page 12.)

[Manning2010] Manning, M. L., Foty, R. A., Steinberg, M. S. & Schoetz, E.-M. Coaction of intercellular adhesion and cortical tension specifies tissue surface tension. *PNAS* **107**, 12517–12522 (2010). (Cited on pages 64 and 78.)

[Marchetti2013] Marchetti, M., Joanny, J. F., Ramaswamy, S., Liverpool, T. B., Prost, J., Rao, M. & Simha, R. A. Hydrodynamics of soft active matter. *Rev. Mod. Phys.* **85**, 1143–1189 (2013). (Cited on pages 12, 13, 14, 15, 27, 30, and 32.)

[Marcq2011] Marcq, P., Yoshinaga, N. & Prost, J. Rigidity Sensing Explained by Active Matter Theory. *Biophys. J.* **101**, PL33–L35 (2011). (Cited on page 35.)

[Marel2014] Marel, A.-K., Zorn, M., Klingner, C., Wedlich-Söldner, R., Frey, E. & Rädler, J. O. Flow and Diffusion in Channel-Guided Cell Migration. *Biophys. J.* **107**, 1054–1064 (2014). (Cited on page 14.)

[Maroudas-Sacks2021] Maroudas-Sacks, Y., Garion, L., Shani-Zerbib, L. *et al.* Topological defects in the nematic order of actin fibres as organization centres of Hydra morphogenesis. *Nat. Phys.* **17**, 251–259 (2021). (Cited on page 14.)

[Martinez2016] Martinez, J. S., Schlenoff, J. B. & Keller, T. C. Collective epithelial cell sheet adhesion and migration on polyelectrolyte multilayers with uniform and gradients of compliance. *Exp. Cell Res.* **346**, 17–29 (2016). (Cited on page 82.)

[Mayer2010] Mayer, M., Depken, M., Bois, J. S., Jülicher, F. & Grill, S. W. Anisotropies in cortical tension reveal the physical basis of polarizing cortical flows. *Nature* **467**, 617–621 (2010). (Cited on page 11.)

[Mayor2010] Mayor, R. & Carmona-Fontaine, C. Keeping in touch with contact inhibition of locomotion. *Trends Cell Biol.* **20**, 319–328 (2010). (Cited on pages 4 and 27.)

[Mayor2016] Mayor, R. & Etienne-Manneville, S. The front and rear of collective cell migration. *Nat. Rev. Mole. Cell Biol.* **17**, 97–109 (2016). (Cited on pages 8, 10, and 27.)

[Maître2011] Maître, J. L. & Heisenberg, C. P. The role of adhesion energy in controlling cell-cell contacts. *Curr. Opin. Cell Biol.* **23**, 508–514 (2011). (Cited on page 64.)

[Murrell2015] Murrell, M., Oakes, P., Lenz, M. & Gardel, M. L. Forcing cells into shape: the mechanics of actomyosin contractility. *Nat. Rev. Molec. Cell Biol.* **16**, 486–498 (2015). (Cited on page 2.)

[Münster2013] Münster, S., Jawerth, L. M., Leslie, B. A., Weitz, J. I., Fabry, B. & Weitz, D. A. Strain history dependence of the nonlinear stress response of fibrin and collagen networks. *PNAS* **110**, 12197–12202 (2013). (Cited on page 90.)

[Needleman2017] Needleman, D. & Dogic, Z. Active matter at the interface between materials science and cell biology. *Nat. Rev. Mat.* **2**, 17048 (2017). (Cited on page 16.)

[Ng2012] Ng, M. R., Besser, A., Danuser, G. & Brugge, J. S. Substrate stiffness regulates cadherin-dependent collective migration through myosin-II contractility. *J. Cell Biol.* **199**, 545–563 (2012). (Cited on pages 10 and 12.)

[Nguyen2000] Nguyen, B. P., Ryan, M. C., Gil, S. G. & Carter, W. G. Deposition of laminin 5 in epidermal wounds regulates integrin signaling and adhesion. *Curr. Opin. Cell Biol.* **12**, 554–562 (2000). (Cited on page 6.)

[Nguyen2019] Nguyen, T., Duchesne, L., Narayana, G. H. N. S., Boggetto, N., Fernig, D. D., Murade, C. U., Ladoux, B. & Mège, R. M. Enhanced cell–cell contact stability and decreased N-cadherin-mediated migration upon fibroblast growth factor receptor-N-cadherin cross talk. *Oncogene* **38**, 6283–6300 (2019). (Cited on page 57.)

[Nguyen2012] Nguyen-Ngoc, K. V., Cheung, K. J., Brenot, A., Shamir, E. R., Gray, R. S., Hines, W. C., Yaswen, P., Werb, Z. & Ewald, A. J. ECM microenvironment regulates collective migration and local dissemination in normal and malignant mammary epithelium. *PNAS* **109**, E2595–E2604 (2012). (Cited on page 12.)

[Nier2015] Nier, V., Deforet, M., Duclos, G., Yevick, H. G., Cochet-Escartin, O., Marcq, P. & Silberzan, P. Tissue fusion over nonadhering surfaces. *PNAS* **112**, 9546–9551 (2015). (Cited on page 196.)

[Nédélec1997] Nédélec, J., Surrey, T., Maggs, A. & Leibler, S. Self-organization of microtubules and motors. *Nature* **389**, 305–308 (1997). (Cited on page 13.)

[Oakes2012] Oakes, P. W., Beckham, Y., Stricker, J. & Gardel, M. L. Tension is required but not sufficient for focal adhesion maturation without a stress fiber template. *J. Cell Biol.* **196**, 363–374 (2012). (Cited on page 63.)

[Obyrne2022] O'Byrne, J., Kafri, Y., Tailleur, J. & van Wijland, F. Time irreversibility in active matter, from micro to macro. *Nat. Rev. Phys.* **4**, 167–183 (2022). (Cited on page 13.)

[Oriola2017] Oriola, D., Alert, R. & Casademunt, J. Fluidization and Active Thinning by Molecular Kinetics in Active Gels. *Phys. Rev. Lett.* **118**, 088002 (2017). (Cited on pages 30 and 41.)

[Ozawa2020] Ozawa, M., Hiver, S., Yamamoto, T., Shibata, T., Upadhyayula, S., Mimori-Kiyosue, Y. & Takeichi, M. Adherens junction regulates cryptic lamellipodia formation for epithelial cell migration. *J. Cell Biol.* **219**, e202006196 (2020). (Cited on page 9.)

[Padmanaban2019] Padmanaban, V., Krol, I., Suhail, Y., Szczerba, B. M., Aceto, N., Bader, J. S. & Ewald, A. J. E-cadherin is required for metastasis in multiple models of breast cancer. *Nature* **573**, 439–444 (2019). (Cited on page 57.)

[Pallarès2023] Pallarès, M. E., Pi-Jaumà, I., Fortunato, I. C. *et al.* Stiffness-dependent active wetting enables optimal collective cell durotaxis. *Nat. Phys.* **19**, 279–289 (2023). (Cited on pages 57, 89, 136, 146, and 147.)

[Palsson2000] Palsson, E. & Othmer, H. G. A model for individual and collective cell movement in Dictyostelium discoideum. *PNAS* **97**, 10448–10453 (2000). (Cited on page 6.)

[Paluch2013] Paluch, E. K. & Raz, E. The role and regulation of blebs in cell migration. *Curr. Opin. Cell Biol.* **25**, 582–590 (2013). (Cited on page 5.)

[Parsons2010] Parsons, J., Horwitz, A. & Schwartz, M. Cell adhesion: integrating cytoskeletal dynamics and cellular tension. *Nat. Rev. Molec. Cell Biol.* **11**, 633–643 (2010). (Cited on page 4.)

[Petrie2009] Petrie, R. J., Doyle, A. D. & Yamada, K. M. Random versus directionally persistent cell migration. *Nat. Rev. Molec. Cell Biol.* **10**, 538–549 (2009). (Cited on page 6.)

[Plotnikov2012] Plotnikov, S. V., Pasapera, A. M., Sabass, B. & Waterman, C. M. Force Fluctuations within Focal Adhesions Mediate ECM-Rigidity

Sensing to Guide Directed Cell Migration. *Cell* **151**, 1513–1527 (2012). (Cited on page 7.)

[Pollard2003] Pollard, T. D. & Borisy, G. G. Cellular Motility Driven by Assembly and Disassembly of Actin Filaments. *Cell* **112**, 453–465 (2003). (Cited on pages 115 and 116.)

[Pollard2009] Pollard, T. D. & Cooper, J. A. Actin, a central player in cell shape and movement. *Science* **326**, 1208–1212 (2009). (Cited on page 90.)

[Poujade2007] Poujade, M., Grasland-Mongrain, E., Hertzog, A., Jouanneau, J., Chavrier, P., Ladoux, B., Buguin, A. & Silberzan, P. Collective migration of an epithelial monolayer in response to a model wound. *PNAS* **104**, 15988–15993 (2007). (Cited on pages 9, 10, and 126.)

[Poukkula2011] Poukkula, M., Cliffe, A., Changede, R. & Rørth, P. Cell behaviors regulated by guidance cues in collective migration of border cells. *J. Cell Biol.* **192**, 513–524 (2011). (Cited on page 6.)

[Prescott2021] Prescott, T. P., Zhu, K., Zhao, M. & Baker, R. E. Quantifying the impact of electric fields on single-cell motility. *Biophys. J.* **120**, 3363–3373 (2021). (Cited on page 6.)

[Prost2015] Prost, J., Jülicher, F. & Joanny, J. F. Active gel physics. *Nat. Phys.* **11**, 111–117 (2015). (Cited on pages 13, 17, 27, and 30.)

[Pérez-González2019] Pérez-González, C., Alert, R., Blanch-Mercader, C., Gómez-González, M., Kolodziej, T., Bazellieres, E., Casademunt, J. & Trepat, X. Active wetting of epithelial tissues. *Nat. Phys.* **15**, 79–88 (2019). (Cited on pages 9, 14, 18, 19, 20, 24, 26, 27, 28, 29, 30, 31, 32, 33, 37, 58, 64, 65, 66, 71, 76, 78, 81, 109, 117, 119, 122, 129, 148, 164, 165, 169, 170, 184, 195, and 196.)

[Recho2013] Recho, P., Putelat, T. & Truskinovsky, L. Contraction-Driven Cell Motility. *Phys. Rev. Lett.* **111**, 2–6 (2013). (Cited on pages 46 and 51.)

[Recho2016] Recho, P., Ranft, J. & Marcq, P. One-dimensional collective migration of a proliferating cell monolayer. *Soft Matter* **12**, 2381–2391 (2016). (Cited on page 14.)

[Richardson2010] Richardson, B. E. & Lehmann, R. Mechanisms guiding primordial germ cell migration: Strategies from different organisms. *Nat. Rev. Mol. Cell Biol.* **11**, 37–49 (2010). (Cited on page 57.)

[Ricoult2015] Ricoult, S. G., Kennedy, T. E. & Juncker, D. Substrate-bound protein gradients to study haptotaxis. *Front. Bioeng. Biotechnol.* **3**, 40 (2015). (Cited on page 6.)

[Riveline2001] Riveline, D., Zamir, E., Balaban, N. Q., Schwarz, U. S., Ishizaki, T., Narumiya, S., Kam, Z., Geiger, B. & Bershadsky, A. D. Focal Contacts as Mechanosensors: Externally Applied Local Mechanical Force Induces Growth of Focal Contacts by an mDia1-dependent and ROCK-independent Mechanism. *J. Cell Biol.* **153**, 1175–1185 (2001). (Cited on page 61.)

[Ronnov-Jessen1996] Ronnov-Jessen, L., Petersen, O. W. & Bissell, M. J. Cellular changes involved in conversion of normal to malignant breast: importance of the stromal reaction. *Physiol. Rev.* **76**, 69–125 (1996). (Cited on page 110.)

[Rossen2014] Rossen, N. S., Tarp, J. M., Mathiesen, J., Jensen, M. H. & Oddershede, L. B. Long-range ordered vorticity patterns in living tissue induced by cell division. *Nat. Commun.* **5**, 5720 (2014). (Cited on page 10.)

[Rossetti2024] Rossetti, L., Grosser, S., Abenza, J. F., Valon, L., Roca-Cusachs, P., Alert, R. & Trepat, X. Optogenetic generation of leader cells reveals a force–velocity relation for collective cell migration. *Nat. Phys.* **20**, 1659–1669 (2024). (Cited on page 12.)

[Ryan2001] Ryan, P. L., Foty, R. A., Kohn, J. & Steinberg, M. S. Tissue spreading on implantable substrates is a competitive outcome of cell-cell vs. cell-substratum adhesivity. *PNAS* **98**, 4323–4327 (2001). (Cited on pages 18 and 65.)

[Sabass2008] Sabass, B., Gardel, M. L., Waterman, C. M. & Schwarz, U. S. High Resolution Traction Force Microscopy Based on Experimental and Computational Advances. *Biophys. J.* **94**, 207–220 (2008). (Cited on page 90.)

[Saez2010] Saez, A., Anon, E., Ghibaudo, M., du Roure, O., Di Meglio, J.-M., Hersen, P., Silberzan, P., Buguin, A. & Ladoux, B. Traction forces exerted by epithelial cell sheets. *J. Phys. Condens. Matter* **22**, 194119 (2010). (Cited on pages 35 and 89.)

[Saez2005] Saez, A., Buguin, A., Silberzan, P. & Ladoux, B. Is the Mechanical Activity of Epithelial Cells Controlled by Deformations or Forces? *Biophys. J.* **89**, L52–4 (2005). (Cited on page 89.)

[Salbreux2009] Salbreux, G., Prost, J. & Joanny, J. Hydrodynamics of Cellular Cortical Flows and the Formation of Contractile Rings. *Phys. Rev. Lett.* **103**, 058102 (2009). (Cited on page 17.)

[Sanchez2012] Sanchez, T., Chen, D. T., DeCamp, S. J., Heymann, M. & Dogic, Z. Spontaneous motion in hierarchically assembled active matter. *Nature* **491**, 431 (2012). (Cited on page 16.)

[Saraswathibhatla2021] Saraswathibhatla, A., Henkes, S., Galles, E. E., Sknepnek, R. & Notbohm, J. Coordinated tractions increase the size of a collectively moving pack in a cell monolayer. *Extreme Mech. Lett.* **48**, 101438 (2021). (Cited on page 171.)

[Saw2017] Saw, T. B., Doostmohammadi, A., Nier, V., Kocgozlu, L., Thampi, S., Toyama, Y., Marcq, P., Lim, C. T., Yeomans, J. M. & Ladoux, B. Topological defects in epithelia govern cell death and extrusion. *Nature* **544**, 212–216 (2017). (Cited on pages 14 and 17.)

[Saw2018] Saw, T. B., Xi, W., Ladoux, B. & Lim, C. T. Biological Tissues as Active Nematic Liquid Crystals. *Adv. Mat.* **30**, 1–12 (2018). (Cited on page 16.)

[Schedin2004] Schedin, P. & Elias, A. Multistep tumorigenesis and the microenvironment. *Breast Cancer Res.* **6**, 93–101 (2004). (Cited on page 110.)

[Schweitzer2003] Schweitzer, F. *Brownian Agents and Active Particles: Collective Dynamics in the Natural and Social Sciences* (Springer, Berlin, 2003). (Cited on page 12.)

[Seetharaman2020] Seetharaman, S. & Etienne-Manneville, S. Cytoskeletal Crosstalk in Cell Migration. *Trends in Cell Biol.* **30**, 720–735 (2020). (Cited on page 3.)

[Sens2013] Sens, P. Rigidity sensing by stochastic sliding friction. *Europhys. Lett.* **104**, 38003 (2013). (Cited on page 35.)

[Serra-Picamal2012] Serra-Picamal, X., Conte, V., Vincent, R., Anon, E., Tambe, D. T., Bazellieres, E., Butler, J. P., Fredberg, J. J. & Trepat, X. Mechanical waves during tissue expansion. *Nat. Phys.* **8**, 628–634 (2012). (Cited on pages 17, 58, 126, 129, 146, and 147.)

[Shamir2014] Shamir, E. R., Pappalardo, E., Jorgens, D. M., Coutinho, K., Tsai, W. T., Aziz, K., Auer, M., Tran, P. T., Bader, J. S. & Ewald, A. J.

Twist1-induced dissemination preserves epithelial identity and requires E-cadherin. *J. Cell Biol.* **204**, 839–856 (2014). (Cited on page 57.)

[Shekhar2003] Shekhar, M. P. V., Pauley, R. & Heppner, G. Host microenvironment in breast cancer development: extracellular matrix–stromal cell contribution to neoplastic phenotype of epithelial cells in the breast. *Breast Cancer Res.* **5**, 130–135 (2003). (Cited on page 110.)

[Shellard2021a] Shellard, A. & Mayor, R. Collective durotaxis along a self-generated stiffness gradient in vivo. *Nature* **600**, 690–694 (2021). (Cited on pages 12, 55, 56, and 82.)

[Shellard2021b] Shellard, A. & Mayor, R. Durotaxis: The Hard Path from In Vitro to In Vivo. *Dev. Cell* **56**, 227–239 (2021). (Cited on pages 57 and 82.)

[Shimizu2005] Shimizu, T., Yabe, T., Muraoka, O., Yonemura, S., Aramaki, S., Hatta, K., Bae, Y. K., Nojima, H. & Hibi, M. E-cadherin is required for gastrulation cell movements in zebrafish. *Mech. Dev.* **122**, 747–763 (2005). (Cited on page 57.)

[Smeets2016] Smeets, B., Alert, R., Pešek, J., Pagonabarraga, I., Ramon, H. & Vincent, R. Emergent structures and dynamics of cell colonies by contact inhibition of locomotion. *PNAS* **113**, 14621–14626 (2016). (Cited on pages 27 and 28.)

[Smutny2010] Smutny, M., Cox, H. L., Leerberg, J. M. *et al.* Myosin II isoforms identify distinct functional modules that support integrity of the epithelial zonula adherens. *Nat. Cell Biol.* **12**, 696–702 (2010). (Cited on page 63.)

[Sonal2018] Sonal, Ganzinger, K. A., Vogel, S. K., Mücksch, J., Blumhardt, P. & Schwille, P. Myosin-II activity generates a dynamic steady state with continuous actin turnover in a minimal actin cortex. *J. Cell Sci.* **132**, jcs219899 (2018). (Cited on page 5.)

[Song2020] Song, D. *et al.* Recovery of Tractions Exerted by Single Cells in Three-Dimensional Nonlinear Matrices. *J. Biomech. Eng.* **142**, 081012 (2020). (Cited on page 90.)

[Steinwachs2016] Steinwachs, J. *et al.* Three-dimensional force microscopy of cells in biopolymer networks. *Nat. Methods* **13**, 171–176 (2016). (Cited on page 90.)

[Stirbat2013] Stirbat, T. V., Mgharbel, A., Bodennec, S., Ferri, K., Mertani, H. C., Rieu, J. P. & Delanoë-Ayari, H. Fine Tuning of Tissues' Viscosity and Surface Tension through Contractility Suggests a New Role for α-Catenin. *PLoS One* **8**, e52554 (2013). (Cited on page 196.)

[Storm2005] Storm, C., Pastore, J. J., MacKintosh, F. C., Lubensky, T. C. & Janmey, P. A. Nonlinear elasticity in biological gels. *Nature* **435**, 191–194 (2005). (Cited on pages 90, 91, 93, and 127.)

[Stricker2013] Stricker, J., Beckham, Y., Davidson, M. W. & Gardel, M. L. Myosin II-Mediated Focal Adhesion Maturation Is Tension Insensitive. *PLoS One* **8**, e70652 (2013). (Cited on page 63.)

[Sunyer2016] Sunyer, R., Conte, V., Escribano, J., Elosegui-Artola, A., Labernadie, A., Valon, L., Navajas, D., García-Aznar, J. M., Muñoz, J. J., Roca-Cusachs, P. & Trepat, X. Collective cell durotaxis emerges from long-range intercellular force transmission. *Science* **353**, 1157–1161 (2016). (Cited on pages 12, 23, 24, 25, 27, 31, 32, 39, 41, 48, 49, 57, 63, 82, 126, and 196.)

[Sunyer2012] Sunyer, R., Jin, A. J., Nossal, R. & Sackett, D. L. Fabrication of Hydrogels with Steep Stiffness Gradients for Studying Cell Mechanical Response. *PLoS One* **7**, e46107 (2012). (Cited on pages 7 and 58.)

[Sunyer2020] Sunyer, R. & Trepat, X. Durotaxis. *Curr. Biol.* **30**, R371–R392 (2020). (Cited on page 6.)

[Svitkina1999] Svitkina, T. M. & Borisy, G. G. Arp2/3 complex and actin depolymerizing factor/cofilin in dendritic organization and treadmilling of actin filament array in lamellipodia. *J. Cell Biol.* **145**, 1009–1026 (1999). (Cited on page 4.)

[Tan2003] Tan, J. L. *et al.* Cells lying on a bed of microneedles: An approach to isolate mechanical force. *PNAS* **100**, 1484–1489 (2003). (Cited on page 11.)

[Tang2017] Tang, D. D. & Gerlach, B. D. The roles and regulation of the actin cytoskeleton, intermediate filaments and microtubules in smooth muscle cell migration. *Respir. Res.* **18**, 54 (2017). (Cited on page 4.)

[Tanimoto2014] Tanimoto, H., Sano, M., Ishihara, S. & Sugimura, K. A Simple Force-Motion Relation for Migrating Cells Revealed by Multipole Analysis of Traction Stress. *Biophys. J.* **106**, 16–25 (2014). (Cited on page 5.)

[Theveneau2013] Theveneau, E. & Mayor, R. Collective cell migration of epithelial and mesenchymal cells. *Cell. Mol. Life Sci.* **70**, 3481–3492 (2013). (Cited on page 27.)

[Thomas2013] Thomas, W. A., Boscher, C., Chu, Y. S., Cuvelier, D., Martinez-Rico, C., Seddiki, R., Heysch, J., Ladoux, B., Thiery, J. P., Mege, R. M. & Dufour, S. α-Catenin and Vinculin Cooperate to Promote High E-cadherin-based Adhesion Strength. *J. Biol. Chem.* **288**, 4957–4969 (2013). (Cited on page 30.)

[Thoresen2011] Thoresen, T., Lenz, M. & Gardel, M. L. Reconstitution of Contractile Actomyosin Bundles. *Biophys. J.* **100**, 2698 (2011). (Cited on page 16.)

[Toyjanova2014] Toyjanova, J. *et al.* High Resolution, Large Deformation 3D Traction Force Microscopy. *PLoS One* **9**, e90976 (2014). (Cited on page 90.)

[Trepat2009] Trepat, X., Wasserman, M. R., Angelini, T. E., Millet, E., Weitz, D. A., Butler, J. P. & Fredberg, J. J. Physical forces during collective cell migration. *Nat. Phys.* **5**, 426–430 (2009). (Cited on pages 11, 27, 58, 71, 90, 92, 95, 146, 195, and 196.)

[Trichet2012] Trichet, L., Le Digabel, J., Hawkins, R. J., Vedula, S. R. K., Gupta, M., Ribrault, C., Hersen, P., Voituriez, R. & Ladoux, B. Evidence of a large-scale mechanosensing mechanism for cellular adaptation to substrate stiffness. *PNAS* **109**, 6933–6938 (2012). (Cited on pages 35 and 89.)

[Tse2010] Tse, J. R. & Engler, A. J. Preparation of Hydrogel Substrates with Tunable Mechanical Properties. *Curr. Protoc. Cell Biol.* **47**, 10.16.1–10.16.16 (2010). (Cited on page 128.)

[Tse2011] Tse, J. R. & Engler, A. J. Stiffness Gradients Mimicking In Vivo Tissue Variation Regulate Mesenchymal Stem Cell Fate. *PLoS One* **6**, e15978 (2011). (Cited on page 7.)

[Uroz2018] Uroz, M., Wistorf, S., Serra-Picamal, X., Conte, V., Sales-Pardo, M., Roca-Cusachs, P., Guimerà, R. & Trepat, X. Regulation of cell cycle progression by cell-cell and cell-matrix forces. *Nat. Cell Biol.* **20**, 646–654 (2018). (Cited on pages 58, 126, 148, 164, 165, 169, and 183.)

[vanderLinden2019] van der Linden, M. N., Alexander, L. C., Aarts, D. G. A. L. & Dauchot, O. Interrupted Motility Induced Phase Separation in Aligning Active Colloids. *Phys. Rev. Lett.* **123**, 098001 (2019). (Cited on page 13.)

[vanKempen2003] van Kempen, L. C., Ruiter, D. J., van Muijen, G. N. & Coussens, L. M. The tumor microenvironment: a critical determinant of neoplastic evolution. *Eur. J. Cell Biol.* **82**, 539–548 (2003). (Cited on page 110.)

[Vassaux2020] Vassaux, M., Pieuchot, L., Anselme, K., Bigerelle, M. & Milan, J.-L. *Developments and Novel Approaches in Biomechanics and Metamaterials* (Springer International Publishing, Cham, 2020). (Cited on page 6.)

[Vasudevan2023] Vasudevan, J., Jiang, K., Fernandez, J. & Lim, C. T. Extracellular matrix mechanobiology in cancer cell migration. *Acta Biomater.* **163**, 351–364 (2023). (Cited on page 110.)

[Vedula2013] Vedula, S. R. K., Ravasio, A., Lim, C. T. & Ladoux, B. Collective Cell Migration: A Mechanistic Perspective. *Physiol.* **28**, 370–379 (2013). (Cited on pages 8 and 27.)

[Verkhovsky1998] Verkhovsky, A. B., Svitkina, T. M. & Borisy, G. G. Self-polarization and directional motility of cytoplasm. *Curr. Biol.* **9**, 11–20 (1998). (Cited on pages 115 and 116.)

[Vincent2013] Vincent, L. G., Choi, Y. S., Alonso-Latorre, B., del Álamo, J. C. & Engler, A. J. Mesenchymal Stem Cell Durotaxis Depends on Substrate Stiffness Gradient Strength. *Biotechnol. J.* **8**, 472–484 (2013). (Cited on pages 6, 7, and 57.)

[Vincent2015] Vincent, R., Bazellières, E., Pérez-González, C., Uroz, M., Serra-Picamal, X. & Trepat, X. Active Tensile Modulus of an Epithelial Monolayer. *Phys. Rev. Lett.* **115**, 248103 (2015). (Cited on page 17.)

[Voituriez2005] Voituriez, R., Joanny, J. & Prost, J. Spontaneous flow transition in active polar gels. *Europhys. Lett.* **70**, 404 (2005). (Cited on page 17.)

[Voituriez2006] Voituriez, R., Joanny, J. & Prost, J. Generic Phase Diagram of Active Polar Films. *Phys. Rev. Lett.* **96**, 028102 (2006). (Cited on page 17.)

[Walcott2010] Walcott, S. & Sun, S. X. A mechanical model of actin stress fiber formation and substrate elasticity sensing in adherent cells. *PNAS* **107**, 7757–7762 (2010). (Cited on page 35.)

[Wallmeyer2018] Wallmeyer, B., Trinschek, S., Yigit, S., Thiele, U. & Betz, T. Collective Cell Migration in Embryogenesis Follows the Laws of Wetting. *Biophys. J.* **114**, 213–222 (2018). (Cited on page 58.)

[Wang2002] Wang, N., Ostuni, E., Whitesides, G. M. & Ingber, D. E. Micropatterning tractional forces in living cells. *Cell Motil. Cytoskel.* **52**, 97–106 (2002). (Cited on page 126.)

[Weiss1988] Weiss, L. *Cell and Tissue Biology: A Textbook of Histology* (Urban & Schwarzenberg, Munich, 1988). (Cited on page 9.)

[Wong2021] Wong, M. & Gilmour, D. Going your own way: Self-guidance mechanisms in cell migration. *Curr. Opin. Cell Biol.* **72**, 116–123 (2021). (Cited on page 6.)

[Wyatt2016] Wyatt, T., Baum, B. & Charras, G. A question of time: tissue adaptation to mechanical forces. *Curr. Opin. Cell Biol.* **38**, 68–73 (2016). (Cited on page 30.)

[Yeung2005] Yeung, T., Georges, P. C., Flanagan, L. A., Marg, B., Ortiz, M., Funaki, M., Zahir, N., Ming, W., Weaver, V. & Janmey, P. A. Effects of substrate stiffness on cell morphology, cytoskeletal structure, and adhesion. *Cell Motil. Cytoskel.* **60**, 24–34 (2005). (Cited on page 127.)

[Zhao2024] Zhao, Y., Zakine, R., Daerr, A., Kafri, Y., Tailleur, J. & van Wijland, F. Active Young-Dupré Equation: How Self-organized Currents Stabilize Partial Wetting. *bioRxiv* (2024). (Cited on page 65.)

[Zhu2020] Zhu, M., Tao, H., Samani, M., Luo, M., Wang, X., Hopyan, S. & Sun, Y. Spatial mapping of tissue properties in vivo reveals a 3D stiffness gradient in the mouse limb bud. *PNAS* **117**, 4781–4791 (2020). (Cited on pages 12 and 82.)

[Zimmermann2016] Zimmermann, J., Camley, B. A., Rappel, W. J. & Levine, H. Contact inhibition of locomotion determines cell-cell and cell-substrate forces in tissues. *PNAS* **113**, 2660–2665 (2016). (Cited on page 27.)